THERMOMECHANICAL PROPERTIES OF CENTER REINFORCED ALUMINUM

THESIS

Geofrey S. Cox, Captain, USAF

AFIT/GAE/ENY/09-M04

DEPARTMENT OF THE AIR FORCE
AIR UNIVERSITY

AIR FORCE INSTITUTE OF TECHNOLOGY

Wright-Patterson Air Force Base, Ohio

THERMOMECHANICAL PROPERTIES OF CENTER REINFORCED ALUMINUM

THESIS

Presented to the Faculty

Department of Aeronautical and Astronautical Engineering

Graduate School of Engineering and Management

Air Force Institute of Technology

Air University

Air Education and Training Command

In Partial Fulfillment of the Requirements for the

Degree of Master of Science in Aeronautical Engineering

Geofrey S. Cox, B.S.M.E.

Captain, USAF

March 2009

THERMOMECHANICAL PROPERTIES OF CENTER REINFORCED ALUMINUM

Geofrey S. Cox, B.S.M.E.

Captain, USAF

Approved:

_____   3/13/09

Dr. Marina B. Ruggles-Wrenn (Chair)   Date
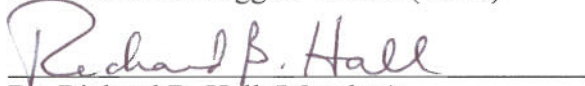
_____   3/13/09

Dr. Richard B. Hall (Member)   Date
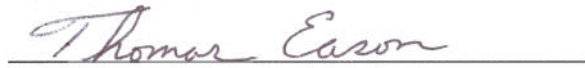
_____   3/13/09

Dr. Thomas G. Eason (Member)   Date

AFIT/GAE/ENY/09-M04

Abstract

This effort explored the performance of an advanced hybrid material, CentrAl (Center-reinforced Aluminum), under monotonic thermo-mechanical loading and dynamic mechanical loading. Mechanical behavior of a single CentrAl variant was predicted using the rule of mixtures and Metal Volume Fraction (MVF) approach, through combination of previously established characteristics of the individual constituent materials. Monotonic and dynamic tests were conducted on coupon-level specimens of CentrAl using standardized testing procedures. Static tests to measure modulus, strength, and blunt notch (open-hole) strength were conducted at three temperature levels (-50C, RT, +80C) on specimens with four different fiber orientations (0°, 45°, 67.5^o, 90°).

Using the metal volume fraction approach, the percent difference between the theoretical elastic modulus values and the room temperature experimentally obtained results for the four fiber orientations (0°, 45°, 67.5^o, and 90°) was 4.07%, 4.59%, 2.59%, and 1.27% respectively. The high metal volume fraction of the CentrAl hybrid material enabled retention of elastic modulus properties at high temperature (+80C) while testing in the elastic regime. The percent change from the room temperature elastic modulus to the elevated temperature modulus value was 0.26%, 0.23%, 1.58% and 0.13% respectively. The same modulus tests were conducted at low temperature (-55C). The percent difference between the reduced and room temperature values were 6.67%, 7.18%, 13.25%, and 6.82%.

The blunt notch tests revealed an overall decreased stiffness magnitude for elevated temperatures, in particular for off-axis (45°, 67.5°, 90°) orientations. The average structural stiffness for the room temperature and reduced temperature results are shown to closely correlate with one another throughout the entire range of fiber angles. The elevated temperature stiffness values, especially for the off-axis results, are shown to be below both the room and reduced temperature tests on the order of 14-17%. With the 45° fiber orientation, the stiffness of the elevated temperature blunt notch test shows a reduction of approximately 21%.

This trend of decreasing ultimate tensile strength as the fiber angle approaches 90° is seen. The room temperature results are still shown to be an approximate median value between the high and low temperature values. The reduced temperature ultimate tensile strength is shown to have the greatest increase over the room temperature results at the 45° fiber angle. This increase is on the order of 13.5%. The elevated temperature results show a relatively small decrease in ultimate tensile strength across the entire range of fiber angles. This decrease in strength is on the order of 5-8% for the intermediate fiber angles of 45° and 67.5° and approximately 1.5-2% for the 0° and 90° fiber angles respectively.

The blunt notch yield strength values follow a similar trend, in that the elevated temperature results are consistently lower than the reduced temperature results. All values approach a minimum at the 90° fiber angle, and the elevated temperature results are consistently lower than both the room and elevated temperature values. In the intermediate fiber angles, 45° and 67.5° respectively, the reduction in yield strength as

measured from the room temperature values was seen to be approximately 6% and 8% respectively.

Dynamic tests to measure fatigue life were conducted on specimens with on-axis (0°) fiber orientation at several stress levels. These tests indicate that the elastic modulus retains integrity until ultimate failure, and the overall number of cycles to failure is predictable.

This effort has successfully characterized CentrAl material for several thermo-mechanical loading conditions and has illustrated the predictability of mechanical performance of this material through analytic and experimental validation.

Acknowledgments

Throughout this endeavor, one phrase was constantly spoken to me: "Geof this is your thesis; it needs to come from within you." While the fruits of my labors are represented in this manuscript, none of this could have been possible without a dedicated team of people who supported my efforts. First of all, I would like to offer a special thanks to Mr. Richard Wiggins, Mr. Brian Smyers, and Mr. Larry Mack, for without their technical expertise, I would have been unable to operate in the laboratory. I would also like to give a special thanks to Dr. Ed Forster. As my thesis sponsor, Ed provided guidance and scope for this research effort. In addition, I need to say thank you to the people at Miami Valley Manufacturing and Assembly, Inc., as they excised and shaped my individual test specimens. I would like to acknowledge Dr. Larry Butkus and his team in the Materials Directorate of the Air Force Research Lab for providing the non-destructive evaluation. I must also publicly thank Col Rob Fredell and Dr. Jim Greer, for without their teachings, my interest in the fiber metal laminates would have never come to be. Last but certainly not least, I would like to express my sincerest gratitude to my thesis advisor, Dr. Marina Ruggles-Wrenn. Her never ending stream of wisdom and curious insight not only bolstered my technical abilities, but also gave me invaluable teachings I will carry with me the rest of my life.

Geofrey S. Cox

Table of Contents

List of Figures

List of Tables

THERMOMECHANICAL PROPERTIES OF CENTER REINFORCED ALUMINUM

I. Material Background and Introduction

The modern day hybrid material, noted by constituents of separate and distinct material families (e.g. metal and fiber reinforced polymers), have been developed in parallel to advanced composites to compete with traditional monolithic metals in aircraft applications. Before any investigation into the behavior of a hybrid material is conducted, an understanding of its fundamental makeup is paramount. This includes exploring the history of the fibrous composite and how its life intertwined with its metallic counterpart.

While commonplace in nature, such as with the makeup of wood, modern advanced composite materials date back only a few decades to which man's study of this material system became a mainstay of research. It was during this initial research that several advantages over conventional metals became obvious. Undoubtedly, the most often cited advantage of fibrous composites is their high specific stiffness and high specific strength as compared with traditional engineering materials [7]. These material properties enable the design of composite structures to exhibit a lighter weight when compared to a similar construction of metallic components. Second, due to their distinct material phase relationship and fiber orientations, composite materials have the ability to be tailored to meet the requirements of a specific design. This not only reduces excess

material, but enables a more efficient use of the available material. Several examples of design options include, but are not limited to, fiber and matrix material choices, fiber and matrix volume fractions, different fabrication techniques, lamina fiber orientation, and total number of lamina comprising the entire material stack. Finally, composites offer a tremendous increase in fatigue life when compared to engineering metals, such as aluminum. This improvement in fatigue life has motivated the aircraft industry to pursue the study of composites for use as primary structure in modern and future aircraft. This ability to stack and otherwise orient and bond lamina to comprise a laminate was the first step taken which led to the modern day fiber metal laminate material family.

Despite a longstanding dominance in the field of aerospace technology, U.S. researchers were not the first to realize the benefits of laminated metallic structures. Experiments conducted at Delft University in the Netherlands had shown that the fracture toughness of laminates was superior to that of monolithic plates. Additionally, several research programs were carried out which examined the crack growth of monolithic and laminated sheets, comparing a laminated material consisting of five sheets, each sheet one millimeter thick, to that of a single monolithic sheet five millimeters thick. Experimental results showed crack growth in the laminated sheet was significantly slower than in the monolithic plate [19]. By mid 1970s, research at Delft University focused on adding fibers to the adhesive layers of the metallic laminates to improve mechanical performance. Damage tolerance experiments showed that the fiber reinforced adhesive laminates exhibited marked improvement over the already impressive strength of traditionally bonded metallic laminates. By adding fibers to the bonding agent, a new door was opened to the researchers into the world of the fiber metal laminate. This

joining together of the fibrous composite and monolithic metal effectively produced a new material which, in effect, provided the best of both worlds. There was the well known and predictable behavior of the metallic constituent and the superior fatigue resistance of the composite portion. The fiber metal laminate exploited the advantages of both metallic and composite components in aircraft application

Researchers at Delft University began exploring this new material type to understand the mechanical interaction of the material constituents and characterize the mechanical behavior of the FML. It was soon discovered that this fiber metal laminate demonstrated damage tolerance capabilities beyond that of the already impressive results from the metallic laminates. The fibers added strength to the laminate, while the metals provided strength perpendicular to the fiber direction. Further testing revealed that crack growth in the fiber metal laminate was two to three times slower than in traditional monolithic aluminum [19]. This experimental research led to the phenomenon known as "fiber-bridging" wherein loads from cracked metallic layers were transferred to the fibers through the fiber-adhesive interface. Fatigue testing indicated the adhesive would eventually begin to separate, or delaminate, from the laminate's metallic layers. Upon first observation, this behavior seems detrimental to the overall laminate's strength capabilities. However, it has been shown that for a cracked condition, had the adhesive not delaminated from the metal, the fibers would, in turn, experience too high of strain and eventually fail. On the other hand, if the delamination is too large within the fiber metal laminate, a crack would be permitted to open too far and thus grow uncontrollably. It is seen therein lies a balance between delamination and crack growth that is assured by the strength of the adhesive and its resistance to delamination [19]. This balance between

the adhesive and metal must be recognized over the entire length of the crack, else failure will occur. If, for instance, loads in the fibers are higher than when compared to the fiber loads in another location along the crack, additional delamination will occur where the loads are higher, and thus reduce the loads on the fiber. During crack growth, Vlot describes, the intact fibers in the wake of the crack considerably restrain the opening of its tip. As a result, fatigue crack growth is effectively slowed down, and even full arrest of crack growth can occur.

Aside from the adhesive to metal interface, experimental research also provided valuable insight into the relationship between metal thickness and delamination. A Master's thesis conducted at Delft revealed that thinner sheets of metal within the laminate effectively reduced unwanted delamination and promoted the material's crack arresting properties via fiber bridging. Previous research had revealed that when the metal layers are too thick, adhesive and fiber loads increase and thus additional delamination occurs. A second outcome of the same thesis research yielded a solution to solve the problem dealing with residual stresses existing due to the mismatch between the constituents' coefficients of thermal expansion. During the cure cycle and subsequent cooling, residual tensile stresses developed within the metallic layers, while residual compression was found in the fibrous layers. These residual stresses could be reversed to create compression in the metal layers and tension in the fibers through a post-stretching operation applied after curing. This was achieved by stretching the fiber-metal laminate to a small plastic strain in the metal layers while the fibers remained elastic. When this was done, the aluminum layers would elongate permanently while the fiber would remain elastic and would want to return to its original length. This counteracted the stresses that

were present in the material after curing [19]. Further research demonstrated that for a post-stretched fiber metal laminate, fatigue crack growth eventually stopped.

During the early 1980s, Delft University focused upon optimizing the metal layer thickness within the laminate. As previously stated, thin metallic layers lend themselves favorably to a balance of stable crack growth and delamination, while thick metallic layers promote adverse delamination. Experimental results showed the optimum metallic layers to be 0.3 or 0.4 millimeter thick.

The first generation of fiber metal laminate (FML) was given the name ARALL, because of its constitutive makeup involving aramid fibers used in conjunction with its aluminum layers. Aramid fibers, manufactured by DuPont under the trade name Kevlar, were selected over carbon fibers to avoid potential galvanic corrosion between constituent materials. The aramid reinforced aluminum laminate (ARALL) was met with great criticism. It was first introduced to the aviation community as a legitimate material system, as opposed to several materials simply glued together. Corrosion experts felt as though the edges of ARALL, left untreated, would degrade over time. Maintenance experts believed the fibrous layers would accelerate wear on drill bits and that the material's layered make-up would prohibit viable inspection techniques for subsurface damage. Doubts in the capabilities were justified, as it had never been proven in actual service, and all it had to show for it were some ambiguous research data from a small lab in a tiny country [19]. Despite resistance, Delft University pushed forward with their new material. One such experiment invalidated the claim by such composites experts saying that, similar to a modern composite, ARALL's untreated edges would allow significant moisture intrusion into the laminate and thus promote hygroscopic effects and

delamination. It was shown since the fiber/epoxy layers are protected by the aluminum layers, the process of the penetration of water into the adhesive, which occurs mainly along the fibers, was very, very slow [19]. This demonstrated an advantage of ARALL over conventional composites. Further testing revealed that the adverse effects of moisture and corrosion of the aluminum layers were lessened in ARALL due to the prevention of through thickness penetration by fiber/epoxy layers. The epoxy did not crack and the lamina did not delaminate uncontrollably. ARALL, as it was contemporarily constructed, withstood the most severe testing [19]. One test, though, proved to be the Achilles heel of such a formidable material: low frequency fatigue loading which simulates the pressurization cycles seen in aircraft fuselages. This material failure was found to lie in the bond line between the aramid fibers and adhesive material. Additionally, research had proven that the aramid fibers exhibit poor compressive strength characteristics. The adverse behavior seriously degrades the material's fiber bridging capabilities. For example, during cyclic loading, a crack in an aluminum layer will open and then close. Upon closing, the subsurface fibers are compressed, slips out of the adhesive, and thus fails once the crack begins to open. Additional testing also uncovered ARALL's somewhat poor impact resistance. While not as sensitive to impact as traditional advanced composites of the day, the material is far more sensitive than monolithic aluminum.

In an effort to develop the FML system beyond what was initially thought of as unfortunate test results, Delft researchers began development on the second generation FML. Since the ultimate demise of ARALL stems from the unsuccessful bond between fiber and adhesive, a new fiber must be found which would offer a better bond with the

6

adhesive. Investigations into potential fiber candidates led to glass fibers, rather than the

conventional aramid type found in traditional ARALL. First of all, glass is

non-conductive, so any potential for galvanic interaction between the constituents is non-

existent. Second, glass fibers are extremely strong. While glass itself is highly brittle, in

fiber form, glass exhibits great flexibility. One early type of glass fiber successfully

applied to the fiber metal laminate was known as R-glass. R-glass resembled the top-

secret American S2-glass fiber, made by Owens and Corning, which could not, at the

time, be applied in fiber metal laminates because it was considered by the United States

government to be a strategic material [19]. After several months of successful testing

with the new R-glass aluminum laminate, the material's name was changed to more

accurately reflect its constitutive make-up: GLARE. Analogous to the name ARALL,

GLARE was an acronym for the reinforcing agent within the laminate. The new glass

reinforced laminate held several advantages over the older ARALL. The new material

exhibited tremendous blunt notch strength and through crack resistance capabilities.

Whereas ARALL had shown poor resistance to impact damage, Delft had shown that at

low velocities, GLARE is as good as monolithic aluminum and superior to carbon fiber

composites, while at higher impact velocities, the glass fiber within the laminate becomes

much stronger and thus the impact properties exceed that of the monolithic aluminum

[19]. Aside from impact resistance, the new GLARE also proved to have superior burn

through resistance when tested against temperatures of 1200C. In contrast to its cousin

ARALL, GLARE successfully withstood the low frequency fatigue loading. GLARE

appeared to be ideally suited for fuselage applications [19] because additional cross ply

fiber layers could be added without adding additional adhesive, due to the stronger bond between the fiber and the adhesive material.

With the success GLARE saw during development as a fuselage material, it follows that its application should be steered toward use on aircraft wings. Because the lower wing skins have traditionally been designed for tensile fatigue loading, the highly fatigue resistant GLARE seems like a logical material for use in this area. Aside from similar coefficients of thermal expansion (CTE) when compared to monolithic aluminum, a significant number of additional benefits could be provided by GLARE to the lower wing structure. These include residual strength after fatigue, impact behavior, ease of repair, and corrosion resistance [15]. However, in the as-manufactured condition, traditional GLARE does have a rather serious setback, especially when considered for use on aircraft with comparatively thick lower wing skins, where the thickness can exceed 8 millimeters. In its applications on fuselages, the GLARE material averages between 1.0 and 3.5 millimeters thick. This thickness limits the GLARE configurations to approximate layups with 6 metal sheets and 5 fibrous layers (a 6/5 condition). Lower wing skins near the wing root may approach 10 to 15 millimeters thick. To replace these thick skins with GLARE would require a 20/19 layup [15]. An additional concern surrounds the use of the larger bolts typically seen in lower wing skins, near the wing root. While traditionally, smaller diameter, countersunk fasteners have been used with GLARE in the past, the larger countersunk fastener would not sufficiently clamp the outer metallic layer in the GLARE laminate. A third disadvantage of using traditional GLARE as a lower wing skin replacement is related to the two types of aluminum currently qualified for use in the GLARE laminate: 2024-T3 and 7075-T761. Improved

performance could be seen through utilizing newer aluminum-lithium alloys in the metallic layers. While certainly stronger and more fatigue resistant than traditional aluminum alloys, the new metal is difficult to roll to the required small thickness [15] for use in GLARE laminates.

To counter the manufacturing difficulties arising with thick GLARE, the issue with large fasteners, and problems dealing with tapering GLARE's thickness along the wing span, the Aluminum Company of America (ALCOA) developed a test program to directly bond GLARE to aluminum panels in an effort to increase the panel's damage tolerance characteristics. Though certainly not a new concept, as Lockheed had successfully applied aluminum and titanium straps [15] to fatigue critical areas of several aircraft. A similar type of reinforcement technique can be seen on several Boeing aircraft as well, in the form of fail-safe straps. ALCOA's idea was to use this concept, referred to as "selective reinforcement", on the much thicker lower wing panels [15].

Center-reinforced aluminum (CentrAl) is the third generation of fiber metal laminate. Fully utilizing the GLARE and ARALL design concepts, ALCOA's first step was to integrate the reinforcing GLARE into the material, in a symmetrical lay-up. The originally thick metal sheet is split into two thinner layers in order to obtain a symmetrical configuration, while the GLARE reinforcement is bonded in between [15]. The fibrous layers within the reinforcing GLARE are S2-glass and FM94K adhesive. In its current configuration, the adhesive layer is optimized for GLARE and is, in turn, not well suited for use in the CentrAl material because of the high load transfer induced from thick cracked metal sheets [15]. Experimental results ultimately solved this problem and led to the development of BondPreg®. This product is a combination of standard

adhesive bondfilm and S2-glass prepreg as used in GLARE. BondPreg® combines the

crack bridging capabilities of the S2-glass prepreg used in GLARE, with the resistance to

delamination similar to that obtained for standard adhesive layers. In other words,

BondPreg® provides an optimized balance between crack bridging and delamination

resistance for thick metal sheets [15]. Created from two layers of S2-glass prepreg and

two layers of FM94K adhesive film, BondPreg® is used as the ideal interface between

GLARE and the thick metal sheets [15]. The use of BondPreg® has also been shown to

reduce the amount of delamination, and thus diminish fatigue crack growth.

II. Thesis Objective

This effort will explore the performance of an advanced hybrid material, CentrAl, to establish the elastic (Young's) modulus, static strength properties (both un-notched and open-hole), and number of cycles to failure for fatigue life. Mechanical behavior of a single CentrAl variant will be predicted using the rule of mixtures and metal volume fraction (MVF) approach. The accuracy of the models will be evaluated through comparison to experimental results. The effect of reduced stiffness due to plasticizing of the epoxy at elevated temperatures will be investigated by experimental testing of specimens with four different fiber orientations (0°, 45°, 67.5^o, 90°) at three temperature levels (-55C, RT, +80C). The effect of temperature on the strength of the hybrid specimens will be examined through un-notched and open-hole destructive testing. Tension-tension fatigue tests will be conducted at ambient temperature on specimens with on-axis (0°) fiber orientation at several stress levels to establish S-N curve behavior. Existing literature on this new material provides real-world fatigue application data which includes the behavior of the laminate under the Transport Wing Standard (TWIST) and Mini-TWIST [4],[15] loading spectra. This effort will characterize behavior of a specific CentrAl material configuration for several thermo-mechanical loading conditions, and illustrate the predictability of mechanical performance of this material through analytic and experimental validation.

Chapter 1 of this thesis report covers a brief background and history of fiber metal laminates, leading up to the development of CentrAl. Chapter 2 outlines the overarching goal of this study. Chapter 3 provides an overall description of the test article,

nomenclature, and constituent breakdown. Chapter 4 details each specimen's geometry,

as well as the overall cutting plan for specimen excision. Chapter 5 discusses the

non-destructive evaluation performed on each specimen in order to detect any subsurface

flaws resulting from any damage or manufacturing. Chapter 6 shows the requisite

theoretical development used in determining the material properties using classical

laminated plate theory and the metal volume fraction technique. This chapter also details

the development of the model used to predict CentrAl's fatigue life. Chapter 7 outlines

the relevant equipment used for each experiment, as well as presents each experimental

procedure. All experimental results are discussed in Chapter 8. Finally, concluding

remarks and recommendations for future research are covered in Chapter 9.

III. Material Description

The material studied was CentrAl, a commercially available laminate manufactured by ALCOA. The test material was supplied in a form of one sheet 36 inches x 50 inches in size. This variant of CentrAl contains an inner core of GLARE 2A-3/2-0.4 and outer layers of thicker (.063 inch) 2024-T3 aluminum. The following figure illustrates the cross sectional makeup of the CentrAl panel used for this research.
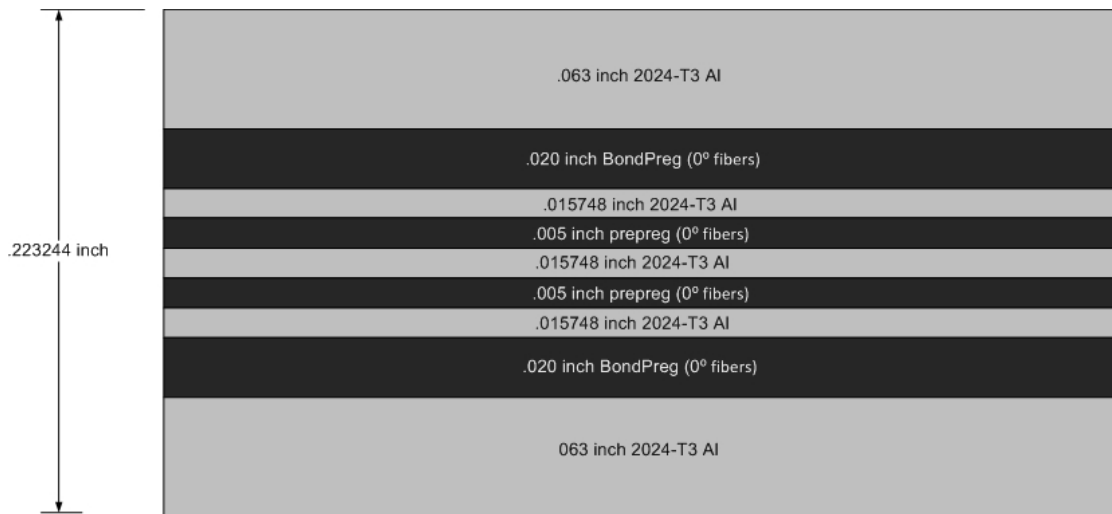
Figure 1 : CentrAl Cross Sectional Makeup

The central GLARE reinforcement is bonded to the thicker outer aluminum layers using two layers of BondPreg®. As developed by ALCOA, standard BondPreg® is composed of four layers. This product is a combination of standard adhesive bond film and S2-glass prepreg as used in GLARE [15]. BondPreg's® first two layers are FM94K adhesive, while the second and third layers are comprised of unidirectional layups of S2-glass prepreg. Figure 2 below illustrates the makeup of BondPreg®.
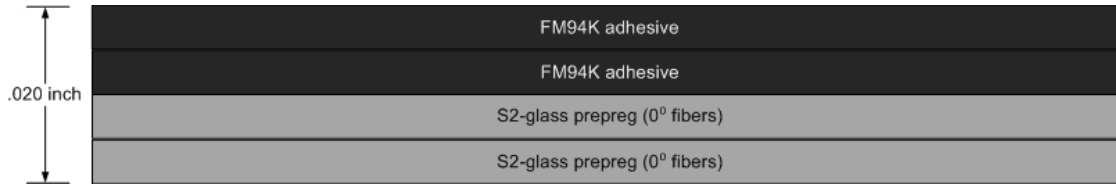
Figure 2 : BondPreg® Makeup

Exploring the material nomenclature for the central GLARE reinforcement provides additional insight in the overall material construction. The first portion of the name - GLARE 2A - indicates the fibers within the prepreg are unidirectional and oriented at 0° to the material axis. Further, each fibrous prepreg layer is 0.254 millimeter thick. The prepreg is comprised of S2-glass fibers and FM94K adhesive. "GLARE 2A" also indicates the aluminum within the material is of the alloy and temper 2024-T3. "3/2" indicates there are three layers of aluminum and two layers of prepreg comprising the GLARE. Finally, "0.4" indicates the thickness of each aluminum layer is 0.4 millimeter thick.

CentrAl Constituents

2024-T3 Aluminum.

Only two alloys of aluminum are currently qualified for use on GLARE material. While CentrAl is a distinctive material system, it does contain a central core of GLARE. In this material, 2024-T3 aluminum is the alloy currently used. The thermal and mechanical properties of 2024-T3 aluminum are well known and available in literature. For the thicknesses (0.010 - 0.128 inch) used in this variant of CentrAl, the following table outlines the thermal and mechanical properties. Note there is a difference amongst both the yield and ultimate strength value with respect to the material's rolling direction, L and LT. The "L" indicates the material rolling direction, or longitudinal direction

14

properties, while the "LT" designator describes the direction perpendicular to the rolling direction, or longitudinal-transverse direction properties. While considered to be an isotropic material, this difference is accounted for in the mathematical models predicting the behavior of the overall laminate.

In the next table, and in the subsequent tables used in describing the laminate properties, the abbreviation "UTS" is used for the ultimate tensile strength and "Y" is used for the material yield strength.

Table 1 : Typical Properties of 2024-T3 Aluminum [14]

Property	Value
UTS (L)	64 ksi
UTS (LT)	63 ksi
Y (L)	47 ksi
Y (LT)	42 ksi
E	10.5 Msi
G_{12}	4 Msi
ν_{12}	0.33

S2 Glass Fiber.

The S2-glass fiber within CentrAl forms the backbone of the composite within the overall laminate. Recall from previous discussion how this fiber is flexible, non-conductive, and extremely strong. The following table depicts the physical properties commonly associated with S2-glass fibers.

Table 2 : Common Properties of S2-Glass [6]

Property	Value
UTS	709 ksi
E	12.6 Msi
G_{12}	5.53 Msi
α_{12}	.0000009 $^\circ F^{-1}$
ν_{12}	0.23

FM94K Adhesive.

Binding the fibers together is a matrix agent known as FM94K adhesive. It is the matrix which effectively transfers loads from the metallic surfaces to the fibers. The table below details the physical properties of this epoxy.

Table 3 : Common Properties of FM94K Adhesive [2],[5]

Property	Value
E (L)	.320 Msi
E (LT)	.320 Msi
ν_{12}	0.33
ν_{21}	0.33
G_{12}	.120 Msi
α_{12}	.0000417 $^\circ$F^{-1}
α_{21}	.0000417 $^\circ$F^{-1}

Unidirectional Lamina (S2-Glass Fiber and FM94K Adhesive).

The unidirectional lamina within CentrAl is found between the metallic layers inside the central GLARE reinforcement. It is this fibrous layer, with 60% fiber by volume, which aids in CentrAl's crack bridging capabilities.

Table 4 : Typical Properties of Unidirectional Laminate

Property	Value
UTS (L)	321 ksi
UTS (LT)	3.2 ksi
Y (L)	51.6 ksi
Y (LT)	7.5 ksi
E (L)	7.688 Msi
E (LT)	.7706 Msi
G_{12}	.2905 Msi
ν_{12}	0.27
ν_{21}	0.027
α_{12}	0.00000161 $^\circ$F^{-1}
α_{21}	0.0000224 $^\circ$F^{-1}

Unidirectional BondPreg®.

Within this configuration of CentrAl, there are two layers of BondPreg®. Each of these layers effectively secure the central GLARE reinforcement to the outer, thicker aluminum sheets. With a 30% fiber volume fraction, BondPreg® is created from S2-Glass fibers and FM94K adhesive.

Table 5 : Unidirectional BondPreg® Properties

Property	Value
UTS (L)	160 ksi
UTS (LT)	3.19 ksi
Y (L)	25.8 ksi
Y (LT)	4.21 ksi
E (L)	4.004 Msi
E (LT)	.4522 ksi
G_{12}	.1699 Msi
ν_{12}	0.30
ν_{21}	0.034
α_{12}	0.00000337 $^{\circ}F^{-1}$
α_{21}	0.00003904 $^{0}F^{-1}$

IV. Specimen Geometry and Cutting Plan

Upon receipt of the material, an initial cutting plan was established in order to maximize the number of specimens to meet the goals of the thesis project. Both straight sided specimens and dog-bone shaped fatigue specimens were cut from the CentrAl sheet. Due to the nature of fibrous composites, physical properties can drastically change as a function of fiber orientation. To investigate this property dependence on fiber angle within CentrAl, specimens were excised at 0°, 45°, 67.5°, and 90° with respect to the material axis. The following figure details the layout of specimens excised from the main CentrAl panel.

The horizontal, or long axis, of the panel represents the 0° fiber orientation from which the off axis specimens were measured and cut. The figure below shows the actual results of specimen excision compared to an approximate template of the CentrAl sheet. Additionally, each specimen's identification numbers can be seen.

Figure 3 : Specimen Layout Compared to Sheet Template

18
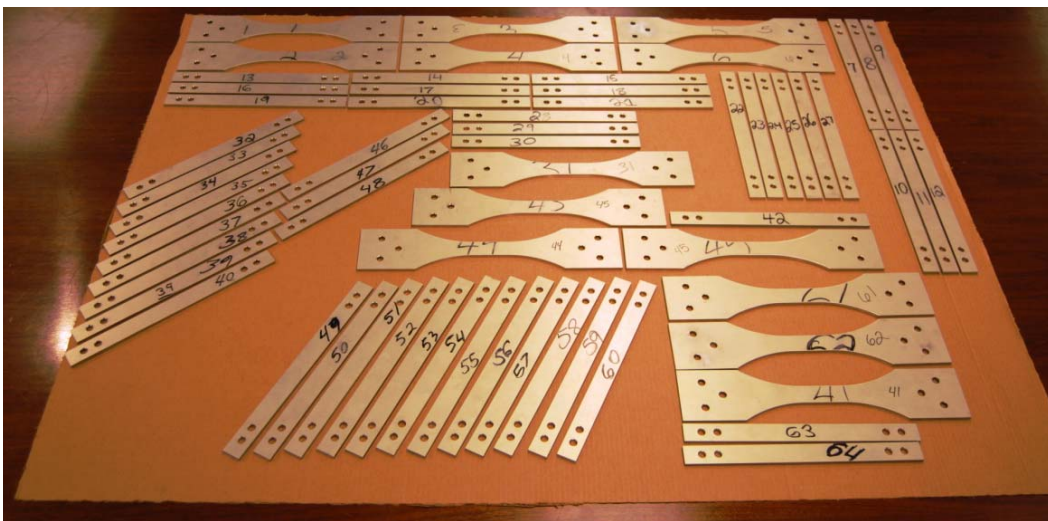
A total of 13 larger fatigue specimens and 51 smaller tensile specimens were excised from the CentrAl sheet. The following figures depict the specimen geometry.
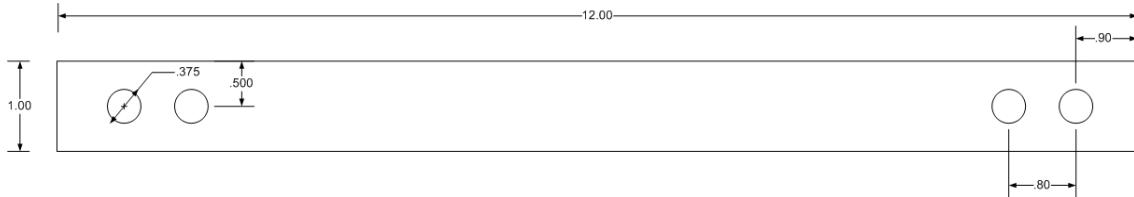
Figure 4 : Straight Sided Specimen
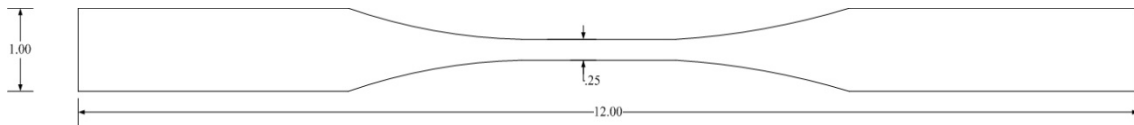
Figure 5 : Dogbone Tensile Specimen Geometry

The next figure shows depicts an actual dogbone tensile specimen.

Figure 6 : Dogbone Tensile Specimen
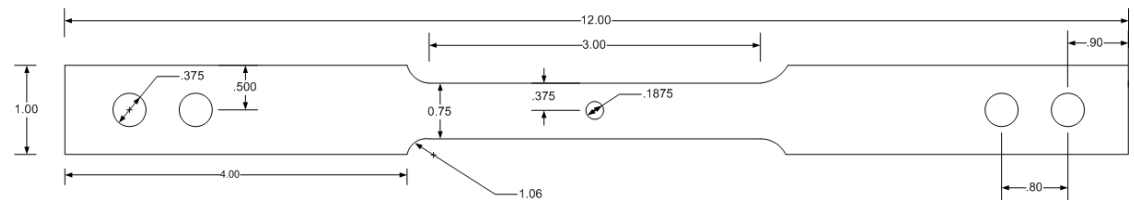
Figure 7 : Blunt Notch Strength Test Specimen Geometry

The figure below depicts an actual blunt notch specimen, while the subsequent figure

shows the geometry of the dogbone fatigue specimen.
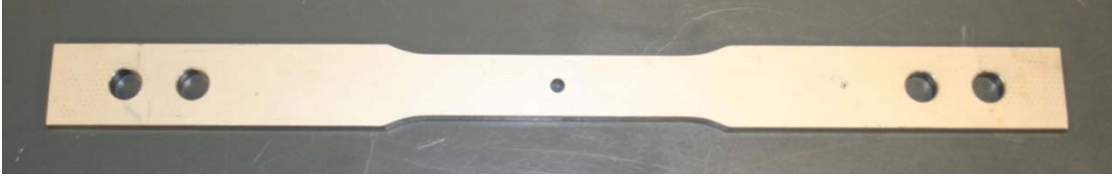
Figure 8 : Blunt Notch Specimen
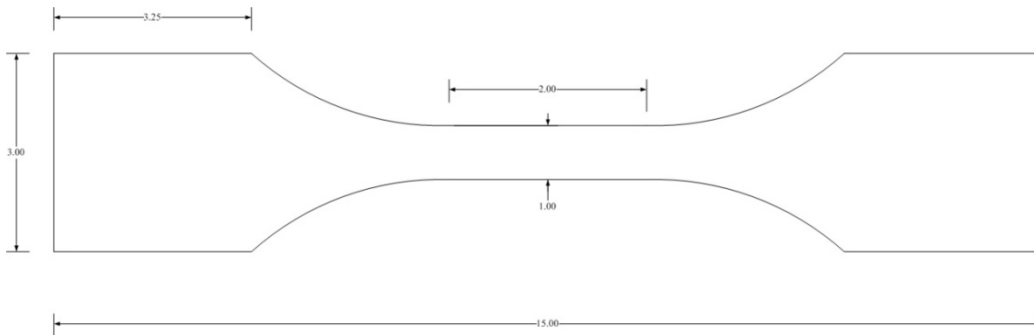
Figure 9 : Dogbone Fatigue Specimen Geometry

V. Material Post-Processing

Prior to testing, each specimen underwent a non-destructive inspection utilizing an IntraSpect Eddy Current and Ultrasonic Inspection System. This was performed to ascertain the subsurface condition of each specimen as the material system is created from multiple layers of differing substrates. The inspection process would reveal any subsurface delamination or crack growth induced from either the manufacturing or excision procedures. The non-destructive inspection revealed that an area of delamination, approximately four inches in diameter, had developed in the upper left quadrant of the specimen sheet. This delamination directly affected specimens 14, 17, 20, 28, and 46. Appendix A shows the direct C-scan results for each specimen. The areas of subsurface delamination can be seen as gray areas in each image. The figure below shows the approximate location of damage to the subsurface layers on the CentrAl panel, superimposed on the overall cutting plan.
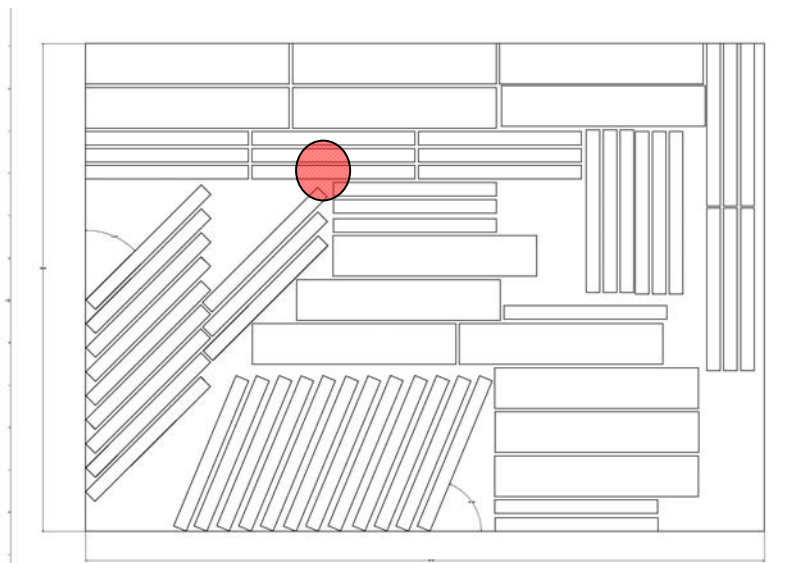
Figure 10 : Approximate Area of Subsurface Damage

Each specimen was positioned within an inspection frame and submerged into the multi-axis C-scan gantry's water tank. The figure below illustrates the typical type of scanner setup utilized for the C-scan inspection process.
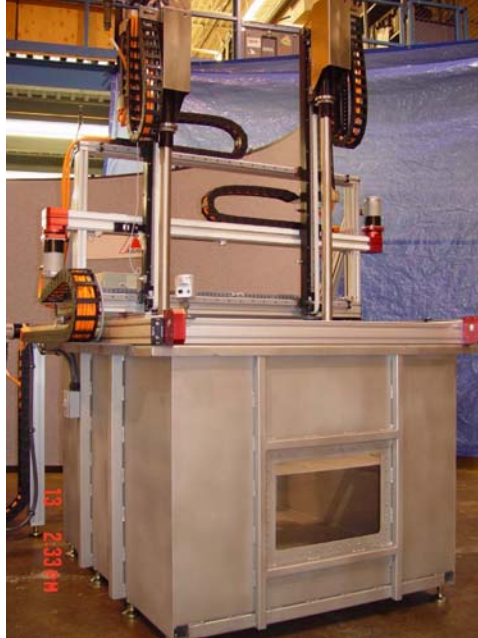
Figure 11 : Typical Multi-Axis C-Scan Gantry [21]

After the C-scan process, each specimen underwent subsequent visual inspection and measurement. Using digital calipers, each specimen thickness and width was recorded. This data would be later used during testing to establish stress levels within the specimens under the applied loads. Data to include specimen width, thickness, surface condition, and fiber orientation were recorded.

VI. Theoretical Development

Experimental research often leads to startling conclusions surrounding a new material's mechanical properties - center reinforced aluminum is no exception. While experimental work is often a venture into the unknown, a theoretical roadmap provides the researcher bounds onto which the experimental results are compared. An alternate method is to perform the experimental research up front and then develop the theory to match the results. The former was the approach taken while studying CentrAl. This method was chosen for several reasons.

First, because the testing procedures are already established, i.e. elastic modulus testing and fatigue testing, the theoretical results and material response could be predicted. Second, because the new material system is composed of both fibrous and metallic layers, a metal volume fraction approach [22] can be applied to ascertain its mechanical properties at a macroscopic level. Whereas, classical laminated plate theory can be used to determine properties of its fibrous constituents.

Elastic Modulus

Theoretical Elastic Modulus - Material 1 Direction.

Recall the material properties shown in Tables 1-5. The basic properties for the CentrAl laminate are built using an elementary mechanics of materials approach, coupled with a fiber volume and then a metal volume fraction methodology.

The theory for ascertaining the properties of fibrous composites is based on the fiber volume fraction, in which the properties are assumed to vary linearly with respect to the amount of fibers present in the composite. Wherein for a 0% fiber volume fraction,

23

only the matrix property is seen and likewise for a 100% fiber volume fraction, only the respective fiber property is seen. This theory is illustrated in the figure below for the theoretical elastic modulus of a fibrous composite.
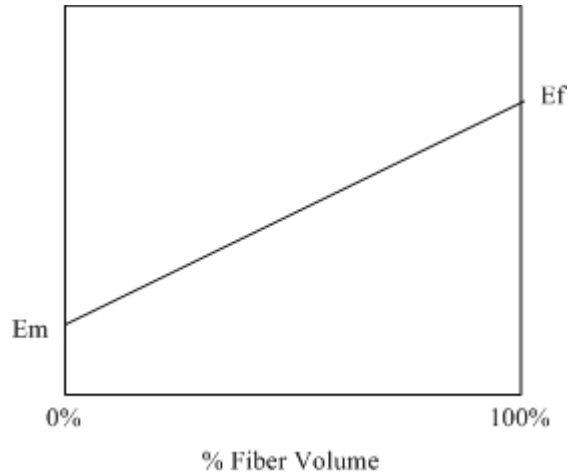
Figure 12 : Fiber Volume Fraction

Analogous to the behavior of a monolithic material when placed under load, the fibrous composite exhibits a strain proportional to the induced stress and elastic modulus. The figure below illustrates the material behavior under load within the elastic region of the fibrous composite's stress-strain relationship.
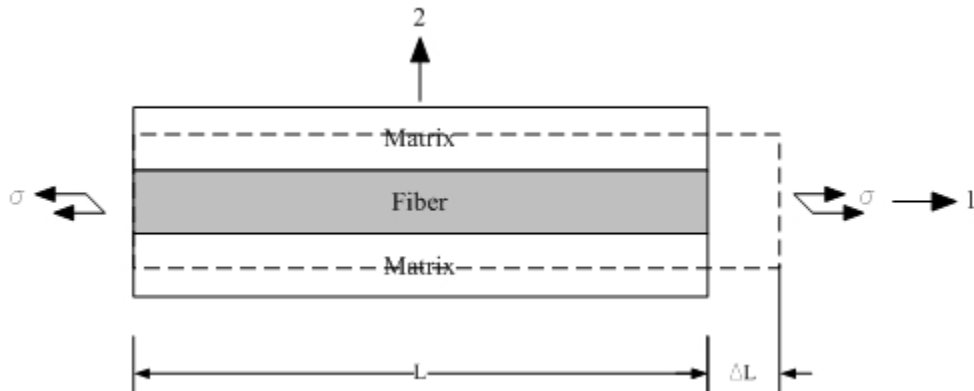
Figure 13 : Representative Volume Element Loaded in the 1 Direction [9]

From elementary mechanics of materials, recall that the strain in the material's 1 direction is given as:

$$\varepsilon_1 = \frac{\Delta L}{L} \tag{1}$$

It is the basic assumption that since the matrix material and fibers are securely bonded, they must exhibit the same strain magnitude. So the above expression applies for the amalgamation of both the matrix and fiber. Since the overall representative volume element is loaded within the elastic regime for both materials, it follows that the stresses induced within the fiber and matrix respectively are determined through:

$$\sigma_f = E_f \varepsilon_1 \tag{2}$$

$$\sigma_m = E_m \varepsilon_1 \tag{3}$$

If the representative volume element figure from above is extended in the 3 direction, it is seen the stress component in the 1 direction, σ, is applied over an overall cross-sectional area, A. Therefore, σ_f acts on the fibrous layer cross section, A_f, while σ_m acts over the matrix cross section, A_m. Since a force, P, is defined as a stress applied over an area, A, the overall force applied to the representative volume element is given by:

$$P = \sigma_1 A = \sigma_f A_f + \sigma_m A_m \tag{4}$$

And given the definition of the total stress in the 1 direction:

$$\sigma_1 = E_1 \varepsilon_1 \tag{5}$$

After performing the necessary substitutions, it follows that:

$$(E_1 \varepsilon_1)A = (E_f \varepsilon_1)A_f + (E_m \varepsilon_1)A_m \tag{6}$$

Dividing by ε_1 and the total area, A, the effective elastic modulus in the material 1 direction can be found.

$$E_1 = E_f \frac{A_f}{A} + E_m \frac{A_m}{A} \qquad (7)$$

Additionally, the fiber and matrix volume fractions respectively are written as:

$$V_f = \frac{A_f}{A} \qquad (8)$$

$$V_m = \frac{A_m}{A} \qquad (9)$$

Therefore the elastic modulus in the material 1 direction, written as a function of the constituent elastic moduli and respective volume fractions is given as:

$$E_1 = E_f V_f + E_m V_m \qquad (10)$$

Unidirectional Prepreg Lamina.

The unidirectional prepreg lamina within the make-up of CentrAl is found sandwiched between the thin aluminum layers inside the Glare reinforcement. As manufactured, the lamina composed of S2-Glass fibers and FM94K adhesive, contains 60% fibers by volume. Thus, its fiber volume fraction is 60% or simply 0.60. Therefore the matrix volume fraction is 40% or simply 0.40. Recall the elastic moduli for both the S2-Glass fiber and FM94K adhesive:

$$E_f = 12.6 \text{ Msi}$$

$$E_m = 0.32 \text{ Msi}$$

Knowing each constituent's elastic modulus and respective volume fraction, the overall effective elastic modulus in the lamina 1 direction can be determined using Equation 10. The result is as follows: $E_1 = 7.699$ Msi.

Unidirectional BondPreg®.

The same methodology can be applied to determine Young's modulus for the BondPreg® material. Because BondPreg® contains the same constituents as the unidirectional prepreg layers, the same property values can be used. The only difference

in the construction of the BondPreg®, aside from its material stacking sequence, is the fiber volume fraction. ALCOA research determined the ideal balance between strength and delamination resistance for the BondPreg® occurred when the amount of fiber was decreased and the volume of adhesive increased. The fiber volume fraction of BondPreg®, as used in this CentrAl panel is 30%. Using Equation 10 once more, the elastic modulus in the material 1 direction is given as: E_1 = 4.004 Msi.

Theoretical Elastic Modulus - Material 2 Direction.

The same mechanics of materials technique is applied to determine the effective elastic modulus in the material 2 direction. The figure below illustrates the loading condition. Using this approach, the same transverse stress, σ_2, is assumed to be applied to both the fiber and the matrix [9] as shown in the figure below.

Since the material is still loaded in the linear elastic range of each of its constituents, it follows that the strain in the fiber and matrix, respectively is given as:

$$\varepsilon_f = \frac{\sigma_2}{E_f} \tag{11}$$

$$\varepsilon_m = \frac{\sigma_2}{E_m} \tag{12}$$
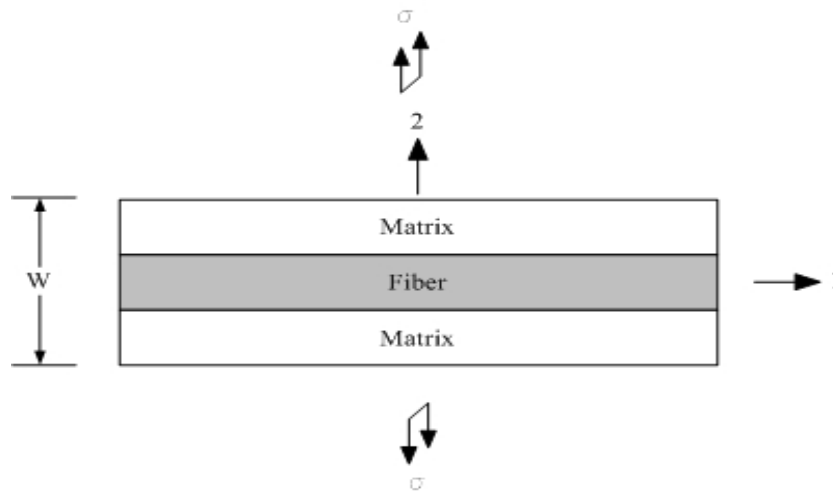
Figure 14 : Representative Volume Element Loaded in the 2 Direction [9]

The portion of the representative volume element in which the strain acts transversely to

the fiber, ε_f, is given as $V_f W$. Similarly, the dimension over which the strain acts

transversely to the matrix, ε_m, is provided by $V_m W$. Because the strain in each of the

constituents is known, the total strain in the element is given through the relationship:

$$\varepsilon_2 W = V_f W \varepsilon_f + V_m W \varepsilon_m \tag{13}$$

Since the vertical dimension, W, is constant, it can be divided out of the above expression

to yield:

$$\varepsilon_2 = V_f \varepsilon_f + V_m \varepsilon_m \tag{14}$$

Then substituting the definitions of the fiber and matrix strains:

$$\varepsilon_2 = V_f \left(\frac{\sigma_2}{E_f}\right) + V_m \left(\frac{\sigma_2}{E_m}\right) \tag{15}$$

But recall that $\sigma_2 = E_2 \varepsilon_2$.

$$\sigma_2 = E_2 \varepsilon_2 = E_2 \left[\left(\frac{V_f \sigma_2}{E_f}\right) + \left(\frac{V_m \sigma_2}{E_m}\right)\right] \tag{16}$$

Finally upon solving for E_2, the result is the mechanics of materials approach for

determining the modulus of elasticity in the material 2 direction.

$$E_2 = \frac{E_f E_m}{V_m E_f + V_f E_m} \tag{17}$$

Unidirectional Prepreg Lamina.

The fiber volume fraction for the prepreg, is given by $V_f = 0.60$. The elastic

moduli for the S2-Glass fiber and FM94K adhesive are given by:

$$E_f = 12.6 \text{ Msi}$$

$$E_m = 0.32 \text{ Msi}$$

Then, using Equation 17, Young's modulus in the material 2 direction for the prepreg is

as follows: $E_2 = 0.771$ Msi

Unidirectional BondPreg®.

Once again, performing the same analysis with the appropriate fiber volume fraction, $V_f = 0.30$, the effective elastic modulus for the BondPreg® in the material 2 direction, found using Equation 17 is thus: $E_2 = 0.452$ Msi.

CentrAl Elastic Modulus - Effect of Fiber Orientation.

Because the overall laminate contains metallic layers interspersed with the fibrous layers, the contribution of the metallic portions must be accounted for in the overall property calculation. It has been previously shown that by taking a metal volume fraction approach [22], the mechanical properties of a fiber metal laminate can be predicted.

With the metal volume fraction approach, each layer's property is weighted by its thickness contribution to the overall laminate thickness. For example, the elastic modulus in terms of CentrAl's constituents is shown in Equation 18 below:

$$E_{1_{CentrAl}} = E_{1_{aluminum}} \left(\frac{total\ aluminum\ thickness}{total\ laminate\ thickness} \right) + E_{1_{prepreg}} \left(\frac{total\ prepreg\ thickness}{total\ laminate\ thickness} \right) + E_{1_{BondPreg}} \left(\frac{total\ BondPreg\ thickness}{total\ laminate\ thickness} \right) \qquad (18)$$

Similarly the elastic modulus in the material 2 direction can be determined via the same methodology. Rather than the 1 direction modulus, the 2 direction modulus is used. As a reference, the table below shows the elastic modulus and thickness for each layer within the CentrAl laminate stack. The properties shown below for the fibrous layers are those calculated using the fiber volume fraction approach shown in the previous sections.

Table 6 : CentrAl Lamina Thickness and Elastic Moduli

Layer	Lamina Thickness (in)	Total Thickness (in)	E1 (Msi)	E2 (Msi)
Outer Aluminum	0.063	0.126	10.5	10.5
BondPreg®	0.02	0.04	4.004	0.4522
GLARE Aluminum	0.015748	0.047244	10.5	10.5
PrePreg	0.005	0.01	7.688	0.7706
Total		0.223244		

Therefore, using Equation 20, the elastic modulus for CentrAl in the material 1 direction, is as follows: $E_1 = 9.21011$ Msi. Following the same methodology for the material 2 direction, Equation 19 is produced below.

$$E_{2_{CentrAl}} = E_{2_{aluminum}} \left(\frac{total\ aluminum\ thickness}{total\ laminate\ thickness} \right) + E_{2_{prepreg}} \left(\frac{total\ prepreg\ thickness}{total\ laminate\ thickness} \right) + E_{2_{BondPreg}} \left(\frac{total\ BondPreg\ thickness}{total\ laminate\ thickness} \right) \quad (19)$$

Therefore, the elastic modulus for CentrAl, in the material 2 direction is given as: $E_2 = 8.26386$ Msi. With the material 1 and 2 direction elastic moduli known, the off-axis values can be determined through a simple axis transformation [7].

$$E_\theta = E_1 m^2 + E_2 n^2 \quad (20)$$

Where:

$$m = \cos \theta \quad (21)$$

$$n = \sin \theta \quad (22)$$

The following table shows the theoretical transformed elastic moduli for CentrAl.

Table 7 : Theoretical Transformed Elastic Moduli

Fiber Angle (deg)	Elastic Modulus (Msi)
0	9.210
45	8.737
67.5	8.402
90	8.264

Displayed graphically, the following figure depicts the dependence CentrAl's theoretical elastic modulus has on fiber orientation.
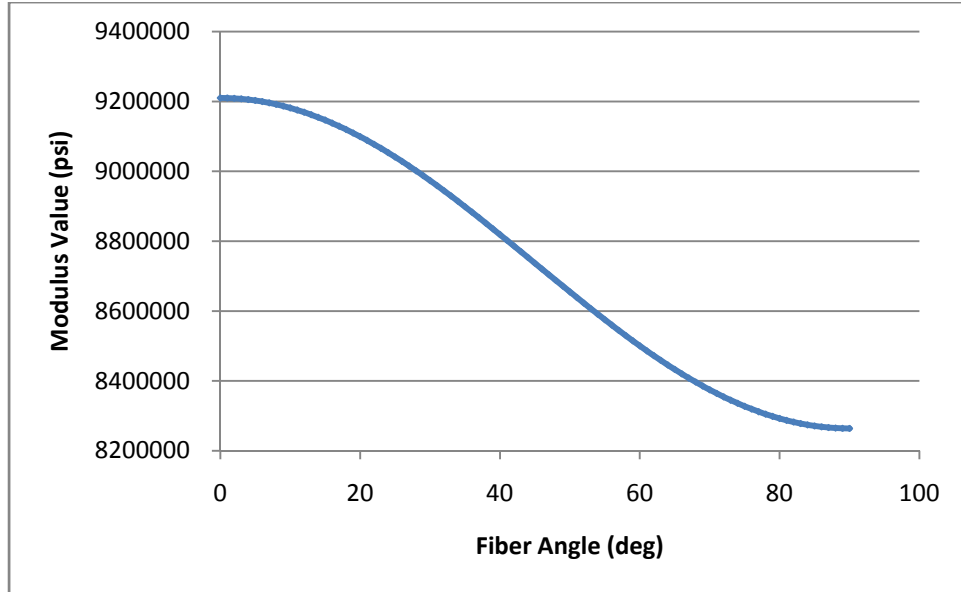
Figure 15 : Theoretical Elastic Modulus vs. Fiber Orientation

Temperature Effects.

Because the effect of temperature on CentrAl's elastic modulus was investigated, the method in which to evaluate the material's elastic modulus under the influence of an elevated or decreased temperature must be developed. It is assumed the room temperature elastic modulus remains essentially neutral in this investigation. It is both the elevated and reduced temperature modulus tests which will be evaluated for significant changes.

At the elevated and decreased temperatures, the total strain in the laminate is represented by the following relationship:

$$\varepsilon_{total} = \varepsilon_{mechanical} + \varepsilon_{thermal} \tag{23}$$

Expanding the mechanical and thermal strain terms into their respective components yields:

$$\varepsilon_{total} = \frac{\sigma}{E} + \Delta T \alpha \tag{24}$$

31

The ΔT term is the temperature differential between the lab air and the test air at the

elevated and decreased temperatures, while the α term is the CTE value for the CentrAl

laminate. Solving for the elastic modulus, E, gives the resulting expression:

$$E = \frac{\sigma}{\varepsilon_{total} - \Delta T \alpha} \tag{25}$$

Ultimate Tensile Strength

Unidirectional Prepreg Lamina - Material 1 and 2 Directions.

The same theoretical development which was shown to develop the elastic

modulus can be used to develop the theoretical ultimate tensile failure stress. Because of

the nature of the FM94K Adhesive itself, a specific ultimate tensile strength does not

necessarily exist. A measureable shear strength can be found, as an adhesive essentially

resists deformation via shear resistance between two substrates.

Since the fibrous prepreg or BondPreg® layers contain no metal, they are defined

as having an MVF equal to 0%. The traditional MVF approach is not used in this

research to establish these properties. Rather, experimental results are used to quantify

the material properties for the adhesive and prepreg combination.

Taken from [5], the figure below details the experimental results from testing the

fibrous prepreg in the primary longitudinal (L) direction.
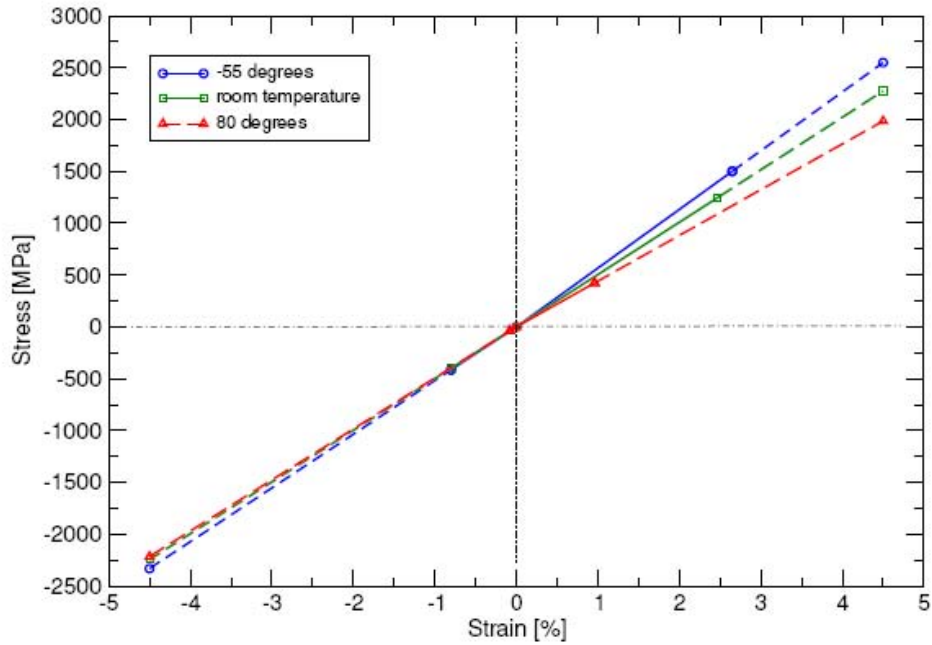
Figure 16 : Extrapolated Stress-Strain Curves for Uni-Directional (L) Prepreg [5]

The extrapolated room temperature ultimate tensile strength from the above figure is

shown as 2,250 MPa. On this figure, it is assumed that the ultimate tensile strain is 4.5%,

which is a general value from GLARE tension test results [5]. For the purpose of this

thesis research, the assumed value for the ultimate tensile strength for the prepreg will be

this experimentally obtained value of 2,250 MPa, which is equal to 326.3 ksi.

The following figure, also taken from [5], shows the experimental results from

testing the fibrous prepreg in the transverse (LT) direction.
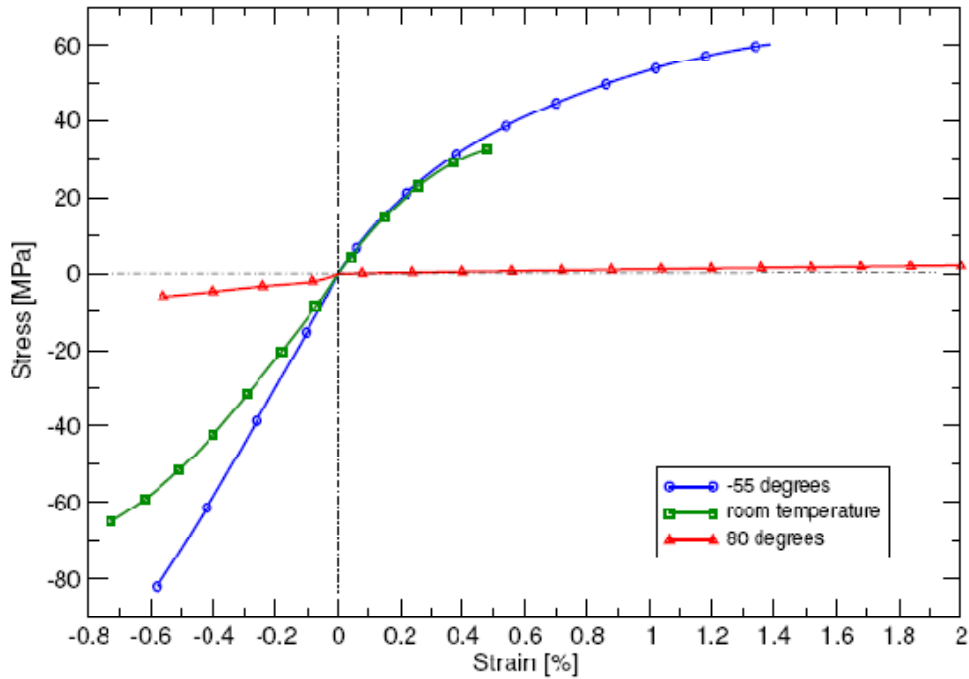
Figure 17 : Extrapolated Stress-Strain Curves for Uni-Directional (LT) Prepreg [5]

It is seen here that the experimentally obtained value for the transverse direction room temperature ultimate tensile strength of unidirectional prepreg is 32 MPa, which is equal to 4.64 ksi. For the purpose of this thesis research, the ultimate tensile strength for the prepreg in the transverse direction is assumed to be 32 MPa.

Unidirectional BondPreg® - Material 1 and 2 Directions.

BondPreg® contains a fiber volume fraction exactly one-half that of the unidirectional prepreg lamina. Since both laminae are constructed from the same constituents, it follows from the fiber volume fraction theory that its respective properties are also reduced by one-half. Because of the linear behavior material properties exhibit with the relative fiber volume fraction, the theoretical values for BondPreg's® UTS are half that of the prepreg.

CentrAl Ultimate Tensile Strength - Material 1 and 2 Directions.

Examining an excerpt from Table 1 : Typical Properties of 2024-T3 Aluminum

[14], the following are the ultimate tensile strength values for monolithic aluminum [14].

Property	Value
UTS (L)	64 ksi
UTS (LT)	63 ksi

The same metal volume fraction approach can be taken to ascertain the ultimate tensile

strength of the overall CentrAl laminate. Recall the nominal thicknesses for each of the

constitutive layer within the laminate.

Table 8 : CentrAl Lamina Thickness and UTS

Layer	Lamina Thickness (in)	Total Thickness (in)	UTS$_1$ (ksi)	UTS$_2$ (ksi)
Outer Aluminum	0.063	0.126	64	63
BondPreg®	0.02	0.04	163.2	2.3
GLARE Aluminum	0.015748	0.047244	64	63
PrePreg	0.005	0.01	326.34	4.6
Total		**0.223244**		

Recall how the metal volume fraction approach allows for the calculation of a

laminate's property. Each layer's property is weighted by its thickness contribution to the

overall laminate thickness. For example, the ultimate tensile strength in terms of

CentrAl's constituents is shown in the equation below:

$$UTS_{1_{CentrAl}} = UTS_{1_{aluminum}}\left(\frac{total\ aluminum\ thickness}{total\ laminate\ thickness}\right) + UTS_{1_{prepreg}}\left(\frac{total\ prepreg\ thickness}{total\ laminate\ thickness}\right) + UTS_{1_{BondPreg}}\left(\frac{total\ BondPreg\ thickness}{total\ laminate\ thickness}\right) \tag{26}$$

Using Equation 26, the UTS in the material 1 direction is found. This value is given as:

UTS$_1$ = 93.53 ksi. Similarly, Equation 27 below shows the relationship for determining

the UTS in the material 2 direction. This value is: UTS$_2$ = 49.51 ksi.

$$UTS_{2_{CentrAl}} = UTS_{2_{aluminum}} \left(\frac{total\ aluminum\ thickness}{total\ laminate\ thickness}\right) + UTS_{2_{prepreg}} \left(\frac{total\ prepreg\ thickness}{total\ laminate\ thickness}\right) + UTS_{2_{BondPreg}} \left(\frac{total\ BondPreg\ thickness}{total\ laminate\ thickness}\right) \quad (27)$$

With the primary and transverse material direction ultimate tensile strengths defined, a

graphical depiction of the property's dependence upon fiber orientation can be

constructed using a slightly modified form of Equation 20. This new model, Equation 28,

is shown below, along with the figure depicting the variation the ultimate tensile strength

exhibits as a function of fiber orientation. Recall Equations 21 and 22 for the definitions

of *m* and *n* respectively.

$$UTS_\theta = UTS_1 m^2 + UTS_2 n^2 \quad (28)$$
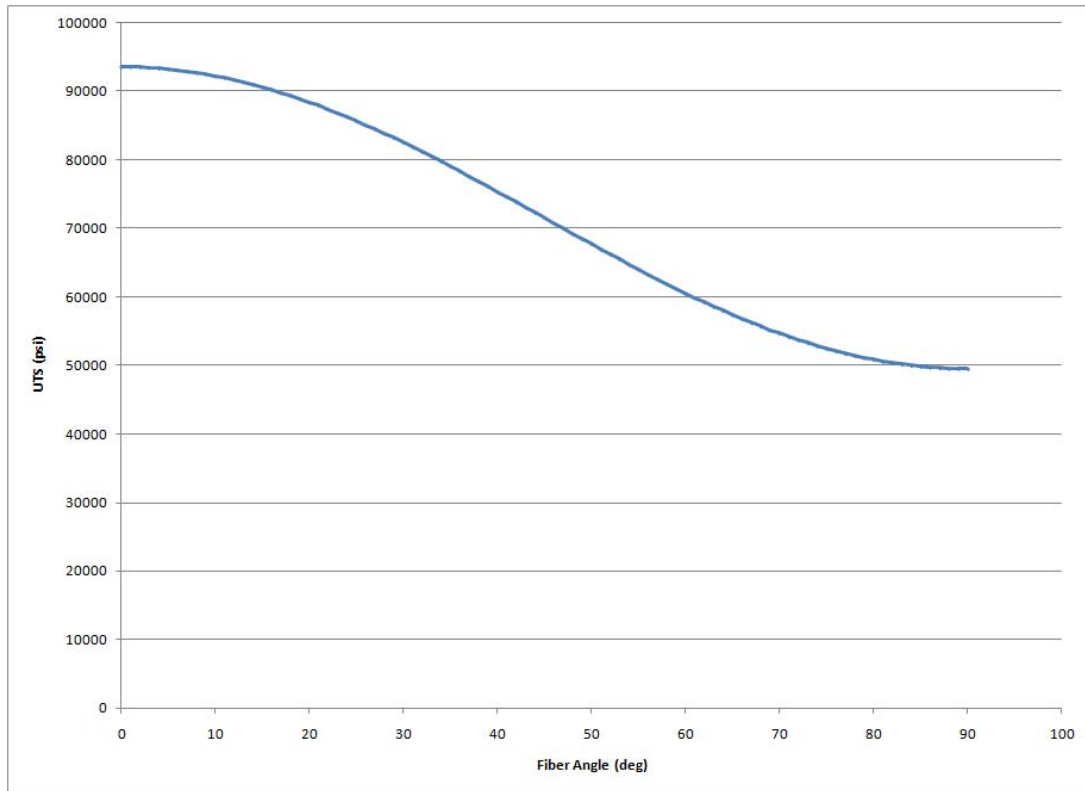
Figure 18 : Theoretical Ultimate Tensile Strength vs. Fiber Orientation

At the four fiber orientations studied as part of this research effort, the following table shows the theoretical ultimate tensile strength at each of these angles.

Table 9 : Theoretical Transformed Ultimate Tensile Strength Values

Fiber Angle (deg)	UTS (ksi)
0	93.53
45	71.29
67.5	55.57
90	49.51

Poisson's Ratio

Theoretical Poisson's Ratio - Material 1-2 Direction.

From elementary mechanics of materials, recall that Posisson's ratio is the ratio of a material's lateral to axial strain. This same definition holds true for a composite material as well. The following figure illustrates the loading condition used in this development.
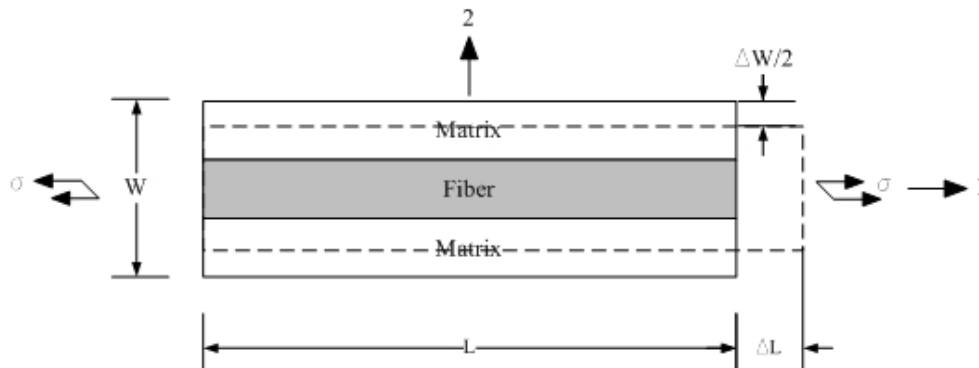
Figure 19 : Representative Volume Element for Poisson's Effect [9]

Examining the deformation of the above element when loaded in the material 1 direction, it is seen there is a lateral contraction of the material. As stated, Poisson's ratio is a ratio of this perpendicular deformation to the deformation seen parallel to the applied load.

This is defined mathematically as:

$$\nu_{12} = -\frac{\varepsilon_2}{\varepsilon_1} \tag{29}$$

If the only applied stress is σ_1 and all other stresses are 0, it follows that the lateral

deformation seen in this representative volume element is given by the expression:

$$\Delta W = -W\varepsilon_2 \tag{30}$$

But the strain seen in the material 2 direction is given through:

$$\varepsilon_2 = -\nu_{12}\varepsilon_1 \tag{31}$$

Therefore:

$$\Delta W = W\nu_{12}\varepsilon_1 \tag{32}$$

Since the matrix and fibers are securely bound, they must strain the same, or exhibit the

same magnitude of deformation. So the total lateral deformation can thus be written as

the sum of the matrix and fiber deformations.

$$\Delta W = \Delta W_m + \Delta W_f \tag{33}$$

Similar to the technique utilized to determine the elastic modulus in the material 2

direction, the matrix and fiber deformation from the applied load in the 1 direction is

given via:

$$\Delta W_m = WV_m\nu_m\varepsilon_1 \tag{34}$$

$$\Delta W_f = WV_f\nu_f\varepsilon_1 \tag{35}$$

Performing the necessary substitutions produces:

$$W\nu_{12}\varepsilon_1 = WV_m\nu_m\varepsilon_1 + WV_f\nu_f\varepsilon_1 \tag{36}$$

$$\nu_{12} = V_m\nu_m + V_f\nu_f \tag{37}$$

Unidirectional Prepreg Lamina - Material 1-2 Direction.

Finding the major Poisson's ratio for the prepreg layer first involves determining the Poisson's ratio of each constituent material. From the manufacturer data, Poisson's ratio for the S-2 Glass fibers is given as:

$$\nu_{12_f} = 0.23$$

Poisson's ratio for the matrix material is given as:

$$\nu_{12_m} = 0.33$$

Recall that in the unidirectional prepreg lamina, the fiber volume fraction is 60%. Therefore, the major Poisson's ratio can be determined by using the aforementioned development from Equation 37, which yields $\nu_{12} = 0.27$.

Unidirectional BondPreg® - Material 1-2 Direction.

Recall that the fiber volume fraction for the BondPreg® is 30%. Since its constitutive materials are the same as those in the unidirectional prepreg lamina, the above model is only slightly altered to determine the major Poisson's ratio for BondPreg®. Thus from Equation 37, BondPreg's® Poisson's ratio is given as: $\nu_{12} = 0.30$.

Theoretical Poisson's Ratio - Material 2-1 Direction.

In order to develop the relationship necessary to calculate the Possion's ratio in the material 2-1 direction, a brief discussion of the material's overall makeup will be held. CentrAl is an orthotropic material. By definition, this means there are two planes of symmetry within the material [7]. Most modern day fibrous composites utilize an orthotropic construction. For a plane stress situation, in which through the thickness

strains are sufficiently small, the compliance matrix (where the compliance matrix is the inverse of the stiffness matrix) for an orthotropic material is given as:

$$\begin{bmatrix} \varepsilon_1 \\ \varepsilon_2 \\ \gamma_{12} \end{bmatrix} = \begin{bmatrix} S_{11} & S_{12} & 0 \\ S_{21} & S_{22} & 0 \\ 0 & 0 & S_{66} \end{bmatrix} \begin{bmatrix} \sigma_1 \\ \sigma_2 \\ \tau_{12} \end{bmatrix} \tag{38}$$

Where the terms of the compliance matrix are as follows:

$$S_{11} = \frac{1}{E_1} \tag{39}$$

$$S_{12} = \frac{-\nu_{21}}{E_2} \tag{40}$$

$$S_{21} = \frac{-\nu_{12}}{E_1} \tag{41}$$

$$S_{22} = \frac{1}{E_2} \tag{42}$$

$$S_{66} = \frac{1}{G_{12}} \tag{43}$$

Since the compliance matrix is symmetric, $S_{12} = S_{21}$. Hence, there exists the reciprocal relationship [7] :

$$\frac{\nu_{21}}{E_2} = \frac{\nu_{12}}{E_1} \tag{44}$$

Because both the material 1 and 2 direction elastic moduli are known, along with the major Poisson's ratio, the unknown Poisson's ratio can be determined.

Unidirectional Prepreg Lamina - Material 2-1 Direction.

Recall the elastic moduli and major Poisson's ratio for the unidirectional prepreg lamina:

$$E_1 = 7.688 \text{ Msi}$$
$$E_2 = .7706 \text{ Msi}$$
$$\nu_{12} = .27$$

Therefore, using the relationship developed above, it follows from Equation 44 that

Poisson's ratio in the material 2-1 direction is given as: $\nu_{21} = .027$.

Unidirectional BondPreg® - Material 2-1 Direction.

Recall the elastic moduli and major Poisson's ratio for the unidirectional

BondPreg® lamina:

$$E_1 = 4.004 \text{ Msi}$$

$$E_2 = .4522 \text{ Msi}$$

$$\nu_{12} = .30$$

Using Equation 44 once more produces the following Poisson's ratio in the material 2-1

direction for the BondPreg®: $\nu_{21} = .034$.

In Plane Shear Modulus

Theoretical In Plane Shear Modulus - Material 1-2 Direction.

Similar in scope to developing the laminate Poisson's ratio, finding the shear

modulus of a lamina involves a mechanics of approach through examining a

representative volume element loaded in shear. The chief assumption of this technique, as

with the others, lies in assuming the shear stresses in both the fiber and matrix are the

same. The non-linear shear stress-shear strain behavior of typical fiber-reinforced

composites is ignored [9] in this development. Figures 20 and 21 below show the loading

state of the element and the deformation due to the shear loading.
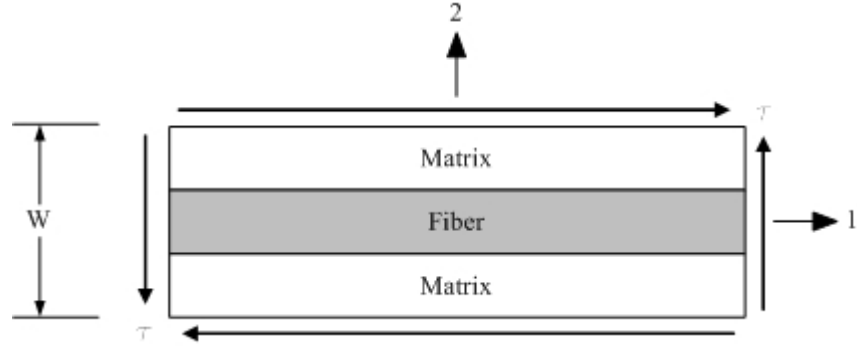
Figure 20 : Representative Volume Element - Shear Loading [9]
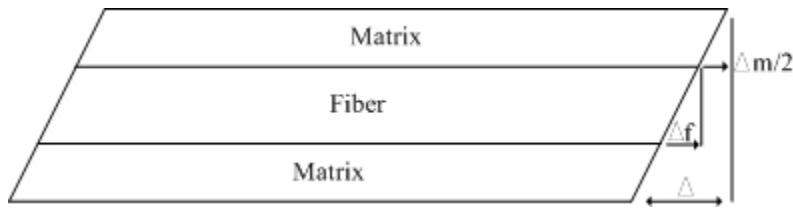
Figure 21 : Representative Volume Element - Shear Deformation [9]

Since the matrix and fiber shear stresses are equal, it follows that they are proportional to

their respective shear moduli and shear strain values. Therefore:

$$\gamma_m = \frac{\tau}{G_m} \tag{45}$$

$$\gamma_f = \frac{\tau}{G_f} \tag{46}$$

And from Figure 21 : Representative Volume Element - Shear Deformation [9] above,

the total shearing deformation can be defined as:

$$\Delta = \gamma W \tag{47}$$

The total shear deformation of the representative volume element is thus made up of the

shear deformation of both the matrix and fiber respectively. The corresponding

proportion of the constituent shear strains is thus a function of the fiber volume fraction.

$$\Delta_m = \gamma_m W V_m \tag{48}$$

$$\Delta_f = \gamma_f W V_f \tag{49}$$

And since the total shear deformation is the sum of the element shear deformations,

substituting Equations 48 and 49 into Equation 47, it follows that:

$$\Delta = \gamma W = \gamma_m W V_m + \gamma_f W V_f$$

$$\gamma = \gamma_m V_m + \gamma_f V_f \tag{50}$$

Now substituting Equations 45 and 46 into Equation 50 produces:

$$\gamma = \frac{\tau}{G_m} V_m + \frac{\tau}{G_f} V_f \tag{51}$$

Further, recognize that the in-plane shear modulus is a function of the total shear strain

and shear stress:

$$\gamma = \frac{\tau}{G_{12}} \tag{52}$$

Therefore, substituting Equation 52 into equation 51 yields:

$$\frac{\tau}{G_{12}} = \frac{\tau}{G_m} V_m + \frac{\tau}{G_f} V_f \tag{53}$$

Finally, solving for G_{12} yields:

$$G_{12} = \frac{G_m G_f}{V_m G_f + V_f G_m} \tag{54}$$

Unidirectional Prepreg Lamina - Material 1-2 Direction.

Determining the in-plane shear modulus for the unidirectional prepreg lamina

requires knowing the shear modulus of each of the constituent elements. The following

table shows the required properties.

Table 10 : Constituent Shear Moduli for CentrAl Fibrous Layers

Element	Volume Fraction	G (Msi)
S2-Glass Fiber	0.60	5.53
FM94K Adhesive	0.40	0.12

Thus from Equation 54, it follows that the in-plane shear modulus is given as:

$G_{12} = 0.290543$ Msi.

Unidirectional BondPreg® - Material 1-2 Direction.

Following the same methodology, recalling reduced fiber volume fraction of the

BondPreg® layer of 30%, the in-plane shear modulus is calculated using Equation 54.

The in-plane shear modulus is as follows: $G_{12} = 0.169849$ Msi.

Coefficient of Thermal Expansion

Theoretical Coefficient of Thermal Expansion - Material 1 Direction.

From [3], the coefficient of thermal expansion in the material 1 direction is given

by:

$$\alpha_1 = \frac{E_f \alpha_f V_f + E_m \alpha_m V_m}{E_f V_f + E_m V_m} \tag{55}$$

Unidirectional Prepreg Lamina - Material 1 Direction.

From the manufacturer data, the CTE for the S2-Glass fibers is

.9 micro-strain per degree Fahrenheit. Further, the CTE for the matrix material is given as

41.7 micro-strain per degree Fahrenheit. The following table summarizes the necessary

parameters needed to determine the unidirectional prepreg's CTE in the material 1

direction.

Table 11 : Property Information for CTE Material 1 Direction Calculation

Element	Volume Fraction	E1 (Msi)	CTE ($\mu\varepsilon$ $^{\circ}F^{-1}$)
S2- Glass Fiber	0.60	12.6	0.9
FM94K Adhesive	0.40	0.32	41.7

Given this information and Equation 55, the unidirectional prepreg's coefficient of

thermal expansion can be determined. This value is as follows: $\alpha_1 = 1.61 \frac{\mu \frac{in}{in}}{F}$

Unidirectional BondPreg® - Material 1 Direction.

Following the same methodology, the CTE for the BondPreg® is found. Recall the fiber volume fraction for this material is 30%. Also from Equation 55, the result is as follows: $\alpha_1 = 3.37 \frac{\mu\frac{in}{in}}{F}$

Theoretical Coefficient of Thermal Expansion - Material 2 Direction.

From [3], the coefficient of thermal expansion in the material 2 direction is given by:

$$\alpha_2 = \alpha_f V_f (1 + \nu_f) + \alpha_m V_m (1 + \nu_m) - \nu_{12}\alpha_1 \tag{56}$$

Using this model, it is seen that the lamina material 2 direction CTE is not only a function of its constituents' volume fractions and individual CTE values, but the lamina's major Poisson's and CTE in the material 1 direction.

Unidirectional Prepreg Lamina - Material 2 Direction.

As a reference, the following table details the properties needed to determine the CTE in the material 2 direction for the unidirectional prepreg lamina.

Table 12 : Property Information for CTE Material 2 Direction Calculation

Element	Volume Fraction	ν_{12}	CTE µε °F^{-1}
S2-Glass Fiber	0.60	0.23	0.90
FM94K Adhesive	0.40	0.33	41.70

Recall that for the unidirectional prepreg lamina, the major Poisson's ratio (ν_{12}) is .27.

The lamina's CTE in the material 1 direction (α_1) is $1.61 \frac{\mu\frac{in}{in}}{F}$. Thus using Equation 56, the CTE in the material 2 direction is determined as follows: $\alpha_2 = 22.4 \frac{\mu\frac{in}{in}}{F}$.

Unidirectional BondPreg® - Material 2 Direction.

With the reduced fiber volume fraction of 30%, the major Poisson's ratio (v_{12}) of

0.034, and material 1 direction CTE of 3.37 $\frac{\mu\frac{in}{in}}{F}$, the CTE for the material 2 direction in

the unidirectional BondPreg® layer is given as: $\alpha_2 = 39.04 \ \frac{\mu\frac{in}{in}}{F}$.

CentrAl CTE Development.

Because of the strain interactions between the laminate layers, a simple metal

volume fraction approach cannot be used to determine the overall laminate CTE value in

either the 1 or 2 material directions. A technique involving classical laminated plate

theory (CLPT) must be employed.

Recall from the development of Poisson's ratio in the 2-1 material direction, for a

plane stress situation, in which through the thickness strains are sufficiently small. The

compliance matrix for an orthotropic lamina was given previously by Equation 38:

$$S_{ij} = \begin{bmatrix} \frac{1}{E_1} & \frac{-v_{12}}{E_1} & 0 \\ \frac{-v_{12}}{E_1} & \frac{1}{E_2} & 0 \\ 0 & 0 & \frac{1}{G_{12}} \end{bmatrix} \qquad (38)$$

Inverting the compliance matrix gives the respective lamina stiffness matrix:

$$Q_{ij} = \begin{bmatrix} \frac{E_1}{1-v_{12}v_{21}} & \frac{v_{12}E_2}{1-v_{12}v_{21}} & 0 \\ \frac{v_{12}E_2}{1-v_{12}v_{21}} & \frac{E_2}{1-v_{12}v_{21}} & 0 \\ 0 & 0 & G_{12} \end{bmatrix} \qquad (57)$$

In order to transform the compliance and stiffness matrices to determine their

respective values coincident to the fiber orientations found within the excised specimens,

46

a system a transformation matrices will be adopted. Taken from [7], the transformation

matrices used in this development are as follows:

$$T1 = \begin{bmatrix} m^2 & n^2 & 2mn \\ n^2 & m^2 & -2mn \\ -mn & mn & m^2 - n^2 \end{bmatrix} \tag{58}$$

$$T2 = \begin{bmatrix} m^2 & n^2 & mn \\ n^2 & m^2 & -mn \\ -2mn & 2mn & m^2 - n^2 \end{bmatrix} \tag{59}$$

Recall the definitions of *m* and *n* are given in Equations 21 and 22 respectively. The

rationale behind the two different transformation matrices stems from the use of

engineering shear strain rather than tensor shear strain. Transformation of the compliance

and stiffness matrices, respectively, are as follows:

$$S_{\theta_{ply}} = [T_2]^{-1}[Q]^{-1}[T_1] \tag{60}$$

$$Q_{\theta_{ply}} = [T_1]^{-1}[Q][T_2] \tag{61}$$

With the above models, the compliance and stiffness matrices for each lamina within

CentrAl can be found. Further, by applying the requisite transformation, each off-axis

compliance and stiffness matrix is calculated.

The first step towards solving for the overall laminate CTE is to determine the

overall laminate stiffness matrix. This involves using a technique similar to that of the

metal volume fraction approach taken to ascertain the overall laminate elastic modulus,

wherein the individual lamina stiffness matrices are weighted according to their thickness

contribution to the overall laminate thickness. The relationships are found in [8].

$$S_{\theta_{laminate}} = \sum_{ply = 1}^{n} (S_\theta)_{ply} \frac{t_{ply}}{t_{laminate}} \tag{62}$$

$$Q_{\theta_{laminate}} = \sum_{ply = 1}^{n} (Q_\theta)_{ply} \frac{t_{ply}}{t_{laminate}} \tag{63}$$

Since there are nine layers within the CentrAl laminate, there will be nine total

terms within the stiffness matrix calculation.

Only the 0 degree total laminate stiffness matrix is shown because the other fiber

orientation stiffness matrices can be found through applying the necessary

transformations. Using Equation 63 for the 0 degree specimen fiber orientation, the

following is the total laminate stiffness matrix.

$$[Q]_{0^\circ laminate} = \begin{bmatrix} 10.215\ Msi & 30.515\ Msi & 0 \\ 30.515\ Msi & 92.607\ Msi & 0 \\ 0 & 0 & 31.476\ Msi \end{bmatrix}$$

The next step in determining the overall laminate CTE is to recognize that cooling down

from the curing temperature will cause a strain in the laminate. All individual layers must

comply with this strain. This leads to the following equilibrium [8] relationship:

$$\sum_{ply\ =\ 1}^{n} (Q_\theta)_{ply} t_{ply} \bar{\alpha}_{ply} = Q_{\theta_{laminate}} t_{laminate} \bar{\alpha}_{laminate} \tag{64}$$

Where each lamina's CTE matrix is given by:

$$\bar{\alpha}_{ply} = \begin{bmatrix} \alpha_1 \cos\theta + \alpha_2 \sin\theta \\ \alpha_1 \sin\theta + \alpha_2 \cos\theta \\ 0 \end{bmatrix} \tag{65}$$

Therefore for the overall laminate, the CTE matrix is given by:

$$\bar{\alpha}_{laminate} = \frac{1}{t_{laminate}} (Q_{\theta_{laminate}})^{-1} \sum_{ply\ =\ 1}^{n} (Q_\theta)_{ply} t_{ply} \bar{\alpha}_{ply} \tag{66}$$

Following this equation, the overall laminate CTE matrix is found. Again, only the

0 degree fiber orientation is shown because the other orientations can be readily found

through applying the requisite transformations.

$$[\bar{\alpha}]_{0^\circ laminate} = \begin{bmatrix} .000011357 \\ .000013087 \\ 0 \end{bmatrix}$$

48

Thus $\alpha_1 = 11.357 \frac{\mu \frac{in}{in}}{F}$ and $\alpha_2 = 13.087 \frac{\mu \frac{in}{in}}{F}$. With the material 1 and 2 direction CTE

values known, the off-axis coefficients of thermal expansion can be determined by using

a system of simple axis transformations.

$$\alpha_\theta = \alpha_1 m^2 + \alpha_2 n^2 \tag{67}$$

where *m* and *n* are defined by Equations 21 and 22 respectively.

Depicted graphically, the following figure shows the dependence fiber orientation

plays on CentrAl's CTE.
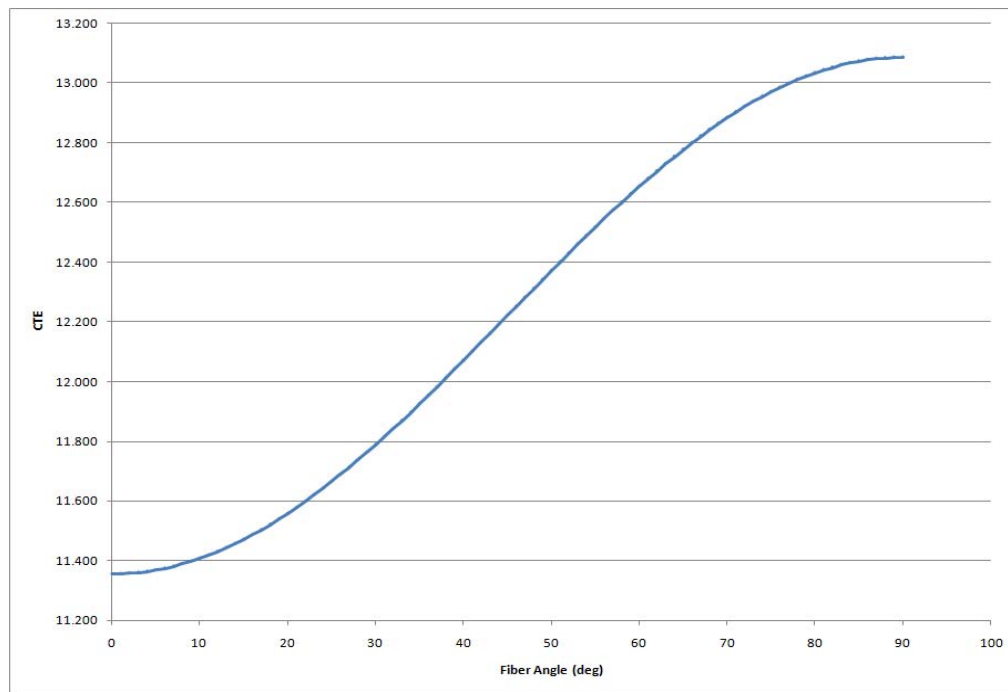
Figure 22 : Theoretical CTE vs. Fiber Orientation

The theoretical thermal strains for each fiber orientation can now be found. Recall the lab

temperature was 23C (66F), the high test temperature was 80C (176F), and the low test

temperature was -55C (-67F). The difference in each temperature is then multiplied by

the respective fiber orientation CTE to arrive at the theoretical thermal strains. Table 21 :

High Temperature Theoretical Steady State Strain shows the high temperature theoretical

strain and Table 22 : Low Temperature Theoretical Steady State Strain shows the corresponding low temperature values.

Theoretical Loading Cycles to Crack Initiation

As previously discussed, fiber metal laminates owe their crack growth resistance to the fibers between the aluminum layers [8]. The fibers themselves retain the ability to remain essentially intact during fatigue loading, as fatigue cracks propagate in the aluminum layers. In fatigue loading, two primary phases of material behavior are seen: the crack initiation phase and the crack propagation phase. In monolithic aluminum, the majority of its fatigue life is spent during the crack initiation phase of fatigue crack growth. Wherein, after the crack has reached its critical length, the final crack propagation is extremely fast and only encompasses a small percentage of the fatigue life. In contrast, the fiber metal laminate, when placed under fatigue loading, spends the majority of its life during the crack propagation phase of fatigue crack growth, as the fibers preclude rapid crack growth in the material.

Since the aluminum layers themselves are primarily affected in the crack initiation phase, as the subsurface fibers remain unbroken, the initiation process will be considered a fatigue process in aluminum. The figure below shows an illustration of the intact subsurface fibers aiding in the fiber bridging phenomenon.
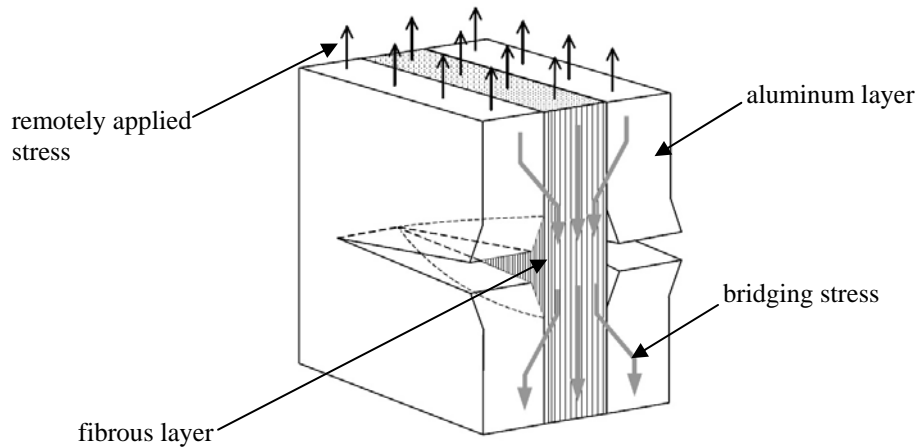
Figure 23 : Fiber Bridging in Fiber Metal Laminates [13]

The consequence of this assumption is that the initiation life of the fiber metal laminates can be directly read from the S-N curves of the constituent metal alloy [8]. Often, the fatigue life of monolithic materials can be directly read from their corresponding S-N curves, but because crack growth in the fiber metal laminate is so slow, the initiation life cannot be estimated using information about the total fatigue life. Therefore, the assumption made for metals that the number of cycles in the crack initiation phase is about the same as the number of cycles to total fatigue failure cannot be made for fiber metal laminates [8]. This therefore gives an estimate to the number of cycles to crack initiation FML's metallic layers.

Recognizing that the fiber metal laminate is constructed of multiple fibrous and metallic layers, the metallic layers, with their inherent higher stiffness, attract additional load during a fatigue loading cycle. With CentrAl, since the metallic layers are aluminum, these layers exhibit a higher stress magnitude.

The first step in estimating the number of cycles to initiate a crack in CentrAl is to determine the stresses in the laminate's aluminum layers. From the calculated stress cycles for the aluminum layers, the fatigue life can be estimated using the assumption

that the S-N data from the literature can be applied for the life-to-small-crack-initiation, despite the fact that these data are very often life-to-failure data [8].

Before the aluminum layer stresses can be determined, the laminate stiffness matrix must be determined.

Recall from the development of the laminate coefficient of thermal expansion that the definition of the compliance matrix for an orthotropic lamina is given by Equation 38:

$$S_{ij} = \begin{bmatrix} \frac{1}{E_1} & \frac{-v_{12}}{E_1} & 0 \\ \frac{-v_{12}}{E_1} & \frac{1}{E_2} & 0 \\ 0 & 0 & \frac{1}{G_{12}} \end{bmatrix} \tag{38}$$

Inverting this matrix provides the lamina stiffness matrix in Equation 57.

$$Q_{ij} = \begin{bmatrix} \frac{E_1}{1-v_{12}v_{21}} & \frac{v_{12}E_2}{1-v_{12}v_{21}} & 0 \\ \frac{v_{12}E_2}{1-v_{12}v_{21}} & \frac{E_2}{1-v_{12}v_{21}} & 0 \\ 0 & 0 & G_{12} \end{bmatrix} \tag{57}$$

In order to transform the compliance and stiffness matrices to determine their respective values coincident to the fiber orientations found within the excised specimens, a system a transformation matrices will be adopted. Taken from [7], as shown previously in the section developing the laminate's coefficient of thermal expansion, the transformation matrices, Equations 58 and 59 respectively, are as follows:

$$T1 = \begin{bmatrix} m^2 & n^2 & 2mn \\ n^2 & m^2 & -2mn \\ -mn & mn & m^2 - n^2 \end{bmatrix} \tag{58}$$

$$T2 = \begin{bmatrix} m^2 & n^2 & mn \\ n^2 & m^2 & -mn \\ -2mn & 2mn & m^2 - n^2 \end{bmatrix} \tag{59}$$

Where *m* and *n* are defined by Equations 21 and 22 respectively. Transformation of the

compliance and stiffness matrices, respectively, for each ply are as follows:

$$S_{\theta_{ply}} = [T_2]^{-1}[Q]^{-1}[T_1] \tag{60}$$

$$Q_{\theta_{ply}} = [T_1]^{-1}[Q][T_2] \tag{61}$$

With the above models, the compliance and stiffness matrices for each lamina within

CentrAl can be found. Further, by applying the requisite transformation, each off-axis

compliance and stiffness matrix is calculated.

Obtaining the overall laminate compliance and stiffness matrices is needed when

calculating the stresses in the laminate's aluminum layers. Recall from previous

development, this involves using a technique similar to that of the metal volume fraction

approach, wherein the individual lamina stiffness matrices are weighted according to

their thickness contribution to the overall laminate thickness.

$$S_{\theta_{laminate}} = \sum_{ply=1}^{n} (S_\theta)_{ply} \frac{t_{ply}}{t_{laminate}} \tag{62}$$

$$Q_{\theta_{laminate}} = \sum_{ply=1}^{n} (Q_\theta)_{ply} \frac{t_{ply}}{t_{laminate}} \tag{63}$$

Since there are nine layers within the CentrAl laminate, there will be nine total

terms within the stiffness matrix calculation.

Only the 0 degree total laminate stiffness matrix is shown because the other fiber

orientation stiffness matrices are readily obtained through applying the necessary

transformations. For the 0 degree specimen fiber orientation, the following is the total

laminate stiffness matrix.

$$[Q]_{0^o\,laminate} = \begin{bmatrix} 10.215\ Msi & 30.515\ Msi & 0 \\ 30.515\ Msi & 92.607\ Msi & 0 \\ 0 & 0 & 31.476\ Msi \end{bmatrix}$$

From the CTE development, recognize that cooling down from the curing temperature will cause a strain in the laminate. Since, all individual layers must comply with this strain. This leads to the following equilibrium [8] relationship in Equation 64:

$$\sum_{ply=1}^{n} (Q_\theta)_{ply} t_{ply} \bar{\alpha}_{ply} = Q_{\theta_{laminate}} t_{laminate} \bar{\alpha}_{laminate} \tag{64}$$

Where each lamina's CTE matrix is given by Equation 65:

$$\bar{\alpha}_{ply} = \begin{bmatrix} \alpha_1 \cos\theta + \alpha_2 \sin\theta \\ \alpha_1 \sin\theta + \alpha_2 \cos\theta \\ 0 \end{bmatrix} \tag{65}$$

Therefore for the overall laminate, the CTE matrix is given by Equation 66:

$$\bar{\alpha}_{laminate} = \frac{1}{t_{laminate}} (Q_{\theta_{laminate}})^{-1} \sum_{ply=1}^{n} (Q_\theta)_{ply} t_{ply} \bar{\alpha}_{ply} \tag{66}$$

Following this equation, the overall laminate CTE matrix is found. Again, only the 0 degree fiber orientation is shown because the other orientations can be readily found through applying the requisite transformations.

$$[\bar{\alpha}]_{0°_{laminate}} = \begin{bmatrix} .000011357 \\ .000013087 \\ 0 \end{bmatrix}$$

Once the laminate CTE matrix is found, the strain due to thermal expansion can be calculated by recognizing that this strain is merely a product of the laminate CTE matrix and the change in temperature between the local environment and curing temperatures. This is shown in the equation below.

$$\bar{\varepsilon}_{cure} = \bar{\alpha}_{lam} \Delta T \tag{68}$$

Where

$$\Delta T = T_{env} - T_{cure} \tag{69}$$

Thus the internal ply stresses induced by the curing process is given by:

$$\bar{\sigma}_{cure,ply} = (Q_\theta)_{ply} \, (\bar{\varepsilon}_{cure} - \Delta T \bar{\alpha}_{ply}) \tag{70}$$

The internal strain due to an externally applied stress can then be modeled as:

$$\bar{\varepsilon} = (Q_\theta)^{-1}_{laminate} (\bar{\sigma})_{laminate} \tag{71}$$

Where $\bar{\sigma}$ is the vector of externally applied stresses and let $\bar{\sigma} = (\bar{\sigma})_{laminate}$. Thus the stress level in a single ply can be written as:

$$(\bar{\sigma}_\theta)_{ply} = (Q_\theta)_{ply} \, \bar{\varepsilon} \tag{72}$$

$$(\bar{\sigma}_\theta)_{ply} = (Q_\theta)_{ply} \, (Q_\theta)^{-1}_{laminate} (\bar{\sigma})_{laminate} \tag{73}$$

The total stress level in a ply is therefore the sum of the thermally induced stress due to the curing process and the external stress. This can be found by evaluating the following expression.

$$(\bar{\sigma}_\theta)_{ply} = (Q_\theta)_{ply} \, [(Q_\theta)^{-1}_{laminate} (\bar{\sigma})_{laminate} + \Delta T (\bar{\alpha}_{lam} - \bar{\alpha}_{ply})] \tag{74}$$

For this research effort, all fatigue tests are conducted on specimens with fibers oriented in the material 1 direction, at 0°. Since the applied fatigue loads and hence induced stresses are parallel with the fibers, only the stress in this direction will be used to estimate the fatigue life.

To reiterate, only the stress in the aluminum layers will be used. It should be noted that since the aluminum layers with CentrAl exhibit the same properties, as their thickness are somewhat close in value [14], the stress levels in each of these layers are assumed to be the same. Once the internal stress in the aluminum layer is found, the S-N curve for 2024-T3 aluminum is then used to estimate the number of cycles to crack initiation in these layers. Recall 2024-T3 is the alloy used in this investigation's research panel.

The following figure is a typical S-N curve for un-notched aluminum at various stress ratios. The stress ratio for this research is a constant 0.1. Because the research stress ratio is not explicitly stated on the S-N curve, but is within the ranges of stress ratios utilized to produce the curve sets, the equivalent stress model accompanying the S-N curve can be used to predict the number of cycles to initiate a crack in the laminate's metallic layers. The following equations make up the equivalent stress relationship [14].

$$\log N_f = 11.1 - 3.97 \log (S_{eq} - 15.8) \tag{75}$$

Where

$$S_{eq} = S_{max} (1 - R)^{0.56} \tag{76}$$

And S_{max} is the maximum stress seen in the aluminum layer.
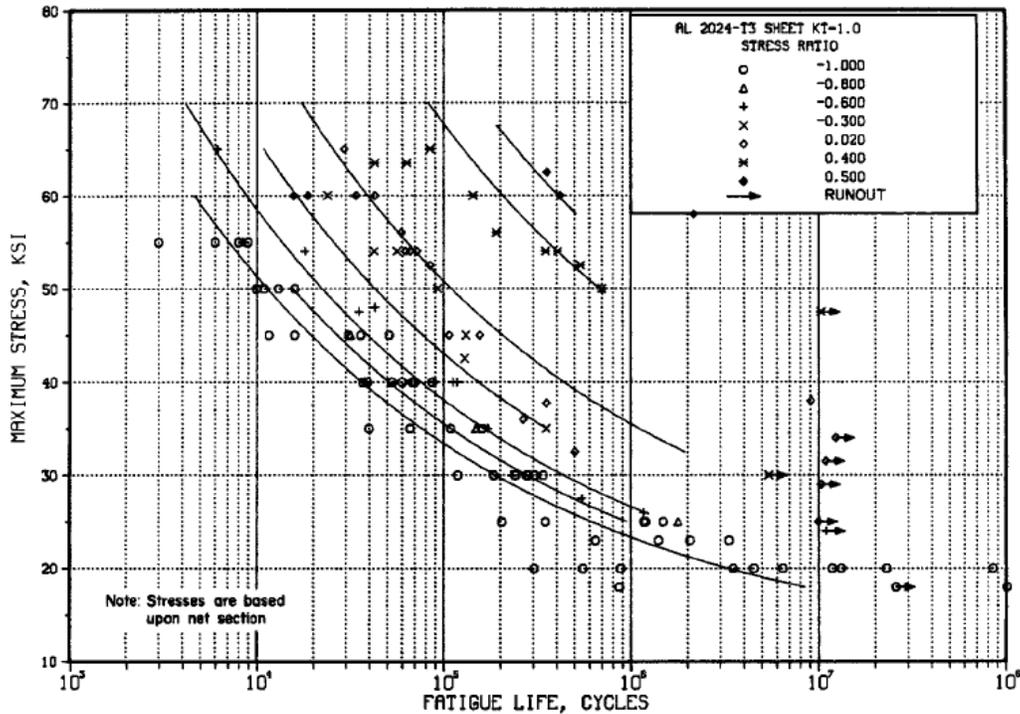
Figure 24 : Best-fit S/N Curves for 2024-T3 Aluminum Sheet, (L) [14]

Given the properties of aluminum in Table 1, the compliance matrix for the aluminum for is constructed.

$$S_{ij} = \begin{bmatrix} \frac{1}{E_1} & \frac{-\nu_{12}}{E_1} & 0 \\ \frac{-\nu_{12}}{E_1} & \frac{1}{E_2} & 0 \\ 0 & 0 & \frac{1}{G_{12}} \end{bmatrix} \tag{38}$$

$$S_{aluminum} = \begin{bmatrix} \frac{1}{10,500,000} & \frac{-0.33}{10,500,000} & 0 \\ \frac{-0.33}{10,500,000} & \frac{1}{10,500,000} & 0 \\ 0 & 0 & \frac{1}{4,000,000} \end{bmatrix}$$

Inverting the compliance matrix gives the stiffness matrix for the aluminum:

$$Q_{ij} = \begin{bmatrix} \frac{E_1}{1-\nu_{12}\nu_{21}} & \frac{\nu_{12}E_2}{1-\nu_{12}\nu_{21}} & 0 \\ \frac{\nu_{12}E_2}{1-\nu_{12}\nu_{21}} & \frac{E_2}{1-\nu_{12}\nu_{21}} & 0 \\ 0 & 0 & G_{12} \end{bmatrix} \tag{57}$$

$$[Q]_{0^o\,aluminum} = \begin{bmatrix} 11,783,200\ psi & 3,888,450\ psi & 0 \\ 3,888,450\ psi & 11,783,200\ psi & 0 \\ 0 & 0 & 4,000,000\ psi \end{bmatrix}$$

And the aluminum CTE matrix is given by:

$$[\bar{\alpha}]_{0^o\,aluminum} = \begin{bmatrix} .00001248 \\ .00001248 \\ 0 \end{bmatrix}$$

Recall that for the 0 degree specimen fiber orientation, the following is the total laminate

stiffness matrix:

$$[Q]_{0^o\,laminate} = \begin{bmatrix} 10,215,000\ psi & 30,515,000\ psi & 0 \\ 30,515,000\ psi & 92,607,000\ psi & 0 \\ 0 & 0 & 31,476,000\ psi \end{bmatrix}$$

The inverse of this matrix, which will be used to determine the stress in the aluminum layers, is given by:

$$[Q]^{-1}{}_{0^o\,laminate} = \begin{bmatrix} \dfrac{92,607}{14,815,280,000} & \dfrac{-6103}{2,963,056,000} & 0 \\ \dfrac{-6103}{2,963,056,000} & \dfrac{2,043}{2,963,056,000} & 0 \\ 0 & 0 & \dfrac{1}{31,476,000} \end{bmatrix}$$

And finally, using Equation 66, the overall laminate CTE matrix is given by:

$$[\bar{\alpha}]_{0^o\,laminate} = \begin{bmatrix} .000011357 \\ .000013087 \\ 0 \end{bmatrix}$$

For common GLARE laminates, the cure temperature is 248F [8]. Since the test temperature was held at a constant 66F, the temperature difference, ΔT, is given as -182F. The vector of applied stress is the only remaining variable in the relationship developed to determine the stress level in CentrAl's aluminum layers. Since the load is applied in the material 1 direction, parallel to the fibers, only the first entry into the stress vector is used.

$$[\bar{\sigma}]_{laminate} = \begin{bmatrix} \sigma \\ 0 \\ 0 \end{bmatrix}$$

The following table provides the stress levels induced into the gauge section during the fatigue investigation.

Table 13 : Fatigue Testing Gauge Section Stresses

Gauge Section Stress (psi)
80000
65000
50763.2
36259.4
20000

Therefore, to determine the stress in the aluminum layers from the gauge section stress of

58

80,000 psi, Equation 74 is used. The following is the resulting stresses in the aluminum
layers:

$$(\bar{\sigma}_0)_{aluminum} = \begin{bmatrix} 93{,}202 \\ -456.55 \\ 0 \end{bmatrix}$$

Following the same process for each of the stresses seen in the gauge section, the
following table shows the respective stresses in the CentrAl aluminum layers.

Table 14 : Aluminum Layer Stresses During CentrAl Fatigue Testing

Gauge Section Stress (psi)	Aluminum Layer Stress (psi)
80000	93202
65000	76098
50763.2	59864
36259.4	43326
20000	24785

With the maximum stresses seen in the aluminum layers now determined, the equivalent
stress can then be determined using Equation 76. It should be noted here that the
maximum stress (S_{max}) in this model is in units of *ksi* not *psi*.

$$S_{eq} = S_{max} (1 - R)^{0.56} \qquad (76)$$

The following table shows the gauge section stress, the maximum stress in the aluminum
layers, and the corresponding equivalent stress magnitudes.

Table 15 : Equivalent Aluminum Layer Stresses During CentrAl Fatigue Testing

Applied Stress (psi)	Max Al Layer Stress (psi)	Equivalent Stress (psi)
80000	93202	87862
65000	76098	71738
50763.2	59864	56434
36259.4	43326	40844
20000	24785	23365

Finally, the number of cycles to crack initiation can be estimated from Equation 75:

$$\log N_f = 11.1 - 3.97 \log (S_{eq} - 15.8) \qquad (75)$$

59

Using this model, the following table is populated with the estimated number of cycles to initiate a crack within the CentrAl laminate.

Table 16 : Predicted Cycles to Crack Initiation for CentrAl Laminate

Gauge Section Stress (psi)	Al Layer Max Stress (psi)	Equivalent Stress (psi)	Predicted Cycles to Crack Initiation
80000	93202	93202	5307
65000	76098	76098	14508
50763.2	59864	59864	51606
36259.4	43326	43326	352510
20000	24785	24785	40852000

Theoretical Stress Concentration Factor

Notches in structures are unavoidable. The disadvantage of notches is that they cause local stress redistributions in the notched material and create stress concentrations. The intensity of these concentrations is described with the stress concentration factor K_t, which is described as the ratio between the maximum stress, σ_{peak}, at the notch root and the average stress, $\sigma_{nominal}$, in the net section [20]. For an isotropic material with an infinite width, the stress concentration factor is given as:

$$Kt = 1 + 2\frac{a}{b} \tag{77}$$

The following figure below defines the variables for this model:
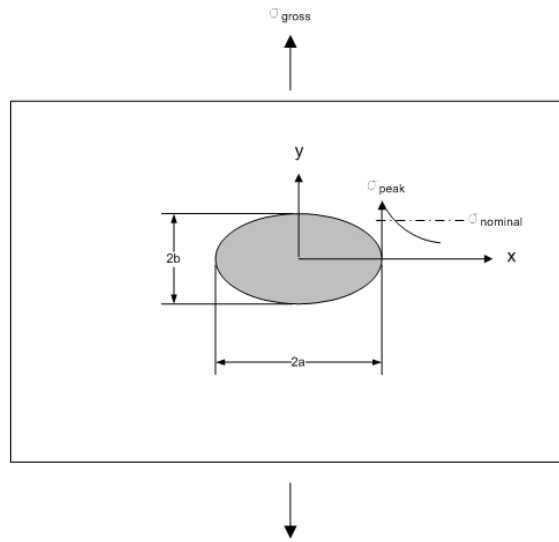
Figure 25 : Stress Concentration Parameters

Therefore, an infinite width isotropic plate has a stress concentration factor equal to 3. To

correct for the finite width of an isotropic blunt notch specimen, the following equation

taken from [23] is used.

$$K_t = 3.00 - 3.13 \left(\frac{2r}{d}\right) + 3.66 \left(\frac{2r}{d}\right)^2 - 1.53 \left(\frac{2r}{d}\right)^3 \qquad (78)$$

Where r is the open-hole radius and d is the specimen width. Further use of this

expression is carried out in the section "Rationale Behind Blunt Notch Testing". From the

resulting discussion in this section, it is shown that the stress concentration factor in the

gauge section of the blunt notch specimens is given as Kt = 2.42.

Because CentrAl is an orthotropic material, the expression for an isotropic

material stress concentration cannot be used by itself. Several solutions have been

presented which describe the stress concentration in an orthotropic material are available

in the open literature [8], [10], [16], [20]. For this research, the stress concentration factor

caused by a circular hole in a laminate of infinite dimensions loaded with a plane stress

system can be expressed as a function of the angularity and the directionality of that laminate [8]. As shown [8] the stress concentration factor for an infinite width fiber metal laminate is given by:

$$Kt = \frac{r(m^2(r+\sqrt{2(r+a)})-n^2)}{n^4+2am^2n^2+r^2m^4} \tag{79}$$

where the definitions of the variables r and a come directly from the laminate's overall compliance matrix, and m and n are represented by Equations 21 and 22 respectively. It must be noted, that the angular displacement, θ, used in the m and n terms in the model do not reflect the angle of the laminate's fiber orientation. Rather, the angular displacement, θ, is the physical location along the edge of the hole. The following equations depict the directionality, r, and angularity, a, respectively:

$$r = \sqrt{\frac{S22}{S11}} \tag{80}$$

$$a = \frac{S12+\frac{S66}{2}}{S11} \tag{81}$$

and the terms within the directionality and angularity variables are entries from the laminate's overall compliance matrix. Recall the definition of the compliance matrix.

$$\begin{bmatrix} \varepsilon_1 \\ \varepsilon_2 \\ \gamma_{12} \end{bmatrix} = \begin{bmatrix} S_{11} & S_{12} & 0 \\ S_{12} & S_{22} & 0 \\ 0 & 0 & S_{66} \end{bmatrix} \begin{bmatrix} \sigma_1 \\ \sigma_2 \\ \tau_{12} \end{bmatrix} \tag{38}$$

Upon inspection of Equation 79, it is seen how the greatest magnitude of stress concentration is at found when $\theta = 0°$. Thus, this will be the only location along the hole used for the present research effort.

To arrive at the stress concentration for each fiber orientation, four separate laminate compliance matrices require construction (corresponding to each of the four specimen fiber orientations), as their terms are required for use in the directionality and

angularity variables. Following the previous development of the laminate's compliance

matrix for a given fiber orientation, and using the definitions for the directionality and

angularity variables, the follow table summarizes the terms necessary for determining the

stress concentration factor.

Table 17: Laminate Stress Concentration Angularity and Directionality Terms

Fiber Orientation (deg)	Angularity (a)	Directionality (r)
0	5.319	2.060
45	0.027	1.138
67.5	0.027	0.696
90	1.254	0.485

From Equation 79, the stress concentration for the fiber metal laminate can now be

determined. Again, only the stress concentration oriented at $\theta = 0^\circ$ will be determined.

The following table shows each fiber orientation's stress concentration factor.

Table 18 : Infinite Width CentrAl Plate Stress Concentration Factors

Fiber Orientation (deg)	Kt
0	2.8649
45	2.3414
67.5	3.4377
90	4.8416

As shown in [20] the finite width orthotropic material stress concentration factor

is found using a combination of the infinite width stress concentration factors for both the

orthotropic and isotropic materials. These values are then used in conjunction with the

finite width isotropic solution. To obtain the stress concentration factor for a finite width

orthotropic material, the infinite plate width orthotropic solution (Table 18 : Infinite

Width CentrAl Plate Stress Concentration Factors) is divided by the infinite plate width

isotropic solution (Equation 77). This result is then multiplied by the finite width

isotropic solution from Equation 78. The following table shows the resulting, finite width

stress concentration factors for the CentrAl blunt notch specimens.

Table 19 : Finite Width CentrAl Plate Stress Concentration Factors

Fiber Orientation (deg)	Kt
0	2.311
45	1.888
67.5	2.773
90	3.906

Using these stress concentration factors requires using the definition of the stress

concentration factor itself. Recall this value is given by the following equation:

$$Kt = \frac{\sigma_{peak}}{\sigma_{nominal}} \qquad (82)$$

where σ_{peak} is the maximum stress at the hole edge and $\sigma_{nominal}$ is the average stress in the

net section. The net section is defined as the cross sectional area remaining after the area

of the hole is removed.

During all blunt notch testing, the strain measured is that of the cross section

containing the hole. This can be thought of as the "intensified" strain. When the raw net

stress is calculated, it is actually the "intensified" or peak stress induced by the hole -

where this raw net stress is simply the applied load divided by the net cross sectional area

in the gauge section. Thus to arrive at the average stress in the net section, the intensified

stress is reduced by a value corresponding to the stress concentration factor. Equation 81

can be rearranged to show this relationship.

$$\sigma_{nominal} = \frac{\sigma_{peak}}{Kt} \qquad (83)$$

The value calculated in Equation 82 will be used when developing stress-strain

relationships for the blunt notch specimens. On the stress-strain curves, the effect of the

hole will be measured through calculating the reduced structural stiffness as indicated by

the slope of the curve's linear region. When this value is compared to the original elastic

modulus, an indication of the decrease in material compliance will be evident. This will

also be seen when comparing the ultimate tensile and yield strength values.

VII. Experimental Equipment, Setup, and Procedure

Experimental Equipment

Elastic Modulus, Tensile, and Blunt Notch Strength Tests.

Two separate sequences of room temperature tests were conducted in order to establish an initial baseline of elastic modulus values to which the theoretical values could be compared. A second reason to perform the two room temperature modulus measurements was to validate the first set of experimentally obtained room temperature elastic modulus results, as two different testing machines were utilized. Since each specimen was loaded within the material's theoretical linear range, the elastic modulus should remain unchanged.

Initial room temperature modulus testing was conducted on both the Material Test Systems (MTS) Alliance RT/10 tabletop testing frame and the MTS Sintech 20 G/D floor mounted testing frame.

The following two figures illustrate each machine's distinct design differences.
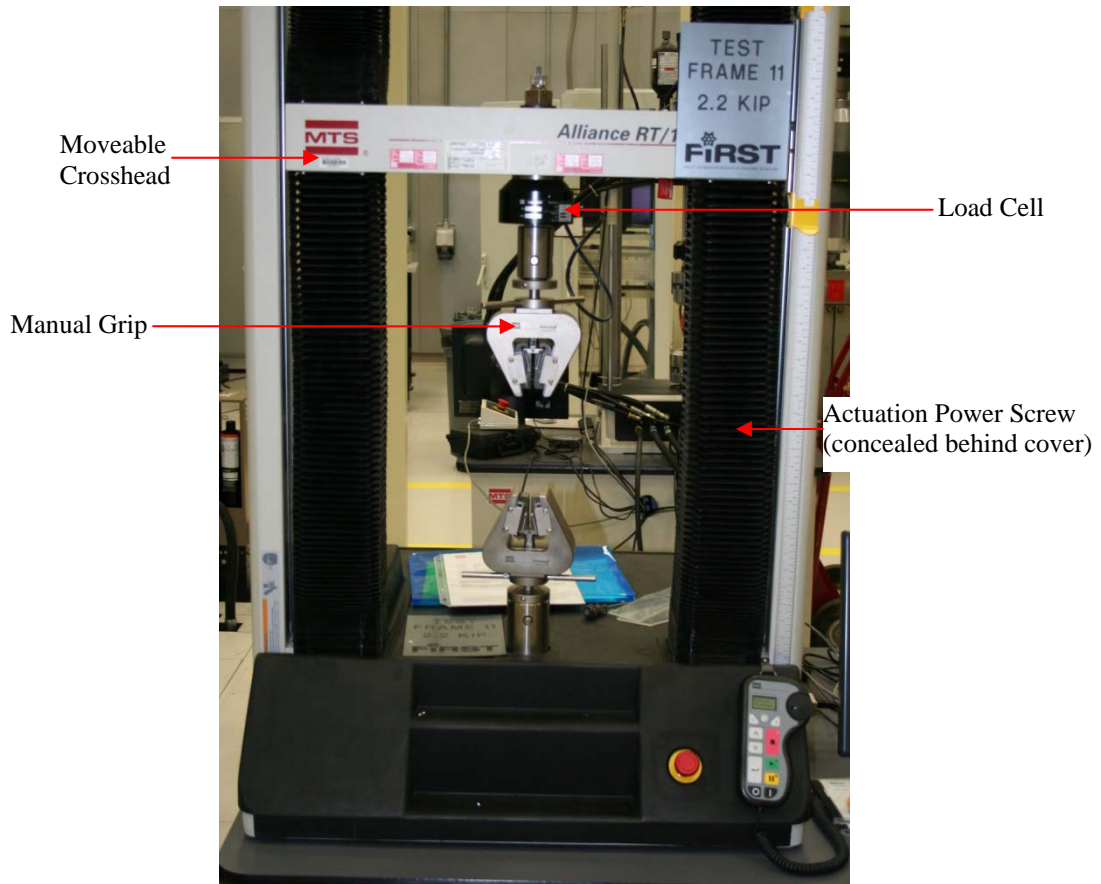
Figure 26 : MTS Alliance RT/10 Tabletop Testing Frame
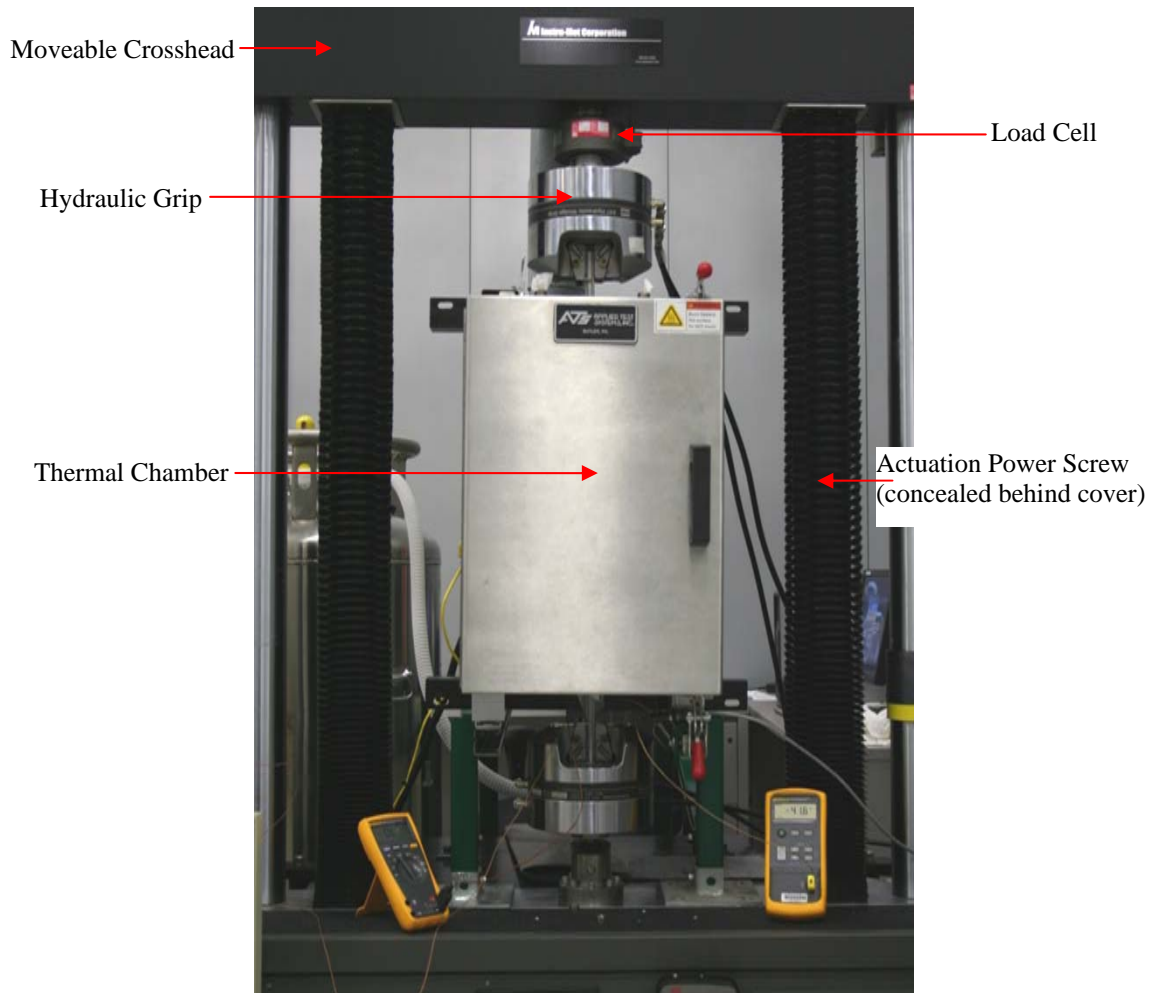
Figure 27 : MTS Sintech 20 G/D Floor Mounted Testing Frame

It is important to note that the option to test in a load control mode was not an option for either static testing frame. These testing frames relied upon power screws to move the crosshead vertically to apply the load. This is in contrast to the servo-hydraulic machines which use hydraulic pressure to move the actuator.

Strain measurements during tests performed on both the Alliance and Sintech machines were sampled at a rate of 100 Hz, and were measured using a standard one inch gauge length, clip on MTS extensometer. The figure below shows the extensometer used for all three temperatures on the electro-mechanical testing stands.

Figure 28 : MTS Extensometer used for Monotonic Testing

As stated, high and low temperature testing was performed using the Sintech 20

G/D floor mounted testing frame. Temperature conditions were maintained using an

Applied Test Systems temperature control system, together with an Applied Test Systems

thermal chamber and pressurized tank of liquid nitrogen. An electronic heating element is

integrated within the walls of the thermal chamber. An additional feature of the thermal

chamber is an internal fan which continuously circulates heated air around the specimen.

This allows for a virtually isothermal testing environment. The temperature control

system attempts to maintain the target temperature within the chamber using both the

integral heating element and liquid nitrogen bath. Figure 29 : Thermal Chamber below

shows the details of the thermal chamber.
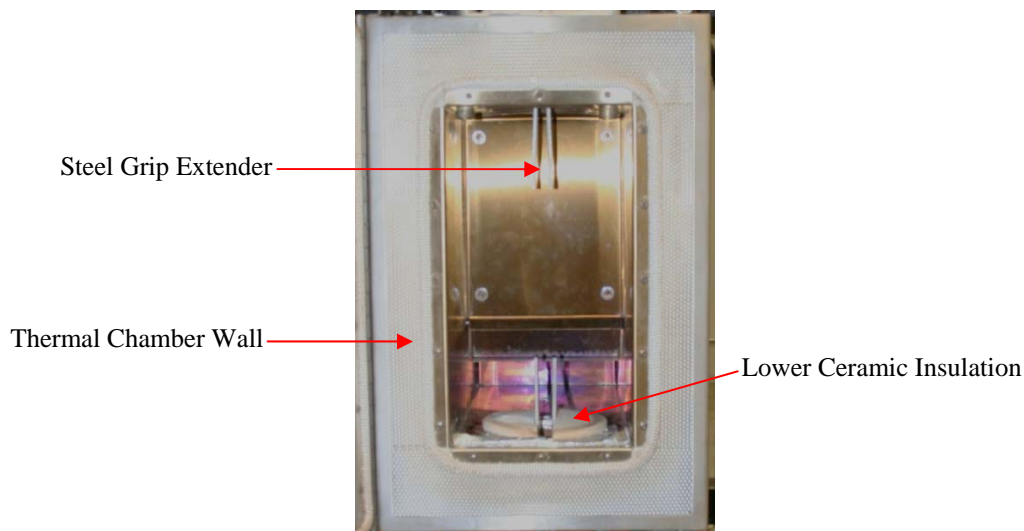
Figure 29 : Thermal Chamber

Despite the near isothermal conditions within the chamber, temperature

measurements were monitored using three K-type thermocouples: the control

thermocouple and two additional readout devices. The control thermocouple fed directly

to the temperature controller, while the two additional readout thermocouples were

monitored using FLUKE thermocouple readers. The figure below shows the typical

FLUKE thermocouple reader used throughout this experimental work.

Figure 30 : Typical Thermocouple Reader

Thermocouples were attached to each specimen using high temperature Kapton

tape. The control thermocouple was attached directly behind the extensometer in the

gauge section, whereas the additional two thermocouples were secured on opposite sides

from one another at the specimen end points. This thermocouple arrangement was chosen

to ensure a uniform temperature distribution was seen and hence measured throughout the

overall specimen. Figure 31 : Typical Specimen Thermocouple Layout below shows the

typical thermocouple layout used on each specimen.
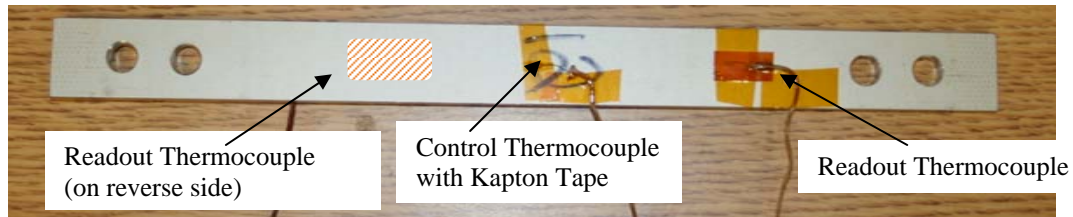
Figure 31 : Typical Specimen Thermocouple Layout

The liquid nitrogen (LN$_2$) tank is a standard cryogenic tank pressurized to 21 psi. It is connected to the thermal chamber's feedback loop through a servo valve system and network of refrigerant hoses. When the temperature of the thermal chamber exceeds the target value, a servo valve within the chamber opens and allows the liquid nitrogen to flow. The refrigerant thus cools the chamber. When the thermal chamber temperature drops below the target value, the valve closes, shutting off the flow of liquid nitrogen, allowing the integral heater within the chamber to raise the internal temperature back to the target value.

An important feature of the LN$_2$ tank is the two valves, which release two different agents. One valve is for releasing cooled nitrogen gas, which can cool the thermal chamber to approximately -5C. This valve is connected to the thermal chamber for the high temperature testing. The second valve releases pure liquid nitrogen, whose temperature ranges between -211C and -196C. This valve is connected to the thermal chamber during the cold temperature testing. The figure below shows the liquid nitrogen tank used during this experimental process.

Figure 32 : Liquid Nitrogen Tank

The schematic below illustrates the basic setup for the feedback control between the LN_2 tank, temperature controller, and thermal chamber. Recall temperature measurements were made continuously via the control thermocouple which was affixed directly to the specimen gauge section.
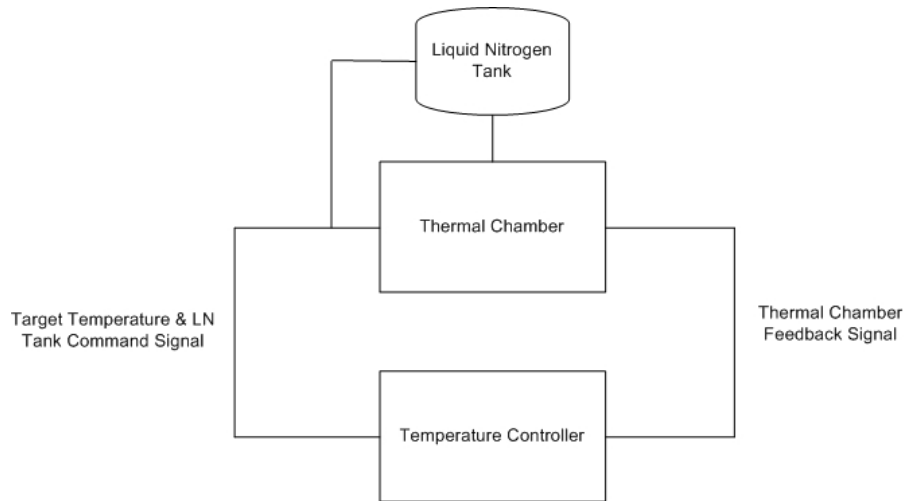
Figure 33 : Control System Schematic

Due to clearance issues between the thermal chamber and grips, stainless steel extensions were fabricated to facilitate gripping the specimen inside the chamber. These grip extensions were used for each test conducted with the MTS Sintech 20 G/D floor mounted testing frame and thermal chamber. An illustration of the grip extender is shown in the section on elevated temperature testing. Because the grip extensions are fabricated of tool steel, and are sandwiching a steel shim the same thickness as the specimens, grip pressure was not a factor for the tests involving the grip extensions. A pressure of 3000 psi was used for each test.

Room Temperature Fatigue Tests.

Tension-tension fatigue testing was conducted on a vertically actuated 22-kip servo-hydraulic MTS machine. A pair of MTS Series 647 wedge grips prepared with a Surfalloy surface were used to grip the specimen. Because of the large size of the fatigue specimen, the MTS machine required tuning to accommodate the specimen geometry. Using the manual tuning feature of the test program, the following gains were set and provided the smallest and most consistent error between the commanded and actual actuator force.

Table 20 : Fatigue Testing Gain Settings

Gain	Value
P	2.40
I	0.10
D	0.00
F	0.00
FL Filter	2048.00

The next figure depicts the machine used for all room temperature fatigue testing.
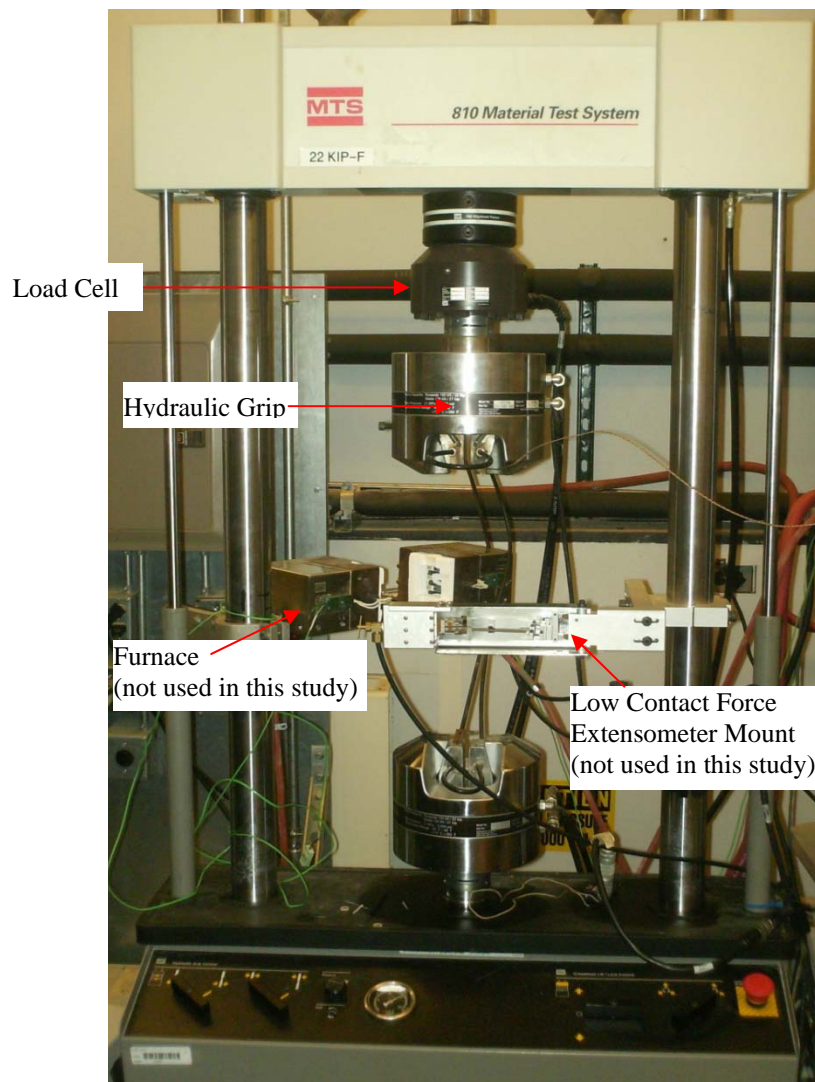
Figure 34 : 22kip MTS Machine used for Fatigue Testing

In contrast to the testing setup carried out with the monotonic testing, the fatigue

tests required much more information than simply taking stress and strain data at 100 Hz.

Using the built-in MTS multi-purpose testware (MPT) program, a fatigue test and data acquisition plan was created.

First, a procedure was selected to collect data using a circular type technique. This data collection technique utilizes a circular buffer which continuously samples data, and once the buffer is full, new data overwrites the old. This technique was employed in an effort to obtain the state of the specimen in the last few moments prior to specimen failure.

Second, data was collected for each "peak and valley" of the loading spectrum. This was performed in order to ensure satisfactory application of load throughout the fatigue test. Recall each specimen was tested in a tension-tension loading spectrum. It was absolutely critical that the specimen not be placed into a state of compression at any time during the test.

Third, full cycle data was collected at a rate of 20 Hz for the first 50 cycles and then in a logarithmic pattern thereafter. After cycle 50, full cycle data was collected every ten cycles from 60 to 100, every 100 cycles from 100 to 1,000, every 1,000 cycles from 1,000 to 10,000, every 10,000 cycles from 10,000 to 100,000, and every 100,000 cycles from 100,000 to 1,000,000. The data was recorded in this manner because it allows for an investigation into the accumulation of damage through elastic modulus examination at the specified cycles. It also served to show strain accumulation and an illustration into the evolution of the specimen's hysteresis loops throughout the fatigue test.

Experimental Setup and Procedure

MTS Alliance RT/10 tabletop testing frame (RT Modulus Testing).

Before any testing was carried out, the MTS extensometer was calibrated using a standard MTS extensometer calibrator. With its internal calibration program, the testing software has the capability to accept virtually any strain measurement device. Following the on-screen prompts, the extensometer was calibrated to a full scale value of 0.2 inch/inch.

The initial room temperature elastic modulus testing was conducted using the MTS Alliance RT/10 tabletop testing frame. Before testing the specimens, the testing software was set to collect data at 100 Hz and the crosshead was set to travel vertically at 0.05 inch per minute. Recall, in contrast to servo-hydraulic machines, this particular piece of equipment does not permit testing in load control. The machine's crosshead displacement rate is controlled during the testing process.

Ensuring proper alignment between the upper and lower gripping mechanisms, the specimen was loaded and the clamps were manually secured. The MTS extensometer was placed at the center of the specimen, both with respect to specimen length and width. Before any actual crosshead movement took place, the testing software required general specimen dimensional information input. The specimen width and thickness required entry into the program. These measurements are used to determine the stress induced within the specimen throughout the duration of the test.

After zeroing the crosshead position and extensometer values, the test was set to begin. Due to machine and load cell limitations, elastic modulus testing on the MTS Alliance RT/10 machine did not exceed 2000 pounds. At the conclusion of each test, the

load was manually removed through moving the crosshead positing downward until the load-cell readout displayed 0 pounds. At this time, the clamps were again manually tightened. The extensometer and crosshead positions were re-zeroed and the modulus test was once again performed. A total of three tests were performed on each straight sided specimen.

After each specimen was tested, a data file was created which displayed test time, crosshead displacement, applied load, stress, and strain. From this information, the elastic modulus was found through plotting the stress and strain data. A linear regression curve was then plotted over the data. The slope of this curve represents the material's elastic modulus.

Tests were performed in batches of fiber orientation - not necessarily in numerical order. This was done purely in an effort to quickly ascertain a single fiber orientation's modulus results and its comparison to the theoretical value. Statistical information to include the overall average, standard deviation, and coefficient of variance was calculated for each specimen batch.

MTS Sintech 20 G/D floor mounted testing frame (RT Modulus Testing).

A second set room temperature elastic modulus tests were conducted using the MTS Sintech 20 G/D floor mounted testing frame. Before testing the specimens, the testing software was set to collect data at 100 Hz and the crosshead was set to travel vertically at 0.05 inch/min. The MTS extensometer was calibrated once more in the same manner as performed with the MTS Alliance machine.

The second set of room temperature tests were conducted for two reasons. First, these tests provided confidence in the results produced during the first set of tests.

77

Second, due to the physical constraints of the thermal chamber, grip extensions were added to the load train. This second testing sequence allowed for an investigation into the test data variability with the additional material added in series between the specimen and grips.

Unlike the MTS Alliance RT/10 machine, the MTS Sintech machine was equipped with hydraulic grips and an external hydraulic pump with reservoir. This provided a more consistent gripping force throughout the testing sequence and mitigated the need to readjust the grips after each test. Figure 35 : Hydraulic Reservoir and Pump below shows the external hydraulic reservoir and pump used for testing with the MTS Sintech machine.

Figure 35 : Hydraulic Reservoir and Pump

Room Temperature Modulus Testing.

Room temperature modulus tests were conducted in a manner similar to those used on the MTS Alliance RT/10 machine. There are two primary differences between the testing methods used on each machine. First, testing on the larger MTS Sintech machine required the use of grip extensions. Four 3/16 inch thick stainless steel grip

extensions were fabricated based on the dimensions in the figure below. These grip

extensions were needed to ensure the specimens cleared the thermal chamber walls so the

hydraulic grips could effectively secure them.
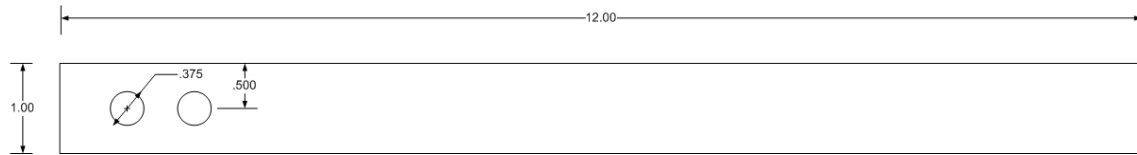
Figure 36 : Grip Extender

The figure below shows the arrangement of bolts and grip extensions.
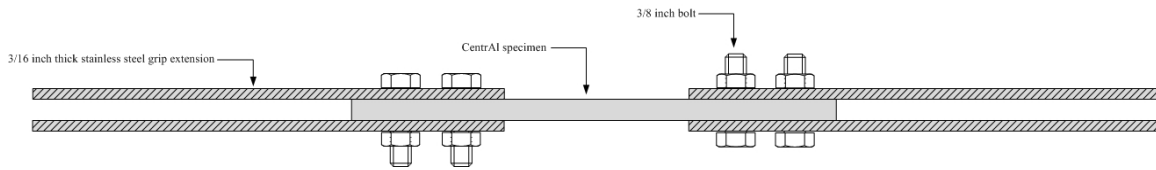
Figure 37 : Grip Extensions with Specimen

A torque of 15 foot-pounds was applied to each bolt, ensuring a positive connection

between the grip extensions and specimen.

The second difference between testing in the Sintech machine lies in the gripping

mechanisms themselves. As previously stated, the gripping system used on this machine

is equipped with a dedicated hydraulic pump and reservoir. Manual application of grips is

unnecessary with this equipment as the hydraulic pressure maintains the specimen

position within the grips. Within the grip wedges themselves, a stainless steel bar,

0.228 inch thick, was used as a shim between each of the grip extenders. Figure 38 : Grip

Extender Configuration Within Hydraulic Wedge Grip below shows the configuration of

the grip extenders and steel shim within the upper grip fixture. The lower grip fixture is

configured in the same manner.
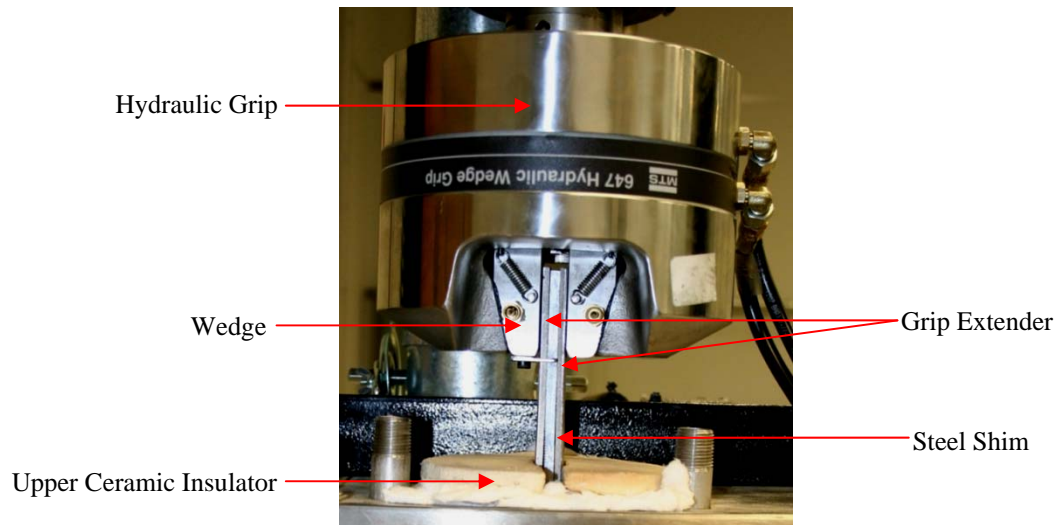
Figure 38 : Grip Extender Configuration Within Hydraulic Wedge Grip

The specimen mounting differences between the two testing machines notwithstanding, the room temperature testing procedure is carried out exactly as with the MTS Alliance machine, with the exception of the maximum load reached during the test. Because the Sintech testing machine is equipped with a load cell rated to 22,000 pounds, the test load was increased from 2000 pounds to 5000 pounds.

Each specimen was tested in laboratory air, held at a constant 23C, without the thermal chamber in place. Since the thermal chamber was mounted on a rail system, it was permitted to slide free of the gripping mechanisms to facilitate the room temperature testing.

The same type data file is produced, as each machine uses identical testing software. After reaching the maximum test load, the load was manually removed until the load cell display read 0 pounds. Each specimen was tested three times. Again, statistical information to include the overall average, standard deviation, and coefficient of variance was calculated for each specimen fiber orientation batch.

High Temperature Modulus Testing.

Because the scope of this thesis research is to isolate the temperature effects on CentrAl's mechanical properties, high temperature testing was performed only on certain specimens. Chosen at random within each of the four specimen fiber orientations, three specimens from each orientation were identified as candidates for the high temperature testing. The test matrix identifying each specimen and its use is shown in Appendix B. Additionally, because of CentrAl's relatively unknown behavior at elevated temperatures, the maximum load during the high temperature modulus evaluation was limited to 3000 pounds.

Prior to mounting the specimen, the gas only valve on the LN_2 tank was connected to the thermal chamber. The temperature controller target temperature was set to 80C.

Analogous to the specimen setup used for room temperature testing, each specimen was mounted into the grip extenders; see Figure 37 : Grip Extensions with Specimen. After sliding the thermal chamber into place, the specimen grip extenders and shim were fed through the upper thermal chamber opening, into the upper wedge grip, as shown in Figure 38 : Grip Extender Configuration Within Hydraulic Wedge Grip. The grip was then locked.

An arrangement of ceramic insulation disks and heat resistant fabric wadding sealed the upper and lower chamber openings around the specimen grip extenders. This ensured the temperature within the thermal chamber stayed constant and did not deviate from the target value through leakage around the specimen.

It should be noted that the upper wedge grip remained locked throughout the duration of all testing. This was merely done in an effort to minimize the amount of time needed to align the grip extenders and shim within the wedges themselves. The lower wedge grip was mounted in a similar manner. The overall configuration of the specimen, grip extenders, and extensometer are shown in the figure below.

Figure 39 : Specimen Setup with Grip Extenders Inside Thermal Chamber

During heating, to take into account CentrAl's thermal expansion characteristics, the lower grip was not immediately secured. The free lower end allowed for the specimen to expand without restraint. The lower grip was tightened only after a steady state strain was seen on the extensometer readout. The theoretical strain values for each of the four fiber orientations are shown in the table below. The development of the theoretical

coefficient of thermal expansion (CTE) was shown in the "Theoretical Development" section. In the material 1 and 2 directions respectively, the theoretical CTE is given as 0.00001136 $^\circ$F^{-1} and 0.00001309 $^\circ$F^{-1}.

Table 21 : High Temperature Theoretical Steady State Strain

Fiber Orientation Angle (deg)	Strain (in/in)
0	0.00199936
45	0.0021516
67.5	0.00225925
90	0.00230384

After mounting the specimen and extensometer within the chamber, the extensometer signal, load, and crosshead displacement readings were zeroed. Upon closing the chamber door, the internal heating element and fan immediately begin to warm and circulate the air within the chamber. A steady state strain for each specimen was reached in approximately 15 minutes. After a steady state strain is seen, the lower hydraulic grip was secured.

This steady state strain and temperature readings from each of the thermocouples was recorded. This information was used to determine the specimen's thermally induced strain for the particular modulus evaluation. The specimen was then loaded to 3000 pounds. At the completion of the loading cycle, the load was manually removed to 0 pounds, just as with the room temperature testing.

Because of the combine thermal and mechanical strain conditions present, the lower grip was released after unloading the specimen. This ensured any residual strain was removed. The second test run was performed in the same manner as the first. The thermal strain, along with the three temperature readings was recorded. After zeroing the

load cell output, the lower grip was then re-activated and the test performed. This cycle was performed three times for each high temperature specimen.

As with the data collection for the room temperature testing, a data file was created which displayed test time, crosshead displacement, applied load, stress, and total strain. Mechanical strain was later obtained through subtracting off the respective thermal strain component. From this information, the elastic modulus was found through plotting the stress and strain data. A linear regression curve was then plotted over the data. The slope of this curve represents the material's elastic modulus.

Again, statistical information to include the overall average, standard deviation, and coefficient of variance was calculated for each specimen batch.

Low Temperature Modulus Testing.

Just as in the elevated temperature testing, the low temperature testing was performed only on certain specimens. Chosen at random within each of the four specimen fiber orientations, three specimens from each orientation were identified as candidates for the high temperature testing. The test matrix identifying each specimen and its use is shown in Appendix B. Additionally, because of CentrAl's relatively unknown behavior at the lower temperatures, the maximum load during the low temperature evaluation was limited to 3000 pounds.

Prior to mounting the specimen, the liquid only valve on the LN_2 tank was connected to the thermal chamber. The temperature controller target temperature was set to -55C.

Analogous to the specimen setup used for room temperature testing, each specimen was mounted into the grip extenders; see Figure 37 : Grip Extensions with

Specimen. After sliding the thermal chamber into place, the specimen grip extenders and shim was fed through the upper thermal chamber opening, into the upper wedge grip, as shown in Figure 38 : Grip Extender Configuration Within Hydraulic Wedge Grip. The grip was then locked.

An arrangement of ceramic insulation disks and heat resistant fabric wadding sealed the upper and lower chamber openings around the specimen grip extenders. This ensured the temperature within the thermal chamber stayed constant and did not deviate from the target value through leakage around the specimen.

It should be noted that the upper wedge grip remained locked throughout the duration of all testing. This was merely done in an effort to minimize the amount of time needed to align the grip extenders and shim within the wedges themselves. The lower wedge grip was mounted in a similar manner.

During the cooling process, to take into account CentrAl's thermal expansion characteristics, the lower grip was not immediately secured. The free lower edge allowed for the specimen to contract without restraint. The lower grip was tightened only after a steady state strain was seen on the extensometer readout. The following table illustrates the theoretical steady state strain values seen during the cooling process.

Table 22 : Low Temperature Theoretical Steady State Strain

Fiber Orientation Angle (deg)	Strain (in/in)
0	-0.00076112
45	-0.000819075
67.5	-0.000860055
90	-0.00087703

After mounting the specimen and extensometer within the chamber, the extensometer signal, load, and crosshead displacement readings were zeroed. Upon

closing the chamber door, the internal servo-valve opened and allowed the LN_2 to flow, thus immediately cooling the air within the chamber. A steady state strain for each specimen was reached in approximately 15 minutes. After a steady state strain is seen, the lower hydraulic grip was secured.

This experimental steady state strain and temperature readings from each of the thermocouples was recorded. This information was used to determine the specimen's thermally induced strain for the particular modulus evaluation. The specimen was then loaded to 3000 pounds. At the completion of the loading cycle, the load was manually removed to 0 pounds, just as with the room and high temperature testing.

Because of the thermal strain conditions present, the lower grip was released after unloading the specimen. This ensured any mechanical strain was removed. The second test run was performed just with the first. The thermal strain, along with the three temperature readings was recorded. After zeroing the load cell output, the lower grip was then re-activated and the test performed again. This cycle was performed three times for each low temperature specimen.

As with the data collection for the room and high temperature testing, a data file was created which displayed test time, crosshead displacement, applied load, stress, and total strain. Mechanical strain was later obtained through subtracting off the respective thermal strain component. From this information, the elastic modulus was found through plotting the stress and strain data. A linear regression curve was then plotted over the data. The slope of this curve represents the material's elastic modulus.

Again, statistical information to include the overall average, standard deviation, and coefficient of variance was calculated for each specimen batch.

Tensile Testing

Room Temperature Tensile Testing.

To extend the research into the behavior of CentrAl, tensile tests were conducted to determine the laminate's actual stress-strain behavior. Analogous to any tensile test, this testing sequence was just an extension of the modulus testing already conducted on the specimens. Appendix B depicts the use for each specimen.

The primary reason for the room temperature tensile testing is to establish, experimentally, the room temperature stress and strain behavior for the laminate. Because this laminate contains unidirectional fibrous layers, the four specimen orientations will provide insight into the influence fiber orientation has on the laminate strength. Secondly, since the fatigue tests were conducted at room temperature, the stress-strain behavior at the 0° fiber orientation provided valuable insight into the requisite loads for the fatigue tests.

For the room temperature tensile tests, the straight-sided specimens, as identified in Appendix B, required their gauge section widths to be reduced, ensuring failure in this region. In accordance with ASTM Standard E8-04, the straight sided specimens were machined to mirror the same proportions as the pin-loaded tension test specimen in Figure 7 of the ASTM standard [1]. The resulting specimen is shown in Figure 5 : Dogbone Tensile Specimen Geometry.

Four tensile tests were carried out at room temperature. Each test utilized a single specimen from each of the four fiber orientations. The tests were conducted using the floor mounted Sintech machine. The same elastic modulus test data acquisition and crosshead vertical travel rates were used. Rather than stopping the load at a specified

value, the test program was allowed to continue the test until specimen failure or the machine's calibrated load cell capability (20,000 pounds) was exceeded. Reaching the load cell capability was a non-issue as the specimen would fail before this limit was reached. The following table shows the theoretical ultimate failure load for each specimen. The development of this theoretical ultimate tensile strength was shown in the "Theoretical Development" section.

Table 23 : Theoretical Failure Loads for Dogbone Specimens

Fiber Orientation (º)	Nominal Area (in²)	UTS (psi)	Failure Load (lbf)
0	0.057	94265	5373.1
45	0.057	72710.9	4144.5
67.5	0.057	57469.9	3275.8
90	0.057	51156.9	2915.9

As in the case of modulus testing, the specimen was mounted to the steel extenders. This setup is shown in Figure 37 : Grip Extensions with Specimen. In contrast to the modulus testing however, the bolts were not tightened for the tensile tests. This was done to simulate a pinned boundary condition for the duration of the test. After mounting the specimen, the extensometer was secured in the same manner as with the elastic modulus testing. The testing configuration was similar to that of the elastic modulus tests and is seen in

Figure 39 : Specimen Setup with Grip Extenders Inside Thermal Chamber.

It should be noted that the upper wedge grip remained locked throughout the duration of all testing. This was merely done in an effort to minimize the amount of time needed to align the grip extenders and shim within the wedges themselves. The lower wedge grip was mounted in a similar manner. The overall configuration of the specimen,

grip extenders, and extensometer are shown in Figure 38 : Grip Extender Configuration Within Hydraulic Wedge Grip.

Prior to starting the test, the extensometer, load, and crosshead displacement readings were zeroed. The specimen gauge section dimensions were entered into the test program. These dimensions were used in conjunction with the applied load to calculate the induced state of stress within the specimen gauge section. The test was set to begin.

Again, just as with the room temperature modulus testing, the data during the test was output to a file which included strain, crosshead displacement, applied load, stress, and time. From this data, stress-strain curves for each specimen fiber orientation were constructed.

High Temperature Tensile Testing.

The elevated temperature tensile testing was performed only on those specimens already exposed to the higher temperatures during the modulus investigation. As with the room temperature tensile testing, four specimens were chosen to represent the four specimen orientations within the CentrAl panel. Appendix B shows the specimens used for the high temperature tensile testing.

Consistent with the room temperature tensile testing, the high temperature tensile tests were conducted using the floor mounted Sintech machine. The same elastic modulus test data acquisition and crosshead vertical travel rates were used. Similarly, rather than stopping the load at a specified value, the test program was allowed to continue the test until specimen failure or the machine's calibrated load cell capability (20,000 pounds) was exceeded. As was shown in the section describing the room temperature tensile

testing, Table 23 : Theoretical Failure Loads for Dogbone Specimens details the theoretical maximum loads to failure for each specimen's fiber orientation.

As shown in the experimental results from the high temperature modulus testing, there is only a slight variation between the room temperature and high temperature modulus values. Because of this small variation and small gauge section cross sectional area, the load cell capability was not in jeopardy of being exceeded.

Prior to mounting the specimen, the gas only valve on the LN_2 tank was connected to the thermal chamber. The temperature controller target temperature was set to 80C. Using high temperature Kapton tape, three thermocouples were secured to the specimen. The same thermocouple arrangement from the previous high and low temperature modulus testing was used for the tensile test. The control thermocouple was attached to the specimen backside, immediately opposite the extensometer. The two additional thermocouples were affixed to the specimen in the manner depicted in Figure 31 : Typical Specimen Thermocouple Layout.

Analogous to the specimen setup used for the room temperature tensile testing, each specimen was mounted into the grip extenders; see Figure 37 : Grip Extensions with Specimen. After the thermal chamber was slid into place, the specimen grip extenders and shim was fed through the upper thermal chamber opening, into the upper wedge grip. This is the same configuration as seen in Figure 38 : Grip Extender Configuration Within Hydraulic Wedge Grip. Identical to the room temperature tensile tests, the bolts connecting the specimens to the specimen extenders were not tightened. The upper grip was then secured.

An arrangement of ceramic insulation disks and heat resistant fabric wadding sealed the upper and lower chamber openings around the specimen grip extenders. This ensured the temperature within the thermal chamber stayed constant and did not deviate from the target value through leakage around the specimen.

It should be noted that the upper wedge grip remained locked throughout the duration of all testing. This was merely done in an effort to minimize the amount of time needed to align the grip extenders and shim within the wedges themselves. The lower wedge grip was mounted in a similar manner.

As with the high temperature modulus tests, in order to take into account CentrAl's thermal expansion characteristics, the lower grip was not immediately secured. The free lower end allowed for the specimen to expand without restraint. The lower grip was tightened only after a steady state strain was seen on the extensometer readout. These theoretical strain values for each of the four fiber orientations are shown in Table 21 : High Temperature Theoretical Steady State Strain.

After mounting the specimen and extensometer within the chamber, the extensometer signal, load, and crosshead displacement readings were zeroed. Upon closing the chamber door, the internal heating element and fan immediately began to warm and circulate the air within the chamber. A steady state strain for each specimen was reached in approximately 15 minutes. After a steady state strain is seen, the lower hydraulic grip was secured.

This steady state strain and temperature readings from each of the thermocouples was recorded. This information was used to determine the specimen's thermally induced strain during the tensile test.

As with the data collection for the room temperature tensile test, a data file was created which displayed test time, crosshead displacement, applied load, stress, and total strain. Mechanical strain was later obtained through subtracting off the respective thermal strain component. From this information, the stress-strain curve for the specimen at this elevated temperature was constructed.

Low Temperature Tensile Testing.

The low temperature tensile testing was performed only on those specimens already exposed to the lower temperatures during the modulus investigation. As with the room temperature tensile testing, four specimens were chosen to represent the four specimen orientations within the CentrAl panel. Appendix B shows the specimens used for the low temperature tensile testing.

Consistent with the room temperature and high temperature tensile testing, the low temperature tensile tests were conducted using the floor mounted Sintech machine. The same test data acquisition and crosshead vertical travel rates were used. Similarly, rather than stopping the load at a specified value, the test program was allowed to continue the test until specimen failure or the machine's calibrated load cell capability (20,000 pounds) was exceeded. As was shown in the section describing the room temperature tensile testing, Table 23 : Theoretical Failure Loads for Dogbone Specimens details the theoretical maximum loads to failure for each specimen's fiber orientation.

As shown in the experimental results from the low temperature modulus testing, there is only a slight variation between the room temperature and low temperature modulus values. Because of this small variation and small gauge section cross sectional area, the load cell capability was not in jeopardy of being exceeded.

Prior to mounting the specimen, the liquid only valve on the LN$_2$ tank was connected to the thermal chamber. The temperature controller target temperature was set to -55C. Using high temperature Kapton tape, three thermocouples were secured to the specimen. The same thermocouple arrangement from the previous high and low temperature modulus testing was used for the tensile test. The control thermocouple was attached to the specimen backside, immediately opposite the extensometer. The two additional thermocouples were affixed to the specimen in the manner depicted in Figure 31 : Typical Specimen Thermocouple Layout.

Analogous to the specimen setup used for the high temperature tensile testing, each specimen was mounted into the grip extenders; see Figure 37 : Grip Extensions with Specimen. After the thermal chamber was slid into place, the specimen grip extenders and shim was fed through the upper thermal chamber opening, into the upper wedge grip. This is the same configuration as seen in Figure 38 : Grip Extender Configuration Within Hydraulic Wedge Grip. Identical to the high temperature tensile tests, the bolts connecting the specimens to the specimen extenders were not tightened. The upper grip was then secured.

An arrangement of ceramic insulation disks and heat resistant fabric wadding sealed the upper and lower chamber openings around the specimen grip extenders. This ensured the temperature within the thermal chamber stayed constant and did not deviate from the target value through leakage around the specimen.

It should be noted that the upper wedge grip remained locked throughout the duration of all testing. This was merely done in an effort to minimize the amount of time

needed to align the grip extenders and shim within the wedges themselves. The lower wedge grip was mounted in a similar manner.

As with the low temperature modulus tests, in order to take into account CentrAl's thermal expansion characteristics, the lower grip was not immediately secured. The free lower end allowed for the specimen to contract without restraint. The lower grip was tightened only after a steady state strain was seen on the extensometer readout. These theoretical strain values for each of the four fiber orientations are shown in Table 22 : Low Temperature Theoretical Steady State Strain.

After mounting the specimen and extensometer within the chamber, the extensometer signal, load, and crosshead displacement readings were zeroed. Upon closing the chamber door, the internal servo-valve opened and allowed the LN_2 to flow, thus immediately cooling the air within the chamber. A steady state strain for each specimen was reached in approximately 15 minutes. After a steady state strain is seen, the lower hydraulic grip was secured.

This steady state strain and temperature readings from each of the thermocouples was recorded. This information was used to determine the specimen's thermally induced strain during the tensile test.

As with the data collection for the high temperature tensile test, a data file was created which displayed test time, crosshead displacement, applied load, stress, and total strain. Mechanical strain was later obtained through subtracting off the respective thermal strain component. From this information, the stress-strain curve for the specimen at this elevated temperature was constructed.

Blunt Notch Strength Testing

  Rationale Behind Blunt Notch Testing.

  Monotonic tensile testing provides the researcher an indication into the static strength of a material system. While critical to understanding the ultimate strength properties, blunt notch strength can be argued to provide an indication into a more realistic application of a material's strength capabilities. The blunt notch strength of a material is defined as the strength of the structure containing a hole. This blunt notch strength is an important design parameter because a fuselage structure contains many holes at locations where connections are made. Moreover, blunt notches occur in various other forms in an airframe, such as windows, doors, and hatches [18].

  The blunt notch behavior of CentrAl was investigated by tensile testing specially prepared specimens at the three temperatures studied for this thesis research. A single 3/16 inch hole was drilled in the center of the gauge section of selected elastic modulus specimens, delineated in Appendix B. For each of the four specimen fiber orientations, three blunt notch test specimens were machined.

  Blunt Notch Strength Specimen Geometry.

  During the blunt notch testing sequence, the final shape of these specimens was not initially known. An iterative, yet somewhat cumbersome approach was taken to finalize the overall configuration of the specimen geometry. The final shape is shown in Figure 7 : Blunt Notch Strength Test Specimen Geometry.

  The first iteration was to investigate the stress concentration effects of having both pinned ends and an open hole centered in the specimen gauge section. It should be noted that the bolt hole were not perfectly filled with the mounting bolts, as the holes

were required to be slightly larger than the mounting bolts, else installation would be impossible. The following figure depicts this initial blunt notch test specimen.
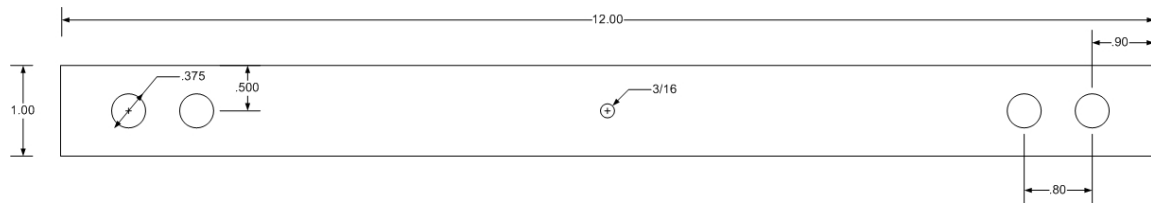
Figure 40 : Initial Blunt Notch Specimen Design

The results of this initial blunt notch test were unsuccessful as failure occurred at the gripping bolt hole. Additional discussion from this trial is discussed in the "Experimental Results" section. From this failure, it was determined additional analysis into the specimen geometry was needed, as the pseudo-filled mounting holes appeared to behave the same as an open hole of the same diameter in this laminate.

Since the pseudo-filled bolt hole behaved in the same manner as an open hole, the presence of the mounting bolts themselves were assumed to not exist for the purposes of refining the blunt notch specimen geometry. From [23], the following polynomial equation was used to determine the localized stress concentration for the specimen.

$$K_t = 3.00 - 3.13 \left(\frac{2\,r}{d}\right) + 3.66 \left(\frac{2\,r}{d}\right)^2 - 1.53 \left(\frac{2\,r}{d}\right)^3 \tag{77}$$

Where r is the open-hole radius and d is the specimen width. Using Equation 77, the localized stress concentration for the mounting bolt region is thus given as: $K_t = 2.26$.

Two options exist to increase the stress concentration at the gauge section. The center hole diameter can be increased or the overall width of the gauge section can be reduced. Though both avenues achieve the same desired result, the decision was made to reduce the gauge section width to reach the desired stress concentration value. This desired value was one which was higher than the value calculated for the mounting bolts.

96

For a gauge width of 0.75 inch, using Equation 77 once more, the following is the stress

concentration factor for the gauge section hole: $K_t = 2.42$.

With the increased stress concentration at the gauge section, failure at the central

hole will theoretically occur before failure at the mounting bolt holes. Shown in Figure 7

: Blunt Notch Strength Test Specimen Geometry two test specimens were machined and

tested. With the success of these two tests (results discussed in "Experimental Results"

section), the remaining specimens were machined according to this new geometry.

With the reduced gauge section width, the ultimate failure load required

calculation to ensure the testing machine had sufficient capability to perform the test. The

following table shows the theoretical ultimate tensile failure loads for a blunt notch

specimen at each of the four specimen fiber orientations.

Table 24 : Blunt Notch Specimen Theoretical Ultimate Tensile Strength

Fiber Orientation (°)	Net Area (in²)	UTS (psi)	Failure Load (lbf)
0	0.12825	94265	12089.5
45	0.12825	72710.9	9325.2
67.5	0.12825	57469.9	7370.5
90	0.12825	51156.9	6560.9

RT Blunt Notch Strength Testing.

Just as with the elastic modulus and tensile testing, the blunt notch strength tests

were carried out using the floor mounted MTS Sintech machine. The room temperature

blunt notch strength tests were conducted in the same manner as the room temperature

tensile testing. The data acquisition rate remained at 100 Hz and the crosshead

displacement rate remained at 0.05 inch per minute. The only difference with the testing

program was in the specimen measurements which were entered before every test. Rather

than entering in the overall width and thickness of the specimen, the gross width and

thickness were entered. The net area was accounted for later while creating the blunt notch specimen stress-strain curve.

Mounting the blunt notch strength specimen was identical to that of the room temperature tensile test. The specimen, along with the steel specimen extenders were fed into the upper and lower grips. Again, the upper grip was arranged and secured as seen in Figure 38 : Grip Extender Configuration Within Hydraulic Wedge Grip. The lower grip was arranged in a similar manner. It should be noted that as with the tensile tests, the bolts were not fully tightened. This was done so as to simulate a pinned condition. Upon securing the extensometer to the specimen, the strain readout, crosshead displacement, and load cell readout were zeroed. The test was set to begin.

As with the tensile tests performed on the MTS Sintech machine, information to include time, crosshead displacement, applied load, stress, and strain were recorded. A separate data file was created for each specimen.

High Temperature Blunt Notch Strength Testing.

The elevated temperature blunt notch strength testing was performed only on those specimens already exposed to the higher temperatures. As with the room temperature blunt notch strength testing, three specimens were chosen from the four specimen fiber orientations. Appendix B shows the specimens used for these high temperature blunt notch tests.

Consistent with the room temperature blunt notch strength testing, the high temperature blunt notch tests were conducted using the floor mounted Sintech machine. The same test data acquisition and crosshead vertical travel rates were used. Just as in performing the room temperature blunt notch strength tests, the gauge section gross width

and thickness were entered into the testing software prior to testing. The net area and hence net stress was calculated prior to developing each specimen's respective stress-strain curve.

As with the other high temperature tests, the gas only valve on the LN_2 tank was connected to the thermal chamber. The temperature controller target temperature was set to 80C. Using high temperature Kapton tape, three thermocouples were secured to the specimen. The same thermocouple arrangement from the previous high temperature modulus testing was used for the tensile test. The control thermocouple was attached to the specimen backside, immediately opposite the extensometer. The two additional thermocouples were affixed to the specimen in the manner depicted in Figure 31 : Typical Specimen Thermocouple Layout.

Analogous to the specimen setup used for the room temperature bunt notch strength testing, each specimen was mounted into the grip extenders; see Figure 37 : Grip Extensions with Specimen. After the thermal chamber was slid into place, the specimen grip extenders and shim was fed through the upper thermal chamber opening, into the upper wedge grip. This is the same configuration as seen in Figure 38 : Grip Extender Configuration Within Hydraulic Wedge Grip. Identical to the high temperature tensile tests, the bolts connecting the specimens to the specimen extenders were not tightened. Again, this was done to simulate a pinned condition. The upper grip was then secured.

An arrangement of ceramic insulation disks and heat resistant fabric wadding sealed the upper and lower chamber openings around the specimen grip extenders. This

ensured the temperature within the thermal chamber stayed constant and did not deviate from the target value through leakage around the specimen.

It should be noted that the upper wedge grip remained locked throughout the duration of all testing. This was merely done in an effort to minimize the amount of time needed to align the grip extenders and shim within the wedges themselves. The lower wedge grip was mounted in a similar manner.

During heating, to take into account CentrAl's thermal expansion characteristics, the lower grip was not immediately secured. The free lower end allowed for the specimen to expand without restraint. The lower grip was tightened only after a steady state strain was seen on the extensometer readout.

After mounting the specimen and extensometer within the chamber, the extensometer signal, load, and crosshead displacement readings were zeroed. Upon closing the chamber door, the internal heating element and fan immediately began to warm and circulate the air within the chamber. A steady state strain for each specimen was reached in approximately 15 minutes. After a steady state strain is seen, the lower hydraulic grip was secured.

This steady state strain and temperature readings from each of the thermocouples was recorded. This information was used to determine the specimen's thermally induced strain during the test.

As with the data collection for the high temperature tensile test, a data file was created which displayed test time, crosshead displacement, applied load, stress, and total strain. Mechanical strain was later obtained through subtracting off the respective thermal

strain component. From this information, the stress-strain curve for the specimen at this elevated temperature was constructed.

Low Temperature Blunt Notch Strength Testing.

The low temperature blunt notch strength testing was performed only on those specimens already exposed to the decreased temperatures. As with the room temperature and elevated temperature blunt notch strength testing, three specimens were chosen from the four specimen fiber orientations. Appendix B shows the specimens used for these low temperature blunt notch tests.

Consistent with the room temperature and high temperature blunt notch strength testing, the low temperature blunt notch tests were conducted using the floor mounted Sintech machine. The same test data acquisition and crosshead vertical travel rates were used. Just as in performing the previous blunt notch strength tests, the gross gauge section width and thickness were entered into the testing software prior to testing. The net area and hence net stress was calculated prior to developing each specimen's respective stress-strain curve.

Coincident with the previous low temperature tests, the liquid only valve on the LN_2 tank was connected to the thermal chamber. The temperature controller target temperature was set to -55C. Using high temperature Kapton tape, three thermocouples were secured to the specimen. The same thermocouple arrangement from the previous high and low temperature tests was used for the tensile test. The control thermocouple was attached to the specimen backside, immediately opposite the extensometer. The two additional thermocouples were affixed to the specimen in the manner depicted in Figure 31 : Typical Specimen Thermocouple Layout.

Analogous to the specimen setup used for the high temperature bunt notch strength testing, each specimen was mounted into the grip extenders, per Figure 37 : Grip Extensions with Specimen. After the thermal chamber was slid into place, the specimen grip extenders and shim was fed through the upper thermal chamber opening, into the upper wedge grip. This is the same configuration as seen in Figure 38 : Grip Extender Configuration Within Hydraulic Wedge Grip. Identical to the low temperature tensile tests, the bolts connecting the specimens to the specimen extenders were not tightened. Again, this was done to simulate a pinned condition. The upper grip was then secured.

An arrangement of ceramic insulation disks and heat resistant fabric wadding sealed the upper and lower chamber openings around the specimen grip extenders. This ensured the temperature within the thermal chamber stayed constant and did not deviate from the target value through leakage around the specimen.

It should be noted that the upper wedge grip remained locked throughout the duration of all testing. This was merely done in an effort to minimize the amount of time needed to align the grip extenders and shim within the wedges themselves. The lower wedge grip was mounted in a similar manner.

During the cooling process, to take into account CentrAl's thermal expansion characteristics, the lower grip was not immediately secured. The free lower end allowed for the specimen to contract without restraint. The lower grip was tightened only after a steady state strain was seen on the extensometer readout.

After mounting the specimen and extensometer within the chamber, the extensometer signal, load, and crosshead displacement readings were zeroed. Upon

closing the chamber door, the internal servo-valve opened and allowed the LN_2 to flow, thus immediately cooling the air within the chamber. A steady state strain for each specimen was reached in approximately 15 minutes. After a steady state strain is seen, the lower hydraulic grip was secured.

This steady state strain and temperature readings from each of the thermocouples was recorded. This information was used to determine the specimen's thermally induced strain during the test.

As with the data collection for the room temperature tensile test, a data file was created which displayed test time, crosshead displacement, applied load, stress, and total strain. Mechanical strain was later obtained through subtracting off the respective thermal strain component. From this information, the stress-strain curve for the specimen at this elevated temperature was constructed.

Room Temperature Fatigue Testing

As previously mentioned, all room temperature fatigue testing was conducted using a vertically actuated 22-kip servo-hydraulic MTS machine. Mounting each specimen within this machine required much more care than what was taken during mounting inside the screw actuated testing machines for the modulus and tensile tests. This is because the servo-hydraulic machine has the capability to test in both load and displacement control modes.

Because of the specimen width, extreme care was taken to ensure each specimen was centered in the top grip. Beginning in displacement control, the specimen was mounted in the top grip. After which, the signal auto-offset on the system controller was zeroed. At this time, the lower grip was moved into place and secured. The system was

immediately placed into load control mode. The extensometer used during the fatigue

tests was an MTS Model 632 clip-on unit. The figure below shows this device.

Figure 41 : MTS Extensometer used for Fatigue Testing

The overall setup for the fatigue test is shown in the following figure.
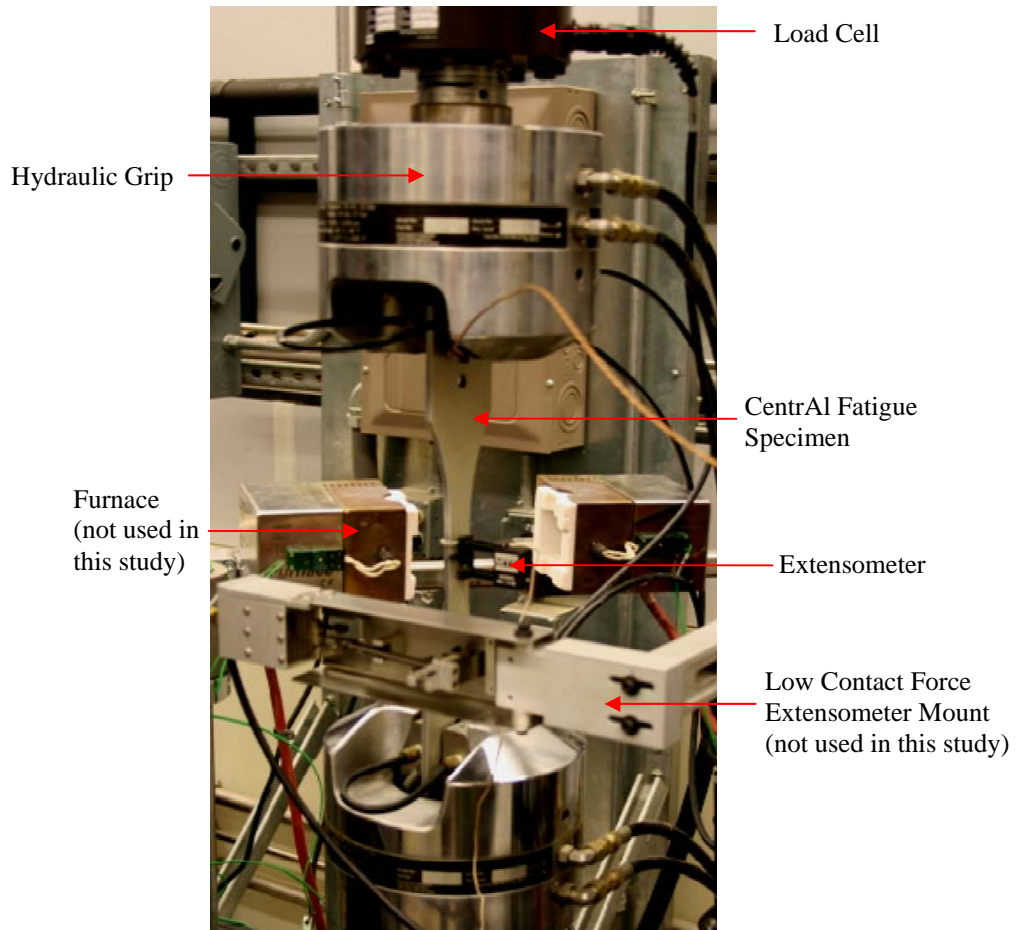
Figure 42 : Fatigue Setup

Because one goal of this thesis research is to investigate the S-N behavior for CentrAl,

several specimens were needed to accomplish this task. Further, several stress levels were

used to ensure the overall fatigue behavior could be accurately seen. Since each fatigue

specimen has the same 0° fiber orientation, this variable now remains a constant and is

thus not a factor in the fatigue test.

A constant stress ratio of 0.1 was used throughout the testing. This is consistent

with the testing conducted in [17]. Additionally, the fatigue tests in this paper were

performed using a maximum stress of 18 ksi. However, for the current research, the stress

was increased to 20 ksi. It should be noted that this stress level represents a stress

approaching less than 50% of the material's experimentally obtained 0.2% offset yield

strength. The 20 ksi point provided a single stress level for developing the S-N curve.

The additional test stresses were found via examining a stress strain curve obtained from

a test specimen. A fatigue test was conducted at this stress level to ascertain initial

material behavior in accordance with the procedure described in the ensuing section

entitled "Fatigue Testing Procedure". The results of this initial fatigue test are discussed

in the "Experimental Results" section.

Determination of Additional RT Fatigue Stress Levels.

Fatigue testing was conducted in parallel with the elastic modulus and tensile

tests. That is, both sets of tests were conducted at the same time, utilizing two different

machines. At the time the fatigue tests began, a viable stress-strain curve was not yet

available for the CentrAl material.

To construct this stress-strain curve, fatigue specimen 4 was chosen as the test

subject. This specimen was pulled to failure on the vertically actuated 22-kip servo-

hydraulic MTS machine. The overall configuration of the fatigue specimen is shown in Figure 9 : Dogbone Fatigue Specimen Geometry. The theoretical failure load for this specimen is shown in the table below.

Table 25 : Fatigue Specimen Theoretical Tensile Failure Load

Specimen	Actual Gauge Area (in^2)	UTS (ksi)	Failure Load (lbf)
4	0.2278	94.27	21473.5

The test program was created using the MPT module of the testing software. Because there is only monotonic load applied, and not a cyclic spectrum, the data acquisition method is not as complex. Again, a circular data buffer was utilized, along with continuous data sampling for the duration of the test. In lieu of testing in load control, the testing software was configured to test in displacement control. The displacement rate was again set to 0.05 inch per minute. The test program was set to pull the specimen to a maximum displacement of 3 inches. The maximum displacement was set to ensure specimen failure would occur. Due to the slow displacement rate and relatively short testing duration, no safety interlocks were set as the hydraulics were immediately shut down after specimen failure. The figure below shows the relatively simple procedure used for the tensile test.
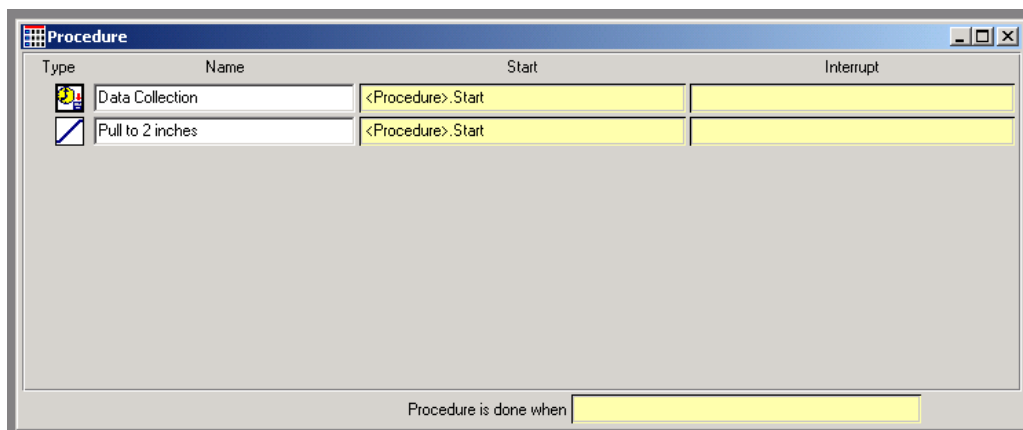
Figure 43 : MPT Tensile Test Procedure

While the theoretical tensile failure load for the specimen is clearly below that of the load cell's maximum 22,000 pound calibrated capacity, the specimen did not fail during the testing procedure. The geometry of this specimen required subsequent modification in order to achieve the desired result. The resulting stress-strain curve is described in the "Experimental Results" section.

The decision was made to reduce the gauge section cross sectional area by a factor of two. This would therefore double the localized stress in this region and thus reduce the require failure load. The figure below illustrates the modified specimen used to establish the stress-strain curve.
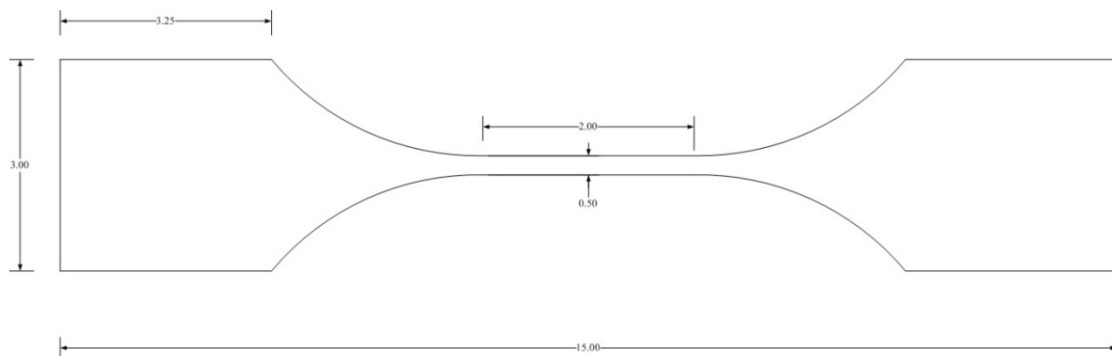
Figure 44 : Reduced Cross Section Dogbone Fatigue Specimen

The following table shows this diminished theoretical ultimate tensile failure load.

Table 26 : Reduced Cross Section Dogbone Specimen Theoretical Tensile Failure Load

Specimen	Reduced Gauge Area (in^2)	UTS (ksi)	Failure Load (lbf)
4	0.114	94.27	10746

The resulting stress-strain curve from the successful destructive test is discussed in the "Experimental Results" section.

Fatigue Testing Procedure.

Through examination of the stress-strain curve, and noticing the pronounced yield stress location, the additional stress levels for the fatigue tests were determined. And given the constant stress ratio, the minimum, maximum, and median stresses were readily found for each fatigue test. The following table illustrates the stresses used for the fatigue tests.

Table 27 : Fatigue Test Stress Levels

Max Stress (MPa)	Min Stress (MPa)	Mean Stress (MPa)
138	13.8	75.9
250	25	137.5
350	35	192.5
448	44.8	246.4
551	55.1	303.05

Unique to each test was the loading magnitude. While the stresses may stay the same, the loads used on each specimen to achieve the desired stresses are a function of the specimen gauge area. The following chart details the specimens tested and the corresponding load levels.

Table 28 : Fatigue Specimen Load Levels

Specimen	Gauge Section Area (m^2)	Max Load (N)	Min Load (N)	Mean Load (N)
5	0.000146802	51380.9	5138.09	28259.4
61	0.000146802	51380.9	5138.09	28259.4
2	0.000146949	36737.3	3673.73	20205.5
45	0.00014848	37120	3712	20416
4	0.000146967	20281.4	2028.14	11154.8
31	0.000147096	65922.6	6592.26	36257.4
43	0.00014566	80343.5	8043.33	44188.9

Corresponding to each specimen's maximum load levels, the grip pressure required

adjustment. The following equation is used to determine the grip pressure necessary for

the fatigue test [11].

$$P(psi) = \frac{1.2 \times Max\ Load(lbf)}{Area\ (in^2)} \tag{83}$$

The load and area are measured in English as the grip pressure indication gauge on the

MTS machine is displayed in English units of pounds-force per square inch. The "max

load" is the maximum load seen during the fatigue test, while the area is the grip piston

area. The model 647-10A grip used in the fatigue tests has a piston area of 10.30 square

inches. The following table details the required grip pressure used for each fatigue test.

Table 29 : Fatigue Testing Required Grip Pressure

Specimen	Max Load (N)	Max Load (lbf)	Grip Pressure (psi)
43	80343.3	18061.9	2104.3
31	65922.6	14820	1726.6
5	51280.9	11550.9	1345.7
61	51280.9	11550.9	1345.7
2	36737.3	8258.88	962.2
45	37120	8344.92	972.2
4	20281.4	4559.44	531.3

With the data acquisition information set as described in the previous section, the

fatigue program was set to ramp linearly to the respective specimen's mean load value. In

an effort to avoid any time dependent and load rate dependent effects, the loading rate

was set at 1000 Newtons per second. As soon as the specified mean load value was

reached, the system began cycling the specimen at 5 Hz between the maximum and

minimum load. The program continues to cycle the specimen until failure occurred. The

following figure shows the procedure used for each of the fatigue tests in this research. It

should be noted that the only variable was the mean load to which the specimen was

initially loaded and the two loads between which the specimen was cycled.

Figure 45 : MPT Typical Fatigue Test Procedure

Because fatigue tests consume longer time durations than simple monotonic tests,

it was critical that internal safety interlocks be set on the machine. These interlocks were

set in such a manner so as to close down the hydraulic power supply to the machine once

a specified displacement was achieved. On the MTS series of servo-hydraulic testing

machines, it is imperative to remember that down is defined as positive displacement.

Because of this fact, the positive, or upper bound, on the displacement was set to

0.5 inch, while the negative, or lower bound, was set to -0.2 inch. This ensured hydraulic

power was shut down if the specimen's vertical displacement reached 0.5 inch due to a

tensile load or -0.2 inch due to a compressive load. The 0.5 inch positive displacement

necessary to interrupt hydraulic power was set to such a magnitude in the positive

direction to ensure a fatigue failure had occurred before the system was shut down. Similarly, the negative displacement was set to such a value so as to shut down hydraulic power at the slightest indication of an application of a compressive load.

VIII. Experimental Results

Elastic Modulus - Experimental Results

Room Temperature Modulus Results.

The elastic modulus of the CentrAl laminate was evaluated in an effort to both validate the theoretical predictions from using the metal fraction technique and to investigate the material's ability to maintain its relative stiffness properties at various temperatures. Recall the room temperature modulus values were evaluated on both the MTS Alliance RT/10 tabletop testing frame and the MTS Sintech 20 G/D floor mounted testing frame. The subsequent tables display the room temperature testing results for both the Alliance and Sintech machines at the four fiber orientation angles: 0°, 45°, 67.5°, and 90°. Additionally, statistical information to include the average experimental value, standard deviation, and correlation coefficient are shown.

From the results produced by testing on the Alliance machine, the following table details the elastic modulus values for each specimen with fibers oriented in the material 1 direction (0°).

Table 30 : Room Temperature Elastic Modulus Results - 0° (Alliance Machine)

Specimen Number	Fiber Angle	Elastic Modulus (Msi)
13	0	9.594
14	0	9.701
15	0	9.472
16	0	9.590
17	0	9.795
18	0	9.540
19	0	9.616
20	0	9.162
21	0	9.220
28	0	9.208
29	0	9.880
30	0	9.781
42	0	9.616
63	0	9.412
64	0	9.725

Recall each of these values is the average of three separate tests. The following table shows the average value, standard deviation, and correlation coefficient for the results shown above.

Table 31 : Statistical Information for Elastic Modulus - 0° (Alliance Machine)

Average Value (Msi)	Standard Deviation (Msi)	Correlation Coefficient
9.554	0.222	2.32%

Since the correlation coefficient is less than 5%, the experimental results are shown to exhibit good linear precision around a similar value.

From the results produced by testing on the Sintech machine, the following table details the elastic modulus values for each specimen with fibers oriented in the material 1 direction (0°).

Table 32 : Room Temperature Elastic Modulus Results - 0⁰ (Sintech Machine)

Specimen Number	Fiber Angle	Elastic Modulus (Msi)
13	0	9.621
14	0	9.883
15	0	9.796
16	0	9.655
17	0	9.205
18	0	9.555
19	0	9.437
20	0	9.089
21	0	9.793
28	0	*cannot grip*
29	0	9.726
30	0	9.246
42	0	9.763
63	0	9.563
64	0	9.862

Recall each of these values is the average of three separate tests. The following table

shows the average value, standard deviation, and correlation coefficient for the results

shown above.

Table 33 : Statistical Information for Elastic Modulus - 0⁰ (Sintech Machine)

Average Value (Msi)	Standard Deviation (Msi)	Correlation Coefficient
9.585	0.254	2.56%

Similar to the test results shown from modulus testing on the Alliance, the experimental

results found from testing on the Sintech machine, the correlation coefficient is less than

5%. Thus the experimental results are shown to exhibit good linear precision around a

similar value.

For the 45⁰ fiber orientation, the Alliance machine modulus testing results are

shown below.

Table 34 : Room Temperature Elastic Modulus Results - 45° (Alliance Machine)

Specimen Number	Fiber Angle	Elastic Modulus (Msi)
32	45	8.608
33	45	8.407
34	45	8.548
35	45	8.596
36	45	8.784
37	45	8.459
38	45	8.374
39	45	8.576
40	45	8.608
46	45	8.642
47	45	8.456
48	45	8.647

As with the previous modulus tests, each of these values is the average of three separate tests. The following table shows the average value, standard deviation, and correlation coefficient for the Alliance testing results shown above.

Table 35 : Statistical Information for Elastic Modulus - 45° (Alliance Machine)

Average Value (Msi)	Standard Deviation (Msi)	Correlation Coefficient
8.559	0.117	1.36%

Then for the Sintech machine, the following table shows the room temperature modulus results for the 45° fiber orientation.

Table 36 : Room Temperature Elastic Modulus Results - 45⁰ (Sintech Machine)

Specimen Number	Fiber Angle	Elastic Modulus (Msi)
32	45	8.515
33	45	8.532
34	45	8.024
35	45	8.685
36	45	8.617
37	45	8.059
38	45	8.306
39	45	8.377
40	45	8.518
46	45	8.236
47	45	7.910
48	45	8.520

The statistical information for this testing batch is therefore given in the table below:

Table 37 : Statistical Information for Elastic Modulus - 45⁰ (Sintech Machine)

Average Value (Msi)	Standard Deviation (Msi)	Correlation Coefficient
8.358	0.252	3.02%

In following, the table below shows the testing results for CentrAl's 67.5⁰ fiber

orientation for the Alliance machine.

Table 38 : Room Temperature Elastic Modulus Results - 67.5⁰ (Alliance Machine)

Specimen Number	Fiber Angle	Elastic Modulus (Msi)
49	67.5	8.254
50	67.5	8.347
51	67.5	8.541
52	67.5	8.576
53	67.5	8.702
54	67.5	8.508
55	67.5	8.449
56	67.5	8.607
57	67.5	8.516
58	67.5	8.329
59	67.5	8.738
60	67.5	8.550

The table below shows the statistical information for the experimental results of

CentrAl's elastic modulus at 67.5° on the Alliance machine.

Table 39 : Statistical Information for Elastic Modulus - 67.5° (Alliance Machine)

Average Value (Msi)	Standard Deviation (Msi)	Correlation Coefficient
8.510	0.146	1.71%

Similarly, the following table details the room temperature elastic modulus results at

67.5° for those evaluated on the Sintech machine.

Table 40 : Room Temperature Elastic Modulus Results - 67.5° (Sintech Machine)

Specimen Number	Fiber Orientation	Elastic Modulus (Msi)
49	67.5	8.079
50	67.5	8.286
51	67.5	7.961
52	67.5	7.961
53	67.5	8.060
54	67.5	8.471
55	67.5	8.565
56	67.5	8.381
57	67.5	8.428
58	67.5	8.136
59	67.5	8.334
60	67.5	8.015

The table below shows the statistical information for the experimental results of

CentrAl's elastic modulus at the 67.5° fiber orientation angle on the Sintech machine.

Table 41 : Statistical Information for Elastic Modulus - 67.5° (Sintech Machine)

Average Value (Msi)	Standard Deviation (Msi)	Correlation Coefficient
8.223	0.213	2.58%

The final set of room temperature elastic modulus tests conducted on the Alliance

machine was for the 90° fiber orientation. The following table shows the results of this

final room temperature elastic modulus testing.

Table 42 : Room Temperature Elastic Modulus Results - 90° (Alliance Machine)

Specimen Number	Fiber Orientation	RT Modulus (Msi)
7	90	8.582
8	90	8.797
9	90	8.833
10	90	8.947
11	90	8.657
12	90	9.256
22	90	8.779
23	90	8.459
24	90	8.635
25	90	8.673
26	90	8.739
27	90	8.860

The statistical information for this elastic modulus evaluation is shown below.

Table 43 : Statistical Information for Elastic Modulus - 90° (Alliance Machine)

Average Value (Msi)	Standard Deviation (Msi)	Correlation Coefficient
8.768	0.203	2.32%

And finally, the room temperature elastic modulus results for the Sintech machine are given below.

Table 44 : Room Temperature Elastic Modulus Results - 90° (Sintech Machine)

Specimen Number	Fiber Angle	Elastic Modulus (psi)
7	90	8.549
8	90	7.939
9	90	8.545
10	90	8.117
11	90	8.263
12	90	8.624
22	90	8.606
23	90	8.021
24	90	8.687
25	90	8.553
26	90	8.003
27	90	8.515

Lastly, the statistical information for this testing run is shown below.

Table 45 : Statistical Information for Elastic Modulus - 90⁰ (Sintech Machine)

Average Value (Msi)	Standard Deviation (Msi)	Correlation Coefficient
8.369	0.279	3.33%

From each of the experimental results' correlation coefficients, it is seen that good agreement exists between the modulus values obtained. Because the Sintech machine was used for the elevated and decreased temperature testing as well, only the room temperature results from this machine will be used for the results of this research effort.

When compared to the theoretical elastic modulus values, those obtained via testing exhibit good agreement showing only a small percent difference between the two. The following table shows the theoretical elastic modulus value, the average value for the respective fiber orientation, and the percent difference.

Table 46 : Comparison Between Theoretical and Experimental RT Modulus Values

Fiber Angle	Theoretical Values (Msi)	Experimental Values (Msi)	Percent Difference (%)
0	9.210	9.585	4.07
45	8.760	8.358	4.59
67.5	8.442	8.223	2.59
90	8.264	8.369	1.27

Elevated Temperature Modulus Results.

The second set of modulus tests involved evaluating the CentrAl laminate at an elevated temperature of 80C (176F). Because each modulus test was conducted three separate times for each specimen, three separate thermal strain values were obtained. For each of the average elastic moduli present, the corresponding average thermal strain will be shown.

For the 0° fiber orientation, the following table shows the average elastic moduli

for the specimens tested at 80C and their respective average thermal strains.

Table 47 : 80C Elastic Modulus and Thermal Strain Values, 0° Fiber Orientation

Specimen	Fiber Angle	Modulus (Msi)	Thermal Strain (in/in)
21	0	9.724	0.00172
63	0	9.397	0.00164

For this group of tests, the following table shows the calculated statistical information.

Table 48 : Statistical Information for 80C Modulus Tests, 0° Fiber Orientation

Average Modulus (Msi)	Standard Deviation (Msi)	Correlation Coefficient	Average Strain (in/in)	Standard Deviation (in/in)	Correlation Coefficient
9.560	0.231	2.42	0.00168	0.00005657	3.37

While the test matrix in Appendix B shows specimen 15 was a candidate for the elevated

temperature modulus testing, this specimen was destroyed during its test and was thus

unable to be used for subsequent evaluation.

Continuing, the next table displays the results for the 45° fiber orientation elastic

modulus tests.

Table 49 : 80C Elastic Modulus and Thermal Strain Values, 45° Fiber Orientation

Specimen	Fiber Angle	Modulus (Msi)	Thermal Strain (in/in)
33	45	8.556	0.00161
37	45	8.316	0.00185
47	45	8.144	0.00164

And the next table gives the statistical information for this testing sequence.

Table 50 : Statistical Information for 80C Modulus Tests, 45° Fiber Orientation

Average Modulus (Msi)	Standard Deviation (Msi)	Correlation Coefficient	Average Strain (in/in)	Standard Deviation (in/in)	Correlation Coefficient
8.339	0.207	2.48	0.00170	0.000131	7.69

Following, the next table shows the results for testing CentrAl's elastic modulus at the

67.5° fiber angle.

Table 51 : 80C Elastic Modulus and Thermal Strain Values, 67.5° Fiber Orientation

Specimen	Fiber Angle	Modulus (Msi)	Thermal Strain (in/in)
50	67.5	8.548	.00192
54	67.5	8.317	.001487
59	67.5	8.194	.001833

And the statistical information is as follows:

Table 52 : Statistical Information for 80C Modulus Tests, 67.5° Fiber Orientation

Average Modulus (Msi)	Standard Deviation (Msi)	Correlation Coefficient	Average Strain (in/in)	Standard Deviation (in/in)	Correlation Coefficient
8.353	0.180	2.15	.001747	.000229	13.1

And finally for the 90° fiber orientation specimens, the next table shows the experimental

results.

Table 53 : 80C Elastic Modulus and Thermal Strain Values, 90° Fiber Orientation

Specimen	Fiber Angle	Modulus (Msi)	Thermal Strain (in/in)
8	90	8.543	.001887
12	90	8.404	.00186
26	90	8.126	.00185

And the table showing the statistical calculation is shown below:

Table 54 : Statistical Information for 80C Modulus Tests, 90° Fiber Orientation

Average Modulus (Msi)	Standard Deviation (Msi)	Correlation Coefficient	Average Strain (in/in)	Standard Deviation (in/in)	Correlation Coefficient
8.358	0.212	2.54	.001866	.0000191	1.02

While the information in the preceding tables certainly shows the modulus

behavior of CentrAl at the elevated temperature, comparing these results to the

experimentally obtained room temperature results provides an indication to the relative change due to temperature. The next table details the ratio between the experimentally obtained elevated elastic modulus values to their respective room temperature value.

Table 55 : 80C to RT Modulus Comparison

Fiber Angle	Avg. 80C Elastic Modulus (Msi)	Avg. RT Elastic Modulus (Msi)	80C Modulus / RT Modulus	Percent Difference
0	9.560	9.585	0.997	0.26
45	8.339	8.358	0.998	0.23
67.5	8.353	8.223	1.016	1.58
90	8.358	8.369	0.999	0.13

From this table, it is clearly seen that the elevated temperature does not affect the elastic modulus property a great deal. As shown, the greatest percent difference between the 80C and room temperature moduli is on the order of 1.58 percent. This is seen in the 67.5° fiber angle. At this angle, the elastic modulus is shown to increase, while at 0°, 45°, and 90°, the elastic modulus decreases by 0.26%, 0.23%, and 0.13% respectively.

Reduced Temperature Modulus Results.

The final set of modulus tests involved evaluating the CentrAl laminate at a reduced temperature of -55C (-67F). As with the elevated temperature testing, each modulus test was conducted three separate times for each specimen, three separate thermal strain values were obtained. For each of the average elastic moduli present, the corresponding average thermal strain will be shown.

For the 0° fiber orientation, the following table shows the average elastic moduli for the specimens tested at -55C and their respective average thermal strains.

Table 56 : -55C Elastic Modulus and Thermal Strain Values, 0° Fiber Orientation

Specimen	Fiber Angle	Modulus (Msi)	Thermal Strain (in/in)
13	0	10.069	-.003118
64	0	10.380	-.00343

For this group of tests, the following table shows the calculated statistical information.

Table 57 : Statistical Information for -55C Modulus Tests, 0° Fiber Orientation

Average Modulus (Msi)	Standard Deviation (Msi)	Correlation Coefficient	Average Strain (in/in)	Standard Deviation (in/in)	Correlation Coefficient
10.225	0.220	2.16	-.003274	.00022	6.72

Similarly as with the elevated temperature modulus testing, a 0° specimen was unable to be tested at the decreased temperature. The test matrix in Appendix B shows specimen 28 was to be tested at the decreased temperature. This specimen sustained a sufficient amount of delamination in the grip region such that testing was impossible.

Continuing, the next table displays the results for the 45° fiber orientation elastic modulus tests.

Table 58 : -55 C Elastic Modulus and Thermal Strain Values, 45° Fiber Orientation

Specimen	Fiber Angle	Modulus (Msi)	Thermal Strain (in/in)
32	45	8.709	-.003463
38	45	8.720	-.00409
48	45	9.446	-.00336

And the next table gives the statistical information for this testing sequence.

Table 59 : Statistical Information for -55C Modulus Tests, 45° Fiber Orientation

Average Modulus (Msi)	Standard Deviation (Msi)	Correlation Coefficient	Average Strain (in/in)	Standard Deviation (in/in)	Correlation Coefficient
8.958	0.422	4.71	-.003638	.000395	10.9

Following, the next table shows the results for testing CentrAl's elastic modulus at the 67.5^o fiber angle.

Table 60 : -55C Elastic Modulus and Thermal Strain Values, 67.5^o Fiber Orientation

Specimen	Fiber Angle	Modulus (Msi)	Thermal Strain (in/in)
49	67.5	9.721	-.003442
55	67.5	9.122	-.003544
60	67.5	9.097	-.003615

And the statistical information is as follows:

Table 61 : Statistical Information for -55C Modulus Tests, 67.5^o Fiber Orientation

Average Modulus (Msi)	Standard Deviation (Msi)	Correlation Coefficient	Average Strain (in/in)	Standard Deviation (in/in)	Correlation Coefficient
9.313	0.354	3.8	-.003534	.0000869	2.46

And finally for the 90° fiber orientation specimens, the next table shows the experimental results.

Table 62 : -55 C Elastic Modulus and Thermal Strain Values, 90° Fiber Orientation

Specimen	Fiber Angle	Modulus (Msi)	Thermal Strain (in/in)
7	90	8.969	-.003683
22	90	8.812	-.003635
27	90	9.040	-.00361

And the table showing the statistical calculation is shown below:

Table 63 : Statistical Information for -55 C Modulus Tests, 90° Fiber Orientation

Average Modulus (Msi)	Standard Deviation (Msi)	Correlation Coefficient	Average Strain (in/in)	Standard Deviation (in/in)	Correlation Coefficient
8.940	0.117	1.31	-.003643	.0000371	1.02

While the information in the preceding tables certainly shows the modulus behavior of CentrAl at the reduced temperature, comparing these results to the

experimentally obtained room temperature results provides an indication to the relative change due to temperature. The next table details the ratio between the experimentally obtained reduced temperature elastic modulus values to their respective room temperature value.

Table 64 : -55C to RT Modulus Comparison

Fiber Angle	Avg. -55C Elastic Modulus (Msi)	Avg. RT Elastic Modulus (Msi)	-55C Modulus / RT Modulus	Percent Difference
0	10.225	9.585	1.07	6.67
45	8.958	8.358	1.07	7.18
67.5	9.313	8.223	1.13	13.25
90	8.940	8.369	1.07	6.82

From this table, it is seen that the decreased temperature appears to affect the elastic modulus property more so than the elevated temperature. Across the entire fiber orientation range, a marked increase in laminate stiffness is realized. As shown, the greatest percent difference between the -55C modulus and room temperature modulus is on the order of 13.25%. This is also seen in the 67.5⁰ fiber angle. In contrast to the elevated temperature modulus testing in which the temperature had very little effect on the modulus, the reduced temperature served to increase the property across all the fiber angles. For the 0⁰, 45⁰, and 90⁰ fiber angles, the percent increase over the room temperature elastic modulus value was 6.67%, 7.18%, and 6.82% respectively.

Monotonic Tension - Experimental Results

The tensile test provides a great deal of information concerning a material's behavior through the generation of a stress-strain curve. These curves were produced for each fiber orientation and at each of the three temperatures studied. Information to include the elastic modulus, ultimate tensile strength, and yield strength can be

determined. Additionally, from these curves, comparisons can be made to the elastic moduli found in the previous elastic modulus tests. It is important to note here that results from the previous elastic modulus tests are those found using the Sintech machine.

Room Temperature Results.

The room temperature results were the first to be determined because baseline properties are needed in an effort to establish any sort of property dependence on this variable. Naturally, fiber orientation also plays a role in property variance.

The following figure depicts the stress strain curve generated from the room temperature specimen with fibers oriented at 0°.

Figure 46 : RT Stress-Strain Curve, 0° Fiber Orientation

From the experimental data obtained while performing this test, the following table details the information gleaned from this curve.

Table 65 : RT Stress-Strain Curve Information, 0$^{\mathbf{o}}$ Fiber Orientation

Elastic Modulus (Msi)	UTS (ksi)	Y (ksi)	$\varepsilon_{\textbf{failure}}$ (in/in)
9.461	117.8	55.67	0.04761

Exactly as performed with the elastic modulus testing, the value obtained for the tensile test was done in the same manner. The slope of the linear-elastic region was measured in order to determine CentrAl's 0$^{\mathbf{o}}$ elastic modulus. The laminate's ultimate tensile strength was found by simply examining the data and finding the greatest stress seen prior to failure. This is also the same technique used to find the strain at the time of failure.

The experimental yield stress was found by using the 0.2% offset technique. In this method, a line, parallel to the stress-strain curve's linear region, was draw beginning at the graph's abscissa at a strain reading of 0.002 in/in. This line was then extended upward until intersecting the curve. The point on the curve where this intersection occurs is defined as the 0.2% offset yield strength.

The table below compares the elastic modulus measured in this room temperature tensile test to both the theoretical and average experimental values found from the dedicated room temperature modulus testing. The percent difference shown is taken as the difference between the theoretical value and the respective value obtained via the stress-strain curve and the dedicated modulus testing.

Table 66 : RT Modulus Comparison, 0$^{\mathbf{o}}$ Fiber Orientation

Theoretical Modulus (Msi)	Stress-Strain Modulus (Msi)	Modulus Test Result (Msi)	Stress-Strain Percent Difference	Modulus Test Percent Difference
9.210	9.461	9.585	2.73	4.07

From the relatively small percent difference between the theoretically and experimentally obtained elastic modulus values, it is inferred that the metal volume fraction approach to finding CentrAl's modulus of elasticity is relatively accurate for this particular fiber orientation.

Additionally, the theoretical ultimate tensile strength value found from this first test, compared to the predicted value, is shown in the table below.

Table 67 : RT UTS Comparison, 0° Fiber Orientation

Theoretical UTS (ksi)	Experimental UTS (ksi)	Percent Difference
93.53	117.8	25.95

The increased value of the ultimate tensile strength could be attributed to the specimen itself exhibiting a higher than average elastic modulus. The specimen itself could have been inherently stiffer than what was otherwise predicted by the theory. Further, when examining the tensile data for the specimen, which was tested in an effort to ascertain the additional fatigue loads, the ultimate tensile strength was seen to be 104,907 psi. Possibly the metal volume fraction approach to the laminate's ultimate tensile strength provides a value which is consistently lower than what is actually seen. Perhaps this technique can be used as a conservative estimate for design purposes. Examining the additional fiber orientations will give additional insight into this behavior.

Upon failure, it is interesting to note how the overall specimen did not completely sever into two separate pieces, as typically seen with tensile testing. Rather, the outer, thicker aluminum layers remained intact while the subsurface aluminum and fibrous layers were destroyed. The following figure shows this failure mechanism. The region within the gauge section is shown outlined in the figure. Subsequently, minor delamination also occurred within the gauge section, located a small distance from the

region of primary failure. This delamination is most likely attributed to adhesive failure between the BondPreg® and central GLARE reinforcement as the thinner aluminum layers within the GLARE began to yield.
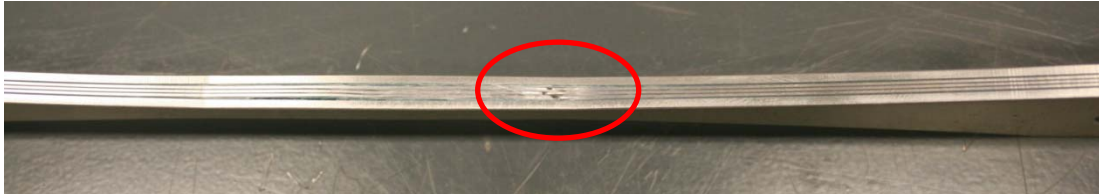
Figure 47 : Failed RT Tensile Specimen, 0⁰ Fiber Orientation

Following, the next figure depicts the stress strain curve generated from the room temperature specimen with fibers oriented at 45⁰.
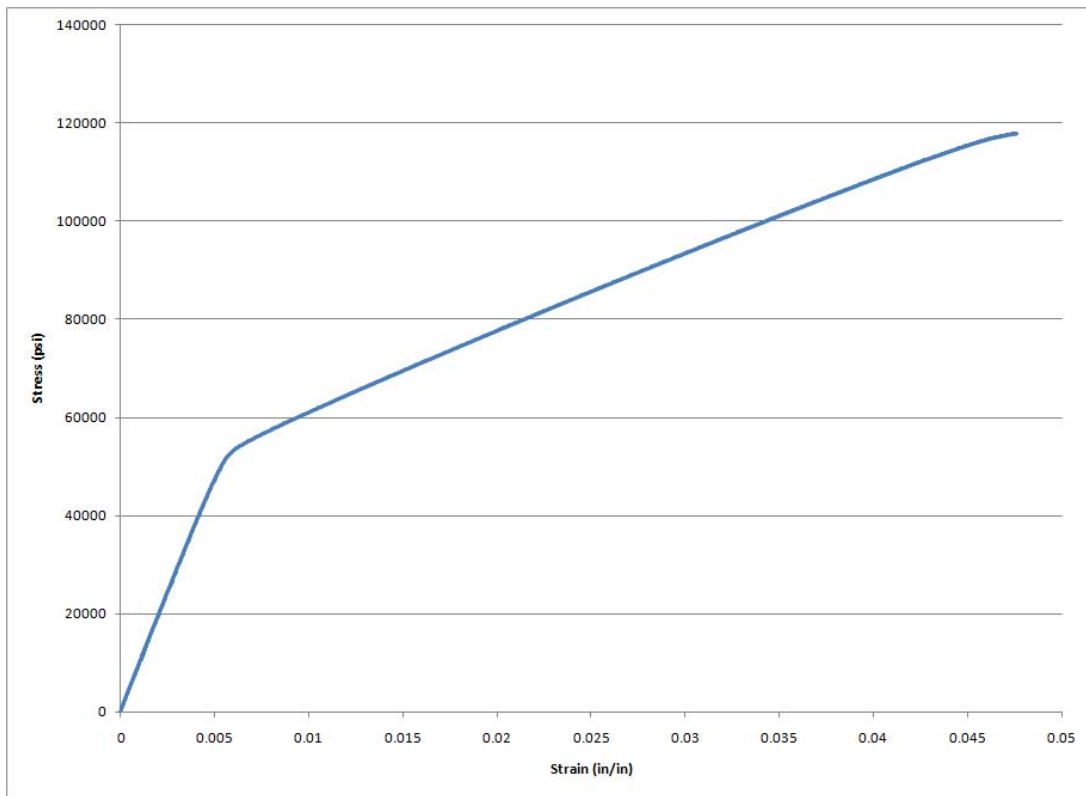

Figure 48 : RT Stress-Strain Curve, 45⁰ Fiber Orientation

Again, from the experimental data obtained in this test, the following table details the information gleaned from this curve.

Table 68 : RT Stress-Strain Curve Information, 45° Fiber Orientation

Elastic Modulus (Msi)	UTS (ksi)	Y (ksi)	$\varepsilon_{failure}$ (in/in)
7.887	50.25	31.22	0.16567

Immediately from this table, it is noted how the fiber orientation influences the properties under investigation. Because the matrix is now more dominant in the loading direction, when compared to that of the 0° fiber orientation, the laminate has essentially become more compliant. This is seen especially in the strain at failure. CentrAl's ultimate and 0.2% offset yield strength values have also decreased - indicative of the now more prominent matrix influence with the 45° fiber orientation.

Once more, the table below compares the elastic modulus measured in this room temperature tensile test to both the theoretical and average experimental values found from the dedicated room temperature modulus testing. As with the 0° fiber orientation comparison, the percent difference shown is taken as the difference between the theoretical value and the respective value obtained via the stress-strain curve and the dedicated modulus testing.

Table 69 : RT Modulus Comparison, 45° Fiber Orientation

Theoretical Modulus (Msi)	Stress-Strain Modulus (Msi)	Modulus Test Result (Msi)	Stress-Strain Percent Difference	Modulus Test Percent Difference
8.760	7.887	8.358	9.97	4.59

The somewhat high percentage difference between the elastic modulus obtained via the stress-strain curve and the theoretical result is not out of order. Specimen 34 was used for this tensile test, and it is noted from Table 36 : Room Temperature Elastic Modulus Results - 45° (Sintech Machine) that specimen 47 saw a similar elastic modulus value of 7.910 Msi. Because these two specimens were cut from the same area on the original

CentrAl panel, seen in Figure 3 : Specimen Layout Compared to Sheet Template, their similar elastic moduli may be indicative of an unforeseen or unknown anomaly. Both specimens also exhibit excellent C-Scan transmission results, as seen in Appendix A.

Again, the theoretical ultimate tensile strength value found during this test, compared to the predicted value, is shown in the table below.

Table 70 : RT UTS Comparison, 45° Fiber Orientation

Theoretical UTS (ksi)	Experimental UTS (ksi)	Percent Difference
71.29	50.25	29.51

Different than the 0° fiber orientation, the theoretical prediction for the 45° specimen was much higher than what was actually measured during the tensile test. Possibly this larger difference can also be attributed to the same anomaly present which showed a marked decrease in the specimen's elastic modulus as compared to the overall average.

In contrast to the failure mechanism seen at the 0° fiber orientation, the 45° specimen did indeed fail into two separate pieces. The figure below shows the specimen, post failure.

Figure 49 : Failed RT Tensile Specimen, 45° Fiber Orientation

Of interest with the off-axis specimen failures is that failure occurs along a line equal to that of the specimen fiber angle. At this 45° angle specimen, it was seen that the subsurface fibrous layers failed in this manner. The following figure, a close up of the failure region, shows this behavior.

Figure 50 : Failure Region of RT Tensile Specimen, 45° Fiber Orientation

The next specimen tested was the 67.5^o fiber orientation. The following figure

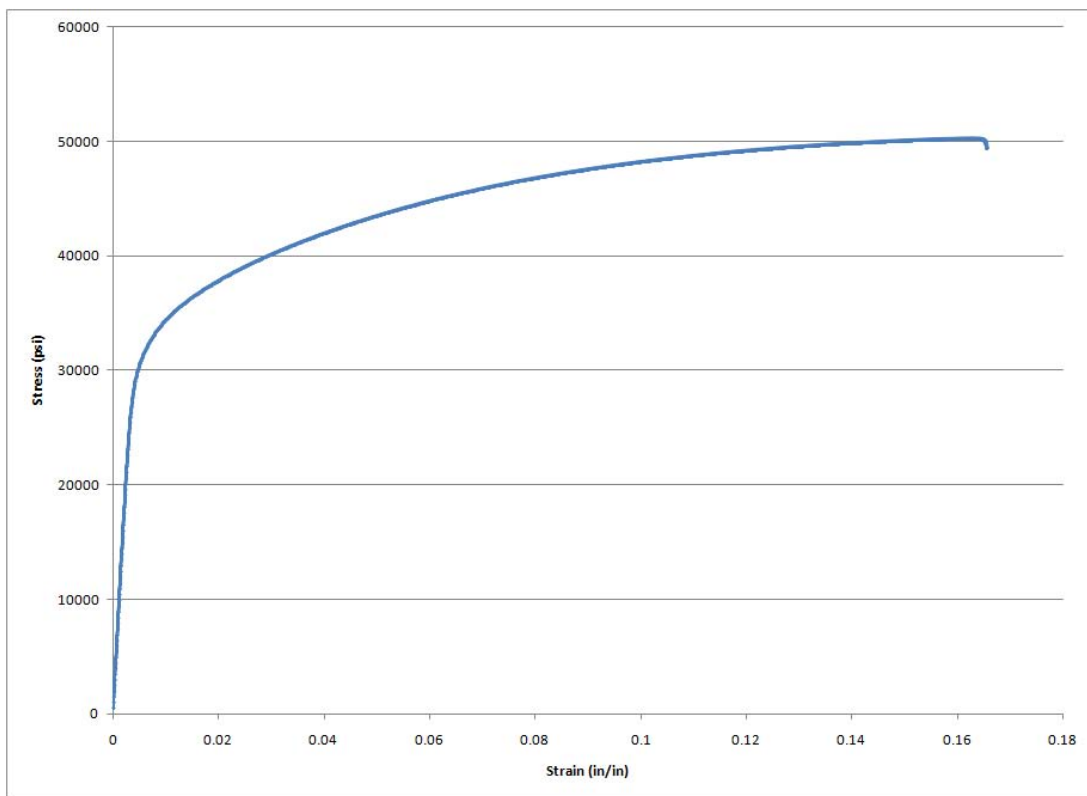shows the stress-strain curve obtained from the results of this test.
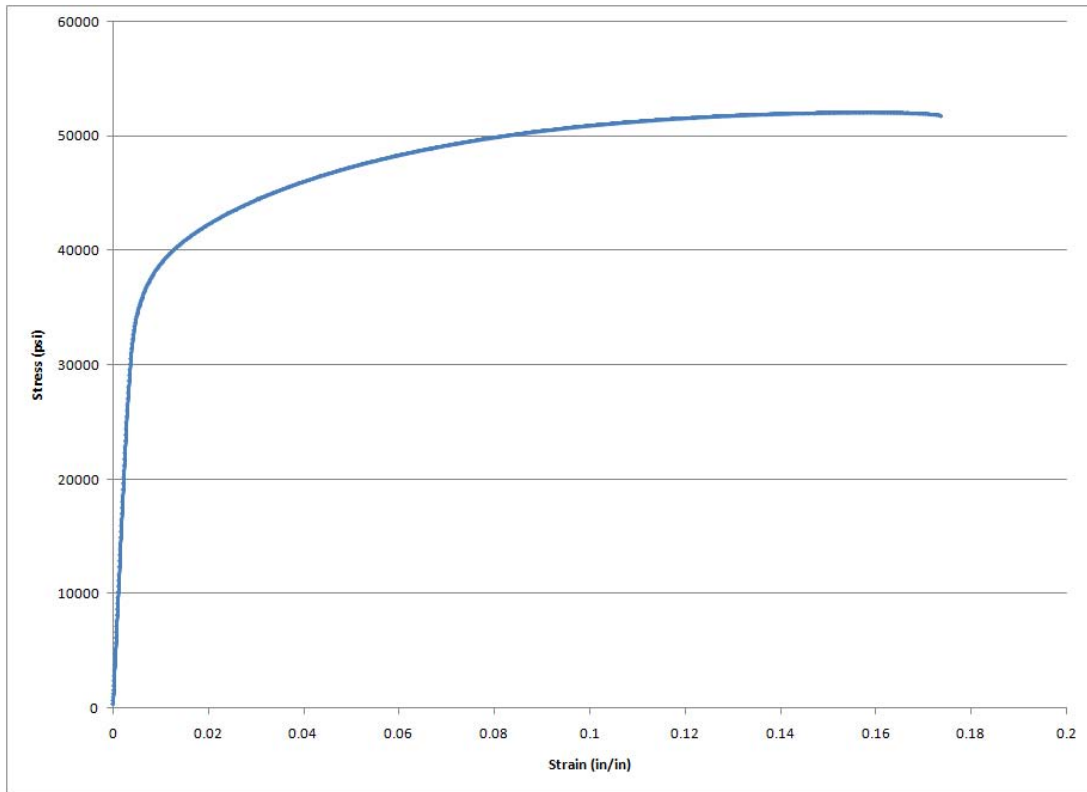
Figure 51 : Room Temperature Stress-Strain Curve, 67.5^o Fiber Orientation

Examining the experimental data obtained in this test, the following table details the

information gleaned from this curve.

Table 71 : RT Stress-Strain Curve Information, 67.5° Fiber Orientation

Elastic Modulus (Msi)	UTS (ksi)	Y (ksi)	$\varepsilon_{failure}$ (in/in)
8.768	52.06	35.02	0.17361

It should be noted here that as the fiber orientation continues to be rotated closer to perpendicular to the loading direction, the strain to failure is also continuously increasing. This observation is coincident with the behavior of other common unidirectional composite materials as a failure in the matrix becomes more dominant. The FM94K Adhesive exhibits much greater plasticity than is seen in the S2-Glass fibers, thus permitting the higher strain magnitudes at the off-axis fiber orientations. This phenomenon is also seen in the relationship between the laminate's ultimate tensile strength and yield strength. As the material is permitted to strain to greater values, the ultimate strength appears to depend more upon the metallic layers and the fibrous layers. It is also worth noting that with the off-axis fiber orientation angles, the overall difference between the ultimate and yield strength values begin diminish.

The following table compares the elastic modulus measured in this room temperature tensile test to both the theoretical and average experimental values found from the dedicated room temperature modulus testing. As with the previous comparisons, the percent difference shown is taken as the difference between the theoretical value and the respective value obtained via the stress-strain curve and the dedicated modulus testing.

Table 72 : RT Modulus Comparison, 67.5° Fiber Orientation

Theoretical Modulus (Msi)	Stress-Strain Modulus (Msi)	Modulus Test Result (Msi)	Stress-Strain Percent Difference	Modulus Test Percent Difference
8.442	8.768	8.223	3.86	2.59

From the relatively small percent difference between the theoretically and experimentally

obtained elastic modulus values, it is again confirmed that by using the metal volume

fraction approach to finding CentrAl's modulus of elasticity, a relatively accurate

theoretical prediction of the elastic modulus can be made can be made.

The table below shows the comparison between the theoretical ultimate tensile

strength value found during this test to that of the predicted value.

Table 73 : RT UTS Comparison, 67.5^o Fiber Orientation

Theoretical UTS (ksi)	Experimental UTS (ksi)	Percent Difference
55.57	52.06	6.32

The smaller percentage difference between the two values gives confidence to using the

metal volume fraction method to approximate the ultimate tensile strength. However, out

of the three tests conducted thus far, this technique gives rise to questions as to the

accuracy of the method, as this test was the first of the three to yield reasonable results.

Another explanation stems from the nature of experimental and statistical work itself.

The specimens previously tested at the 0° and 45° fiber angles exhibited somewhat

outlying behavior with regard to their inherent elastic modulus values. Thus, it is natural

for these specimens to show mechanical properties with greater deviation from the

theoretical predictions.

The following figure shows the failed specimen.

Figure 52 : Failed RT Tensile Specimen, 67.5^o Fiber Orientation

Similar to the failed 45° specimen, the specimen in this test also failed into two separate

pieces. Additionally, as shown in the 45° specimen, failure in the subsurface fibrous

layers occurred at an angle equal to the fiber orientation. The following figure shows a

close up view of the failure region for the 67.5° specimen. Also with this failure, the

outer aluminum layers appeared to have failed along the same line.
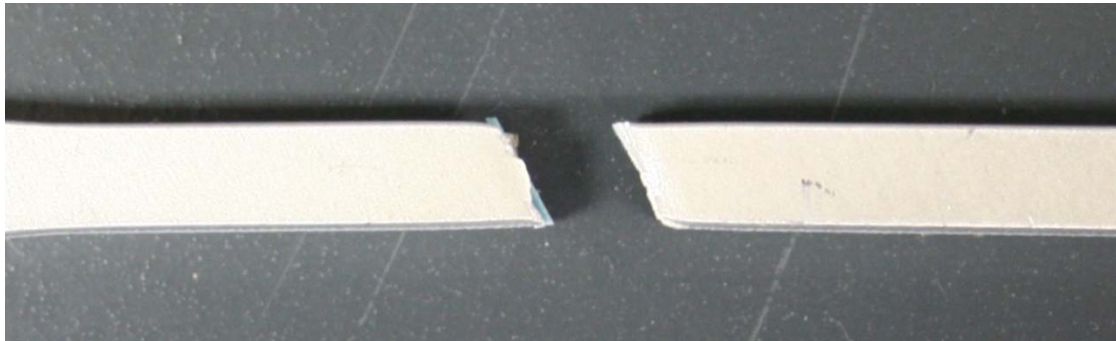
Figure 53 : Failure Region of RT Tensile Specimen, 67.5° Fiber Orientation

Due to a data collection error, information concerning the stress-strain curve for

the 90° specimen does not exist. However, the theoretical predictions are still useful as

they can provide trend information to help isolate the laminate's behavior. The following

table summarizes the theoretical behavior for the 90° specimen.

Table 74 : RT Comparison, 90° Fiber Orientation

Theoretical Modulus (Msi)	Modulus Test Result (Msi)	Modulus Percent Difference	Theoretical UTS (ksi)
8.264	8.369	1.27	49.06

Even though the test data from the 90° specimen no longer exists, the fact that the

theoretical modulus and the average value of all the dedicated modulus tests are so close,

once again shows good agreement between the experimental results and predictions made

from using the metal volume fraction technique.

The figure below shows the 90° specimen after failure occurred.

135
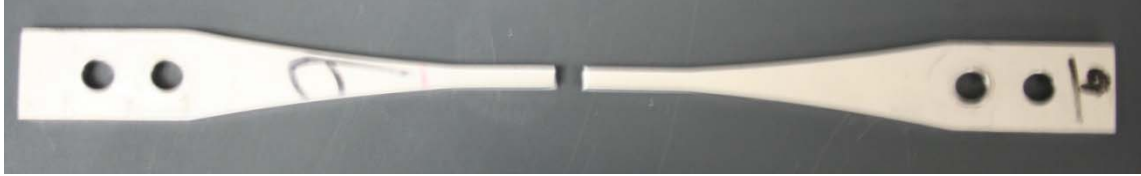
Figure 54 : Failed RT Tensile Specimen, 90⁰ Fiber Orientation

And following with the same failure phenomenon, the 90⁰ specimen is seen to have

failure at an angle perpendicular to the loading direction. Examining the trend of the

previous subsurface fibrous layer failure angles, this specimen failed as predicted. The

fracture occurred at the angle equal to its fiber orientation. The next figure shows a close

up view of the failure region.
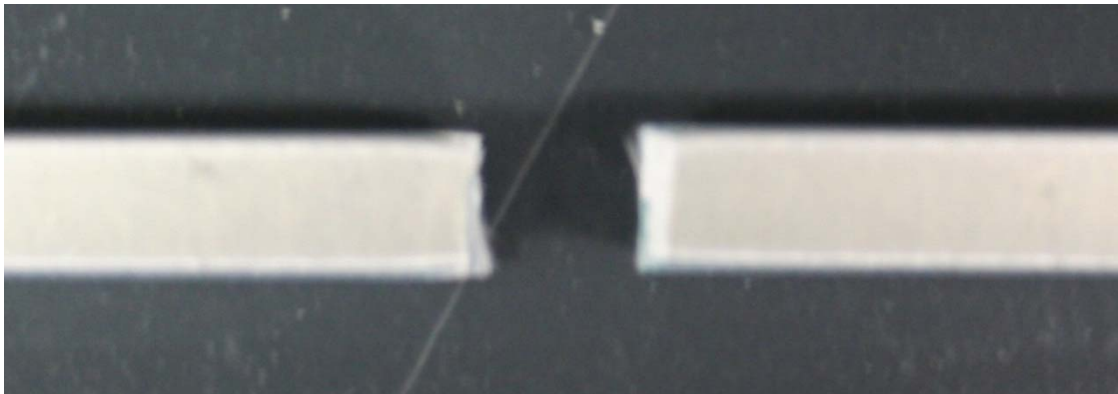
Figure 55 : Failure Region of RT Tensile Specimen, 90⁰ Fiber Orientation

Combined Room Temperature Specimen Results.

Since the temperature was held constant during this initial testing sequence, it

serves to examine each specimen's stress strain curve on the same graph. This provides

valuable insight into the dependence the laminate's mechanical properties have on fiber

orientation. The figure below shows a side-by-side comparison of each of the specimens

tested at room temperature. The specimens are arranged, from top to bottom, in order to

increasing fiber angle: 0⁰, 45⁰, 67.5⁰, and 90⁰.

Figure 56 : Comparison of Room Temperature Tensile Specimens

The following figure shows the stress-strain curve for specimens with fiber orientations of 0⁰, 45⁰, and 67.5⁰.
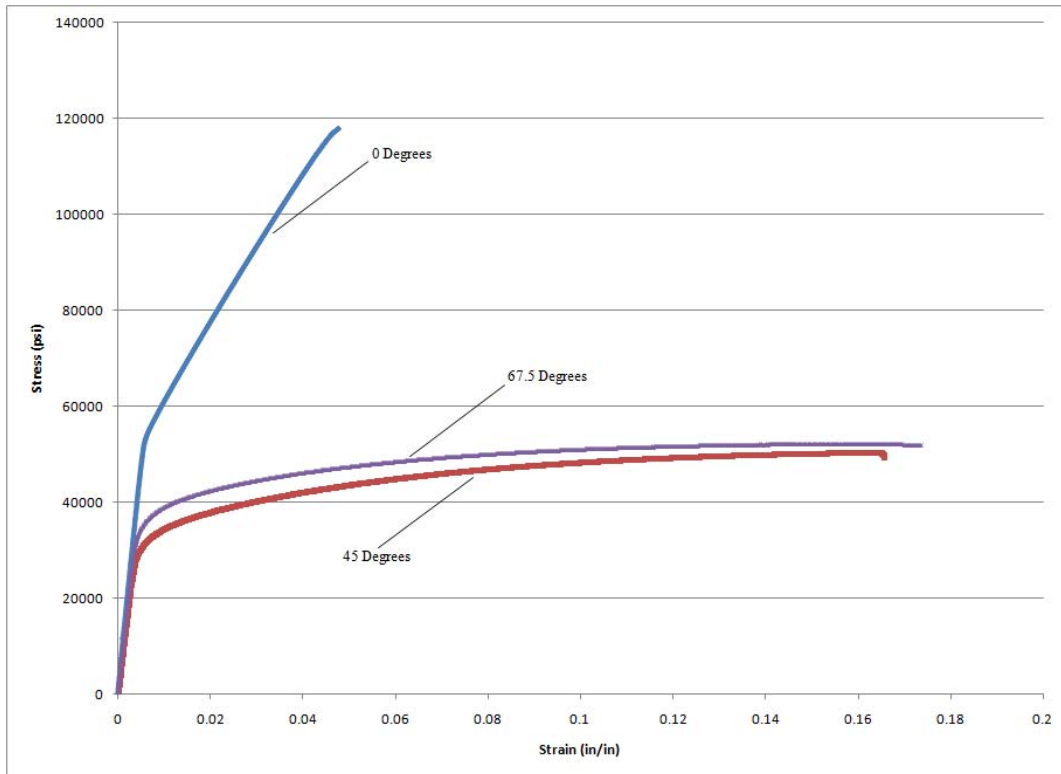
Figure 57 : RT Stress-Strain Curves

Immediately evident from these curves is the dependence the laminate's ultimate tensile strength has on fiber orientation. This is rightfully so as the fibrous layers are unidirectional S2-Glass Fibers. The glass fibers themselves have an ultimate tensile strength greater than that of monolithic aluminum. In a loading direction parallel to the fibers, the S2-Glass is permitted to carry the majority of the load. In the off-axis directions, the matrix material begins to have more of an effect on the laminate's ultimate tensile strength. It is also seen that as the fiber orientation approaches that of 90°, the ultimate tensile strength and the yield strength difference begins to diminish. This is caused in part by the influence the matrix material has on the overall laminate strength, whereby the laminate is permitted to strain more prior to failure. As shown on the 0° curve, the strain at failure is approximately 4.5 times less than that of the off-axis specimens.

Further, because of the apparent anomaly associated with the 45° specimen, this curve should lie above the curve representing the 67.5°. Refer back to the explanations for the subsurface fibrous layer failure angles. Since more of the fiber is aligned in the loading direction with the 45° specimens, it should follow that its ultimate tensile strength would be higher as well. Conversely, because more matrix material is in the load path of the 67.5° specimens, its ultimate tensile strength should be lower than that seen in the 45° specimen.

The following figure shows the comparison between each of the test's experimental elastic moduli.
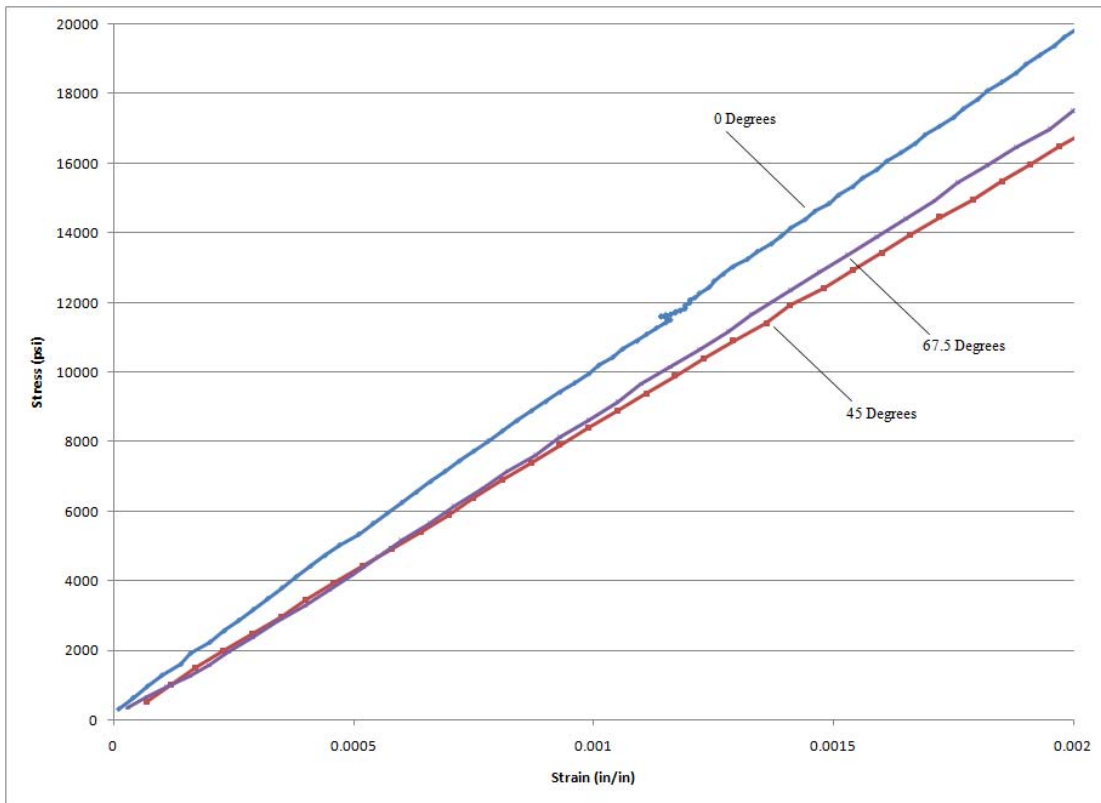
Figure 58 : RT Elastic Stress-Strain Curves Used for Modulus Calculations

This figure shows a portion of each stress-strain curve's linear region. While the numerical value of the elastic modulus has been previously given, this figure clearly shows the effect the fiber orientation has on the laminate's modulus of elasticity. Again, theory says that the 45° modulus should be greater than that seen with the 67.5° specimen. Because this 45° specimen appears to have been an anomaly, its elastic modulus also is shown to be less than that of the 67.5° specimen.

Elevated Temperature (80C) Results.

The next series of tests were tensile tests conducted at 80C. These tests were performed in an effort to show the effect a higher temperature has on CentrAl's mechanical properties. Using the test procedures outlined in the "Experimental

Procedure" section, the following stress-strain curve was produced for the 0° fiber

orientation specimen.
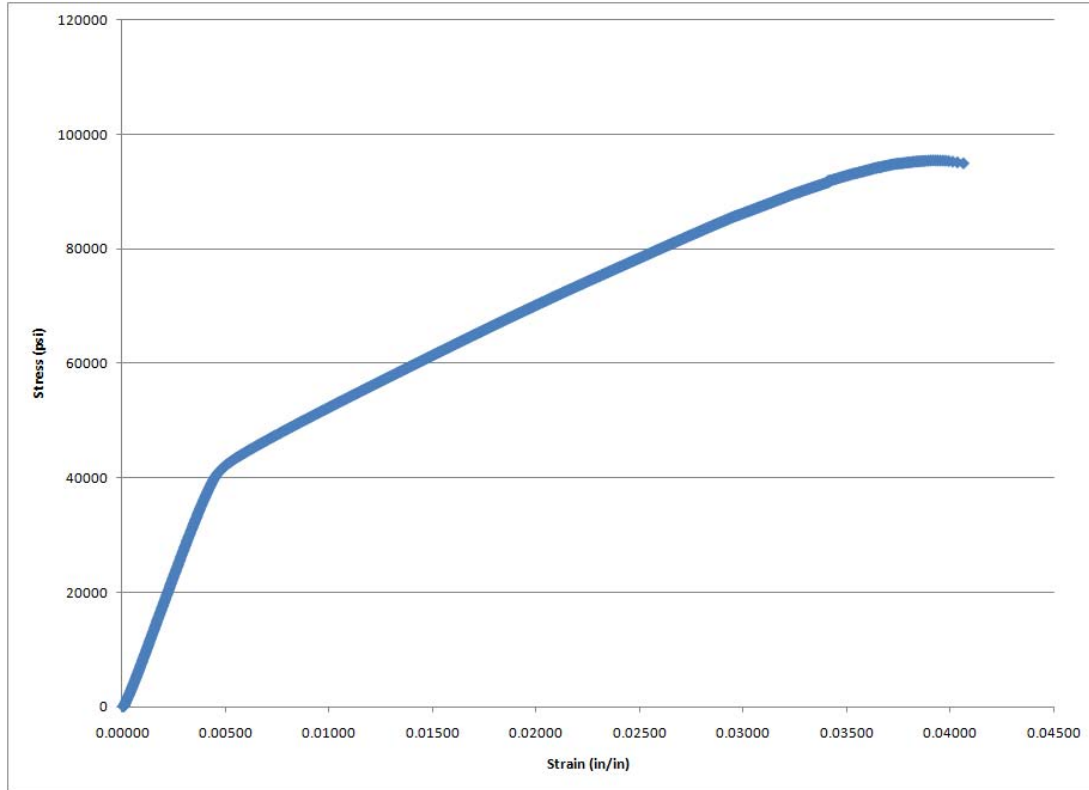
Figure 59 : 80C Stress-Strain Curve, 0° Fiber Orientation

From the experimental data obtained while performing this elevated temperature test, the

following table details the information gleaned from this curve.

Table 75 : 80C Stress-Strain Curve Information, 0° Fiber Orientation

Elastic Modulus (Msi)	UTS (ksi)	Y (ksi)	$\varepsilon_{failure}$ (in/in)
9.506	95.50	45.48	0.04066

The table below compares the elastic modulus measured in this elevated temperature

tensile test to both the theoretical and average experimental values found from the

dedicated elevated temperature modulus testing. The percent difference shown is taken as

the difference between the theoretical value and the respective value obtained via the

stress-strain curve and the dedicated modulus testing.

Table 76 : Elevated Temperature Modulus Comparison, 0° Fiber Orientation

Theoretical Modulus (Msi)	Stress-Strain Modulus (Msi)	Modulus Test Result (Msi)	Stress-Strain Percent Difference	Modulus Test Percent Difference
9.210	9.506	9.560	3.21	3.8

From this table, it is seen that the experimentally obtained modulus from both the

dedicated modulus testing and the tensile test continue to produce good agreement with

the value found by using the metal volume fraction method.

The table below shows the comparison between the theoretical ultimate tensile

strength value found during this test to that of the predicted value.

Table 77 : 80C UTS Comparison, 0° Fiber Orientation

Theoretical UTS (ksi)	Experimental UTS (ksi)	Percent Difference
93.53	95.50	2.11

As shown in this table, the metal volume fraction technique shows good agreement with

the experimental value, despite the temperature elevation in the test. This result differs

from the ultimate tensile test results shown in the room temperature tensile test at this

same fiber orientation. Possibly the effect of heat serves to reduce the experimentally

obtained ultimate tensile strength value down to that of the theoretical prediction.

Additionally, with the new data obtained from the elevated temperature test,

comparisons to the room temperature results can now be made. The next series of tables

shows the comparison between each of the properties obtained through the high

temperature test compared to the baseline room temperature test.

Table 78 : RT to 80C Property Comparison, 0° Fiber Orientation

	Elastic Modulus (Msi)	UTS (ksi)	Y (ksi)	$\varepsilon_{failure}$ (in/in)
RT	9.461	117.8	55.67	0.04761
80C	9.506	95.50	45.48	0.04066
% Difference	0.48	18.93	18.30	14.60

Examining this data shows that the elastic modulus between the two temperatures remains relatively constant. From these two tests, it is seen that the elevated temperature has virtually no effect on the laminate's elastic modulus property.

From the data table, it is noted how the ultimate tensile strength appears to have greatly diminished due to the increased temperature. It is true the FM94K Adhesive matrix material does exhibit a more dramatic temperature dependence upon its mechanical properties, as noted by its higher coefficient of thermal expansion when compared to both the aluminum and S2 Glass fibers. The 0° fiber orientation seen on this specimen is dominated by the fibers and not the matrix. It would thus follow that the mechanical properties would exhibit more stability in this orientation, in contrast to a fiber orientation more dominated by the matrix. Though the decrease from the room temperature value is quite dramatic, it would not typically be likely with fibers oriented parallel to the loading direction. Only a slight decrease would be expected, as shown in [5].

This specimen produced an ultimate tensile strength which more closely matches that of the theoretical prediction. A further conjecture may be that the theoretical prediction indeed does show an accurate value for CentrAl's ultimate tensile strength, and that the specimens tested prior to this particular specimen were simply statistical outliers.

CentrAl's yield strength is shown to also decrease slightly at the elevated

temperature. This is coincident with the behavior seen from the literature, as the elevated

temperature tends to soften the matrix material, thus causing an overall decrease in the

property value. This magnitude of decrease will be further examined through the other

specimens tested at the elevated temperature.

What is interesting, however, is that the results of this elevated temperature tensile

test show a marked decrease in the laminate's ultimate strain value. Though a strain of

approximately 0.007 in/in is a small value, the correctness of this difference will be easier

to comment upon when examining the strain differences with the remaining tensile and

blunt notch tests.

Mirroring the failure mechanisms seen with the room temperature 0° tensile test

specimen, the 80C test showed a failure only in the subsurface layers of the laminate. The

following figure shows the specimen at the completion of this elevated temperature

tensile test.

Figure 60 : Failed 80C Tensile Specimen, 0° Fiber Orientation

Again as with the 0° specimen tested at room temperature, the failure region was limited

to the subsurface layers. The figure below shows this region of the elevated temperature

0° specimen. The figure below is highlighted in the region showing fiber failures. Of

interest, it was seen that the actual aluminum layers within the GLARE reinforcement

remained intact; it was the fibers in the prepreg which suffered the failure. This could

143

offer an explanation to the decreased overall strain at failure as seen in this elevated temperature test.
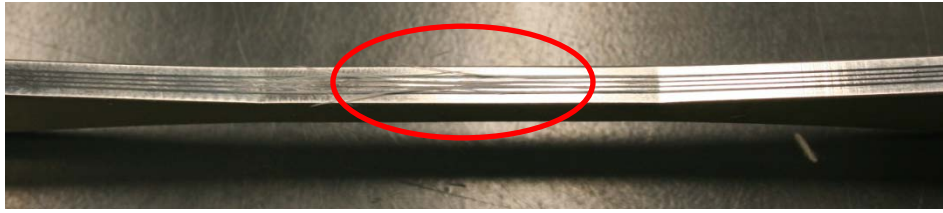
Figure 61 : Failure Region of 80C Tensile Specimen, 0° Fiber Orientation

Following the 0° test, the elevated temperature 45° specimen was tested. The following figure shows the stress-strain curve produced during this test.
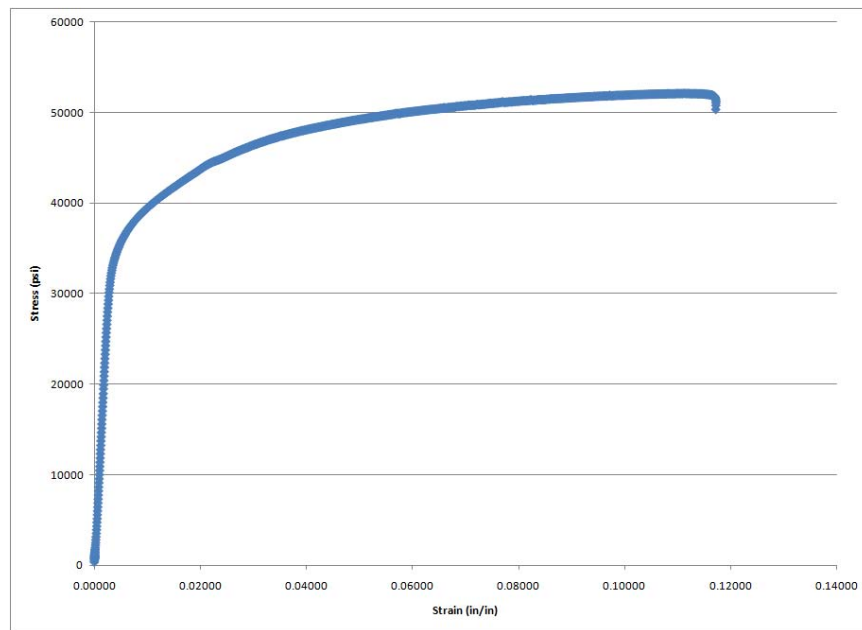
Figure 62 : 80C Stress-Strain Curve, 45° Fiber Orientation

Gathered from the information obtained by examining this chart, the following table shows the pertinent data for this test.

Table 79 : 80C Stress-Strain Curve Information, 45° Fiber Orientation

Elastic Modulus (Msi)	UTS (ksi)	Y (ksi)	$\varepsilon_{failure}$ (in/in)
11.117	52.09	38.46	0.11732

Again, the table below compares the elastic modulus measured in this elevated temperature tensile test to both the theoretical and average experimental values found from the dedicated elevated temperature modulus testing. The percent difference shown is taken as the difference between the theoretical value and the respective value obtained via the stress-strain curve and the dedicated modulus testing.

Table 80 : Elevated Temperature Modulus Comparison, 45⁰ Fiber Orientation

Theoretical Modulus (Msi)	Stress-Strain Modulus (Msi)	Modulus Test Result (Msi)	Stress-Strain Percent Difference	Modulus Test Percent Difference
8.760	11.117	8.339	26.91	4.81

From this test, it is seen that that modulus measured in this elevated temperature tensile test has increased dramatically from that seen in the initial, 0⁰ degree test, and also from the theoretical value.

From the logic surrounding how a unidirectional composite will exhibit its greatest strength when its fibers are aligned with the loading direction, this specimen appears to defy this behavior. It can be assumed that this specimen is indeed a statistical outlier. At the elevated temperature, if any change were to occur, it would be expected that the modulus would decrease slightly from the room temperature value.

Following, the table below shows the comparison between the theoretical ultimate tensile strength value found during this test to that of the predicted value.

Table 81 : 80C UTS Comparison, 45⁰ Fiber Orientation

Theoretical UTS (ksi)	Experimental UTS (ksi)	Percent Difference
71.29	52.09	26.93

Further, with the new data obtained from the elevated temperature test, comparisons to the room temperature results can now be made. The next table shows the comparison

between each of the properties obtained through the high temperature test compared to

the baseline room temperature test.

Table 82 : RT to 80C Property Comparison, 45° Fiber Orientation

	Elastic Modulus (Msi)	UTS (ksi)	Y (ksi)	$\varepsilon_{failure}$ (in/in)
RT	7.887	50.25	31.22	0.16567
80C	11.117	52.09	38.46	0.11732
% Difference	40.95	3.66	23.19	29.18

From these two tables, it appears as though the metal volume fraction approach does not

accurately predict the material properties. The elastic modulus has increased, despite a

decreased amount of fiber influence in the loading direction. This is the same for both the

ultimate tensile and yield strength values as well. However, to coincide with a stiffer,

more brittle specimen, its strain at failure was shown to decrease.

Though, the metal volume fraction approach has followed the theory with good

agreement thus far, it can be assumed that the specimen is indeed a statistical outlier. This

statement can be made because the behavior seen at this elevated temperature defies the

behavior of both the adhesive and the prepreg from [5]. Previous experimental research

showed that both the prepreg and adhesive do not exhibit an increase in strength at

elevated temperatures. In fact, quite the contrary is observed.

The following figure shows the specimen at the completion of the tensile test.

Figure 63 : Failed 80C Tensile Specimen, 45° Fiber Orientation

The next figure shows a close up view of the failure region.
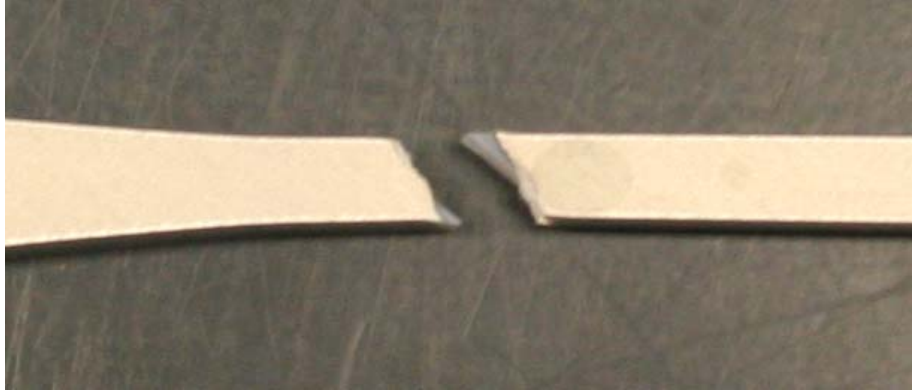
Figure 64 : Failure Region of 80C Tensile Specimen, 45⁰ Fiber Orientation

Just as with the 45⁰ specimen tested at room temperature, the failure of this elevated

temperature specimen has split into two regions. Failure has once again occurred along a

line with an angle equal to that of the fiber orientation. Despite this commonality with the

room temperature failure, because this specimen has appeared to have actually gained

strength at the elevated temperature, its overall behavior must be concluded as an

anomaly.

The next specimen test was one with a fiber angle of 67.5⁰. The next figure shows

the stress-strain curve obtained from this test.
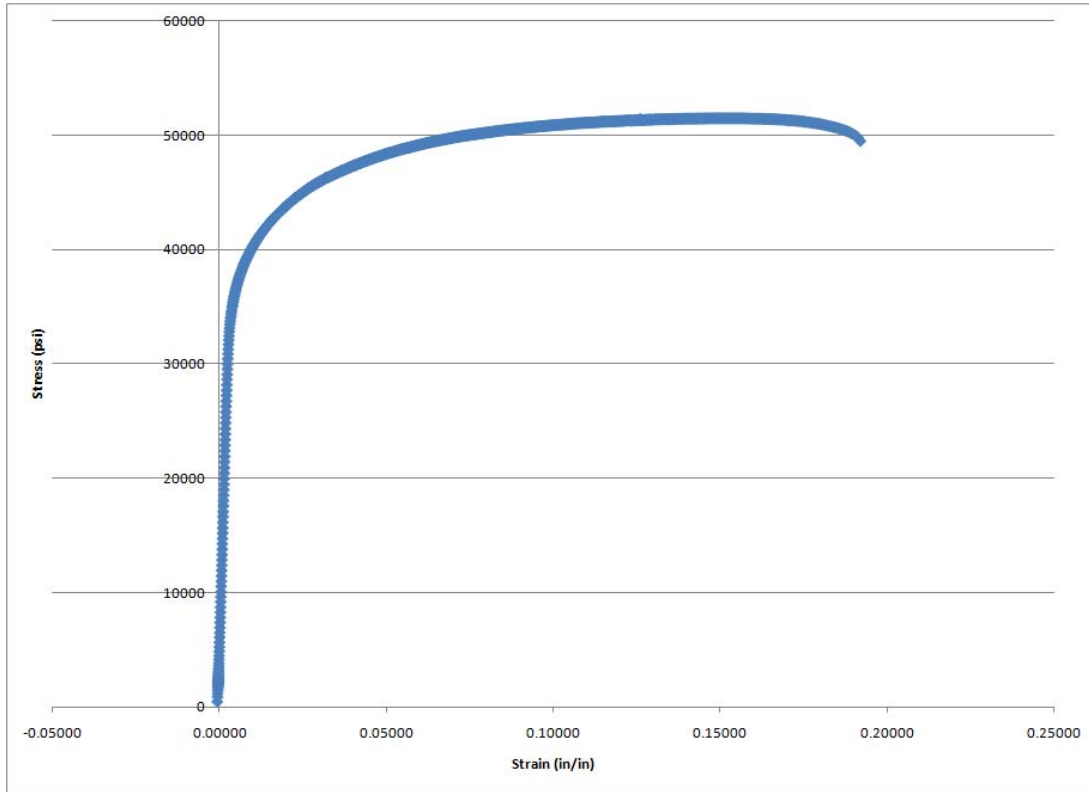
Figure 65 : 80C Stress-Strain Curve, 67.5° Fiber Orientation

Once more, the next table shows the pertinent information which was gleaned from this

particular graph.

Table 83 : 80C Stress-Strain Curve Information, 67.5° Fiber Orientation

Elastic Modulus (Msi)	UTS (ksi)	Y (ksi)	$\varepsilon_{failure}$ (in/in)
10.090	51.49	44.52	0.19193

The following table shows the comparison between the elastic modulus measured in this

elevated temperature tensile test to both the theoretical and average experimental values

found from the dedicated elevated temperature modulus testing. The percent difference

shown is taken as the difference between the theoretical value and the respective value

obtained via the stress-strain curve and the dedicated modulus testing.

Table 84 : Elevated Temperature Modulus Comparison, 67.5° Fiber Orientation

Theoretical Modulus (Msi)	Stress-Strain Modulus (Msi)	Modulus Test Result (Msi)	Stress-Strain Percent Difference	Modulus Test Percent Difference
8.442	10.090	8.353	19.52	1.05

Once again, in this test, it is seen that the experimentally obtained modulus has increased from the room temperature value. While not as dramatic as that seen with the 45° test, the increase does appear to defy the traditional logic traditional logic of that seen with unidirectional composite materials.

Following, the table below shows the comparison between the theoretical ultimate tensile strength value found during this test to that of the predicted value.

Table 85 : 80C UTS Comparison, 67.5° Fiber Orientation

Theoretical UTS (ksi)	Experimental UTS (ksi)	Percent Difference
55.57	51.49	7.34

Further, with the new data obtained from the elevated temperature test, comparisons to the room temperature results can now be made. The next table shows the comparison between each of the properties obtained through the high temperature test compared to the baseline room temperature test.

Table 86 : RT to 80C Property Comparison, 67.5° Fiber Orientation

	Elastic Modulus (Msi)	UTS (ksi)	Y (ksi)	$\varepsilon_{failure}$ (in/in)
RT	8.768	52.06	35.02	0.17361
80C	10.090	51.49	44.52	0.19193
% Difference	15.08	1.1	27.13	10.55

While the elastic modulus in this elevated temperature test shows a slight increase in the corresponding room temperature value, which would indicate a more brittle behavior, the difference between the ultimate and yield strength values is also shown to decrease -

149

indicative of a more brittle behavior. This was the same behavior noted in the room temperature testing sequence. The increased strain to failure is indicative of this trend as the material behaves more compliant. These two simultaneously occurring paradoxical phenomenon contradict one another.

The next figure shows the failed specimen after this elevated temperature test for the 67.5$^{\mathbf{o}}$ fiber orientation.
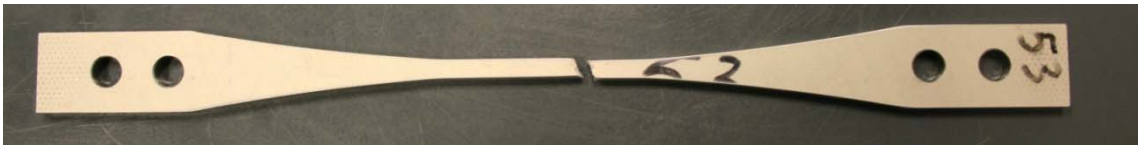
Figure 66 : Failed 80C Tensile Specimen, 67.5$^{\mathbf{o}}$ Fiber Orientation

In following the failure trends, the specimen's subsurface fibrous layers show failure along a line equal to that to the fiber orientation angle. The next series of figures shows close up views of the failure region.

Figure 67 : Failure Region of 80C Tensile Specimen, 67.5$^{\mathbf{o}}$ Fiber Orientation
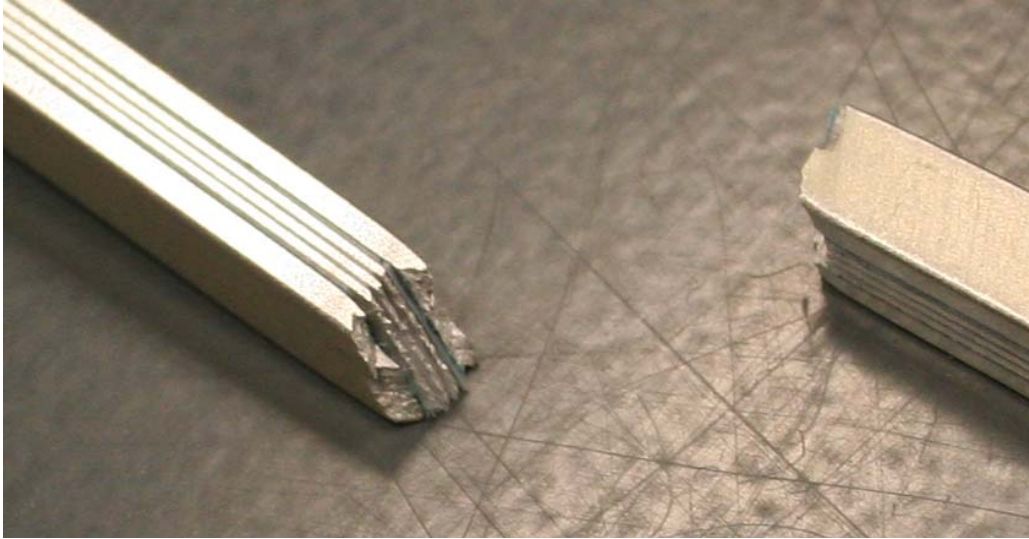
Figure 68 : Second View for Failure Region of 80C Tensile Specimen, 67.5° Fiber Orientation

The final specimen tested at the elevated temperature was for the 90° fiber orientation. The following figure shows the stress-strain curve from this test.
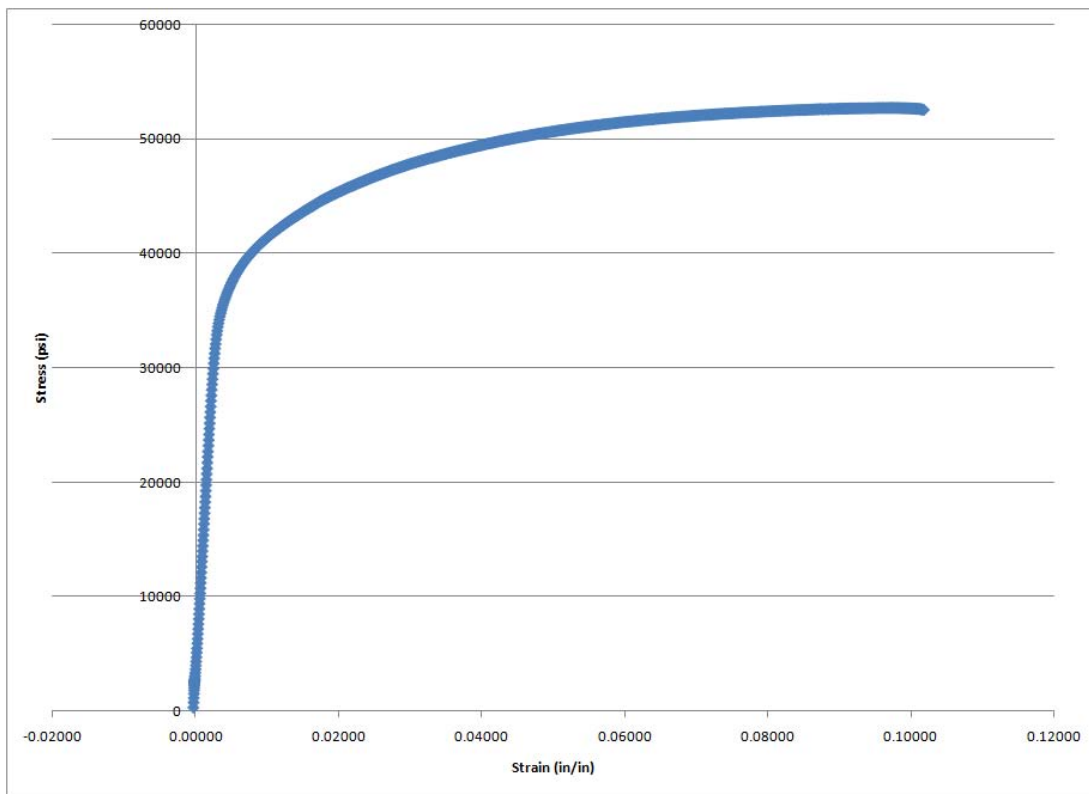
Figure 69 : 80C Stress-Strain Curve, 90° Fiber Orientation

Following, the ensuing table shows the pertinent information which was gleaned from this particular graph.

Table 87 : 80C Stress-Strain Curve Information, 90° Fiber Orientation

Elastic Modulus (Msi)	UTS (ksi)	Y (ksi)	$\varepsilon_{failure}$ (in/in)
10.675	52.71	38.02	0.10182

Once again, the next table compares the differences seen between the elastic modulus measured in this final elevated temperature tensile test to both the theoretical and average experimental values found from the dedicated elevated temperature modulus testing. The percent difference shown is taken as the difference between the theoretical value and the respective value obtained via the stress-strain curve and the dedicated modulus testing.

Table 88 : Elevated Temperature Modulus Comparison, 90° Fiber Orientation

Theoretical Modulus (Msi)	Stress-Strain Modulus (Msi)	Modulus Test Result (Msi)	Stress-Strain Percent Difference	Modulus Test Percent Difference
8.264	10.675	8.358	29.17	1.14

Once more it is seen that the experimentally obtained modulus has increased from the room temperature value. The modulus for the 90° fiber orientation has decreased significantly from that of the 45° specimen, but it has risen slightly from the 67.5° specimen. However, in contrast to available theory, each of these fiber orientations exhibit modulus values greater than that seen in the fiber direction, 0°, itself. This point is further illustrated in the next section detailed the overall relationship of each specimen's stress-strain curve.

Following, the table below shows the comparison between the theoretical ultimate tensile strength value found during this test to that of the predicted value.

Table 89 : 80C UTS Comparison, 90° Fiber Orientation

Theoretical UTS (ksi)	Experimental UTS (ksi)	Percent Difference
49.06	52.71	7.44

Recall that from a data collection error, no room temperature data was collected at the

90° fiber orientation. From the ultimate tensile strength information, the relatively small

percentage difference between the two values shows good agreement between the

theoretical prediction and the experimentally obtained value. The percent difference is on

the order of that seen with the 67.5° fiber orientation specimen.

The following figure shows the resulting specimen after this final elevated

specimen test.

Figure 70 : Failed 80C Tensile Specimen, 90° Fiber Orientation

And the next figure shows the failure region of the same specimen.
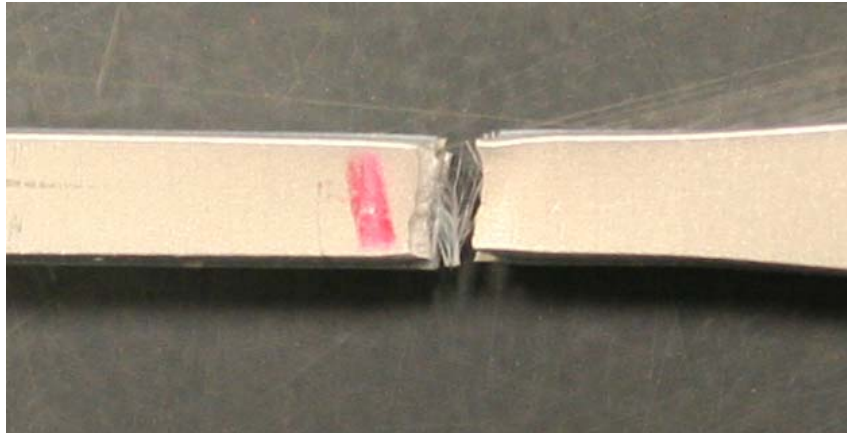
Figure 71 : Failure Region of 80C Tensile Specimen, 90° Fiber Orientation

As has been shown in each of the previous specimens, note the subsurface fibrous layer

failure which occurs at an angle equal to that of the fiber orientation. In this case, it is

clearly seen how the fibers are aligned perpendicular to the loading direction. In the

figure, the fibers are shown oriented vertically.

Combined Elevated Temperature Specimen Results.

Just as with the overall room temperature evaluation, examining the general trend

of each specimen's stress-strain curve provides valuable insight into the dependence its

material behavior has upon the temperature and fiber angle.

The figure below shows a side-by-side comparison of each of the specimens

tested at room temperature. The specimens are arranged, from top to bottom, in order to

increasing fiber angle: 0⁰, 45⁰, 67.5⁰, and 90⁰.

Figure 72 : Comparison of 80C Tensile Specimens

The following figure shows each specimen's stress-strain curve superimposed on one

chart.
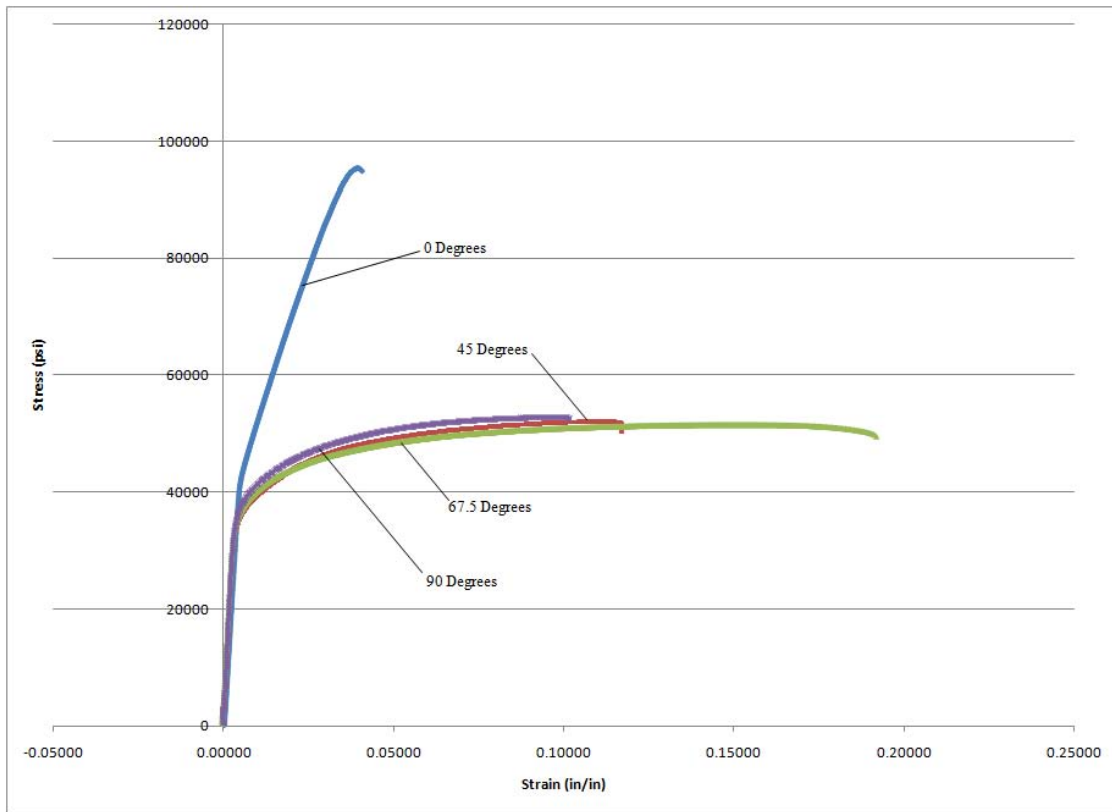
Figure 73 : 80C Stress-Strain Curves

Ignoring any apparent experimental errors or statistical significance of the tested

specimens, like the room temperature test results, it is seen that fiber orientation clearly

plays a role in affecting CentrAl's ultimate tensile strength. This gives confidence in the

applicable theory governing laminated plate and uni-directional fibrous composites as a

whole. Also take note as to how the off-axis ultimate tensile strength and yield strength

values begin to approach one another. As with current laminated plate theory for

unidirectional composites, the off-axis fiber orientations certainly have the capacity to

exhibit additional strain at failure. This is clearly seen for the specimens tested at the 45°,

67.5^o, and 90° fiber orientations.

As with the room temperature results, theory states that the 90° specimen curve

should lie below both the 45° and 67.5^o specimens. The experimental results show that at

the elevated temperature, the 90º specimen lies above both of its off-axis counterparts. This indicates the 90º specimen, with its fibers oriented perpendicular to the loading direction, is actually tougher than both the 45º and 67.5º specimens.

The following figure shows the comparison between each of the test's experimental elastic moduli.
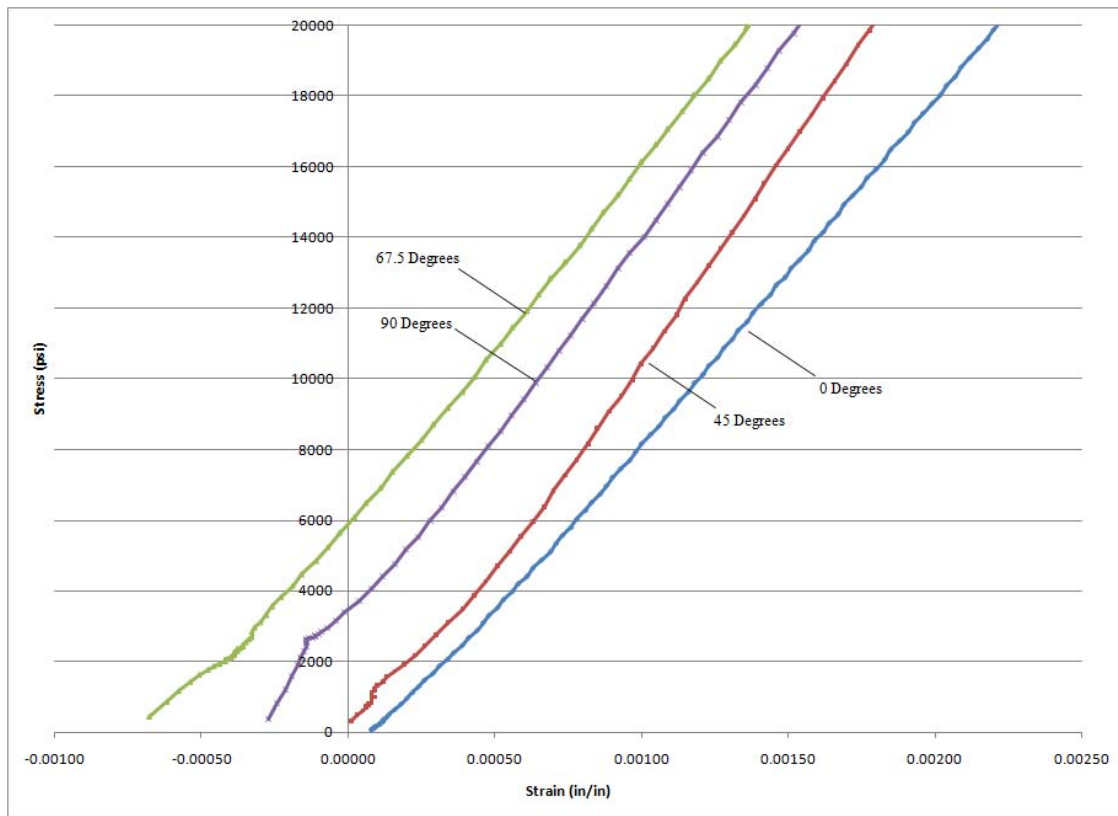
Figure 74 : 80C Elastic Stress-Strain Curves Used for Modulus Calculations

From this figure comparing each of the experimentally obtained elastic moduli, it is immediately evident of one source of experimental error. Because only the mechanical stress-strain curve was plotted, each of the curves should begin at the graph's origin. Because each modulus curve is shown to exhibit some value of strain, based on its point of origin along the abscissa, the final mechanical strain values are incorrect. Despite this setback, the experimental results are not completely useless. Note the relative consistency

156

seen in the general magnitude of the elastic modulus slopes. Because each specimen was tested in an identical manner, it may be said that regardless of the fiber orientation, the general behavior of the elastic modulus remains constant despite the elevated temperature.

Additionally, it should be pointed out how that despite the inconsistencies seen in the individual specimens used for this elevated testing procedure, confidence in the metal volume fraction method is still present due to the close agreement the theoretical elastic modulus values and values obtained through testing several articles at the elevated temperature. No significant reduction in material stiffness was measured.

Decreased Temperature (-55C) Results.

The final series of tests were tensile tests conducted at -55C. These tests were performed in an effort to show the effect a decreased temperature has on CentrAl's mechanical properties. Using the test procedures outlined in the "Experimental Procedure" section, the following stress-strain curve was produced for the 0° fiber orientation specimen.
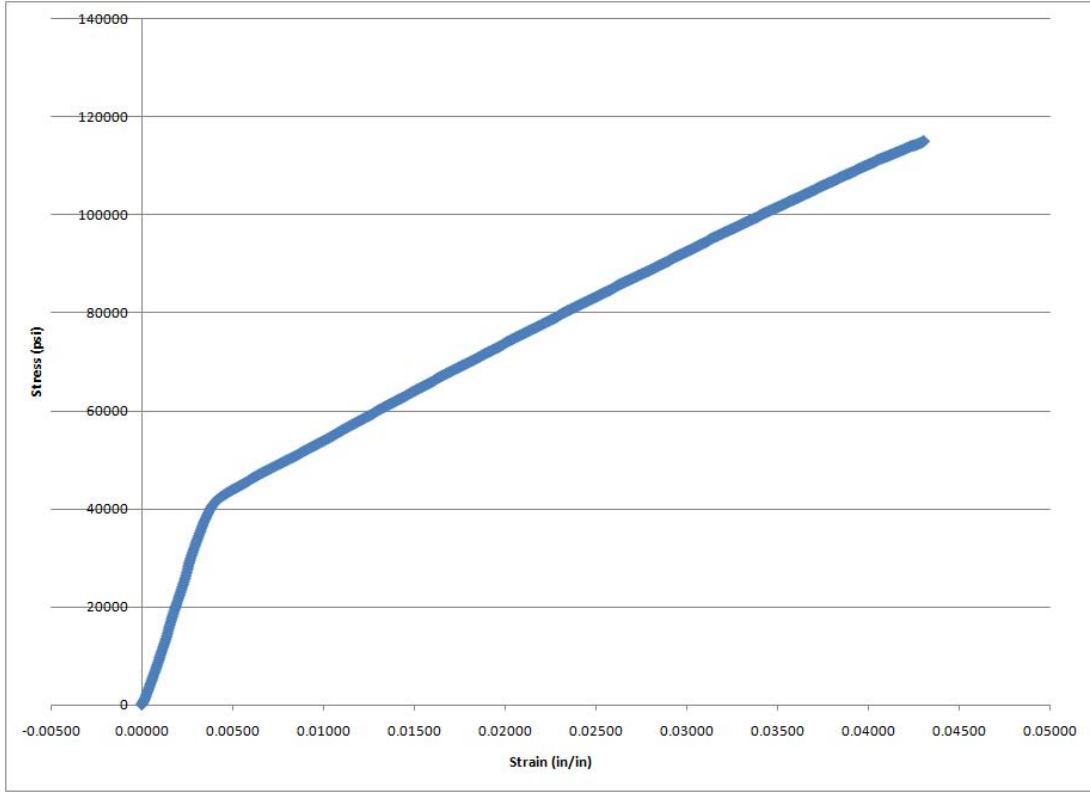
Figure 75 : -55C Stress-Strain Curve, 0° Fiber Orientation

As with the previous tests' stress-strain curves, the following table is produced outlining

the information obtained.

Table 90 : -55C Stress-Strain Curve Information, 0° Fiber Orientation

Elastic Modulus (Msi)	UTS (ksi)	Y (ksi)	$\varepsilon_{failure}$ (in/in)
11.274	115.10	45.55	0.04308

And likewise, the following table shows the comparison between the elastic modulus

measured in this reduced temperature tensile test to both the theoretical and average

experimental values found from the dedicated reduced temperature modulus testing. The

percent difference shown is taken as the difference between the theoretical value and the

respective value obtained via the stress-strain curve and the dedicated modulus testing.

Table 91 : Decreased Temperature Modulus Comparison, 0° Fiber Orientation

Theoretical Modulus (Msi)	Stress-Strain Modulus (Msi)	Modulus Test Result (Msi)	Stress-Strain Percent Difference	Modulus Test Percent Difference
9.210	11.274	10.225	22.41	11.02

While a difference certainly exists between the theoretical and both of the experimental values, and because each of the experimental values are so close, the assertion could be made that decreased temperatures may increase the laminate's brittleness.

Following, the table below shows the comparison between the theoretical ultimate tensile strength value found during this test to that of the predicted value.

Table 92 : -55C UTS Comparison, 0° Fiber Orientation

Theoretical UTS (ksi)	Experimental UTS (ksi)	Percent Difference
93.53	115.10	23.06

Further, with the new data obtained from this initial reduced temperature test, comparisons to the similarly fiber oriented room temperature results can now be made. The next table shows the comparison between each of the properties obtained through the decreased temperature test compared to the baseline room temperature test.

Table 93 : RT to -55C Property Comparison, 0° Fiber Orientation

	Elastic Modulus (Msi)	UTS (ksi)	Y (ksi)	$\varepsilon_{failure}$ (in/in)
RT	9.461	117.82	55.67	0.04761
-55C	11.274	115.10	45.55	0.04308
% Difference	19.16	2.3	18.18	9.5

This data shows that the colder temperature significantly increases the laminate's elastic modulus, as was previous stated. It is also noted that the ultimate strain to failure was decreased slightly. The more brittle material behavior, as seen with the greater elastic

modulus, coupled with the decreased ultimate strain, could serve to drop the yield strength by the percentage shown. The decreased temperatures may force the laminate to plastically deform at a stress lower than what is seen at room temperature. Further investigations of the remaining fiber orientations will held.

The resulting specimen, after this initial reduced temperature test, failed in a manner similar to that seen with each of the other 0° specimens. The outer, thicker aluminum layers remained intact, while the actual physical failure mechanism occurred in the central GLARE reinforcement. Though, in contrast to the room temperature failure, the thin aluminum layers within the GLARE reinforcement remained intact, with the failure restricted to the fibrous prepreg layers. This is shown in the figures below.

Figure 76 : Failed -55C Tensile Specimen, 0° Fiber Orientation
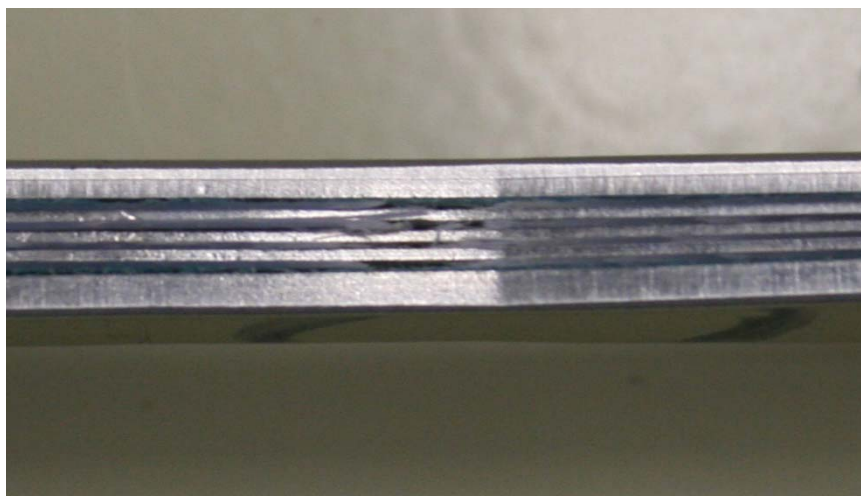
Figure 77 : Failure Region of -55C Tensile Specimen, 0° Fiber Orientation

The second reduced temperature tensile test, similar to the previous two temperatures, was for a specimen whose fibers are oriented at 45°. The following figure shows the stress-strain curve for the specimen with this fiber orientation.
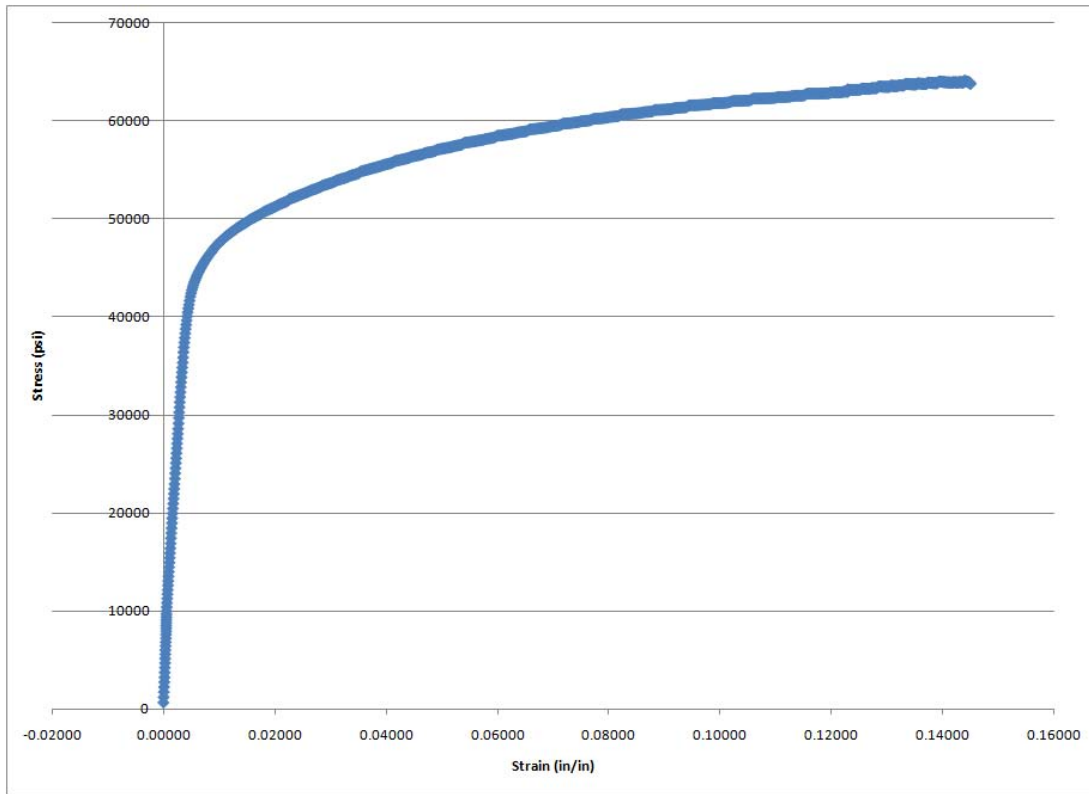
Figure 78 : -55C Stress-Strain Curve, 45° Fiber Orientation

The following table shows the pertinent information found from the stress-strain curve.

Table 94 : -55C Stress-Strain Curve Information, 45° Fiber Orientation

Elastic Modulus (Msi)	UTS (ksi)	Y (ksi)	$\varepsilon_{failure}$ (in/in)
9.311	64.06	44.55	0.14518

And next, the subsequent table shows the comparison between the elastic modulus measured in this reduced temperature tensile test to both the theoretical and average experimental values found from the dedicated reduced temperature modulus testing. The

percent difference shown is taken as the difference between the theoretical value and the respective value obtained via the stress-strain curve and the dedicated modulus testing.

Table 95 : Decreased Temperature Modulus Comparison, 45⁰ Fiber Orientation

Theoretical Modulus (Msi)	Stress-Strain Modulus (Msi)	Modulus Test Result (Msi)	Stress-Strain Percent Difference	Modulus Test Percent Difference
8.760	9.311	8.958	6.29	2.26

With the modulus results from this particular test, it is seen that the difference between each of the experimental values and the theoretical is greatly reduced. This could be due to the statistical error likely seen in the elevated temperature tests. In this reduced temperature test, the specimen behavior was more coincident with the theoretical prediction.

Following, the table below shows the comparison between the theoretical ultimate tensile strength value found during this test to that of the predicted value.

Table 96 : -55C UTS Comparison, 45⁰ Fiber Orientation

Theoretical UTS (ksi)	Experimental UTS (ksi)	Percent Difference
64.06	71.29	11.29

Further, with the new data obtained from this initial reduced temperature test, comparisons to the similarly fiber oriented room temperature results can now be made. The next table shows the comparison between each of the properties obtained through the decreased temperature test compared to the baseline room temperature test.

Table 97 : RT to -55C Property Comparison, 45⁰ Fiber Orientation

	Elastic Modulus (Msi)	UTS (ksi)	Y (ksi)	$\varepsilon_{failure}$ (in/in)
RT	7.887	50.25	31.22	0.16567
-55C	9.311	64.06	44.55	0.14518
% Difference	18.05	27.48	42.7	12.37

Just as with the results shown at the 0° fiber orientation, the decreased

temperature serves to increase the overall laminate's elastic modulus. This increase in

laminate brittleness is also reflected in the near 12% decrease seen in the ultimate failure

strain. Of interest is that despite that observation of the increased elastic modulus, the

overall difference between the ultimate and yield strength vales remains relatively

constant. A difference with the increased fiber angle, when compared to that of the 0°

fiber angle, is that in the case of this 45° specimen, the yield strength actually appears to

increase. This property increase could be due to the same phenomenon present which

induced the increase in elastic modulus; at the colder temperature, the laminate possibly

becomes more brittle.

The following figure shows the failed 45° fiber orientation specimen. Note how

the failure, once more, occurs along a line at angle equal to that of the fiber angle.

Figure 79 : Failed -55C Tensile Specimen, 45° Fiber Orientation

The next two figures show the failure region for this specimen up close.
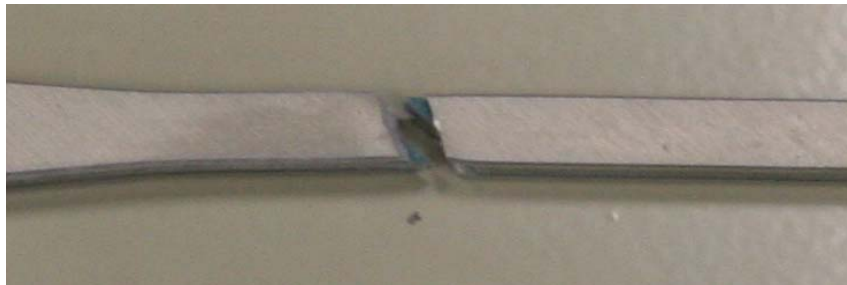

Figure 80 : Failure Region of -55C Tensile Specimen, 45° Fiber Orientation

Figure 81 : Second View for Failure Region of -55C Tensile Specimen, 45° Fiber Orientation

The third specimen tested was for the 67.5° fiber orientation. The next figure shows the stress-strain curve for this test procedure.
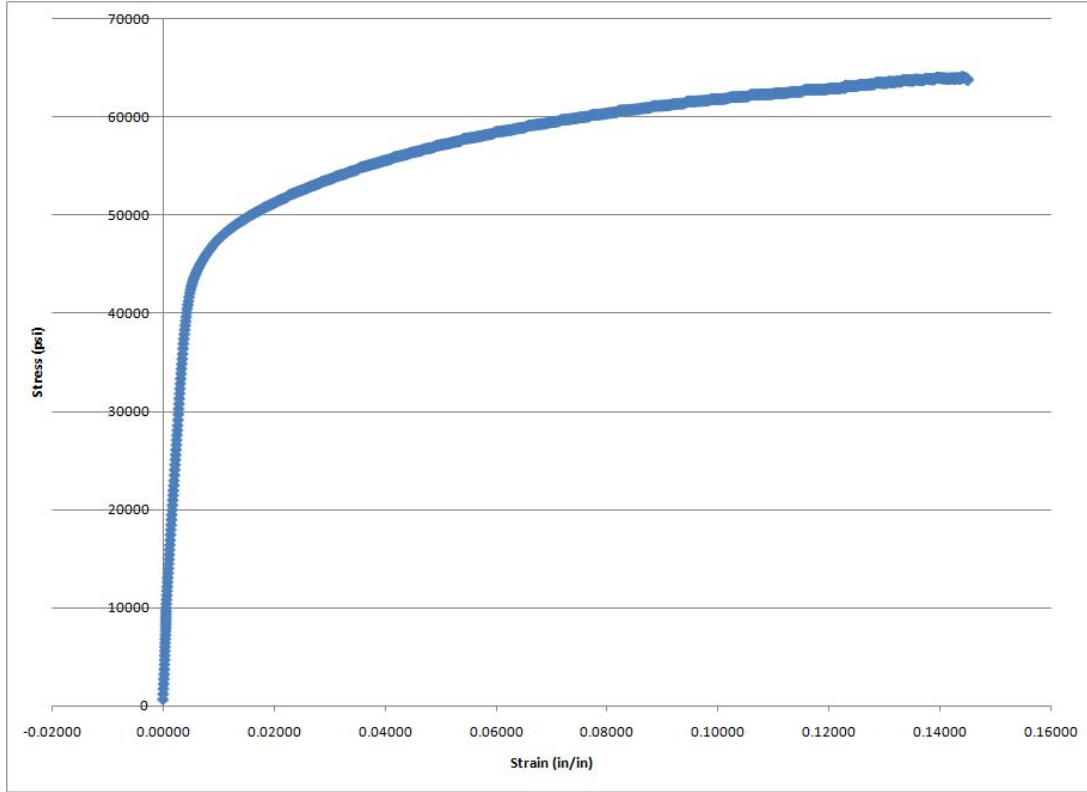

Figure 82 : -55C Stress-Strain Curve, 67.5° Fiber Orientation

As with each of the previous tests, the following table shows the pertinent information found from the stress-strain curve produced from the 67.5° specimen.

Table 98 : -55C Stress-Strain Curve Information, 67.5° Fiber Orientation

Elastic Modulus (Msi)	UTS (ksi)	Y (ksi)	$\varepsilon_{failure}$ (in/in)
8.656	58.47	42.59	0.13564

Following, the next table shows the comparison between the elastic modulus measured in this reduced temperature tensile test to both the theoretical and average experimental values found from the dedicated reduced temperature modulus testing. The percent difference shown is taken as the difference between the theoretical value and the respective value obtained via the stress-strain curve and the dedicated modulus testing.

Table 99 : Decreased Temperature Modulus Comparison, 67.5° Fiber Orientation

Theoretical Modulus (Msi)	Stress-Strain Modulus (Msi)	Modulus Test Result (Msi)	Stress-Strain Percent Difference	Modulus Test Percent Difference
8.442	8.656	9.313	2.53	10.32

With the modulus results from this particular test, it is seen that the difference between each of the experimental values and the theoretical is greatly reduced. This could be due to the statistical error likely seen in the elevated temperature tests. In this reduced temperature test, the specimen behavior was more coincident with the theoretical prediction.

Following, the table below shows the comparison between the theoretical ultimate tensile strength value found during this test to that of the predicted value.

Table 100 : -55C UTS Comparison, 67.5° Fiber Orientation

Theoretical UTS (ksi)	Experimental UTS (ksi)	Percent Difference
55.57	58.47	5.22

Further, with the new data obtained from this initial reduced temperature test, comparisons to the similarly fiber oriented room temperature results can now be made. The next table shows the comparison between each of the properties obtained through the decreased temperature test compared to the baseline room temperature test.

Table 101 : RT to -55C Property Comparison, 67.5^o Fiber Orientation

	Elastic Modulus (Msi)	UTS (ksi)	Y (ksi)	$\varepsilon_{failure}$ (in/in)
RT	8.768	52.06	35.02	0.17361
-55C	8.656	58.47	42.59	0.13564
% Difference	1.28	12.31	21.62	21.87

In contrast to the other two fiber angles previous tested at the lower temperature, the 67.5^o fiber orientation shows virtually no change in its elastic modulus magnitude, when compared to the specimen tested at room temperature. Although the modulus value does not follow the trend exhibited by the other two fiber angle test results, the ultimate strength, yield strength, and strain to failure all serve to decrease. This could possibly be explained by the influence the additional matrix material has on the overall specimen behavior at this decreased temperature. While at the 0° and 45° fiber angles respectively, the matrix is either dwarfed by or in equal proportion to the amount of fiber in the loading direction. Examination of the test results for the specimen oriented at 90° could provide additional insight into this behavior. As shown the resulting 21.87% decrease in ultimate failure strain shows the effect the reduced temperature has on this specimen, which is matrix dominated in the loading direction.

The following figure shows the resulting specimen after this third reduced temperature tensile test.
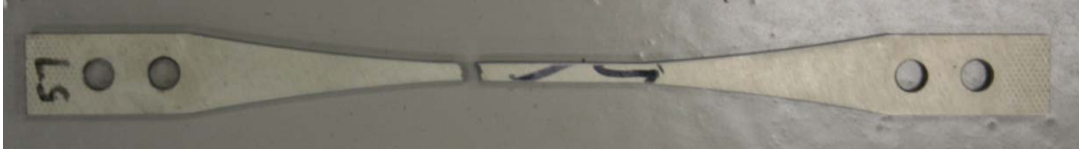
Figure 83 : Failed -55C Tensile Test Specimen, 67.5° Fiber Orientation

The next figure shows the failure region.
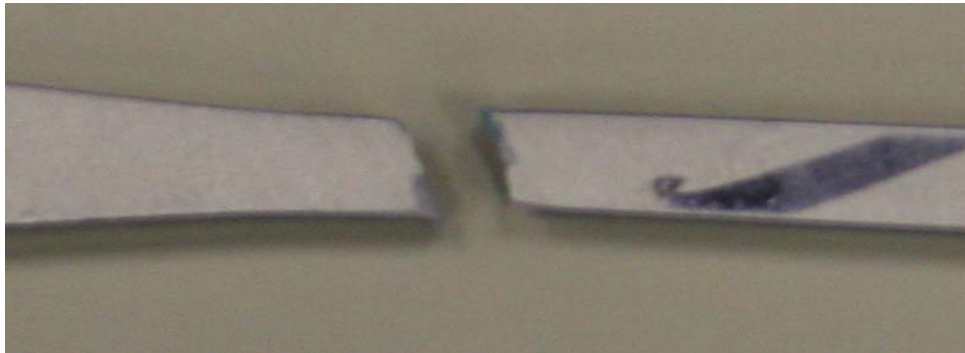
Figure 84 : Failure Region of -55C Tensile Specimen, 67.5° Fiber Orientation

In keeping with the same trend, this specimen also failed along a line in its subsurface layers at an angle equal to its fiber orientation.

The final test at the reduced temperature was for a specimen whose fibers are oriented at 90°. The subsequent figure shows the resulting stress-strain curve for this test.
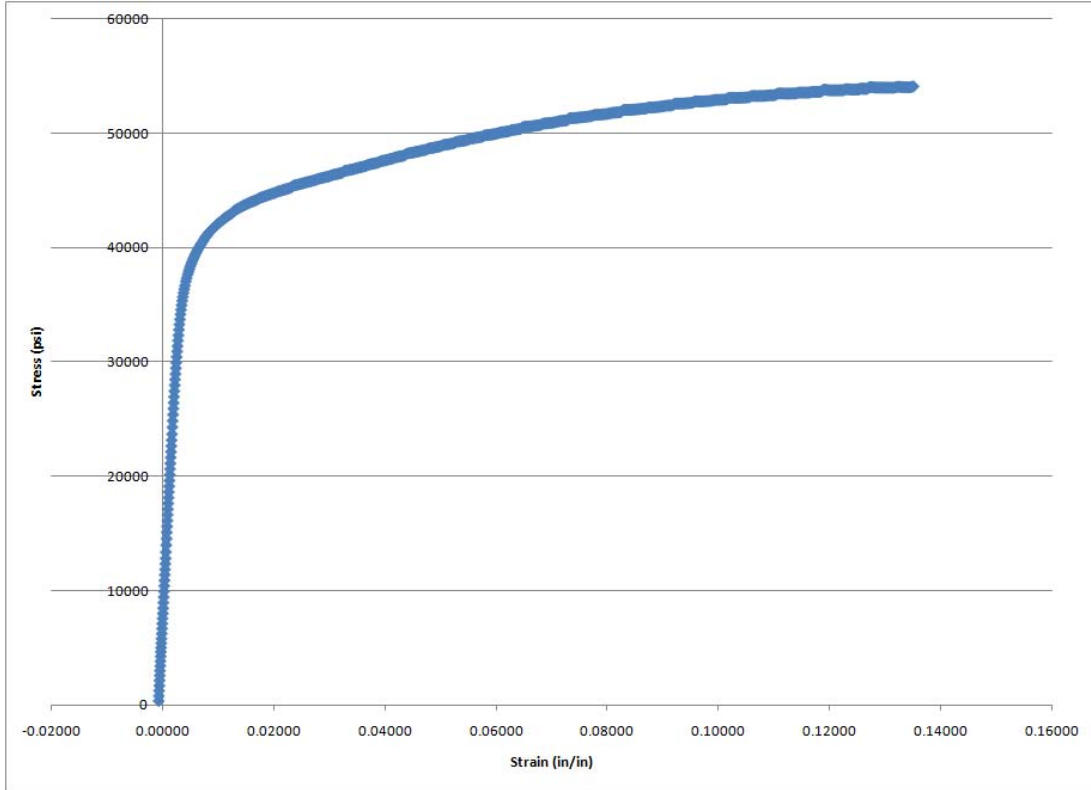
Figure 85 : -55C Stress-Strain Curve, 90° Fiber Orientation

This next table shows the pertinent information found from the stress-strain curve

produced from this final test, the 90° specimen.

Table 102 : -55C Stress-Strain Curve Information, 90° Fiber Orientation

Elastic Modulus (Msi)	UTS (ksi)	Y (ksi)	$\varepsilon_{failure}$ (in/in)
9.318	54.15	39.17	0.13512

And finally, the next table shows the comparison between the elastic modulus measured

in this fourth reduced temperature tensile test to both the theoretical and average

experimental values found from the dedicated reduced temperature modulus testing. As

with each of the previous tables containing similar information, the percent difference

shown is taken as the difference between the theoretical value and the respective value

obtained via the stress-strain curve and the dedicated modulus testing.

Table 103 : Decreased Temperature Modulus Comparison, 90° Fiber Orientation

Theoretical Modulus (Msi)	Stress-Strain Modulus (Msi)	Modulus Test Result (Msi)	Stress-Strain Percent Difference	Modulus Test Percent Difference
8.264	9.318	8.940	12.75	8.18

For this single tensile test, the experimentally obtained elastic modulus was shown to have increased over the theoretical value. This result agrees with the trend shown thus far with the reduced temperature testing. While the value seen in this procedure are shown to be slightly greater than that obtained from the dedicated modulus testing, the variance could be attributed to experimental scatter, as only a single specimen was evaluated.

Following, the table below shows the comparison between the theoretical ultimate tensile strength value found during this test to that of the predicted value.

Table 104 : -55C UTS Comparison, 90° Fiber Orientation

Theoretical UTS (ksi)	Experimental UTS (ksi)	Percent Difference
49.06	54.15	10.38

The strain to failure for the 90° specimen was shown to be nearly identical to that for the 67.5° specimen. Theory states that a fiber orientation dominated more by fiber should strain more than an orientation more so dominated by fiber. The increase in elastic modulus over the 67.5° specimen also appears to defy existing theory. The decreased temperature has been shown to increase the overall laminate's elastic modulus, however the increase seen from the 67.5° to the 90° fiber orientation. Concurring with the existing theory is the decrease in the laminate's ultimate tensile strength. The ultimate tensile strength is shown to be approximately 10.4% higher than the theoretical value at the reduced temperature but lower than that seen at the 67.5° fiber angle. Since there is a

decreased percentage of fiber present in the loading direction for this fiber orientation, it follows that the corresponding ultimate strength would also be reduced.

The next figure shows the resulting failed specimen after this final test.

Figure 86 : Failed -55C Tensile Test Specimen, 90$^{\mathbf{o}}$ Fiber Orientation

The next figure shows a close up view of the specimen's failure region.
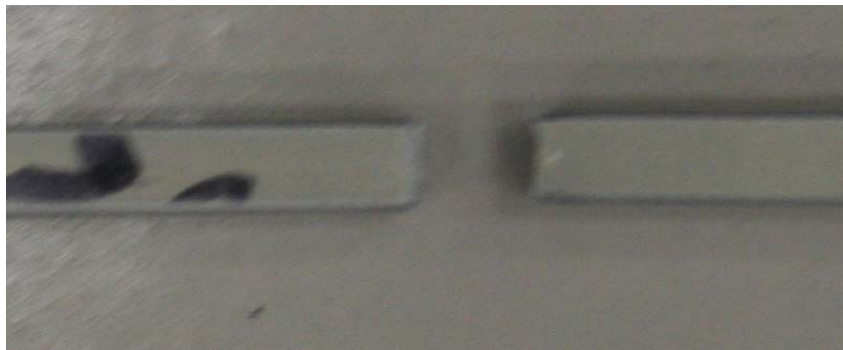
Figure 87 : Failure Region of Failed -55C Tensile Test Specimen, 90$^{\mathbf{o}}$ Fiber Orientation

It is seen for this failure, just as with both the room and elevated temperature 90$^{\mathbf{o}}$ specimens, failure occurred along a line with an angle equal to that of the fiber orientation.

Combined Decreased Temperature Specimen Results.

To evaluate the effect the fiber angle has on the overall behavior for the laminate, each of the stress-strain curves can be superimposed onto the same graph. As done with the overall room temperature and elevated temperature evaluation, examining the general trend of each specimen's stress-strain curve provides valuable insight into the dependence its material behavior has upon the temperature and fiber angle.

The figure below shows a side-by-side comparison of each of the specimens tested at room temperature. The specimens are arranged, from top to bottom, in order to increasing fiber angle: 0⁰, 45⁰, 67.5⁰, and 90⁰.

Figure 88 : Comparison of -55C Tensile Specimens

The following figure shows each specimen's stress-strain curve superimposed on one chart.
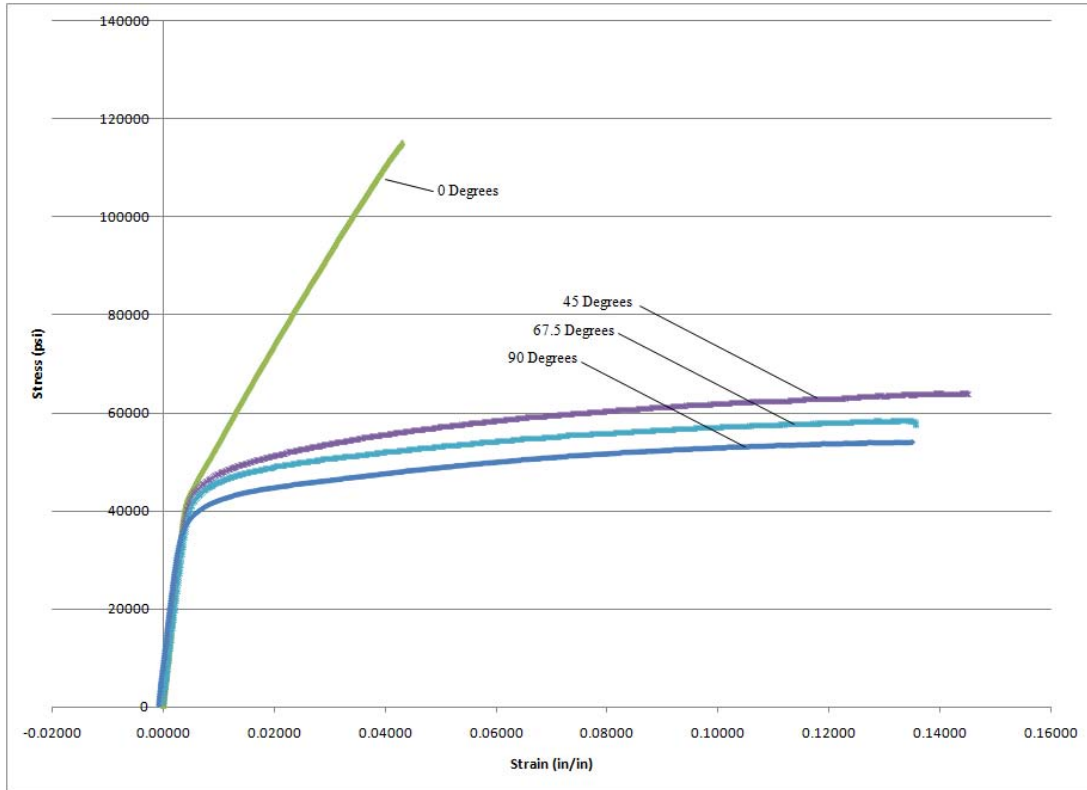
Figure 89 : -55C Stress-Strain Curves

Examination of this chart immediately shows the clear effect fiber orientation has on the laminate tensile strength. In contrast to the elevated temperature test, the results for the reduced temperature test agree with the applicable theory governing laminated plates. This is seen in that the 0° specimen exhibits the highest ultimate tensile strength, as all of its fibers are oriented parallel with the loading direction and the 90° specimen shows the smallest magnitude of ultimate tensile strength, as all of its fibers are perpendicular to the loading direction. Following this theory, the 45° specimen exhibits a greater ultimate strength than the 67.5^o specimen. The magnitude of strain is also of importance. Note the relatively small strain to failure exhibited by the 0° specimen. The small strain to failure associated with this specimen is due to the fibers running parallel to the direction of load.

172

Conversely, the off-axis specimens are shown to demonstrate the influence of matrix in the loading direction through the additional strain accumulation.

The following figure shows the comparison between each of the test's experimental elastic moduli.
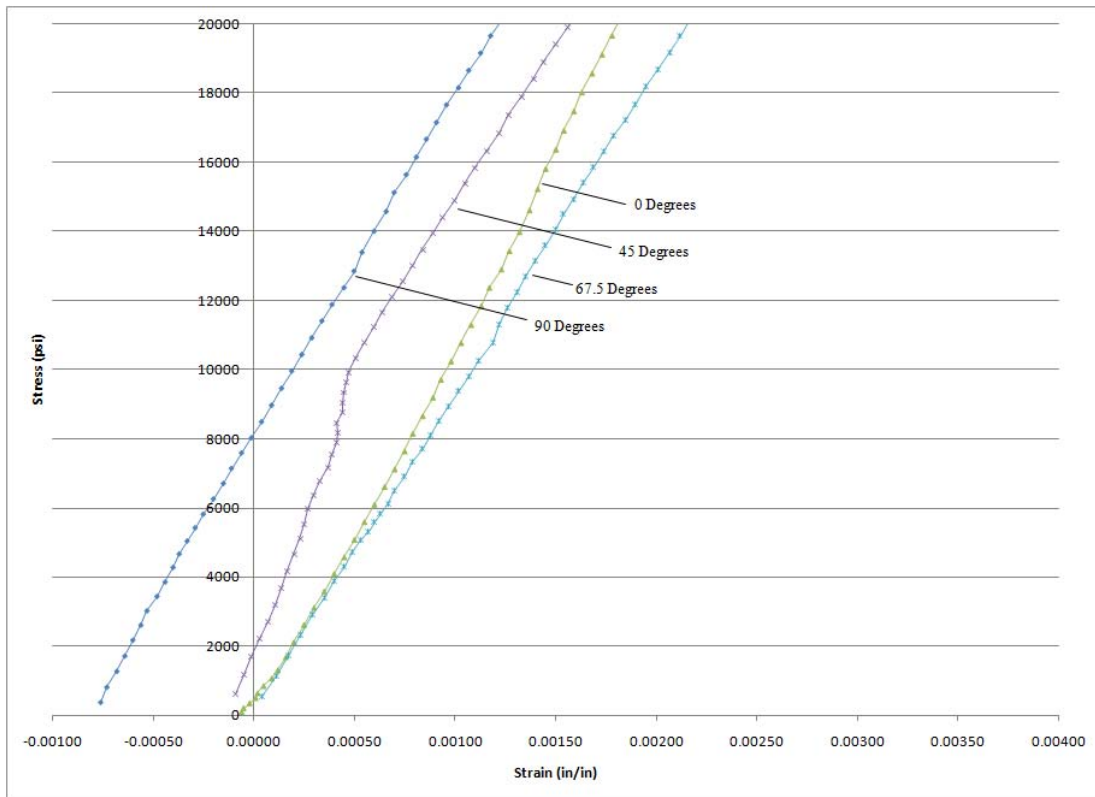
Figure 90 : -55C Stress-Strain Elastic Regions Used for Modulus Calculation

Similar in scope to the elevated temperature tests, this figure shows that there is slight residual thermal strain remaining for the 90 specimen. While not as large in magnitude when compared to the higher temperatures tests, the elastic modulus curves for each of the tests should begin at the axis system's origin. Further, note the relative consistency seen with each fiber orientation's modulus curve. While the different fiber orientations certainly exhibit differing modulus magnitudes, changes in this fiber angle do not show any serious degradation in this property.

173

Overall Dogbone Tensile Testing Results.

While it is certainly of use to examine the stress-strain curves for each temperature test on the same graph to investigate the effects of fiber orientation on mechanical properties, it is also of interest to study the mechanical properties as functions of fiber angle and temperature.

The first figure compares the elastic modulus at all three temperatures to the fiber orientation angle. It is important to note how, along with the theoretical prediction, both of the experimental modulus results are also shown. This includes the average moduli obtained through performing the dedicated modulus experiments and the moduli determined at the conclusion of the tensile tests.
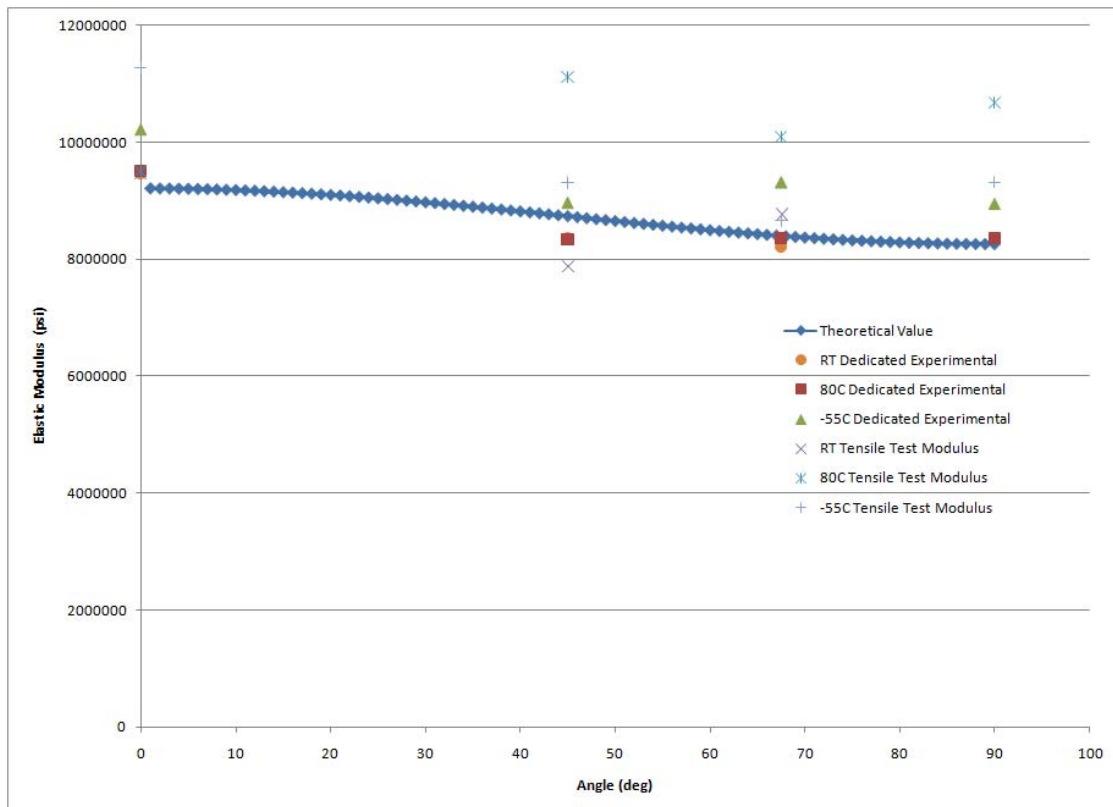

Figure 91 : Overall Modulus Comparison

The theoretical elastic modulus values for CentrAl are clearly marked in this figure. When developing the theoretical curve, as shown in the section "Theoretical Development", no provisions have been made to account for a temperature differential. Thus, the theoretical curve shown above is that for a room temperature elastic modulus curve. Any deviation from this curve would give an indication to the laminate's stiffness at the respective temperature.

Immediately obvious when examining is this chart is the apparent anomaly occurring with the elevated temperature elastic modulus values. As previously discussed, as the temperature is increased, the matrix material tends to plasticize, thus allowing additional strain and reduced brittleness. At the conclusion of the elevated temperature experiments, quite the opposite was observed. This is shown with the modulus values for the higher temperatures greatly exceeding that of both the theoretical and other experimental results. While the tensile tests appear to be in error, the modulus values seen during the dedicated modulus testing seem to show a slight reduction in magnitude across the entire spectrum of fiber angles. This agrees with the results show in [5]. The degree of the "knockdown" exhibited from the experimental data is not as great as that shown in [5] because the amount of aluminum in CentrAl is greater than that used in traditional GLARE, the material studied as part of said research.

It is also noteworthy that for each of the test procedures taking place at the decreased temperature of -55C, the modulus values are consistently higher than that of the predicted room temperature value. Again, this agrees with the results shown in [5]. Recall the explanation surrounding this property change. The matrix material, being more sensitive to the reduced temperature, becomes stiffer at the reduced temperature. This

stiffness increase is more apparent in the off-axis specimens as the fiber orientation lends itself to being dominated more so by the matrix than the glass fibers.

The overall experimental trend is also shown to coincide with the variance the theoretical values exhibit as a function of fiber angle. This gives confidence to the applicable metal volume fraction approach shown to provide an estimate to the laminate's modulus of elasticity.

Continuing, the next figure shows the overall comparison of the laminate's ultimate tensile strength.
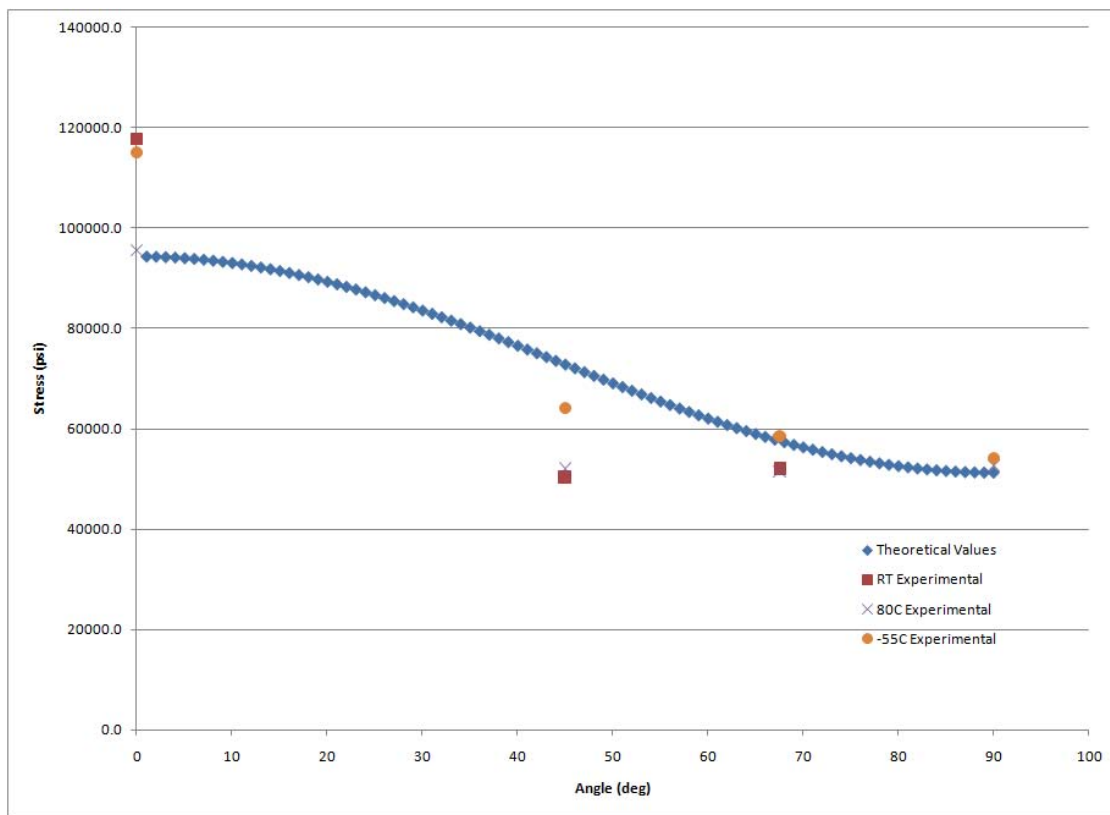

Figure 92 : Overall Ultimate Tensile Strength Comparison

First, notice the trend the experimental values tend to follow. While not necessarily equal in magnitude to the room temperature theoretical values, the

experimental results show a similar behavior of variance across the entire range of fiber angles.

Also of interest is that same behavior seen with the reduced temperature testing. The overall magnitude for the ultimate tensile strength appears to be closest to the theoretical predictions, even when compared to the room temperature values. This is especially true for the off-axis fiber angles. For design purposes this could hold merit, as the metal volume fraction technique used to predict the ultimate tensile strength, has been shown to hold a relative degree of accuracy to that seen in the laboratory under the reduced temperature environment.

Again, ignoring the apparent error seen with the elevated temperature testing, the increase in ultimate tensile strength seen with the reduced temperature over that of the elevated temperature coincides with the applicable theory. Following the same underlying principle for the increase in modulus over the room temperature values, the reduced temperature ultimate tensile strength is also shown to increase.

Next, the figure below shows the overall relationship seen with CentrAl's yield strength.
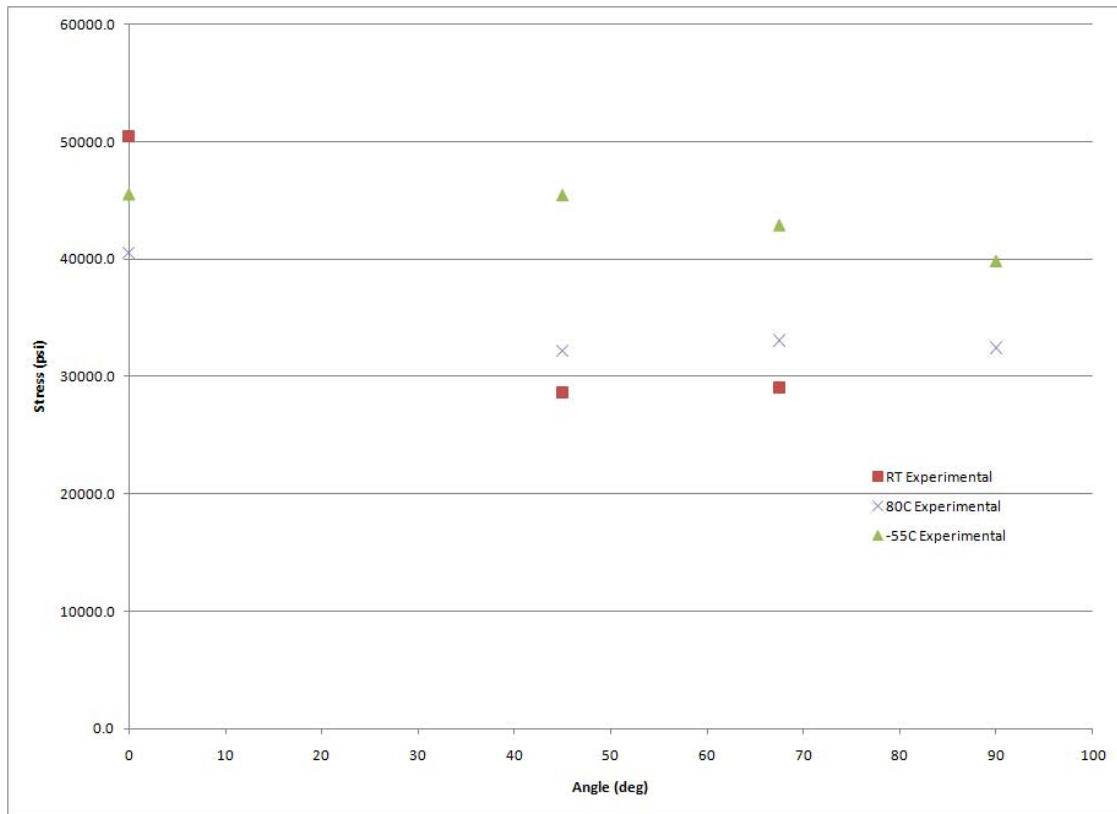
Figure 93 : Overall Yield Strength Comparison

From the above figure, it is clearly seen how temperature plays a significant role in affecting CentrAl's yield strength. Again, especially noticeable with the off-axis specimens, due to their large matrix influence, the yield strength of the reduced temperature specimens exceeds that of the corresponding room temperature specimens. This is caused from the colder temperatures causing excessive brittleness in the matrix material. This observation is more clearly seen in the figures detailing the stress-strain curve comparisons for each temperature, with constant fiber angles.

The first of these figures is for a constant 0° fiber angle. The stress-strain curve for each temperature test is shown on this same graph.

Figure 94 : Overall Stress-Strain Curves, 0° Fiber Orientation

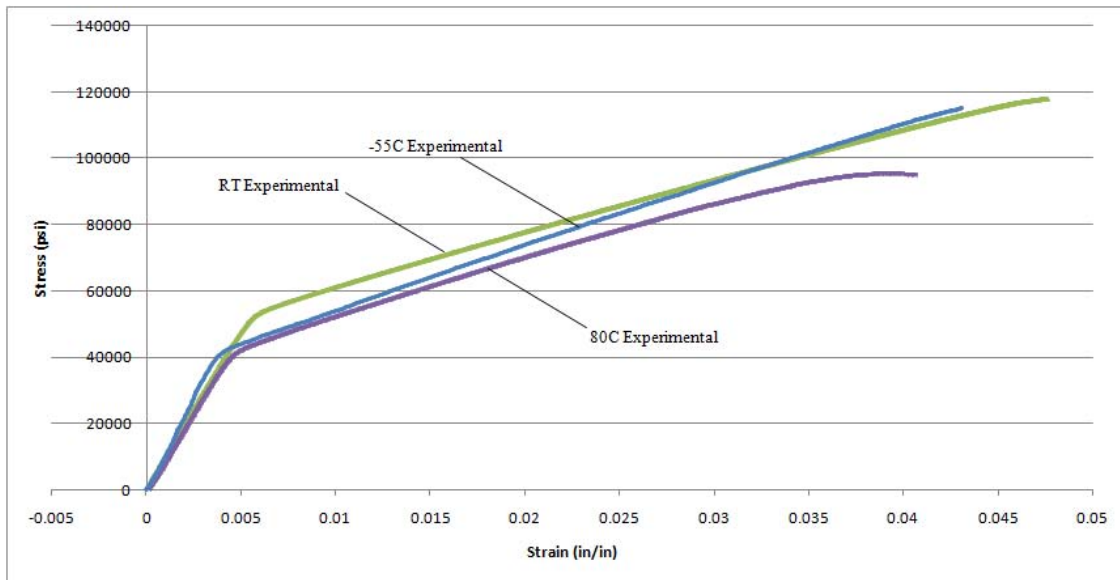In this curve, all the fibers are aligned parallel to the loading direction. Thus, the matrix material, while still viable, plays less of a role in this direction, than in the off-axis specimens. With this curve, the room temperature curve is shown to exhibit not only the greatest yield strength but also the greatest ultimate strength and strain to failure. The reduced temperature stress-strain curve is shown here to exhibit the greatest elastic modulus. While not dominated by the matrix, the 0° fiber orientation is still shown to stiffen at this reduced temperature. Arguably the most important aspect of the data presented in this graph is the lack of any serious deviation from the baseline room temperature stress-strain curve. It is true there is doubt to the accuracy of the elevated temperature results, however, with the results collected, the laminate can be said to exhibit relatively stable thermal behavior in the 0° fiber orientation.

The next figure, each of the stress-strain curves collected for the 45° fiber orientation is shown.
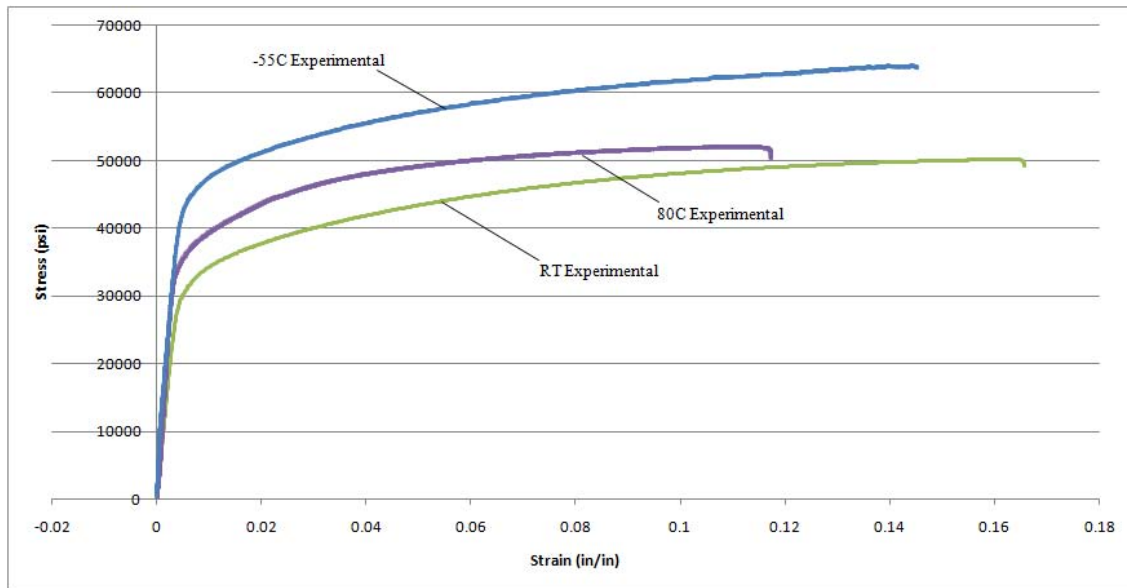
Figure 95 : Overall Stress-Strain Curves, 45° Fiber Orientation

Here, the apparent error with the elevated temperature testing is seen. This is shown as the increased strength the laminate exhibits at the higher temperature than at the initial, room temperature test. It is also seen how the reduced temperature testing reveals a slight strength increase at this 45° fiber direction. This could be caused by the increased stiffness exhibited by the matrix material at this colder temperature. Also noteworthy is the increased yield strength shown at the reduced temperature. The overall difference between the yield strength and ultimate strength is reduced at the lower temperature than is seen in the room temperature results. Emulating the overall relationship seen with the 0° results, the results from testing the 45° specimens do not deviate a great deal from one another. The increased stiffness, shown by the cold test specimen, could be especially useful for design purposes. At altitude, wherein the air temperature is equal to that seen in the reduced temperature testing, the laminate's strength property increases.

The next figure shows the same results as in the previous two figures, except the fiber angle is 67.5°.
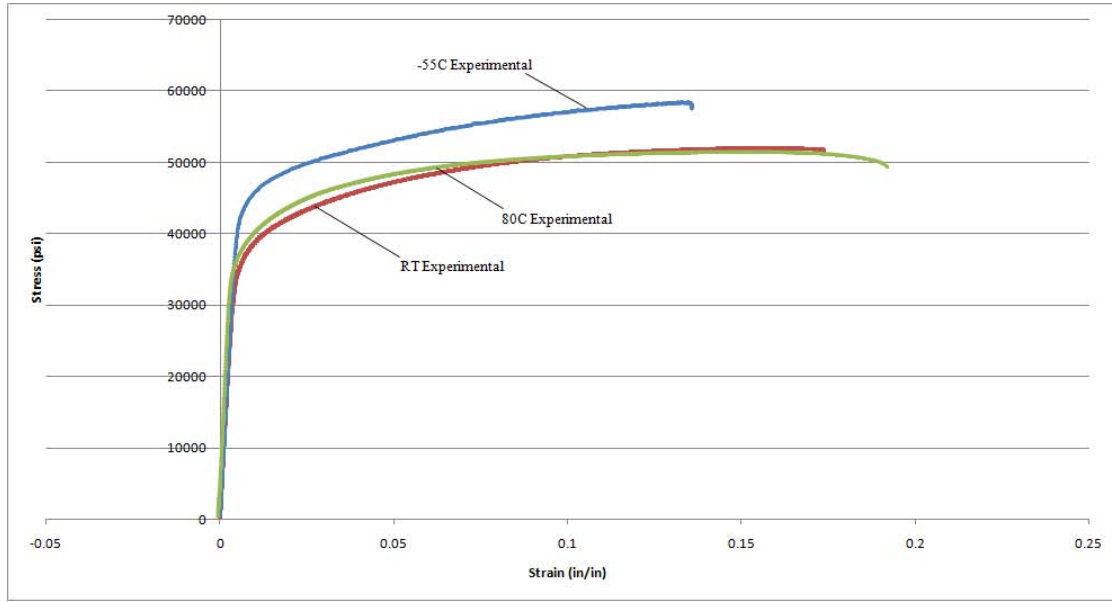
Figure 96 : Overall Stress-Strain Curves, 67.5⁰ Fiber Orientation

From this graph, it is shown how the laminate at the reduced temperature clearly exhibits

greater strength properties than that seen at both the room temperature and elevated

temperature results. Note the difference in the ultimate tensile strength values seen

between the reduced temperature tests results for the 45⁰ specimen and this 67.5⁰. The

ultimate tensile strength in this figure shows a marked decrease when compared to the

same curve in the previous figure. This is caused by the reduction of fiber in the loading

direction; the load path is more dominated by the matrix material in this 67.5⁰ specimen.

Despite the error associated with the elevated temperature testing, very little variance is

seen amongst each of the stress-strain curves. Theory, along with the results from

previous research states that the elevated temperature mechanical properties should be

reduced, especially at the off-axis fiber angles, because of the additional influence the

matrix material has in the load path.

The final figure below shows the same information, but for the 90⁰ fiber angle.
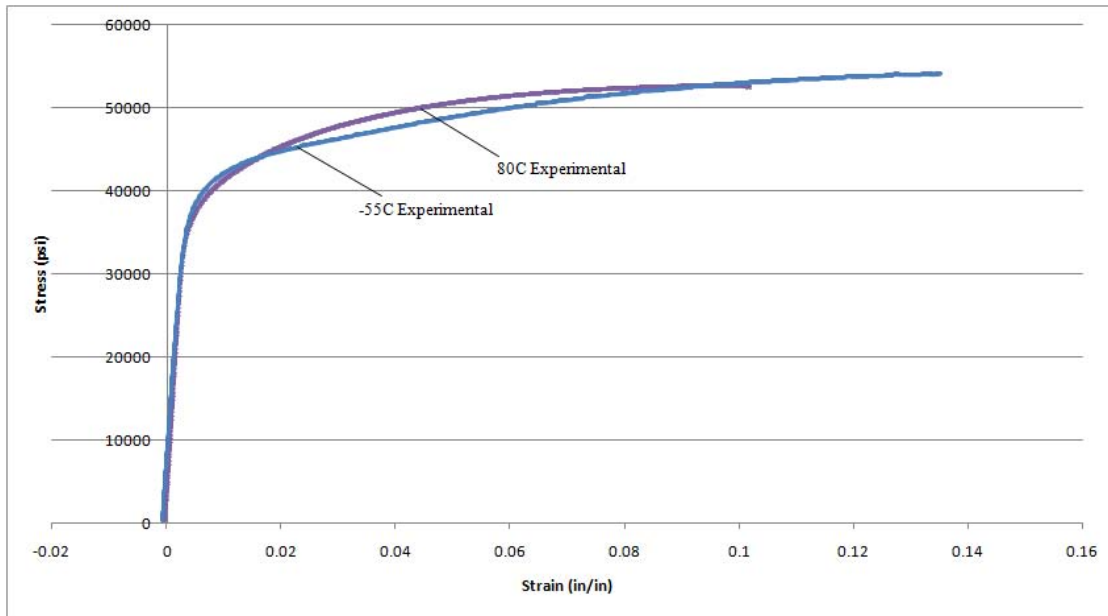
Figure 97 : Overall Stress-Strain Curves, 90° Fiber Orientation

Immediately obvious on this figure is the absence of a room temperature stress-strain curve. Recall that from a data collection error, no room temperature data was recorded for the 90° specimen. In this fiber orientation, the matrix entirely dominates the failure mechanism as no fibers are aligned parallel to the loading direction. Once more, the experimental error is seen in that the elevated temperature results show a general increase in strength over that of the reduced temperature results. This strength increase is especially prominent in the inelastic region of the material's stress-strain curve. Additionally, an increased strain to failure should be seen with the elevated temperature results as the increased temperature allows the matrix dominated cross section to yield further before failure.

Monotonic Blunt Notch Tensile Testing Results

Similar in scope in reporting the results from the dogbone tensile tests, the blunt notch test results will be shown via stress-strain curves and percentage differences compared to the baseline room temperature values. As with the initial un-notched tensile

182

tests, the blunt notch strength tests give great insight as to the strength and behavior of a material. In the case of the blunt notch stress-strain curve, it can be argued that the results are more pragmatic as rarely does material exist in a structure without the presence of some sort of a hole or other void.

Analogous to the dogbone tensile testing, single specimens were pulled to failure as described in the "Experimental Procedures" section. Though in the blunt notch study, rather than single specimens used for each fiber orientations, as many as three specimens were tested. This gives greater confidence into the results and information gleaned from the testing procedure. Again, just as with the initial dogbone tensile tests, the blunt notch tests were conducted at three temperatures: room temperature (23C), 80C, and -55C.

From these blunt notch strength stress-strain curves, information to include the elastic modulus (stiffness), ultimate tensile strength, and yield strength can be determined. For the sake of correctness, the term "stiffness" will be used in lieu of elastic modulus for the blunt notch specimens. While the elastic, or Young's, modulus is a viable material property, simply adding a stress concentration does not alter the laminate's physical properties. The stress concentration serves to provide an indication of the laminate stiffness in the presence of this anomaly.

Additionally, from these curves, comparisons can be made to the elastic moduli found in the previous elastic modulus tests. Also comparisons can be made to the original dogbone tensile tests. This will show any change in material behavior due the presence of the hole.

Blunt Notch Specimen Geometry Development Results.

Recall, however, how an iterative approach to designing the blunt notch specimen was taken as unexpected specimen failure had occurred. Reference the section "Blunt Notch Specimen Geometry Development" and the associated Figure 40 : Initial Blunt Notch Specimen Design. The initial design was simply to place a hole at the center of the gauge section. This specimen ultimately failed at the mounting bolt hole. The following two figures show the specimen failures.
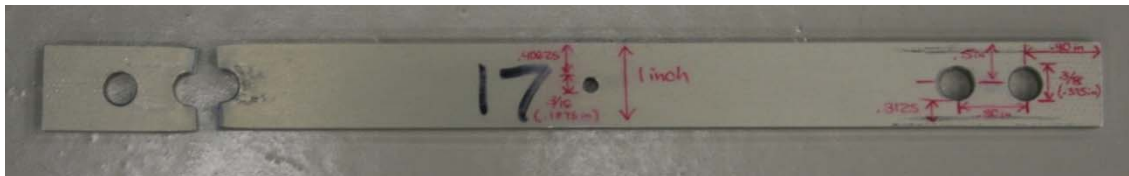

Figure 98 : Failed Blunt Notch Design Specimen 1

Note the obvious hole elongation in the failure region. Specimen 17 has fiber oriented at 0°, which was parallel to the loading direction.

Despite the apparent experimental failure, positive information is still gleaned from this specimen. Because of the hole elongation, an obvious material bearing failure occurred. This is typical behavior of monolithic metals in which the area immediately surrounding a bolt hole will yield prior to failure. This failure mechanism actually aids in inspection, as a sheet material showing signs of bearing failure is much easier to visually inspect than a material which has not deformed. Traditional composite materials, which tend to not dent or plastically deform before failure, are much more difficult to visually inspect for such an impending failure.

The next figure shows a close up region of the failed mounting bolt hole. This figure clearly shows the plastic deformation in the region immediately surrounding the hole.

Figure 99 : Failure Region for Failed Blunt Notch Design Specimen 1

Again, the next figure shows another failed blunt notch test specimen, also with fibers oriented at 0°. Notice once more the prominent area of plastic deformation immediately surrounding the mounting bolt hole.
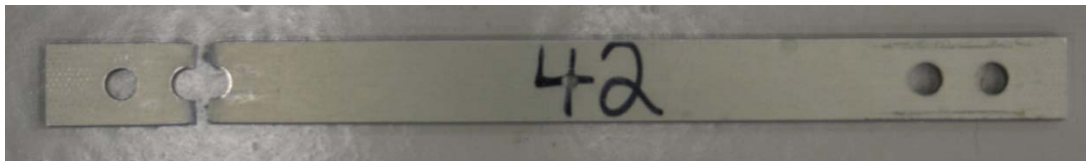

Figure 100 : Failed Blunt Notch Design Specimen 2

Figure 101 : Failure Region for Failed Blunt Notch Design Specimen 2

After evaluating the specimen geometry with respect to specific stress concentration information, the final specimen shape was determined. The final design is shown in Figure 8 : Blunt Notch Specimen. The figure below shows the failed specimen using this geometry.
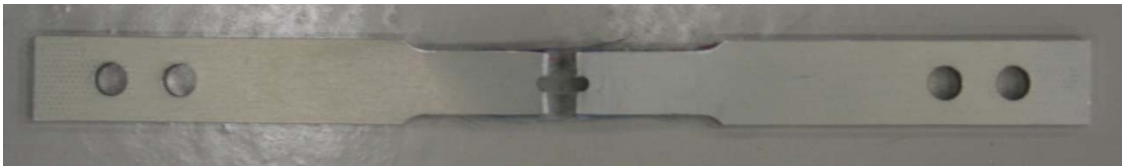
Figure 102 : Failed Blunt Notch Design Specimen 3

Note the desired region of failure in the gauge section at the hole. There is no observed plastic deformation in or around the mounting bolt holes. All yielding is concentrated in the vicinity of the central gauge section hole. The next figure shows the failure region up close.
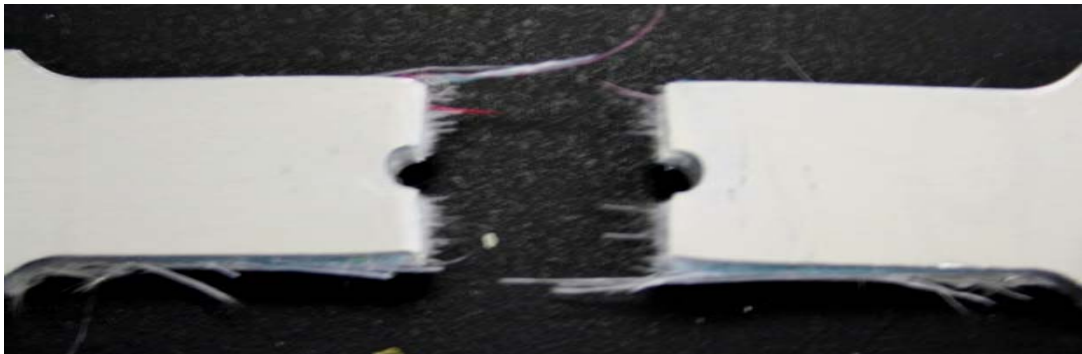
Figure 103 : Failure Region for Failed Blunt Notch Design Specimen 3

This specimen, at a fiber angle of 0°, shows an excessive number of broken glass fibers in the failure region. The following figure provides an additional perspective on the failure region.
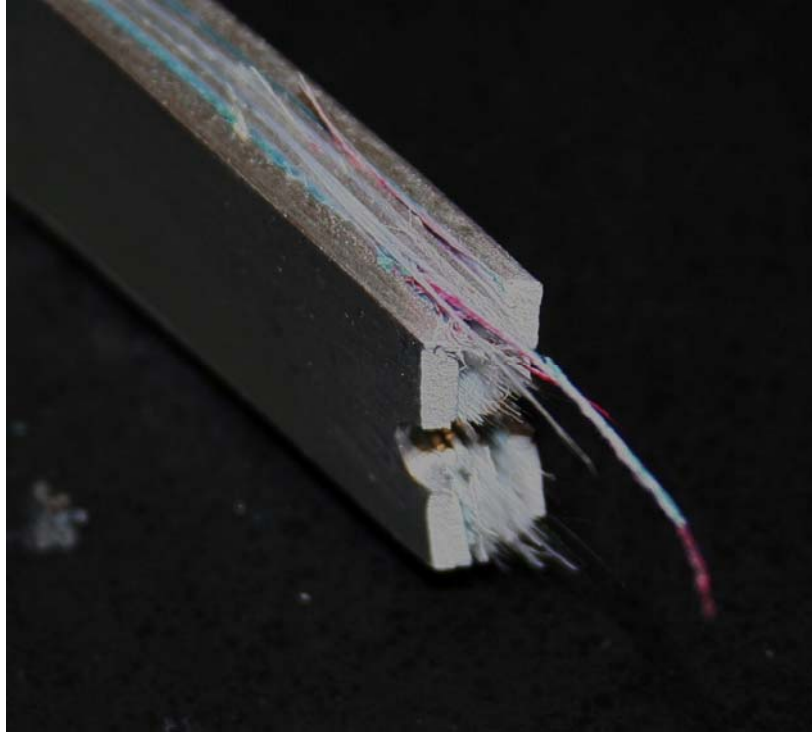
Figure 104 : Another View of Failure Region for Failed Blunt Notch Design Specimen 3

Before continuing, an additional specimen was machine to the same specifications. The

next figure shows the specimen after the room temperature test. Just as with the first

successful trial, note that all material failure is restricted to the gauge section, in the

immediate vicinity of the hole.
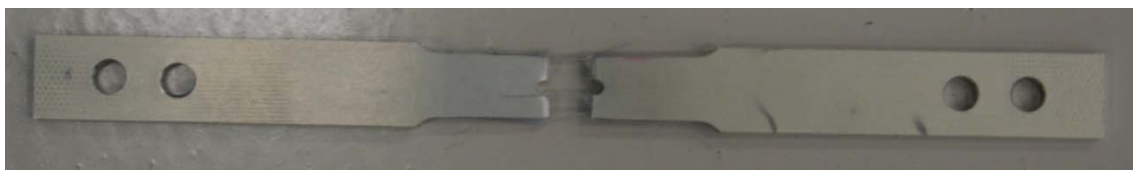
Figure 105 : Failed Blunt Notch Design Specimen 4
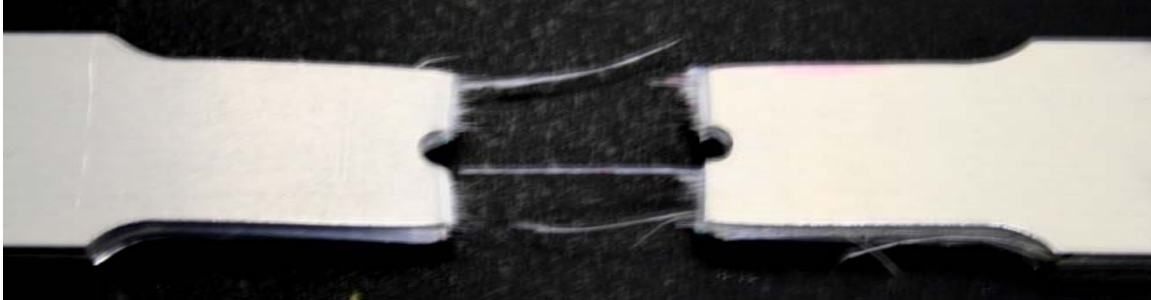
Figure 106 : Failure Region for Failed Blunt Notch Design Specimen 4

With this series of successful testing, the resulting data produced stress strain curves

which provide useful data. The next figure depicts the stress-strain curves for these two

tests.
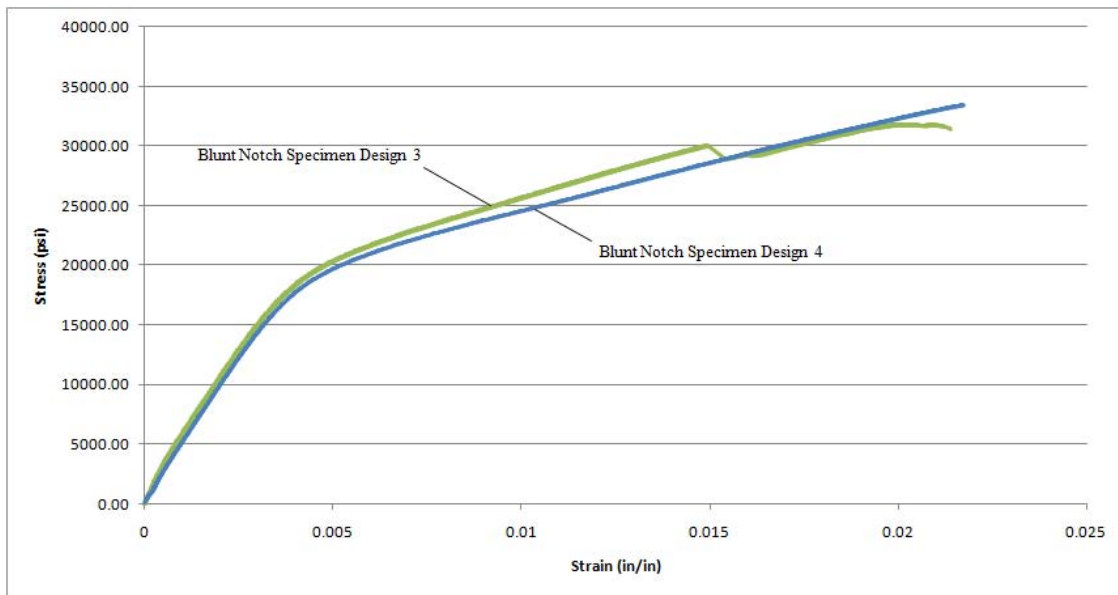
Figure 107 : Blunt Notch Specimen Design Stress-Strain Curves, 0° Fiber Orientation

Just as with the resulting stress-strain curves for the dogbone tensile tests, critical

information can be gleaned from the blunt notch stress strain curves. Though these tests

were merely trial runs to evaluate the specimen design, the results are still viable as part

of the research efforts. The following table details this information.

188

Table 105 : Results from Blunt Notch Design Trial Tests, 0° Fiber Orientation

	Elastic Modulus (Msi)	UTS (ksi)	Y (ksi)	$\varepsilon_{failure}$ (in/in)
Design 3	4.982	31.79	22.29	0.02138
Design 4	4.817	33.43	21.15	0.02173
Average	4.900	32.61	21.72	0.02156

Because of the relative consistency with these two trial tests, the remaining specimens could be machined and the testing procedure begun.

Room Temperature Results.

Again, the room temperature results were first determined in an effort to establish the laminate's baseline blunt notch properties. These are needed in an effort to establish any sort of property dependence on the temperature variable. Naturally, fiber orientation also plays a role in property variance.

In contrast to the dogbone tensile tests, several specimens were available at each fiber orientation for evaluation. Subsequently, the tables shown have the stress-strain curves for each specimen superimposed.

The following figure depicts the stress strain curves generated from the room temperature specimens with fibers oriented at 0°.
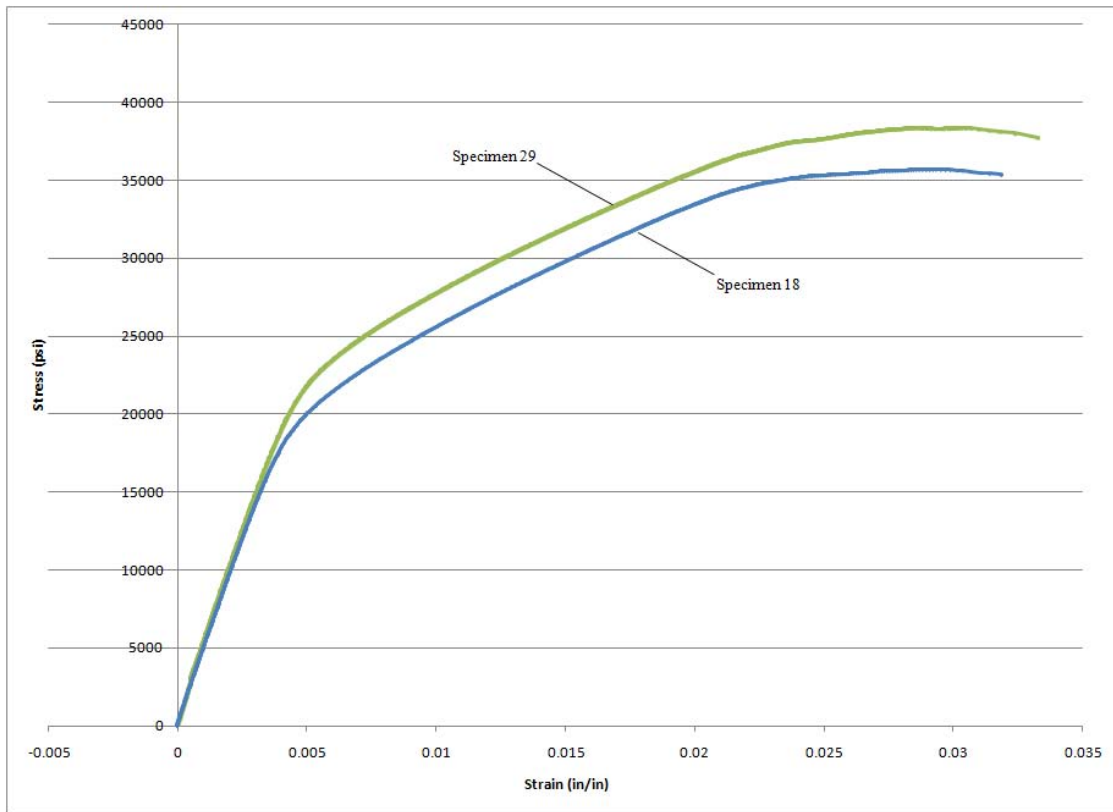
Figure 108 : RT Blunt Notch Stress-Strain Curves, 0° Fiber Orientation

From these curves, the following table is produced showing the resulting data.

Table 106 : RT Blunt Notch Results, 0° Fiber Orientation

	Elastic Modulus (Msi)	UTS (ksi)	Y (ksi)	$\varepsilon_{failure}$ (in/in)
Specimen 18	4.693	38.33	24.04	0.03327
Specimen 29	4.502	35.69	22.31	0.03184
Average	4.598	37.01	23.18	0.03256

Since multiple specimens were evaluated at this 0° fiber orientation, an average value

was taken. This value will be compared to the room temperature monotonic tensile results

for the same fiber orientation. The next table shows this comparison.

Table 107 : RT Dogbone Tensile to Blunt Notch Comparison, 0° Fiber Orientation

	Elastic Modulus (Msi)	UTS (ksi)	Y (ksi)	$\varepsilon_{failure}$ (in/in)
RT Dogbone	9.461	117.82	55.67	0.04761
RT Blunt Notch	4.598	37.01	23.18	0.03256
Percent Difference	51.40	68.59	58.36	31.61

As evident from this initial blunt notch test, it is seen that the ultimate tensile strength decreased by approximately 69%. Also noteworthy, along with the reduction in the ultimate tensile strength, the yield strength is also affected. The yield strength is reduced by 58% when compared to the un-notched value. Further, the reduction in the ultimate strain to failure is of the order of 32%. The laminate's overall stiffness, as indicated by the original, un-notched value for the elastic modulus, is shown to decrease by 51%.

    The actual specimens tested are shown in the figure below.
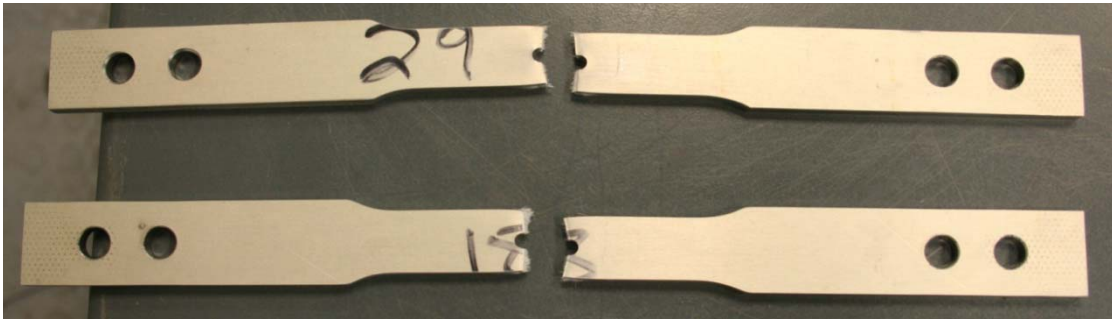
Figure 109 : Failed RT Blunt Notch Specimens, 0° Fiber Orientation

In contrast to dogbone tensile specimens tested, the blunt notch specimen ultimately failed into two separate pieces. Despite the decrease in the overall strength capability, the stress induced within the failure region was substantial enough to cause complete specimen separation. The next figure shows a close up view of the failure region for specimen 18; similar behavior is seen on specimen 29.
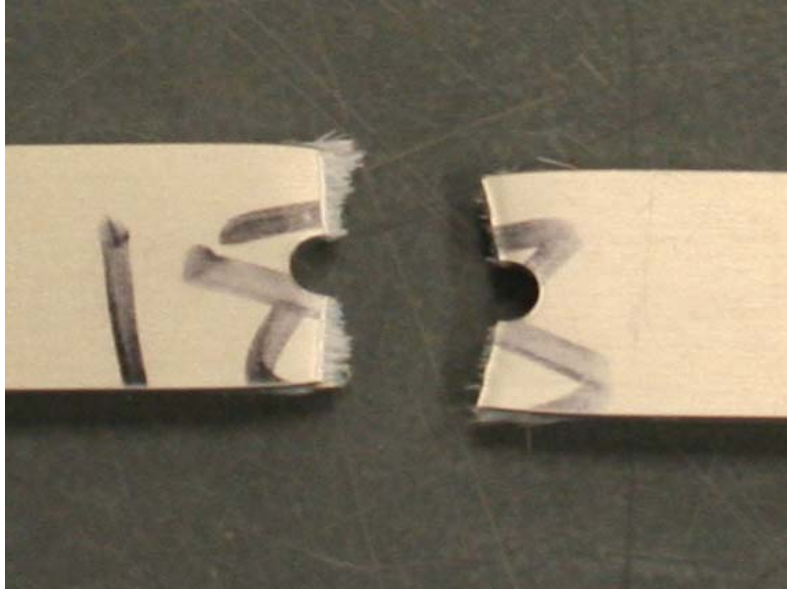
Figure 110 : Failure Region for Failed RT Blunt Notch Specimens, 0⁰ Fiber Orientation

Figure 111 : Another View of Failure Region for Failed RT Blunt Notch Specimens, 0⁰ Fiber Orientation

The second test in the blunt notch procedure involved using specimens with fibers

oriented at 45⁰. The next figure shows the stress-strain curves created from these tests.
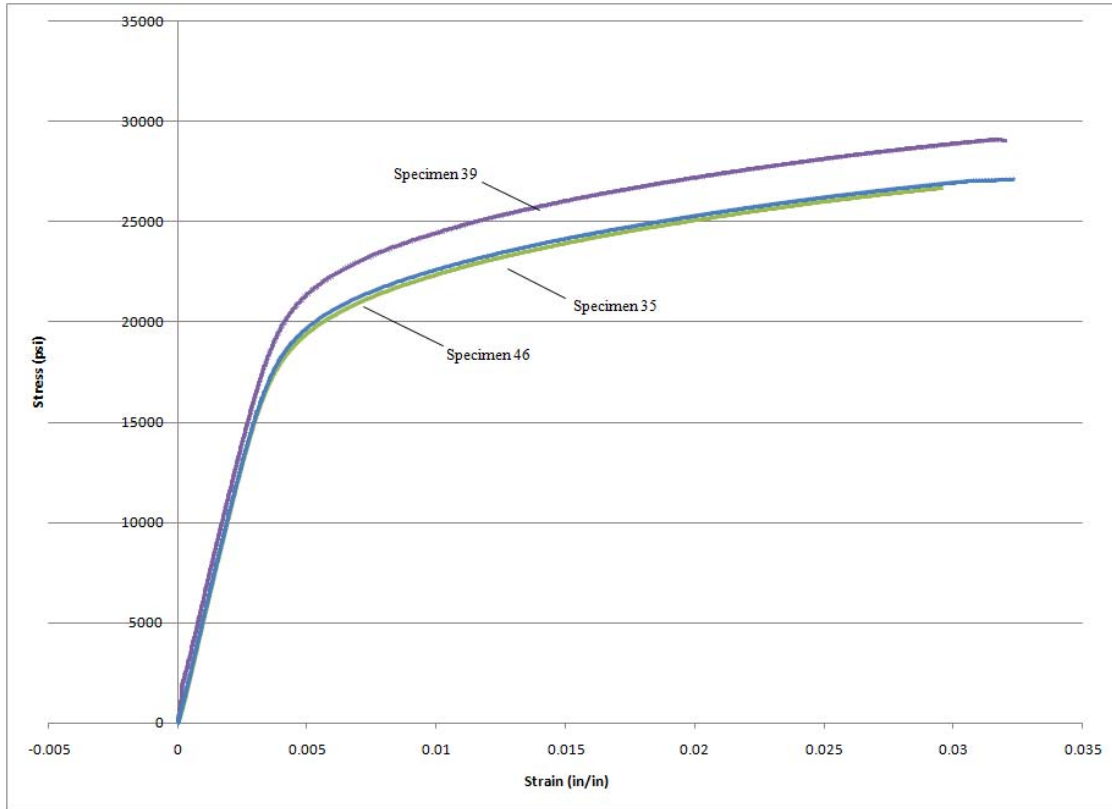
Figure 112 : RT Blunt Notch Stress-Strain Curves, 45$^{\mathbf{o}}$ Fiber Orientation

From these curves, the following table is produced showing the resulting data.

Table 108 : RT Blunt Notch Results, 45$^{\mathbf{o}}$ Fiber Orientation

	Elastic Modulus (Msi)	UTS (ksi)	Y (ksi)	$\varepsilon_{failure}$ (in/in)
Specimen 35	5.034	26.84	20.56	0.02961
Specimen 39	5.241	29.08	22.06	0.03199
Specimen 46	5.121	27.12	20.40	0.03246
Average	5.132	27.68	21.01	0.03135

From the tests conducted at the 45$^{\mathbf{o}}$ fiber angle, immediately noticeable is increase in

elastic modulus but decrease in ultimate tensile and yield strength values when compared

to those at the 0$^{\mathbf{o}}$ fiber orientation. This reduction in ultimate tensile and yield strength is

attributed to the increased influence the matrix material has on the specimen's loading

direction. While in the 0$^{\mathbf{o}}$ orientation, the fibers virtually dominate the entire specimen

193

strength spectrum. At this first off-axis test, the influence of the matrix is clearly shown. Interestingly enough, it is seen how the strain to failure for the off-axis specimen is actually lower than that seen with the 0° specimen. While the 45° dogbone tensile specimen showed an increase in ultimate failure strain, this 45° blunt notch specimen showed quite the opposite. One explanation for the decrease in failure strain for the off-axis specimen stems from the dominance the matrix has with these fiber orientations. Because the localized stresses are much higher, in the presence of such a large stress concentration, this more matrix dominated gauge section fails at a lower strain value.

And once again, the next table takes these average values and provides a direct comparison to the dogbone tensile specimen at the same fiber orientation.

Table 109 : RT Dogbone Tensile to Blunt Notch Comparison, 45° Fiber Orientation

	Elastic Modulus (Msi)	UTS (ksi)	Y (ksi)	$\varepsilon_{failure}$ (in/in)
RT Dogbone	7.887	50.25	31.22	0.16567
RT Blunt Notch	5.132	27.68	21.01	0.03135
Percent Difference	34.93	44.92	32.70	81.08

Similar to the results shown with the 0°, a decrease in stiffness occurred when comparing the initial tensile dogbone specimen elastic modulus to that of the blunt notch test. It is seen how, in the presence of a hole, the structural stiffness decrease by approximately 35%. A 45% decrease in UTS is realized, along with a nearly 33% reduction in yield strength. Again note how the strain to failure with the blunt notch specimen is more than 5 times less than its intact counterpart. This is due to the excessive stress induced at the hole, causing the more matrix dominated cross section to fail sooner.

The next figure shows the 45° blunt notch specimens after the testing procedure.
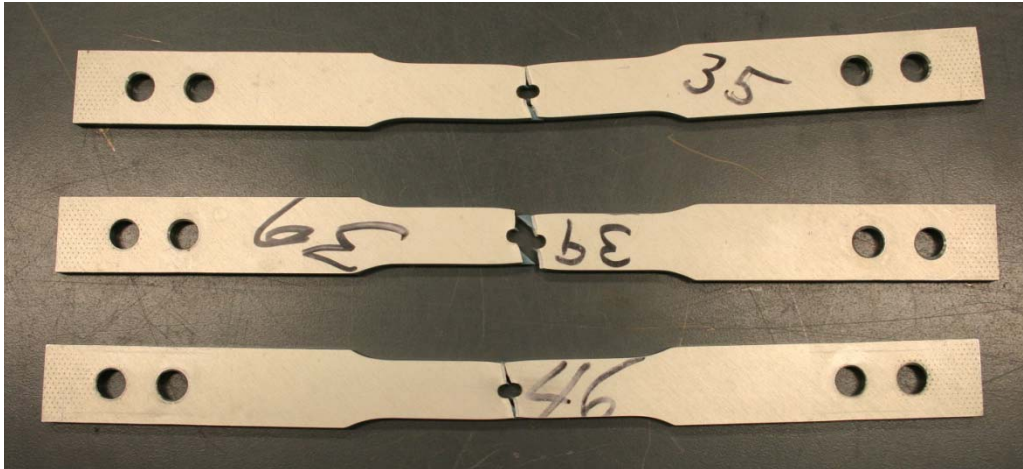
Figure 113 : Failed RT Blunt Notch Specimens, 45° Fiber Orientation

Note in the following figures, the familiar failure mechanism which was seen with the 45° dogbone specimens is seen once more with the blunt notch specimens. Failure occurs along an angle equal to that of the fiber orientation. The close of views of the failure regions clearly show this behavior, in addition to the localized yielding occurring at the central gauge section hole.

Figure 114 : Failure Region for Failed RT Blunt Notch Specimen 39, 45° Fiber Orientation

The next figure shows the resulting stress strain curves generated from the room temperature specimens with fibers oriented at 67.5^o.
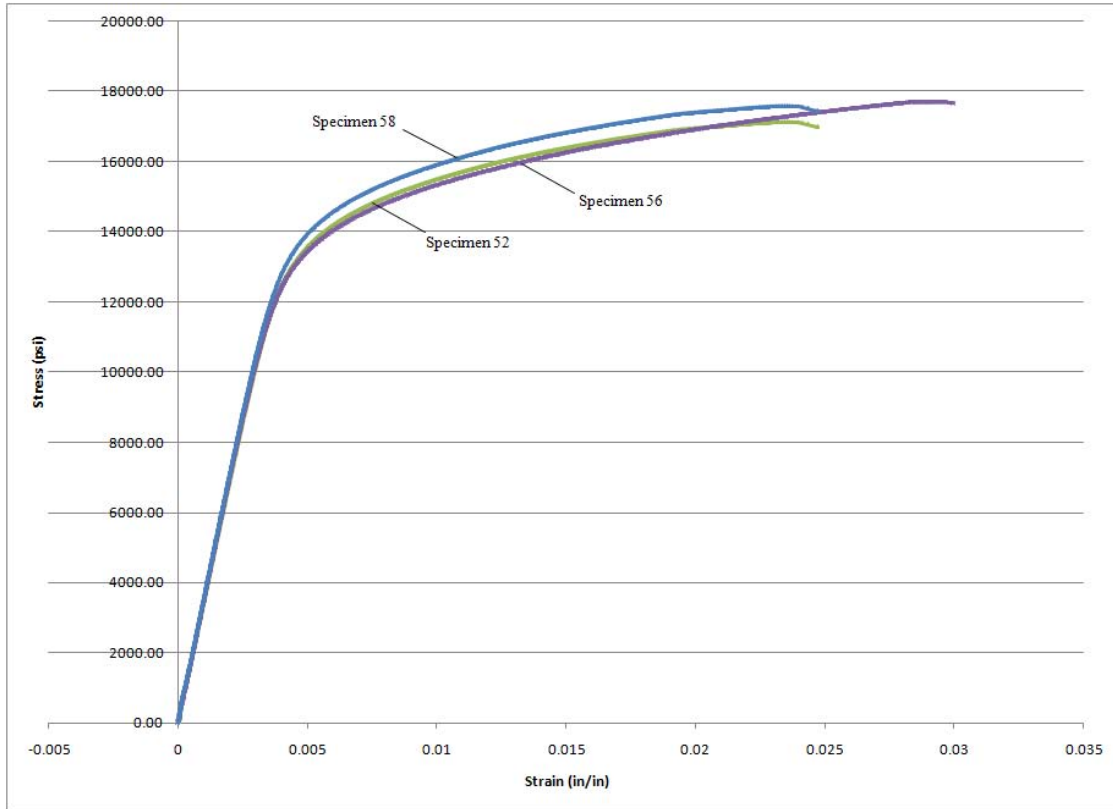
Figure 115 : RT Blunt Notch Stress-Strain Curves, 67.5^o Fiber Orientation

In following with the same analysis procedure, the next table shows the pertinent

information gleaned from this series of curves. Again, an average value is shown.

Table 110 : RT Blunt Notch Results, 67.5^o Fiber Orientation

	Elastic Modulus (Msi)	UTS (ksi)	Y (ksi)	$\varepsilon_{failure}$ (in/in)
Specimen 52	3.431	17.13	14.32	0.02521
Specimen 56	3.503	17.71	14.04	0.03019
Specimen 58	3.522	17.59	14.78	0.02521
Average	3.485	17.48	14.38	0.02687

Aside from the slight increase in stiffness seen with the 45° specimen, the general trend

of decreasing properties is seen here with the results from the 67.5^o specimen tests. This

general reduction trend is attributed to the additional matrix influence on the gauge

section strength. Because of the inherent weakness associated with the FM94K Adhesive

matrix material, and due the more influence the matrix has on the laminate strength at this

196

fiber orientation angle, the weaker the laminate will become. This is clearly seen here as the fiber approaches an angle closer to being normal to the load path.

The next table draws comparisons to the comparable room temperature dogbone specimen.

Table 111 : RT Dogbone Tensile to Blunt Notch Comparison, 67.5° Fiber Orientation

	Elastic Modulus (Msi)	UTS (ksi)	Y (ksi)	$\varepsilon_{failure}$ (in/in)
RT Dogbone	8.768	52.06	35.02	0.17361
RT Blunt Notch	3.485	17.48	14.38	0.02687
Percent Difference	60.25	66.42	58.94	84.52

As with the previous specimens, there is a decrease in the overall elastic modulus and hence structural stiffness with the presence of the hole. As seen with the 45° specimen, there is a drastic reduction in ultimate strain at failure with the 67.5° specimen as well. The laminate need not strain to such an extent to reach its ultimate tensile strength. It is seen that the strain at failure for the 67.5° blunt notch specimen is nearly 6.5 times less than that seen of its un-notched tensile test counterpart. The values for the ultimate tensile and yield strength value have also been substantially reduced due to the stress concentration.

The next figure shows the failed 67.5° blunt notch specimens.

Figure 116 : Failed RT Blunt Notch Specimens, 67.5° Fiber Orientation

The next figure clearly shows the failure, which occurs at the same angle as the fiber orientation. Notice how all yielding is localized to the gauge section hole.
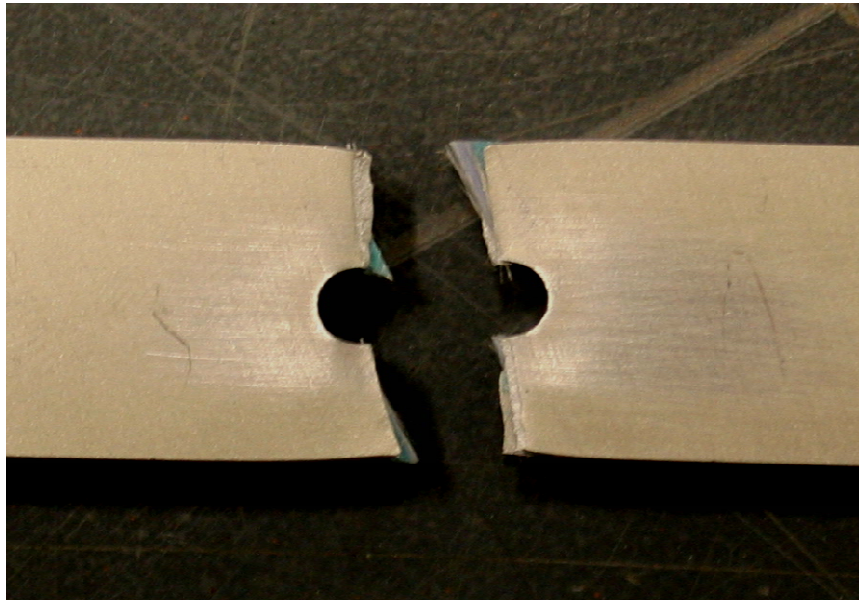

Figure 117 : Failure Region for Failed RT Blunt Notch Specimen 52, 67.5° Fiber Orientation

The final room temperature blunt notch specimens had fiber angles oriented perpendicular to the loading path, at 90°. The following figure shows the resulting stress-strain curves each of the tested specimens.
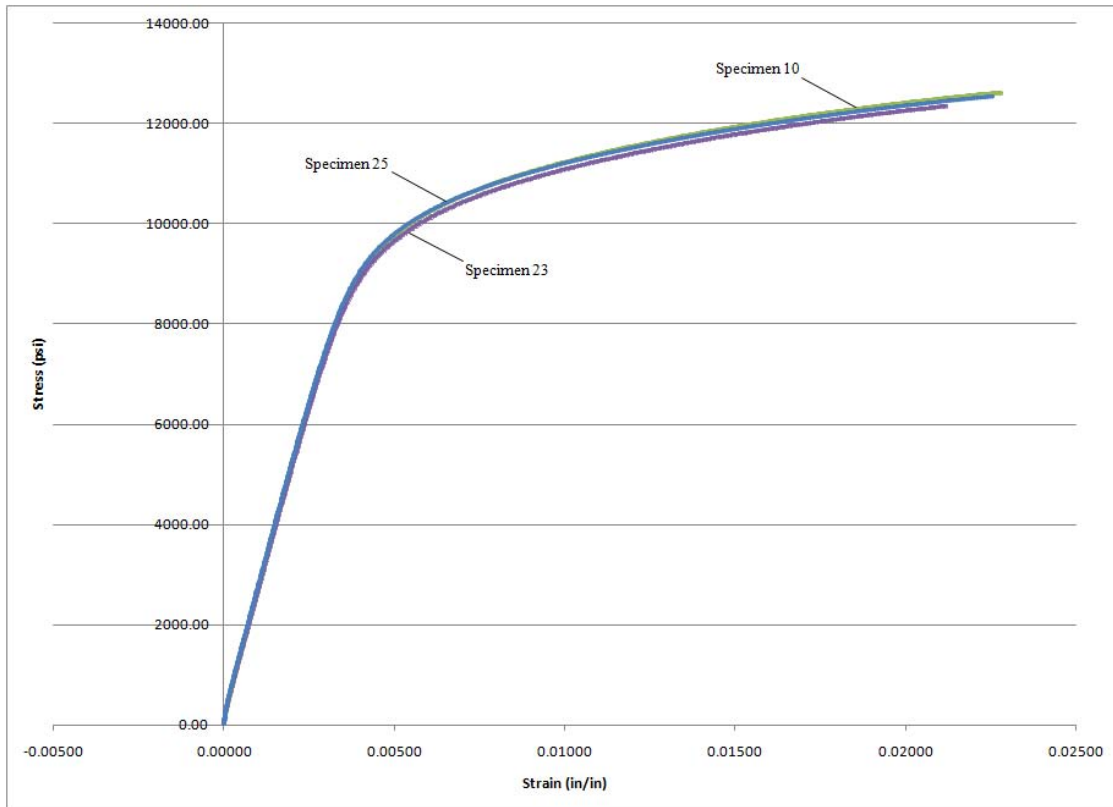
Figure 118 : Room Temperature Blunt Notch Stress-Strain Curves, 90° Fiber Orientation

And following, the next table gives the pertinent data gleaned from these curves.

Table 112 : RT Blunt Notch Results, 90° Fiber Orientation

	Elastic Modulus (Msi)	UTS (ksi)	Y (ksi)	$\varepsilon_{failure}$ (in/in)
Specimen 10	2.505	12.61	10.27	0.02289
Specimen 23	2.458	12.35	10.16	0.02125
Specimen 25	2.553	12.54	10.38	0.02265
Average	2.505	12.50	10.27	0.02226

This final room temperature blunt notch test shows the smallest magnitude in strength properties when compared to the other three fiber orientations. This is because in this fiber orientation, the fibers are placed completely perpendicular to the load path. The

199

entire specimen is dominated by the strength of the aluminum and matrix material. In this fiber orientation, the ability of the laminate to exhibit a large strain at failure is diminished.

Because of the error during data acquisition, there is no room temperature dogbone tensile stress-strain curve information. The following figure shows the specimens evaluated for the 90° fiber orientation blunt notch strength tests.
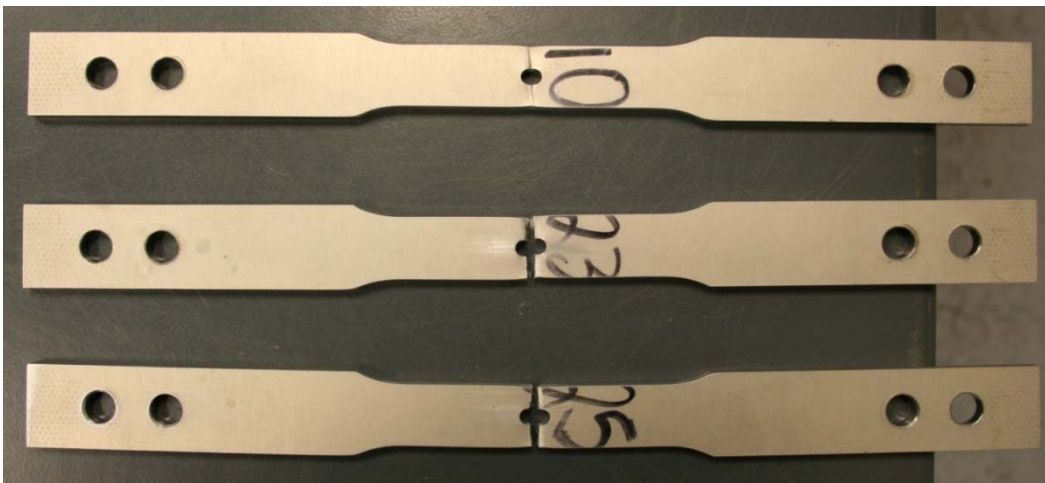
Figure 119 : Failed RT Blunt Notch Specimens, 90° Fiber Orientation

With these specimens, it is seen that specimen 10, upon failure, did not completely sever into separate pieces. While the center gauge section hole clearly yielded, the failure was more located beneath the surface of the outer aluminum layers. The following figure shows a close up view of the failure region for specimen 10.

Figure 120 : Failure Region for Failed RT Blunt Notch Specimen 10, 90° Fiber Orientation

From this view, failure is seen to be within the GLARE aluminum layers. The increased

yielding of these aluminum layers has caused the BondPreg® in the immediate vicinity to

delaminate. This is seen as the slight bulges found around the fractured aluminum.

Two specimens did fail into separate pieces. The next figure shows a close up of

specimen 23. This behavior is common for both specimens.
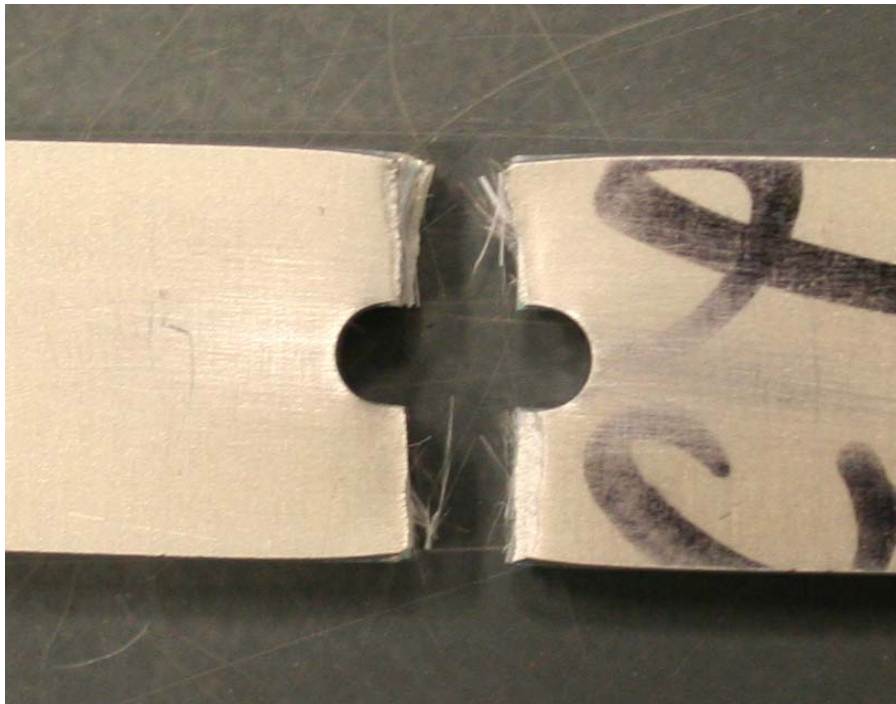
Figure 121 : Failure Region for Failed RT Blunt Notch Specimen 23, 90⁰ Fiber
Orientation

Elevated Temperature Results.

The elevated temperature results are performed in an effort to evaluate the

mechanical properties of the laminate under these conditions. While the elevated

temperature dogbone tensile tests provide baseline strength data, the blunt notch tests

provides a more realistic depiction of the laminate's capabilities. Along with comparisons

with the corresponding dogbone tensile test results at the elevated temperature, these

blunt notch results will also be compared to those obtained during the room temperature

evaluation.

The first specimens tested at the elevated temperature have fibers oriented at 0°.

The following figure shows the stress-strain curves obtained during these tests.
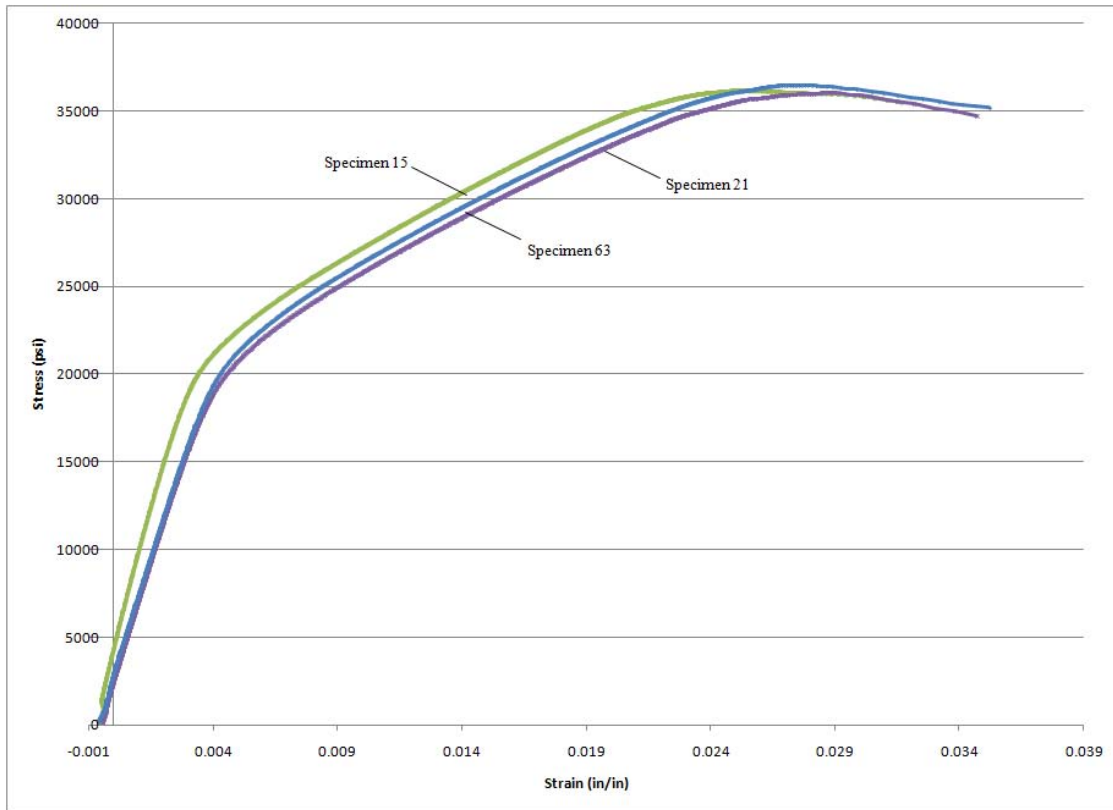
Figure 122 : 80C Blunt Notch Stress-Strain Curves, 0° Fiber Orientation

And from these curves, the following table summarizes the important details obtained

from these first elevated temperature tests.

Table 113 : 80C Blunt Notch Results, 0° Fiber Orientation

	Elastic Modulus (Msi)	UTS (ksi)	Y (ksi)	$\varepsilon_{failure}$ (in/in)
Specimen 15	5.204	36.18	23.88	0.03234
Specimen 21	4.464	36.05	22.94	0.03594
Specimen 63	4.397	36.45	23.87	0.03581
Average	4.688	36.23	23.57	0.03470

For comparison, the next table shows these results versus the results obtained in the room temperature blunt notch test.

Table 114 : RT Blunt Notch to 80C Blunt Notch Comparison, 0° Fiber Orientation

	Elastic Modulus (Msi)	UTS (ksi)	Y (ksi)	$\varepsilon_{failure}$ (in/in)
RT Blunt Notch	4.598	37.01	23.18	0.03256
80C Blunt Notch	4.688	36.23	23.57	0.0347
Percent Difference	1.96	2.11	1.68	6.57

To complete this comparison, the next table draws upon the results from the elevated temperature dogbone tensile tests. Despite the apparent error seen with the results, it may be of use to examine the relative change in property values when the laminate is subjected to a stress concentration.

Table 115 : 80C Dogbone Tensile to 80C Blunt Notch Comparison, 0° Fiber Orientation

	Elastic Modulus (Msi)	UTS (ksi)	Y (ksi)	$\varepsilon_{failure}$ (in/in)
80C Dogbone	9.506	95.5	45.48	0.04066
80C Blunt Notch	4.688	36.23	23.57	0.0347
Percent Difference	50.68	62.06	48.18	14.66

At the completion of the first elevated temperature test, is first seen how the modulus compared to that of the room temperature test has fluctuated very little. This gives rise to the practical application of the laminate in that at higher temperatures, when the fibers are parallel to the fiber direction, there is little to no reduction in elastic modulus. Despite the dominance of the fibers within these 0° specimens, the matrix continues to play a role in the laminate strength behavior.

Similar to the room temperature testing, the effect of the stress concentration serves to decrease the overall laminate strength. This is first seen with the reduction in structural stiffness through the decreased magnitude of elastic modulus by approximately

51%. The ultimate tensile and yield strength values are also reduced by 62% and 48% respectively. The failure strain is reduced by nearly 15% from the un-notched dogbone tensile test. Recall that, when examining these data tables, an unknown inaccuracy was present during the initial elevated temperature tests.

The next figure shows the resulting elevated temperature blunt notch specimens after the experiments were completed.
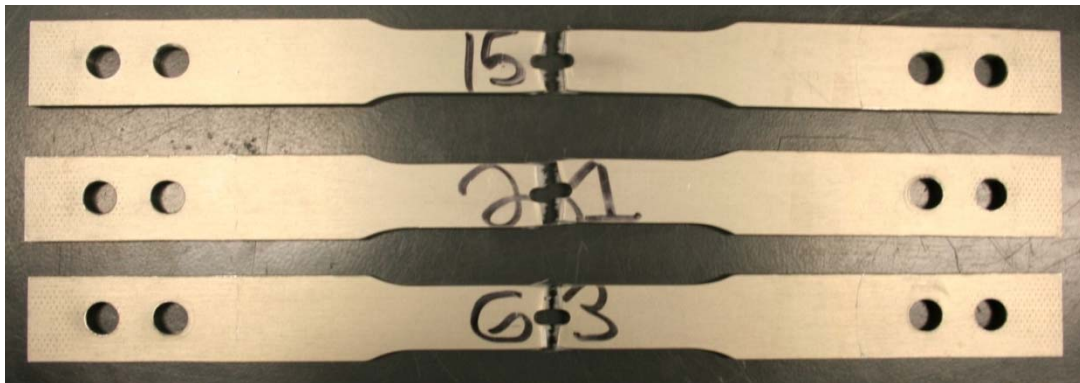

Figure 123 : Failed 80C Blunt Notch Specimens, 0⁰ Fiber Orientation

And the next figure shows a close up view of specimen 63. This failure region is typical of each of the failed specimens.

Figure 124 : Failure Region for Failed 80C Blunt Notch Specimen 63, 0⁰ Fiber Orientation

As shown with each of the previous blunt notch failures, all yielding is localized to the area immediately surrounding the gauge section hole. Again, for practical application, this can aid in inspection as failure in the laminate at these elevated temperatures will be restricted to the anomalies in what would otherwise be a continuous medium.

The second set of elevated temperature tests used specimens whose fibers were oriented at 45°. The following figure shows the resulting stress-strain curves.
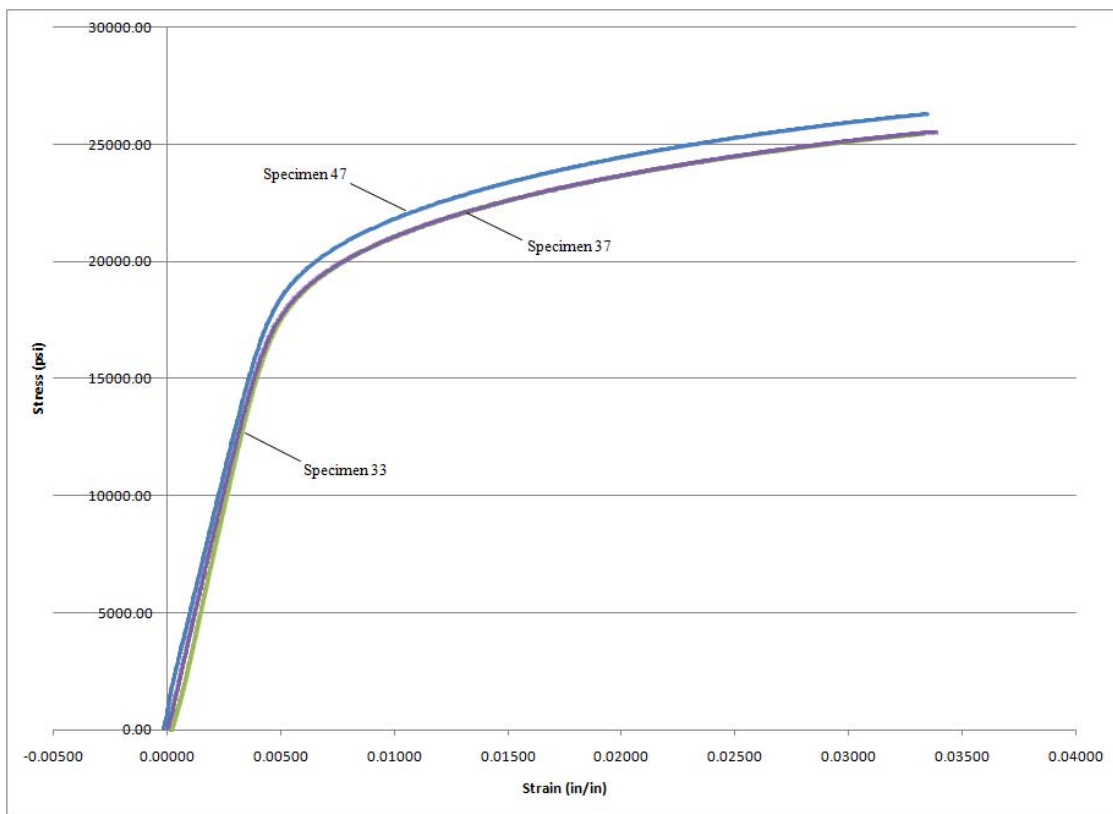
Figure 125 : 80C Blunt Notch Stress-Strain Curves, 45° Fiber Orientation

The next table shows the pertinent data collected from these stress-strain curves.

Table 116 : 80C Blunt Notch Results, 45° Fiber Orientation

	Elastic Modulus (Msi)	UTS (psi)	Y (psi)	$\varepsilon_{failure}$ (in/in)
Specimen 33	4.292	25.45	19.44	0.03338
Specimen 37	4.034	25.53	19.46	0.03406
Specimen 47	3.976	26.31	20.47	0.03357
Average	4.101	25.76	19.79	0.03367

For comparison the next chart shows the results from the average values of the 45° elevated temperature blunt notch tests to the room temperature tests.

Table 117 : RT Blunt Notch to 80C Blunt Notch Comparison, 45° Fiber Orientation

	Elastic Modulus (Msi)	UTS (ksi)	Y (ksi)	$\varepsilon_{failure}$ (in/in)
RT Blunt Notch	5.132	27.68	21.01	0.03135
80C Blunt Notch	4.101	25.76	19.79	0.03367
Percent Difference	20.09	6.94	5.81	7.04

Before the dogbone comparison is made, note the striking decrease in structural stiffness as induced by the elevated temperature. While the 0° specimens showed relatively little change with the elevated temperature, this initial off-axis group of specimens exhibits a significant reduction in elastic modulus, as indicated by the 20% decrease. A behavior common to the blunt notch specimen is the reduction in ultimate tensile strength. Also seen here, caused from the increase in test temperature, is the slight increase in strain to failure. With the off-axis fiber orientation, the laminate is more dominated by the behavior of the matrix. The greater increase in strain shown with the 45° specimens over that measured with the 0° specimens is indicative of this matrix influence.

The next table compared the blunt notch specimen results to those obtained with the elevated temperature dogbone tensile specimens.

Table 118 : 80C Dogbone Tensile to 80C Blunt Notch Comparison, 45° Fiber Orientation

	Elastic Modulus (Msi)	UTS (ksi)	Y (ksi)	$\varepsilon_{failure}$ (in/in)
80C Dogbone	11.117	52.09	38.46	0.11732
80C Blunt Notch	4.101	25.76	19.79	0.03367
Percent Difference	63.11	50.55	50.10	71.30

At the 45° fiber orientation, the general trend of strength reduction is seen. Further, the

decrease in strain is also seen as the stress concentration serves to locally increase stress

and thus induce failure early on.

The next figure shows the failed 45° blunt notch specimen.
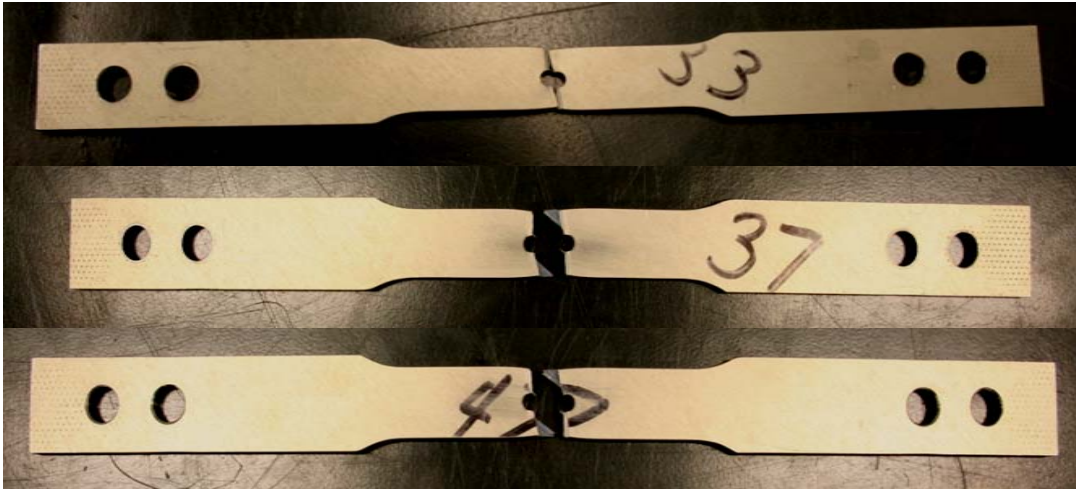
Figure 126 : Failed 80C Blunt Notch Specimens, 45° Fiber Orientation

From these specimens, the fiber angle is clear seen as the failure has occurred along this

line. The next figure shows the typical failure region for these specimens.

Figure 127 : Failure Region for Failed 80C Blunt Notch Specimen 37, 45° Fiber Orientation

Next, blunt notch specimens with fibers oriented at 67.5° were tested. The next

figure shows the resulting stress-strain curves from this series of tests.

Figure 128 : 80C Blunt Notch Stress-Strain Curves, 67.5° Fiber Orientation

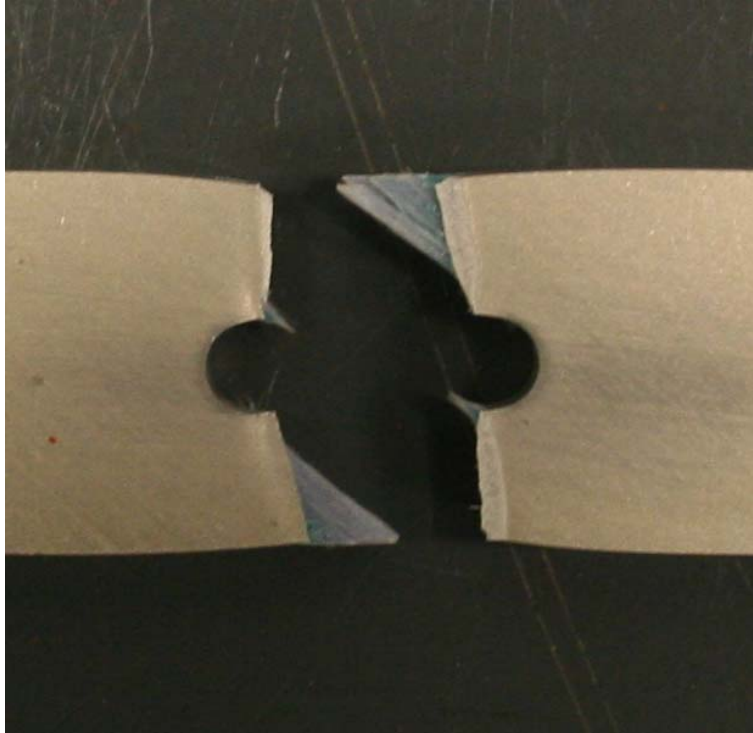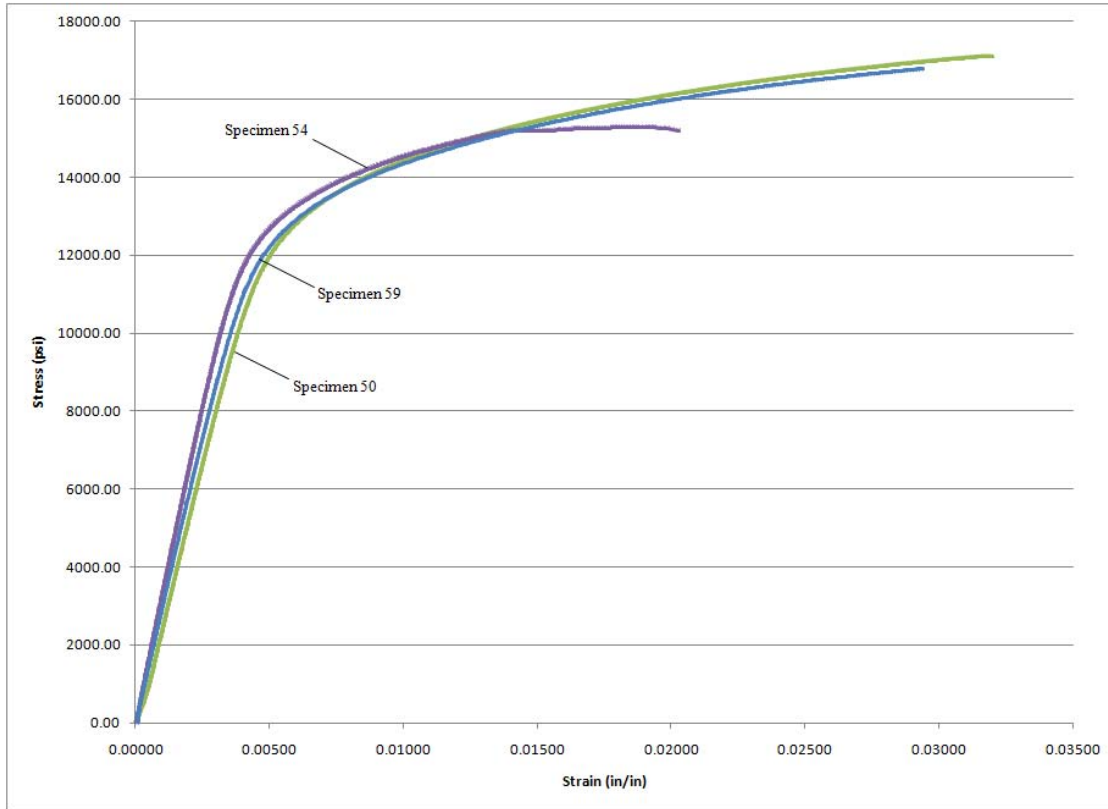The next table shows the information collected from these curves.

Table 119 : 80C Blunt Notch Results, 67.5° Fiber Orientation

	Elastic Modulus (Msi)	UTS (ksi)	Y (ksi)	$\varepsilon_{failure}$ (in/in)
Specimen 50	2.802	17.11	13.13	0.03220
Specimen 54	3.248	15.30	13.34	0.02073
Specimen 59	2.914	16.81	13.06	0.02952
Average	2.988	16.41	13.18	0.02748

It is first interesting to note the average decrease in structural stiffness over the average value for the 45° blunt notch specimens. Due to the increase dominance the matrix plays at this fiber orientation, the laminate's strength characteristics continue to decrease.

The following table illustrates the impact temperature has on CentrAl's blunt notch strength at the 67.5° fiber orientation.

209

Table 120 : RT Blunt Notch to 80C Blunt Notch Comparison, 67.5° Fiber Orientation

	Elastic Modulus (Msi)	UTS (ksi)	Y (ksi)	$\varepsilon_{failure}$ (in/in)
RT Blunt Notch	3.485	17.48	14.38	0.02687
80C Blunt Notch	2.988	16.41	13.18	0.02748
Percent Difference	14.26	6.12	8.34	2.27

As the matrix material begins to dominate more of the specimen geometry, the modulus values continue to decrease. This indicates a relative decrease in structural stiffness. The same trend is noted with both the ultimate and yield strength values. While, on the other hand, the strain to failure has increased. The increase in test temperature causes this increase in matrix plasticity - permitting additional strain.

The final table for this fiber orientation shows the impact the stress concentration has with the overall laminate mechanical properties.

Table 121 : 80C Dogbone Tensile to 80C Blunt Notch Comparison, 67.5° Fiber Orientation

	Elastic Modulus (Msi)	UTS (ksi)	Y (ksi)	$\varepsilon_{failure}$ (in/in)
80C Dogbone	10.09	51.49	44.52	0.19193
80C Blunt Notch	2.988	16.41	13.18	0.02748
Percent Difference	70.39	68.13	70.40	85.68

Despite the error associated with the elevated temperature dogbone tensile testing, in which the values obtained were apparently erroneously high, a more accurate stiffness comparison can be made with the dedicated elevated temperature modulus testing. For this fiber angle, recall the average elastic modulus was measured to be approximately 8.353 Msi. Comparing this experimentally obtained modulus value, to that obtained with the stress concentration present, the stiffness was reduced by an amount of 64.23%. The general trend of the decreased ultimate and yield strength values follows the experimental results thus far, as does the decrease in strain to failure. Because of the effect of the stress

concentration, the ultimate laminate properties are reached at a lower strain value and hence decreased stress levels.

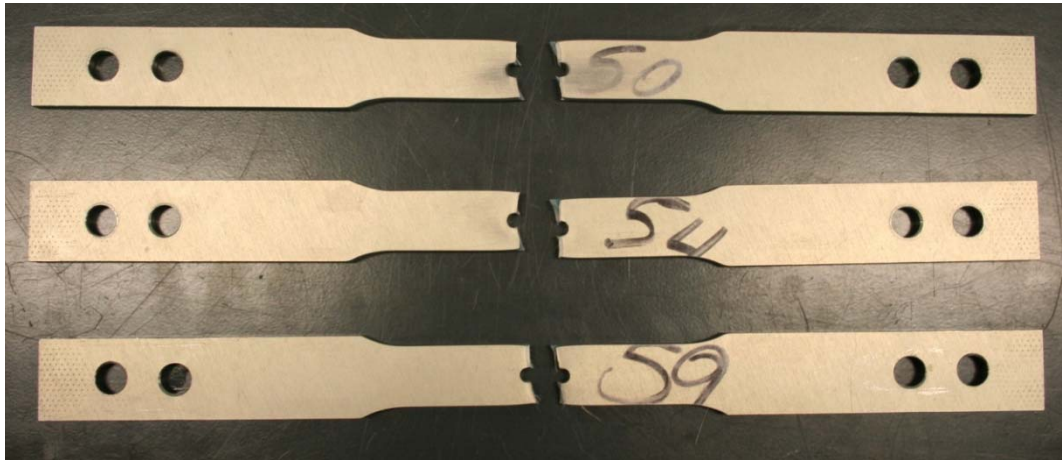The next figure shows the specimens used for this evaluation.

Figure 129 : Failed 80C Blunt Notch Specimens, 67.5⁰ Fiber Orientation

The next figure shows a close up view of the failure region common to the specimens with this fiber orientation. Failure in these specimens also occurred along an angle equal to 67.5⁰. Failure along the fiber angle line is consistent with all of the off-axis specimens tested thus far.
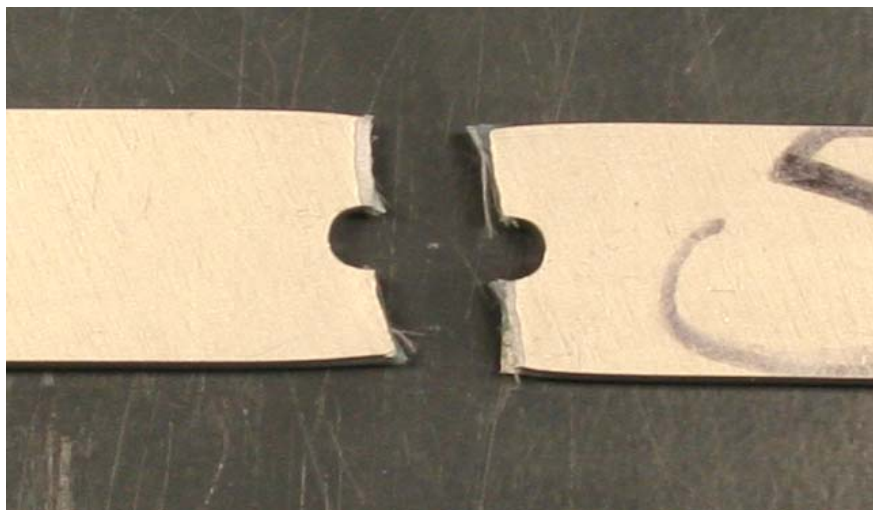

Figure 130 : Failure Region for Failed 80C Blunt Notch Specimen 59 - 67.5⁰

The final batch of blunt notch specimens tested had fibers oriented at 90°. The following figure shows the stress-strain curves from these experiments.
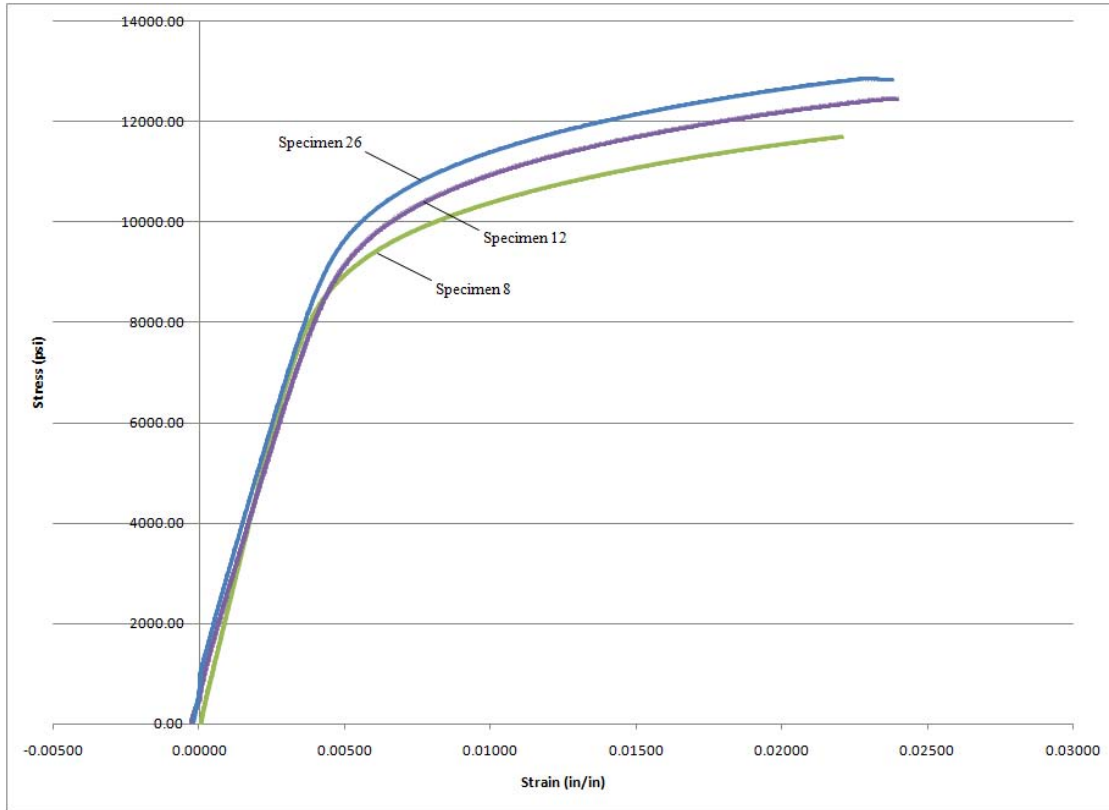

Figure 131 : 80C Blunt Notch Stress-Strain Curves, 90° Fiber Orientation

The next table shows the collection of data obtained from these test results.

Table 122 : 80C Blunt Notch Results, 90° Fiber Orientation

	Elastic Modulus (Msi)	UTS (ksi)	Y (ksi)	$\varepsilon_{failure}$ (in/in)
Specimen 8	2.319	11.71	9.40	0.02212
Specimen 12	1.888	12.45	10.15	0.02415
Specimen 26	2.020	12.85	10.62	0.02390
Average	2.076	12.34	10.06	0.02339

Fully dominated by the matrix material, the strain is seen to the smallest of each fiber orientation group. Each of the other mechanical properties follow the same trend as seen as seen with the previous fiber orientations.

The next table shows the comparison between the blunt notch strength at room temperature and the elevated temperature.

Table 123 : RT Blunt Notch to 80C Blunt Notch Comparison, 90⁰ Fiber Orientation

	Elastic Modulus (Msi)	UTS (ksi)	Y (ksi)	$\varepsilon_{failure}$ (in/in)
RT Blunt Notch	2.505	12.5	10.27	0.02226
80C Blunt Notch	2.076	12.34	10.06	0.02339
Percent Difference	17.13	1.28	2.04	5.08

Of interest with this comparison is the relative consistency seen among the blunt notch properties despite the temperature increase. However, despite the near total dominance of the matrix material in this fiber orientation, the ultimate and yield strength values show little to no variance between the two temperature regions. As was seen with each of the other test results, the strain to failure has increased, due to the additional plasticity within the FM94K matrix.

The next table shows the effect the stress concentration has on specimens tested at the same temperature with the same fiber orientation.

Table 124 : 80C Dogbone Tensile to 80C Blunt Notch Comparison, 90⁰ Fiber Orientation

	Elastic Modulus (Msi)	UTS (ksi)	Y (ksi)	$\varepsilon_{failure}$ (in/in)
80C Dogbone	10.675	52.71	38.02	0.10182
80C Blunt Notch	2.076	12.34	10.06	0.02339
Percent Difference	80.55	76.59	73.54	77.03

Once again, to accommodate the error associated with the initial elevated temperature dogbone tensile tests, a more accurate elastic modulus comparison will be made with the dedicated high temperature results. Recall that for the 90⁰ fiber orientation, the average elastic modulus was measured to be 8.358 Msi. At this fiber orientation, the effect of the stress concentration serves to reduce the stiffness of the un-notched specimen by

approximately 75.2%. The increase in temperature continues the trend of decreasing each of the measured blunt notch properties.

The next figure shows the specimens tested during these elevated temperature blunt notch tests.

Figure 132 : Failed 80C Blunt Notch Specimens, 90° Fiber Orientation

As previously demonstrated, each specimen failed along a line equal in angle to that of the fiber orientation. Notice in the next figure, the relatively clean fracture surface in the gauge section.
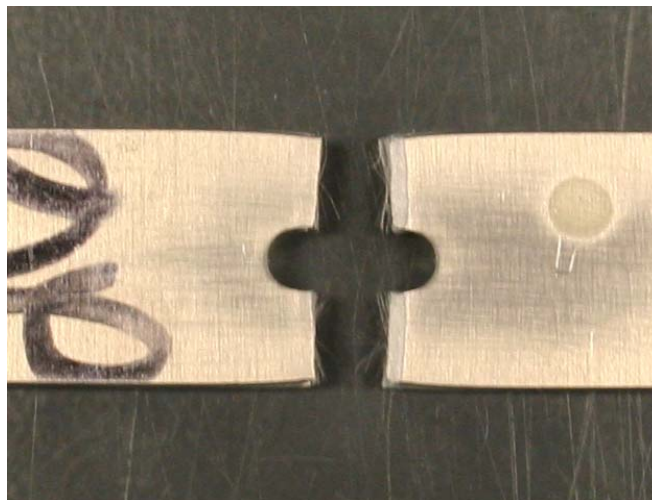

Figure 133 : Failure Region for Failed 80C Blunt Notch Specimen 26, 90° Fiber Orientation

Reduced Temperature Results.

The final set of blunt notch tests involved testing specimens at a temperature of -55C. Along with comparisons with the corresponding dogbone tensile test results at the reduced temperature, these blunt notch results will also be compared to those obtained during the room temperature evaluation. This will provide a comparison of CentrAl's capabilities with and without a stress concentration and the blunt notch capability for the laminate at room temperature versus the reduced temperature.

The first specimens tested at the elevated temperature have fibers oriented at 0°. The following figure shows the stress-strain curves obtained during these tests.
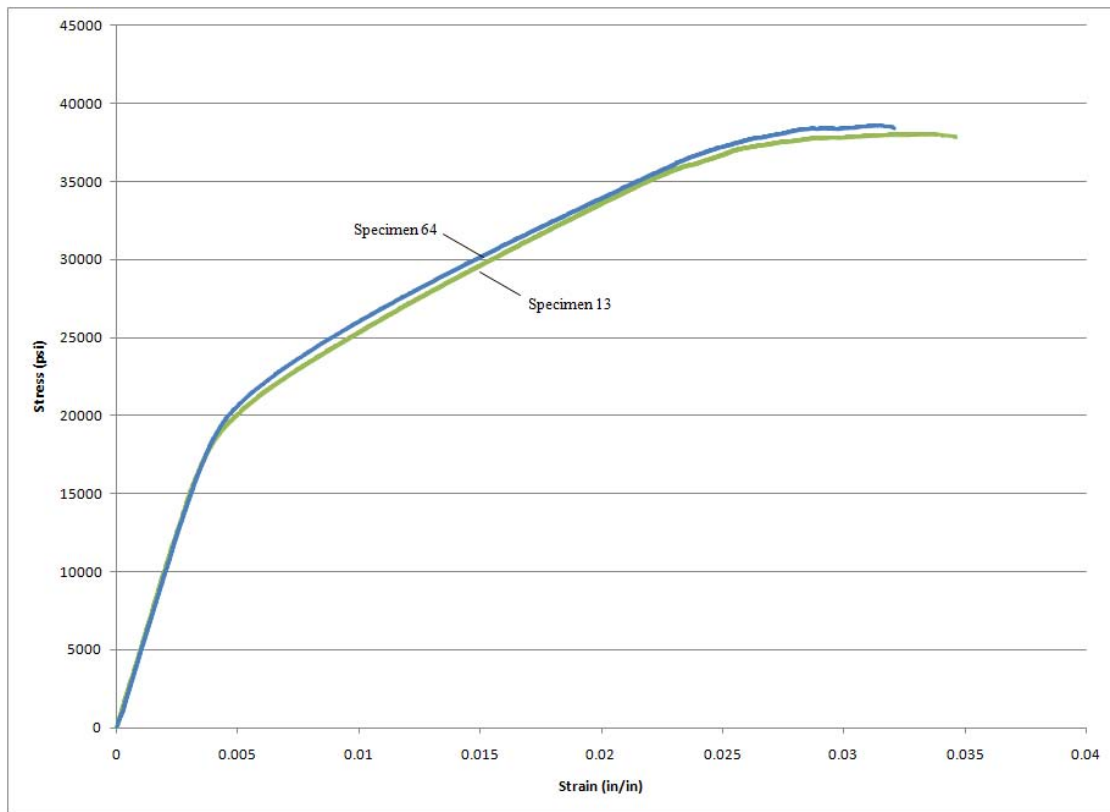

Figure 134 : -55C Blunt Notch Stress-Strain Curves, 0° Fiber Orientation

From these curves, the following table is produces, outlining the pertinent information collected.

Table 125 : -55C Blunt Notch Results, 0° Fiber Orientation

	Elastic Modulus (Msi)	UTS (ksi)	Y (ksi)	$\varepsilon_{failure}$ (in/in)
Specimen 13	5.077	38.05	21.69	0.03554
Specimen 64	4.961	38.59	22.26	0.03210
Average	5.019	38.32	21.98	0.03382

To draw comparisons with the room temperature blunt notch data, the following table is

constructed.

Table 126 : RT Blunt Notch to -55C Blunt Notch Comparison, 0° Fiber Orientation

	Elastic Modulus (Msi)	UTS (ksi)	Y (ksi)	$\varepsilon_{failure}$ (in/in)
RT Blunt Notch	4.598	37.01	23.18	0.03256
-55C Blunt Notch	5.019	38.32	21.98	0.03382
Percent Difference	9.16	3.54	5.18	3.87

From the comparison of the two blunt notch results at the room and reduced temperature,

it is seen how the relative stiffness increases by slightly more than 9%. Further, the

ultimate tensile strength is increased approximately 3.5% while the yield strength

decreased approximately 5%. As with the elevated temperature tests at this same fiber

angle, the reduced temperature tests also show a slight increase in the failure strain

magnitude.

The following table compares the laminate's blunt notch strength at this decreased

temperature to that of the corresponding intact capabilities found during the dogbone

tensile test.

Table 127 : -55C Dogbone Tensile to -55C Blunt Notch Comparison, 0° Fiber
Orientation

	Elastic Modulus (Msi)	UTS (ksi)	Y (ksi)	$\varepsilon_{failure}$ (in/in)
-55C Dogbone	11.273	115.1	45.55	0.04308
-55C Blunt Notch	5.019	38.32	21.98	0.03382
Percent Difference	55.48	66.71	51.75	21.49

When examining the reduced temperature blunt notch strength of CentrAl, the familiar decreased in structural stiffness is seen - indicative of the stress concentration. The effect of the central hole serves to reduce the stiffness by 55.5%. As shown here with the reduced temperature testing, the ultimate tensile strength is reduced by approximately 67%, and the yield strength by nearly 52%. The presence of the stress concentration serves to decrease the strain to failure by 21.5%.

The next figure shows the resulting specimens after this series of initial reduced temperature experiments.

Figure 135 : Failed -55C Blunt Notch Specimens, 0⁰ Fiber Orientation

Immediately noticeable with these specimens is the undesired failure region in the mounting bolt hole for specimen 64. While prominent yielding did occur in the gauge section, as seen in the figure below, ultimate failure occurred at the grip section.
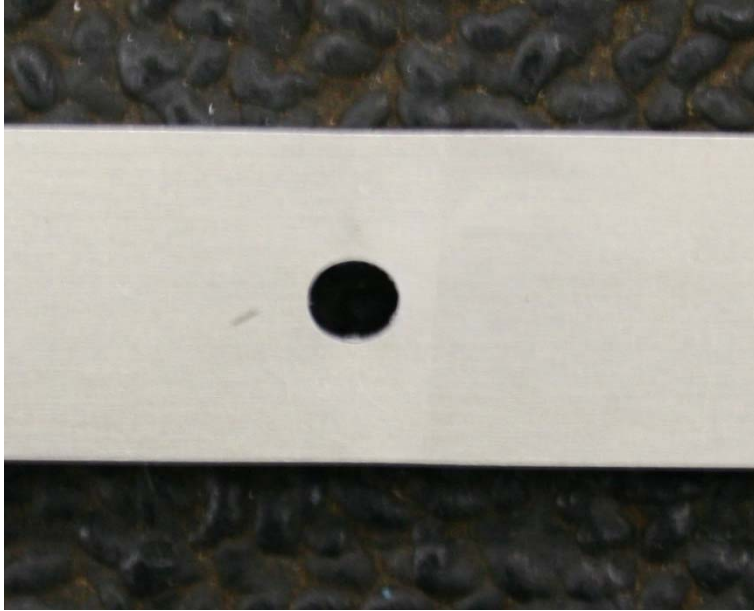
Figure 136 : Yielded Gauge Section Hole for Blunt Notch Specimen 64, 0⁰ Fiber Orientation

With the ultimate strain value seen for this specimen closely mirroring that of specimen 13, the decision was made to preserve the data for use in this blunt notch study. The next figures shows close up views of the ultimate failure regions for specimens 64 and 13, respectively.

Figure 137 : Failure Region for Failed -55C Blunt Notch Specimen 64, 0⁰ Fiber Orientation
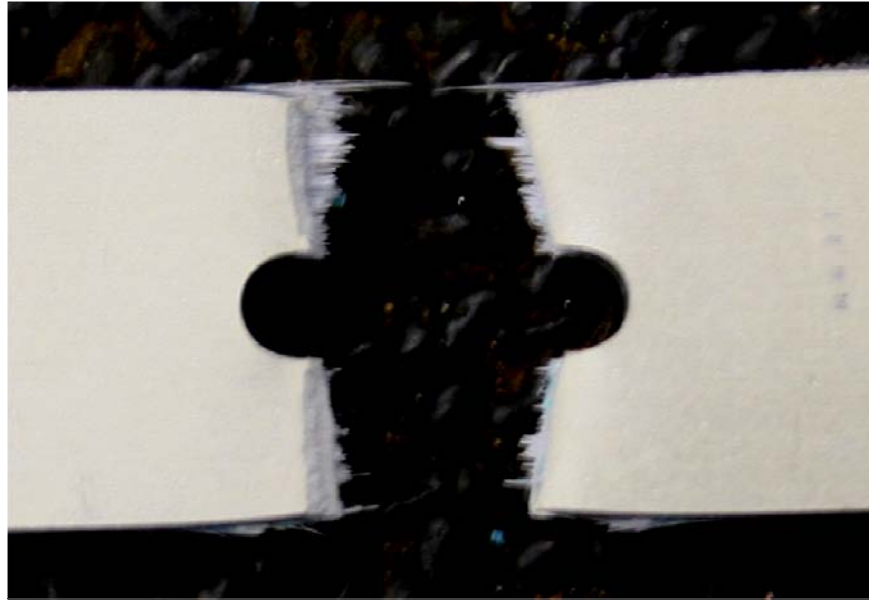
Figure 138 : Failure Region for Failed -55C Blunt Notch Specimen 13, 0⁰ Fiber
Orientation

The second series of reduced temperature blunt notch tests investigated the results

of specimens whose fibers are oriented at 45°. The following figure shows the resulting

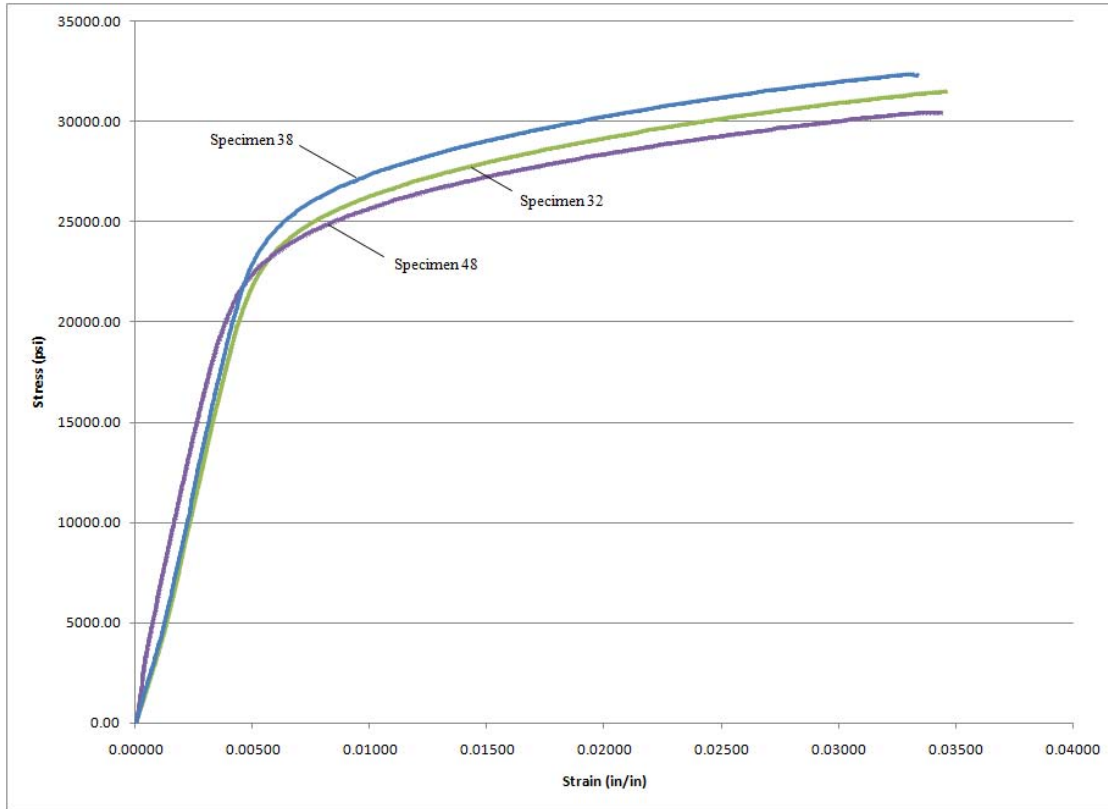stress-strain curves for these tests.

Figure 139 : -55C Blunt Notch Stress-Strain Curves, 45° Fiber Orientation

And from these curves, the next table is constructed which details the information gained

from them.

Table 128 : -55C Blunt Notch Results, 45° Fiber Orientation

	Elastic Modulus (Msi)	**UTS (ksi)**	**Y (ksi)**	$\varepsilon_{failure}$ **(in/in)**
Specimen 32	5.087	31.50	24.47	0.03468
Specimen 38	5.199	30.44	23.68	0.03461
Specimen 48	5.366	32.35	25.75	0.03366
Average	5.217	31.43	24.63	0.03432

Evident from this table is the increase in stiffness when compared to that of the 0° fiber

orientation. This is in contrast to the behavior seen with both the room temperature and

elevated temperature blunt notch tests. The effect of the additional matrix dominance is

seen with the decrease in ultimate tensile strength when compared to the same parameter

for the 0° fiber orientation specimen. Different again from the other specimens, is that

220

despite the decrease in ultimate tensile strength, the yield strength increased slightly

when compared to the on-axis specimens. Further, the ultimate strain to failure is also

shown to increase.

The next chart shows the effect the reduction in temperature has on CentrAl's

blunt notch strength.

Table 129 : RT Blunt Notch to -55C Blunt Notch Comparison, 45° Fiber Orientation

	Elastic Modulus (Msi)	UTS (ksi)	Y (ksi)	$\varepsilon_{failure}$ (in/in)
RT Blunt Notch	5.132	27.68	21.01	0.03135
-55C Blunt Notch	5.217	31.43	24.63	0.03432
Percent Difference	1.66	13.55	17.23	9.47

This table clearly shows the effect of reduced temperature on the blunt notch strength of

CentrAl. When compared directly to the room temperature blunt notch behavior, the

laminate shows a slight increase in structural stiffness. Further, the decreased temperature

shows to increase the remaining properties under investigation. The ultimate tensile

strength increased approximately 13.5%, while the yield strength increased nearly 17%.

There was also a 9.5% increase in ultimate failure strain.

The next table shows the effect of the stress concentration on the laminate.

Table 130 : -55C Dogbone Tensile to -55C Blunt Notch Comparison, 45° Fiber
Orientation

	Elastic Modulus (Msi)	UTS (ksi)	Y (ksi)	$\varepsilon_{failure}$ (in/in)
-55C Dogbone	9.311	64.06	44.55	0.14518
-55C Blunt Notch	5.217	31.43	24.63	0.03432
Percent Difference	43.97	50.94	44.71	76.36

From this chart, the laminate's stiffness is seen to be reduced by nearly 44% due to the

stress concentration. Additionally, the laminate's ultimate tensile strength is decreased by

approximately 51%. The yield strength decreased nearly 45% because of the stress

concentration. The failure strain also decreased, but on the order of 76%. Because of the

gauge section hole, the laminate reaches its ultimate properties at a much lower strain

value.

The next figure shows the resulting blunt notch specimens used for this testing
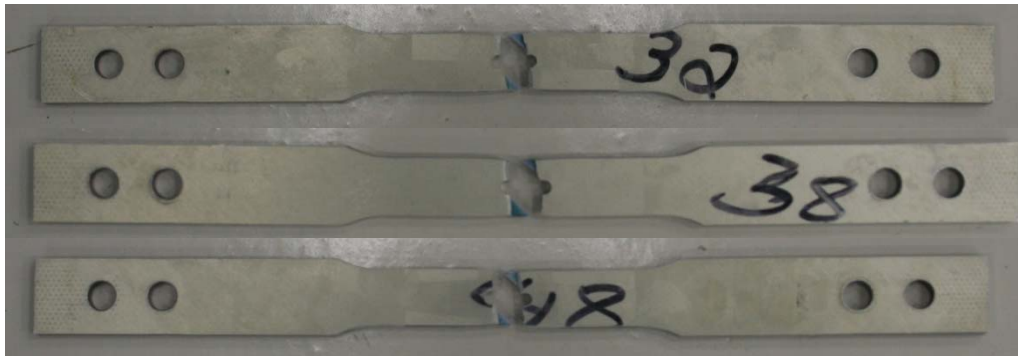
sequence.

Figure 140 : Failed -55C Blunt Notch Specimens, 45° Fiber Orientation

As seen with each of these specimens, the fibrous layer failure occurred along an angle

equal to that of the fiber orientation. The next figure shows a typical failure region for the
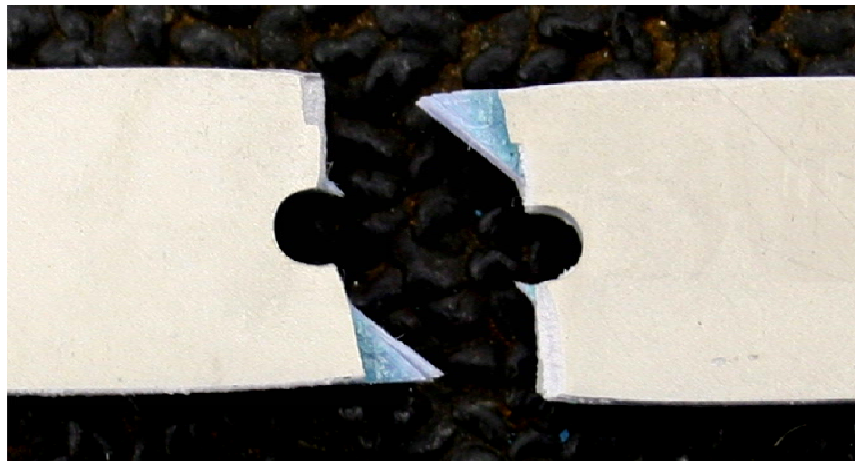
reduced temperature 45° blunt notch specimens.

Figure 141 : Failure Region for Failed -55C Blunt Notch Specimen 32, 45° Fiber
Orientation

The third testing sequence involved blunt notch specimens with fibers oriented at 67.5°. The next figure shows the resulting stress-strain curve from this series of experiments.
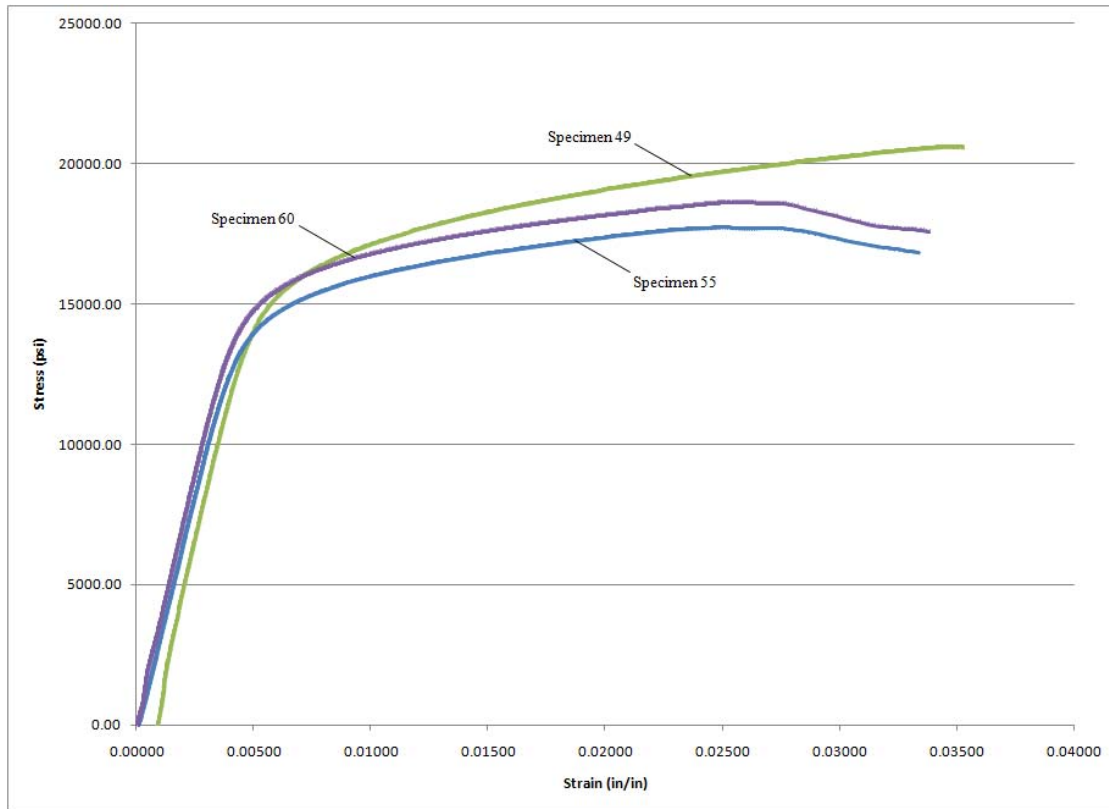

Figure 142 : -55C Blunt Notch Stress-Strain Curves, 67.5° Fiber Orientation

The table below shows the pertinent information taken from these rest results.

Table 131 : -55C Blunt Notch Results, 67.5° Fiber Orientation

	Elastic Modulus (Msi)	UTS (ksi)	Y (ksi)	$\varepsilon_{failure}$ (in/in)
Specimen 49	3.518	20.60	16.24	0.03551
Specimen 60	3.512	18.63	15.83	0.03416
Specimen 55	3.444	17.74	14.90	0.03361
Average	3.491	18.99	15.66	0.03443

From this table, the laminate is shown to have decreased its structural stiffness slightly

over that seen with the 45° specimens. The ultimate tensile and yield strength values are

also seen to decrease over those determined from the 45° tests. This decrease can be

attributed to the additional influence the matrix material plays in this particular fiber

orientation. Of interest, however, is the near constant ultimate strain to failure between

both the 45° and 67.5° specimens. Despite the additional matrix dominance with this

batch of specimens, the ultimate failure strain remains virtually unaffected.

The following table illustrated the comparison between the results found from

these tests to those found during the room temperature blunt notch experiments.

Table 132 : RT Blunt Notch to -55C Blunt Notch Comparison, 67.5° Fiber Orientation

	Elastic Modulus (Msi)	UTS (ksi)	Y (ksi)	$\varepsilon_{failure}$ (in/in)
RT Blunt Notch	3.485	17.48	14.38	0.02687
-55C Blunt Notch	3.491	18.99	15.66	0.03443
Percent Difference	0.17	8.64	8.90	28.14

Here, the effect of the decreased temperature on the more matrix dominated fiber

orientation is seen to have very little effect on the overall structural stiffness. The percent

difference between the room temperature and decreased temperature values is on the

order of 0.17%. At the decreased temperature, the matrix material is shown to stiffen,

thus the increase in both the ultimate tensile strength and yield strength values. However,

this increase in strength values over the room temperature results is seen to occur even

with a near 28% increase in the ultimate strain to failure.

The next table shows the comparison, between that of the blunt notch results to

those obtained with the reduced temperature dogbone tensile test.

Table 133 : -55C Dogbone Tensile to -55C Blunt Notch Comparison, 67.5° Fiber Orientation

	Elastic Modulus (Msi)	UTS (ksi)	Y (ksi)	$\varepsilon_{failure}$ (in/in)
-55C Dogbone	8.656	58.47	42.59	0.13564
-55C Blunt Notch	3.491	18.99	15.66	0.03443
Percent Difference	59.67	67.52	63.23	74.62

From this table, the first obvious effect of the stress concentration is the decrease in stiffness. There is also a nearly 75% decrease in ultimate failure strain. Because of the stress concentration, the laminate's ultimate tensile strength and yield strength has been reduced by 67.5% and 63% respectively. This coincides with the behavior seen of each blunt notch specimen thus far in the experimentation procedure.

The following figure shows the resulting blunt notch specimens used for this fiber orientation.

Figure 143 : Failed -55C Blunt Notch Specimens, 67.5° Fiber Orientation

Just as with each of the other off-axis specimens, failure of the fibrous layers occurred along a line equal in angle to the fiber orientation. The next figure shows the typical failure region for these specimens. This increased fiber angle is seen in the figure through the lack of prepreg visible in the failure region.

Figure 144 : Failure Region for Failed -55C Blunt Notch Specimen 55, 67.5° Fiber Orientation

The final series of test in the reduced temperature blunt notch study involved specimens with a 90° fiber angle. This fiber angle places the fiber perpendicular to the loading direction.

The next figure shows the stress-strain curves found as result of these tests.
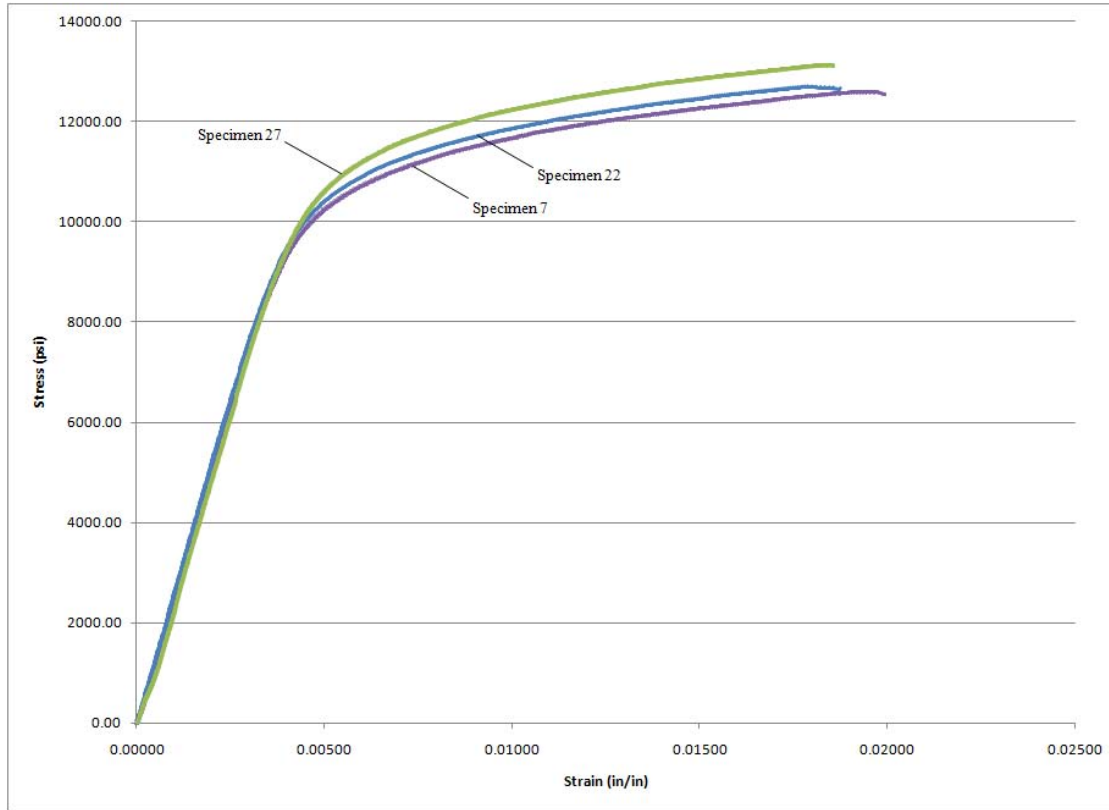

Figure 145 : -55C Blunt Notch Stress-Strain Curves, 90° Fiber Orientation

From these stress-strain curves, the following table is created which details the pertinent

information.

Table 134 : -55C Blunt Notch Results, 90° Fiber Orientation

	Elastic Modulus (Msi)	UTS (ksi)	Y (ksi)	$\varepsilon_{failure}$ (in/in)
Specimen 27	2.554	13.12	11.50	0.01875
Specimen 7	2.574	12.59	10.89	0.02029
Specimen 22	2.615	12.70	11.05	0.01903
Average	2.581	12.80	11.14	0.01936

Examining this table and comparing with the other results shows that average stiffness

values obtained for both the 90° specimens has reached a minimum. As the matrix is now

fully dominant in this fiber orientation, both the ultimate strength and yield strength

values are now at their lowest recorded value. Further, with the matrix fully dominant, the failure strain is also shown to be the lowest.

The next table shows the comparison between the reduced temperature blunt notch results to those found in the room temperature results.

Table 135 : RT Blunt Notch to -55C Blunt Notch Comparison, 90° Fiber Orientation

	Elastic Modulus (Msi)	UTS (ksi)	Y (ksi)	$\varepsilon_{failure}$ (in/in)
RT Blunt Notch	2.505	12.5	10.27	0.02226
-55C Blunt Notch	2.581	12.8	11.14	0.01936
Percent Difference	3.03	2.40	8.47	13.03

It is shown here that temperature has only a slight effect on the laminate in this fiber orientation, save for the nearly 13% reduction in failure strain and 8.5% increase in yield strength. The stiffness for the both the room temperature and reduced temperature blunt notch tests remain virtually unchanged. The same holds true for the ultimate tensile strength. With the reduced strain to failure, typically indicative of a more brittle material, the yield strength increase approaches the value of the ultimate tensile strength. With the more matrix dominated fiber orientation, it is seen here that the reduced temperature serves to make the laminate slightly stiffer, thus reducing its overall compliance.

This final table, shown below, illustrates the effect of a stress concentration on the laminate.

Table 136 : -55C Dogbone Tensile to -55C Blunt Notch Comparison, 90° Fiber Orientation

	Elastic Modulus (Msi)	UTS (ksi)	Y (ksi)	$\varepsilon_{failure}$ (in/in)
-55C Dogbone	9.318	54.15	39.17	0.13512
-55C Blunt Notch	2.581	12.8	11.14	0.01936
Percent Difference	72.30	76.36	71.56	85.67

Once again the effect of the stress concentration in CentrAl, at this reduced temperature, serves to decrease its structural stiffness over its intact counterpart. At the 90° fiber orientation, the same trend of a decreased ultimate tensile strength and increase yield strength value is shown.

The next figure shows the specimens used during these final series of tests.

Figure 146 : Failed -55C Blunt Notch Specimens, 90° Fiber Orientation

In keeping with the trend seen in the failure regions of the other specimens, to include the dogbone tensile and blunt notch designs, the failure occurred at an angle equal to its fiber orientation. In the case of this orientation, the failure occurred perpendicular to the loading direction, indicative of its 90° fiber angle. The next figure shows a close up view of a typical failure region.
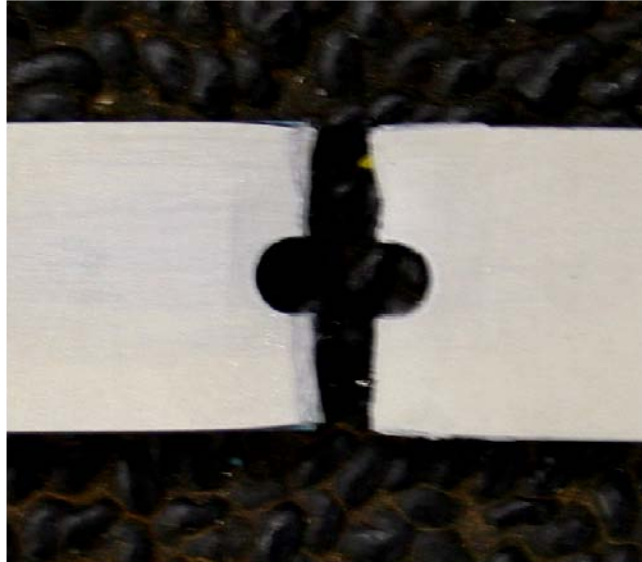
Figure 147 : Failure Region for Failed -55C Blunt Notch Specimen 22, 90° Fiber Orientation

Overall Blunt Notch Results.

The above tables certainly show the results for each of the test temperatures and at each fiber orientation. The overall laminate behavior is more easily seen when the results are compiled onto a single chart. Generalized behavioral observations can more easily be made.

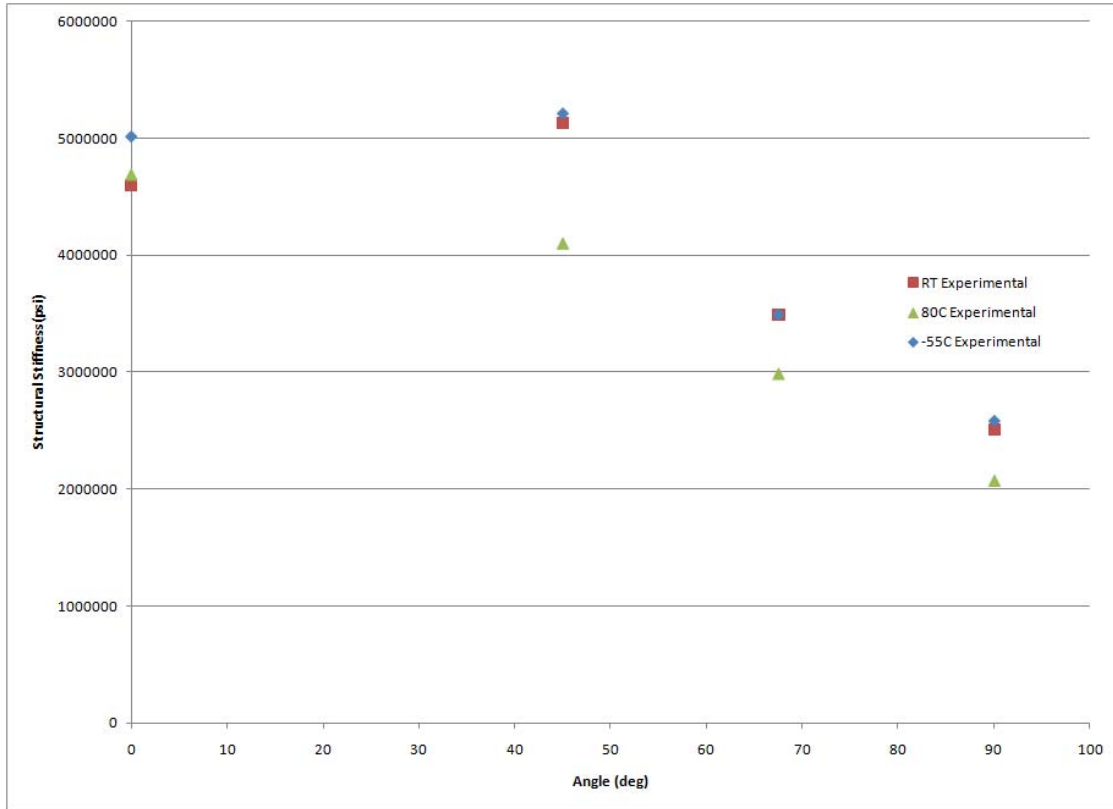The next figure shows each of the stiffness values plotted over the range of fiber angles.

Figure 148 : Overall Blunt Notch Stiffness Values

From this overall view of the blunt notch structural stiffness values, it is seen how close the room temperature and reduced temperature values are across the entire fiber angle spectrum. Despite the reduced temperature, the relative stiffness of the laminate does not change. This is promising in aircraft applications as the majority of flight time is spent in ambient temperatures approaching those of the reduced temperature tests. At the 0⁰ fiber orientation, the reduced temperature is shown to increase the stiffness above both the room and elevated temperature results. It is shown that the elevated temperature stiffness values, overall, are smaller as compared to both the room and decreased temperature experimental values. Additionally, it is observed how at the 45⁰ fiber orientation, the greatest decrease in stiffness occurs with the elevated temperature. At the remaining off-

axis specimens, the stiffness reduction induced by the elevated temperature remains constant.

The next figure shows the relative variance of CentrAl's blunt notch ultimate tensile strength as a function of fiber angle.
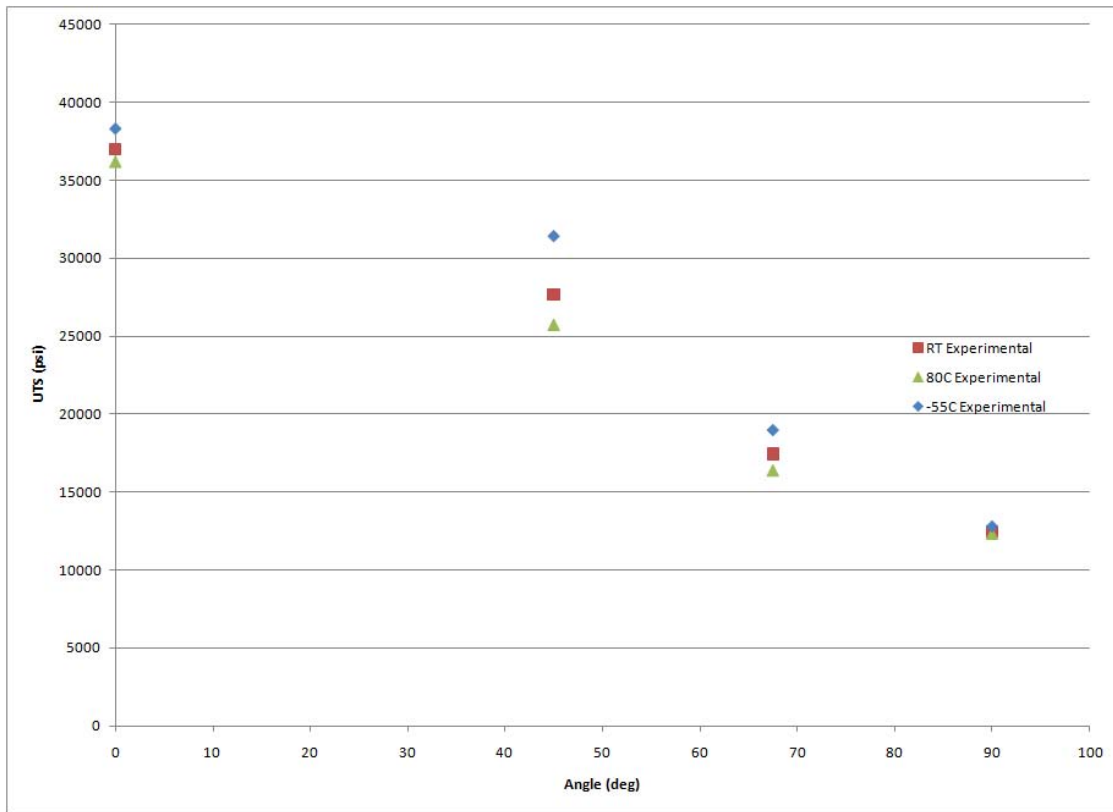

Figure 149 : Overall Blunt Notch Ultimate Tensile Strength Values

Of interest with the ultimate tensile strength values is the general decreasing trend to the minimum at the 90° fiber angle. This is caused by the increase in matrix dominance as the fiber are aligned more perpendicular to the loading direction. Aside from the general decreasing trend, it is seen that the reduced temperature ultimate tensile strength values are consistently higher than those seen with both the room and elevated temperature values. From previous discussion, this strength increase is due to the reaction the FM94K Adhesive matrix material has with the reduced temperature levels; it essentially becomes

232

stiffer in this environment. In contrast to this behavior, the elevated temperature results are shown to be consistently lower than both the room and reduced temperature values. This is due in part to the excessive plasticity and softening of the matrix at these elevated temperatures.

Following, the next figure shows the role both fiber angle and temperature play on affecting CentrAl's blunt notch yield strength.
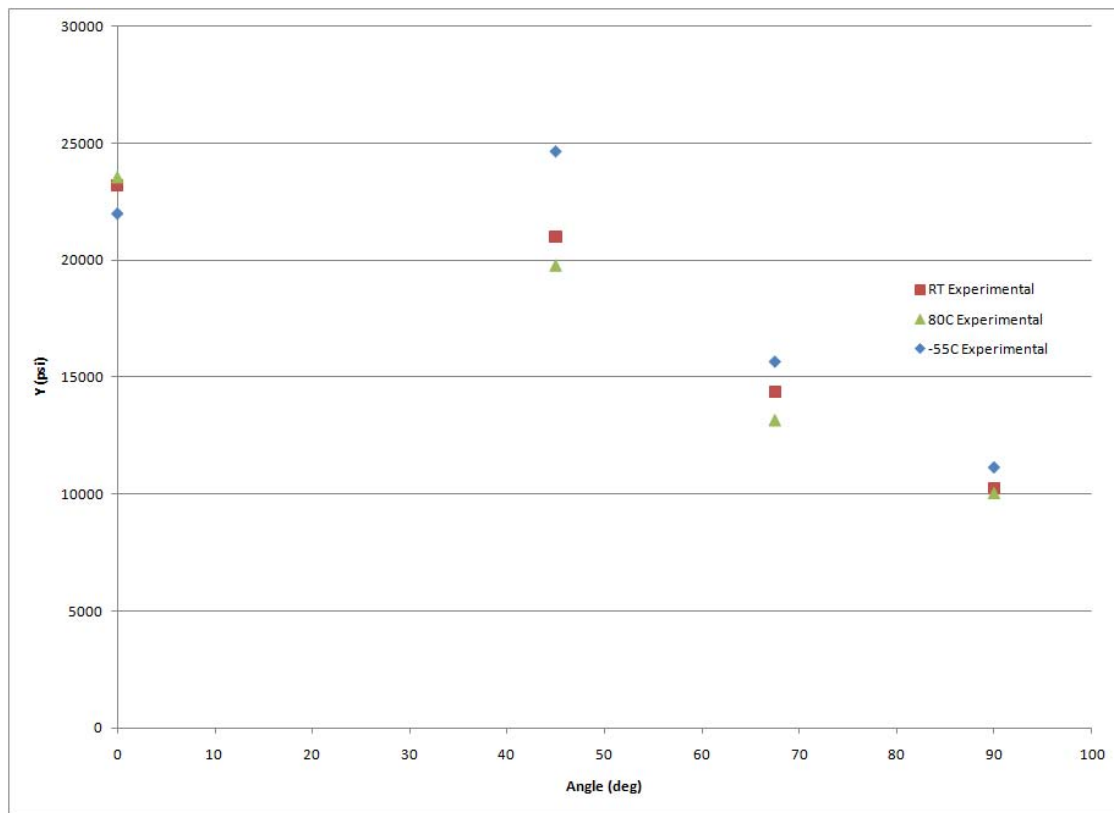

Figure 150 : Overall Blunt Notch Tensile Yield Strength Values

Of interest with the tensile yield strength values is the general decreasing trend to the minimum at the 90° fiber angle. Identical to the influence fiber angle has on the ultimate tensile strength, this is caused by the increase in matrix dominance as the fiber are aligned more perpendicular to the loading direction. Aside from the general decreasing trend, it is seen that the reduced temperature yield strength values are generally higher

than those seen with both the room and elevated temperature values. The exception is that seen at the 0° fiber orientation. From previous discussion, this strength increase is due to the reaction the FM94K Adhesive matrix material has with the reduced temperature levels; it essentially becomes stiffer in this environment. In contrast to this behavior, the elevated temperature results are shown to be generally lower than both the room and reduced temperature values. This is due to the excessive plasticity and softening of the matrix at these elevated temperatures. The exception is seen at the 90° fiber angle, wherein the elevated temperature yield strength is seen to nearly match that of the room temperature value. As seen with the 45° fiber orientation, the reduced temperature results show the greatest increase in the laminate's yield strength. This behavior appears to be contradictory to the general trend of results wherein the increased matrix dominance serves to decrease laminate strength.

The final parameter investigated with the blunt notch investigation was the ultimate strain to failure. The following figure shows the general behavior of the ultimate failure strain influenced by both the temperature and fiber angle variables.
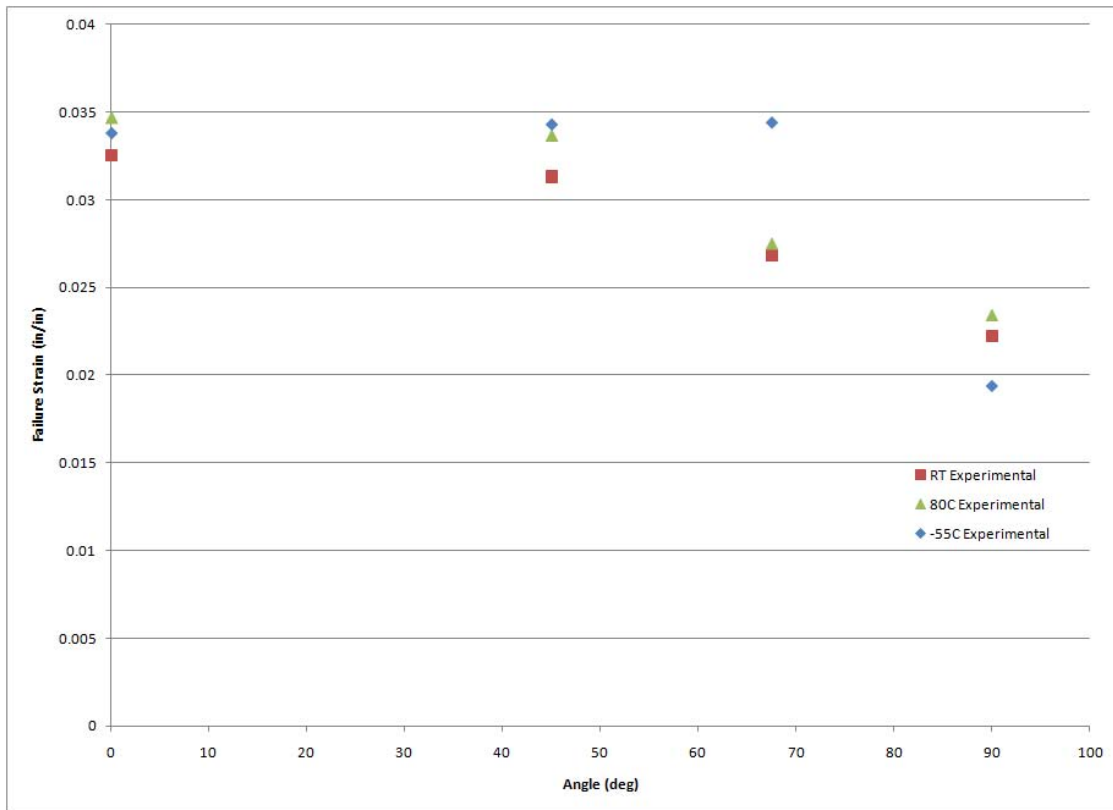
Figure 151 : Overall Blunt Notch Ultimate Failure Strain Values

As with both the ultimate tensile and yield strength values, the ultimate strain to failure is shown to decrease as the fiber angle approaches 90°. Aside from the anomaly seen at 67.5°, the ultimate failure strains seen at each of the temperatures remain closely grouped. Again, as with relative stability the laminate exhibits with regard to its stiffness at the room and reduced temperatures, a closely grouped spectrum of failure strains lends itself well to practical application because of its consistent thermal stability, regardless of the fiber angle.

Room Temperature Tension-Tension Fatigue Testing Results

Recall from the "Experimental Procedure" section, the initial maximum stress induced in the specimen for the first room temperature tension-tension fatigue test resulted in a run-out condition (1,011,170 cycles), as the test was concluded before

specimen failure occurred. From this, it was unsure as to where exactly along the laminate's stress-strain curve this maximum fatigue stress was located. Theoretically, it was less than half of CentrAl's yield strength. To alleviate this problem and more concretely establish the requisite stress levels for the remaining fatigue tests, a tensile test was conducted on the actual fatigue specimen.

Using the procedure described in "Experimental Procedures", the initial tensile test proved to exceed the capacity of the 22-kip servo-hydraulic testing machine. Subsequently, as shown in the "Experimental Procedure" section, the specimen was ultimately altered through reducing its gauge section width by a factor of 2. The second tensile test proved successful and provided the data necessary to establish the remaining fatigue stress levels. The figure below shows the resulting stress-strain curves from each of these tests.
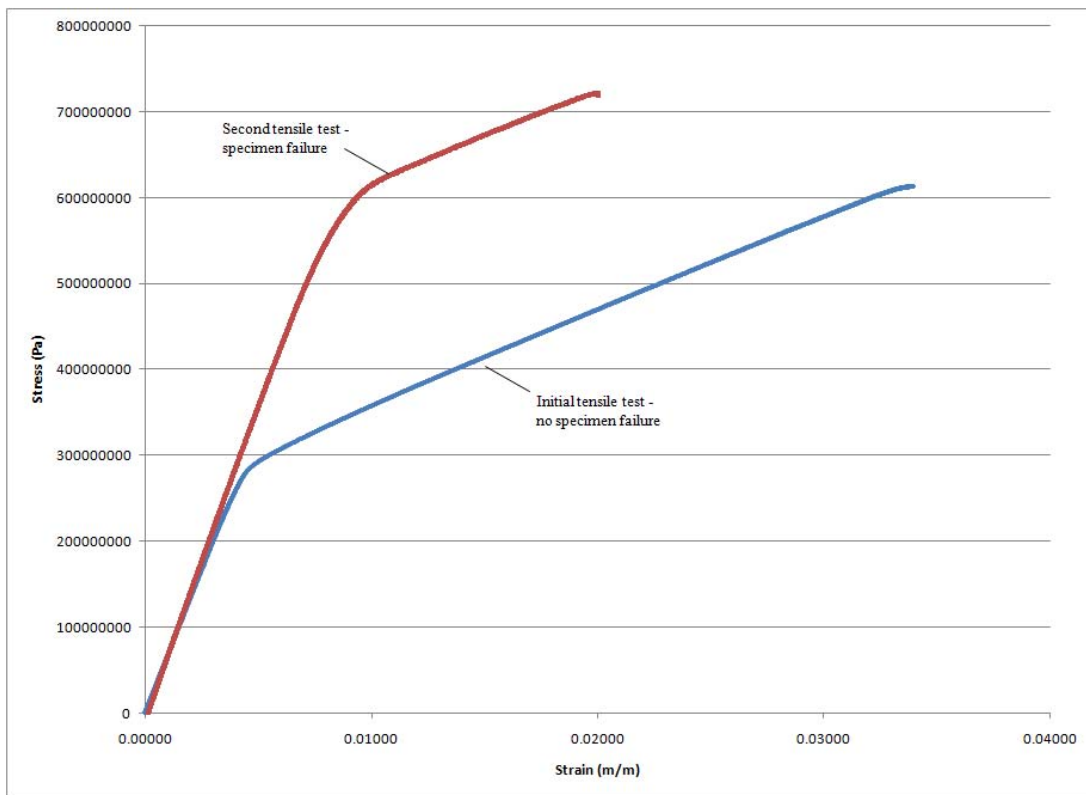

Figure 152 : Stress-Strain Curves for Determining Fatigue Stress Levels

From these curves, the effect of strain hardening is immediately noticeable. As the fist

tensile test, while not inducing complete failure in the specimen, certainly loaded the

laminate past its inherent yield point. Upon unloading and subsequent reloading, the yield

strength in the laminate's yield strength increased. Examining these curves shows the

ultimate stress levels seen in each test. The table below shows these results in both

English and Metric units.

Table 137 : Fatigue Stress Level Ultimate Tensile Strength Values

Test	UTS (MPa)	UTS (ksi)
No specimen failure (original gauge width)	613.25	88.94
Specimen failure (reduced gauge width)	722.62	104.81

It was from the final value of the ultimate tensile strength, measured after the specimen

ultimate failed, that the various fatigue stress levels were determined. Table 27 : Fatigue

Test Stress Levels shows the stress levels used for the fatigue tests.

The figure below shows the resulting specimen at the completion of the successful

tension test.

Figure 153 : Specimen Used for Fatigue Stress Level Determination, 0° Fiber Orientation

The next figure shows a close up view of the failure region within the specimen.

Figure 154 : Failure Region for Fatigue Stress Level Determination Specimen, 0⁰ Fiber Orientation

Though this current discussion is on the effect of fatigue on the CentrAl laminate, it is of interest to note the severe delamination which occurred in this specimen. In contrast to the 0° specimens tested previously, which include the dogbone tensile and blunt notch geometries, this level of delamination was not seen. In fact, with the dogbone tensile geometry, recall failure was restricted to the subsurface layers.

Recall this specimen which was pulled to failure in the tensile test, was not actually a virgin specimen. It had previously been subjected to 1011170 cycles with a maximum stress of 20 ksi at a stress ratio of 0.1, cycled at 5 Hz. This accumulated high cycle fatigue damage resulted in the delamination seen after the tensile test, as shown above. Interestingly enough, despite the run-out condition experienced, there was only a slight change in the laminate's ultimate tensile strength. Recall the ultimate tensile

strength of the un-notched specimen at room temperature was 117.82 ksi. The difference

here is on the order of 11%. Similarly, the elastic modulus, as measured for the tensile

specimen tested to failure was 10.728 Msi. This is a slight increase over the average room

temperature modulus for the laminate of 9.461 Msi. The same measurement was taken on

from the data collected for the initial, incomplete tensile test. The elastic modulus found

for this test was 9.680 Msi. This is nearly identical to the average values seen for virgin

specimens of the same 0° fiber orientations. These simple relationships demonstrate the

retained properties of the laminate.

In total, six fatigue specimens were tested. The results of these tests are shown in

the accompanying figure which depicts both the S-N behavior of the laminate and the

results of the theoretical number of cycles to crack initiation. Note the experimental point

annotated with the arrow. This indicates the fatigue test was manually terminated before

actual specimen failure occurred. This denotes the run-out condition.
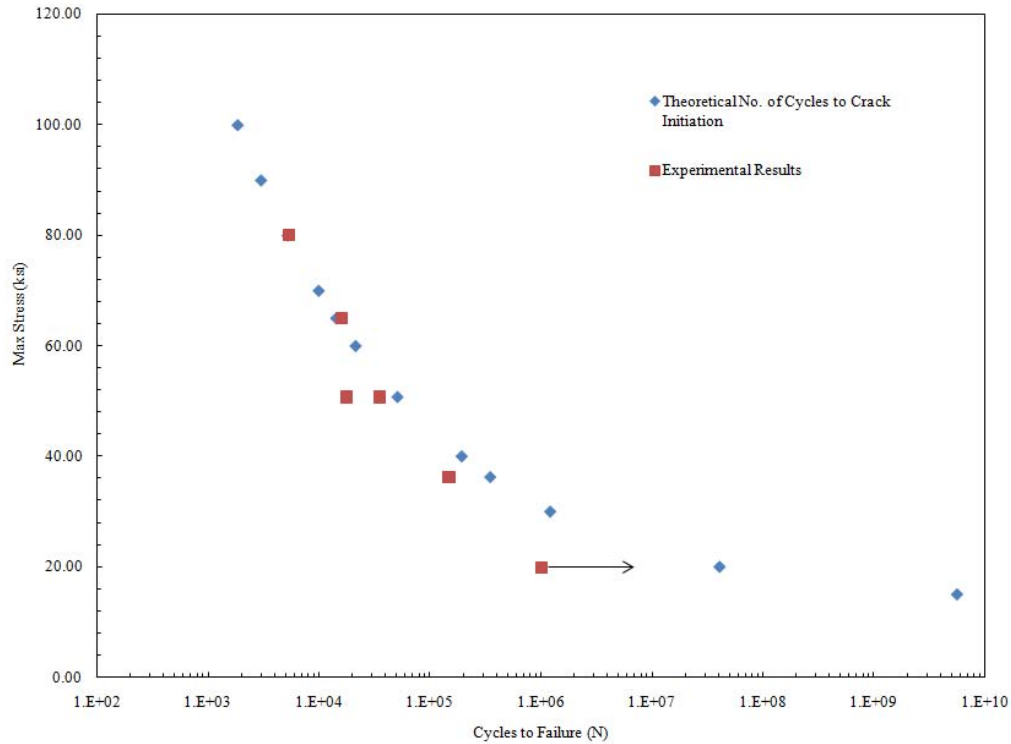
Figure 155 : CentrAl S-N Curve

Of particular interest with this S-N curve is the striking relationship between the experimental results and theoretical prediction to the number of cycles to crack initiation. While fiber metal laminates spend the majority of their life in the crack propagation stage, it is remarkable to the degree of accuracy seen with the number of cycles to crack initiation within the laminate. As this theory was initially developed to predict the number of cycles to initiate a crack in traditional GLARE materials, applying it to CentrAl, which has a greater amount of aluminum per volume, appears to accurately predict the number of cycles to failure.

Aside from producing CentrAl's S-N curve, the laminate's hysteresis response at the various stress levels was constructed. The figures below illustrate the typical stress-strain hysteresis loop for the indicated maximum stress level.
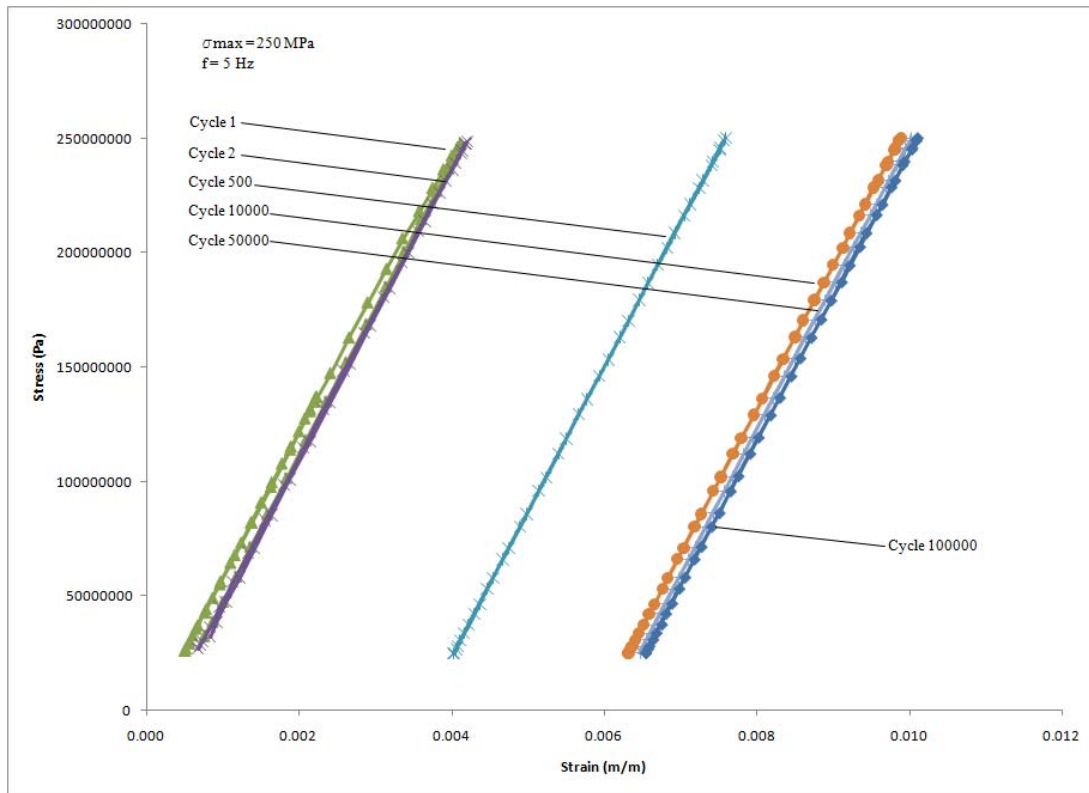
Figure 156 : 250 MPa Hysteresis Loops

From this figure, the strain accumulation throughout the duration of the test is clearly

seen. However, with the relative stability of each hysteresis loop, there is no definite

indication of whether or not one cycle induces more damage into the laminate than

another. This indication of damage would be seen as an obvious separation between the

loading and unloading paths along the stress-strain. This phenomenon is far more

pronounced in the next figures taken from data at the higher fatigue stress levels.
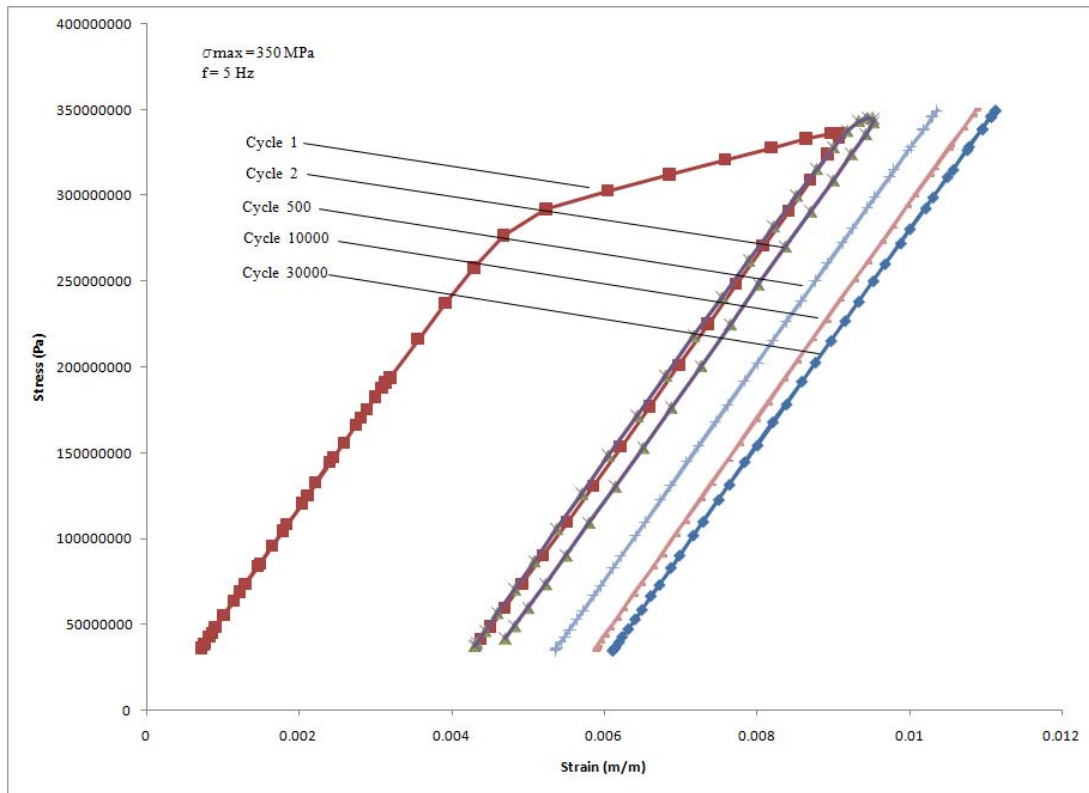
Figure 157 : 350 MPa Hysteresis Loops

In contrast to the lower 250 MPa fatigue stress level, the higher 350 MPa stress clearly

shows the most the significant amount of damage occurring on the first cycle. This

induced damage is seen as the large permanent strain. The amount of accumulated

damage is seen to reduce significantly on the second cycle. As the test progressed, the

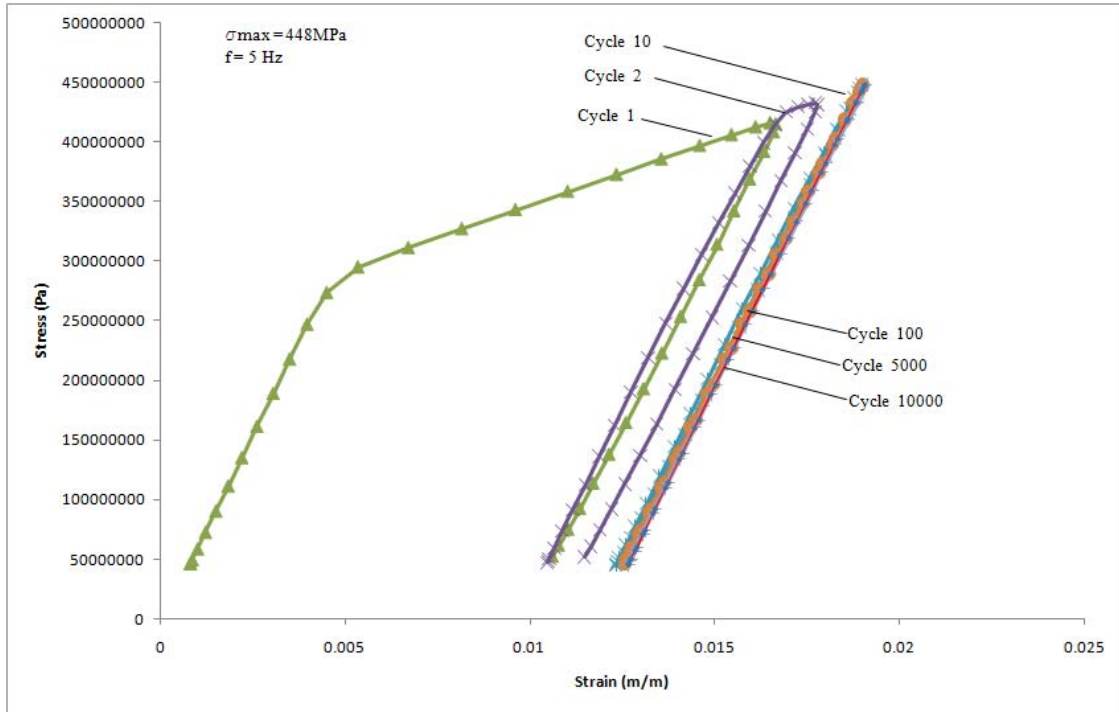loops stabilize, and the amount of accumulated damage reduces considerably. This same

trend is seen on the next figure as well.

Figure 158 : 448 MPa Hysteresis Loops
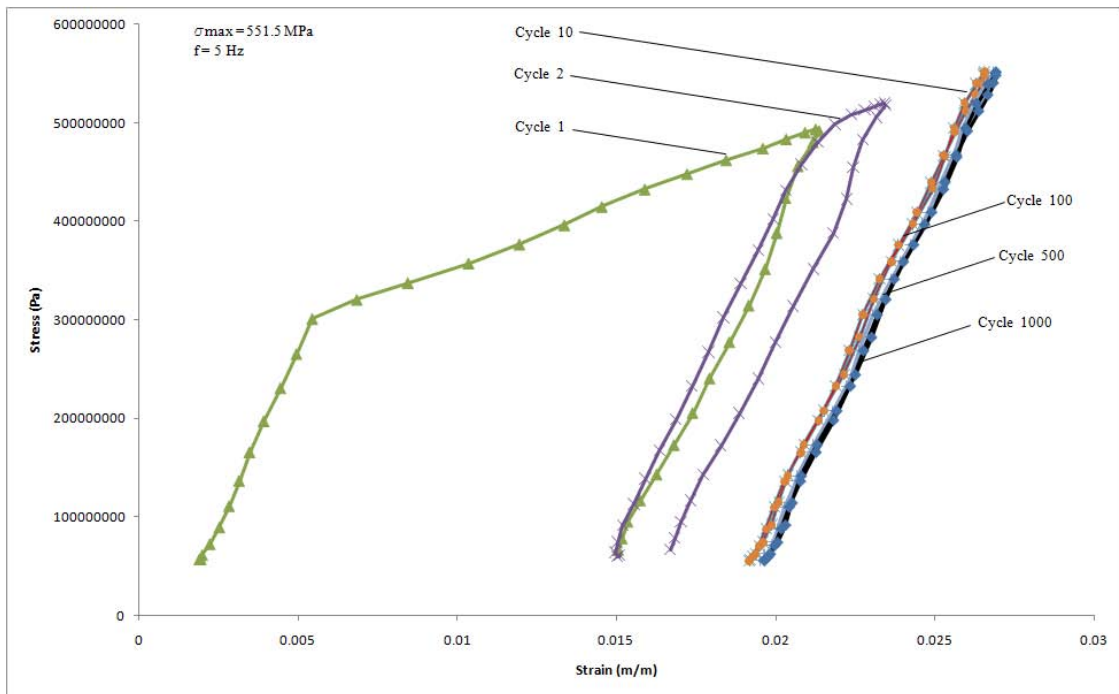
Figure 159 : 551.5 MPa Hysteresis Loops

From these final figures, the large damage accumulation on the first cycle is seen as the significant amount of permanent strain. Aside from the first cycle trend, it is noteworthy

243

to point out the final stress-strain loops on both the 448 and 551.5 MPa curves. There is

virtually no additional strain accumulation during these higher cycle counts.

Another piece of information collected from the fatigue tests is the total amount

of strain accumulation throughout the duration of the tests. While the hysteresis loop

plots give an indication as to the magnitude of accumulated strain, directly plotting this
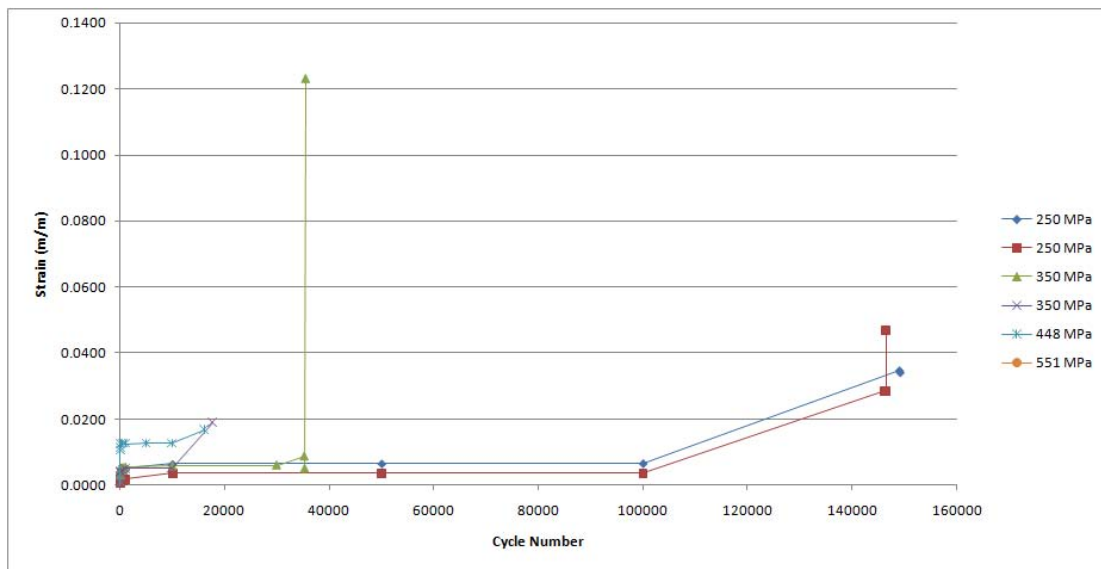
information provides a more clear understanding of this behavior.

Figure 160 : CentrAl Fatigue Test Strain Accumulation

Examining this figure shows a phenomenon known as ratcheting, occurring throughout

the entire range of stress levels. This behavior is defined as a progressive increase in

strain accumulation with increased cycle number. It is most pronounced with the higher

maximum stress levels, as was indicated on the hysteresis loop plots. When examining

the lower stress levels, the accumulated strain is shown to be less dramatic, but it is still

present. The most prominent increase in strain with these lower stress levels is seen in the

moment right before ultimate material failure. This overall behavior of strain

accumulation is shown to mirror that of the elastic modulus evolution. There is a

relatively constant strain in the material, right until the moment of failure, where the strain rapidly increases.

The final piece of information gleaned from the fatigue tests is the evolution of the elastic modulus as measured from the hysteresis loops. These measurements were taken from the minimum and maximum stress and strain levels as measured in the hysteresis loops. The evolution of the elastic modulus gives a direct indication as to the accumulated damage occurring within the fatigue loading spectrum. On the figure below, the elastic modulus is seen normalized against a constant value. Each cycle's elastic modulus was normalized against that value obtained from the second cycle of each fatigue test. This was done because of the large permanent strain observed upon unloading; this is clearly seen in the hysteresis loops for the higher stress levels.
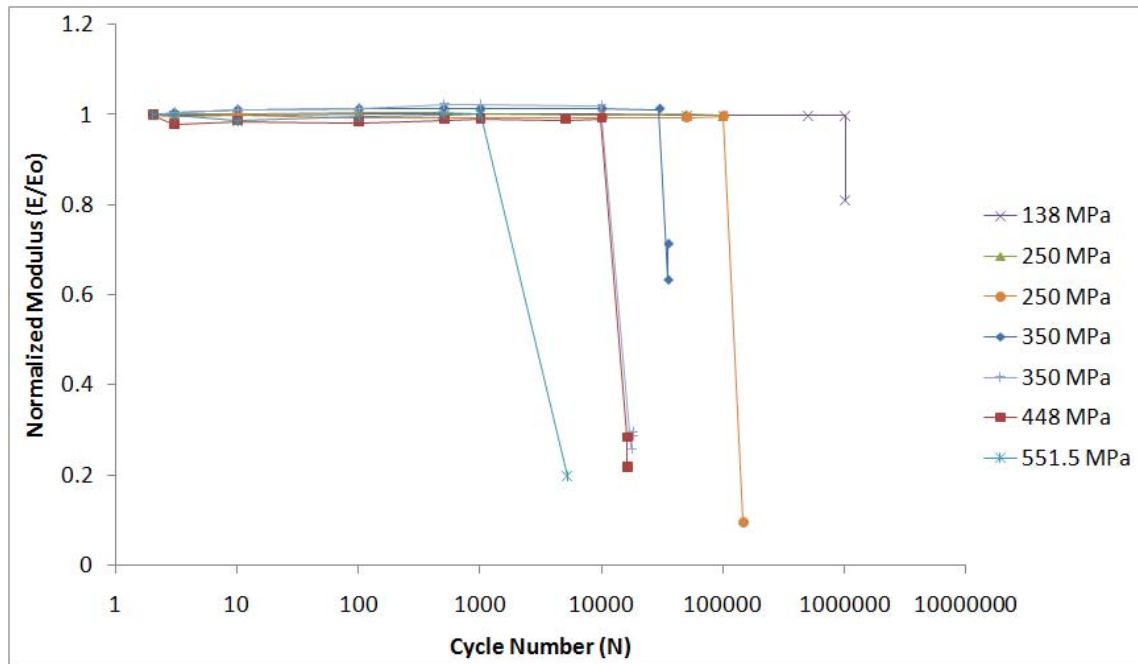

Figure 161 : Modulus Evolution

It is immediately apparent from this figure how relatively stiff the laminate remains throughout its life cycle history. Analogous to the behavior seen in the strain

245

accumulation, the most significant change occurs in the final moment before ultimate

material failure. This behavior shows how the laminate is able to maintain its strength

across a wide range of stress levels. A drawback to this behavior is the lack of indication

of material failure. While many materials will shows serious signs of degradation during

cyclic loading, CentrAl is seen to fail suddenly as exhibited by the modulus curves in

Figure 161 : Modulus Evolution shown above. Note the behavior seen at the final cycle.

There is a steep drop in the laminate's overall stiffness.

Of additional interest is the actual fatigue specimens themselves. After cycling,

the maximum stress level used during the test had a significant impact on the appearance

of the failed specimens. The figure below shows the failed specimen which was subjected

to the highest maximum stress level.

Figure 162 : Failed Fatigue Specimen Number 43 - 551 MPa

Note the way in which the fibrous layers beneath the thicker outer Aluminum facing

sheets remained relatively intact, in that the fibers are still aligned in their original

orientation. This indicates a rapid failure mechanism, as the fibers did not have the

opportunity to distort or realign themselves with the growing crack. Another view of the

failure region is presented below.

Figure 163 : Failure Region for Failed Fatigue Specimen Number 43 - 551 MPa

The maximum fatigue stress level used for specimen 43 is shown to have caused the bond

between the thicker facing sheets and the BondPreg®, along with the bond between the

inner thin sheets and prepreg to fail, thus pulling the aluminum away from its fibrous

reinforcement, hence the exposed fibers.

This behavior is also seen in the failed fatigue specimen in the next figure. Here,

the maximum stress level was slightly less than that used for specimen 43. The maximum

stress for this test was 448 MPa. Again, note the rather "clean" surface across which the

fatigue crack grew and ultimately destroyed the specimen.
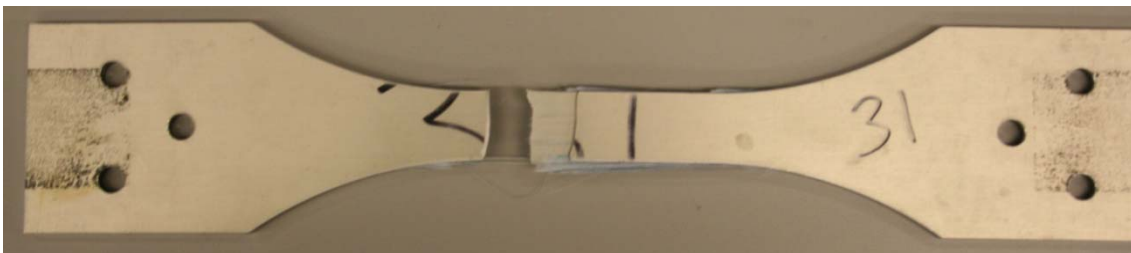
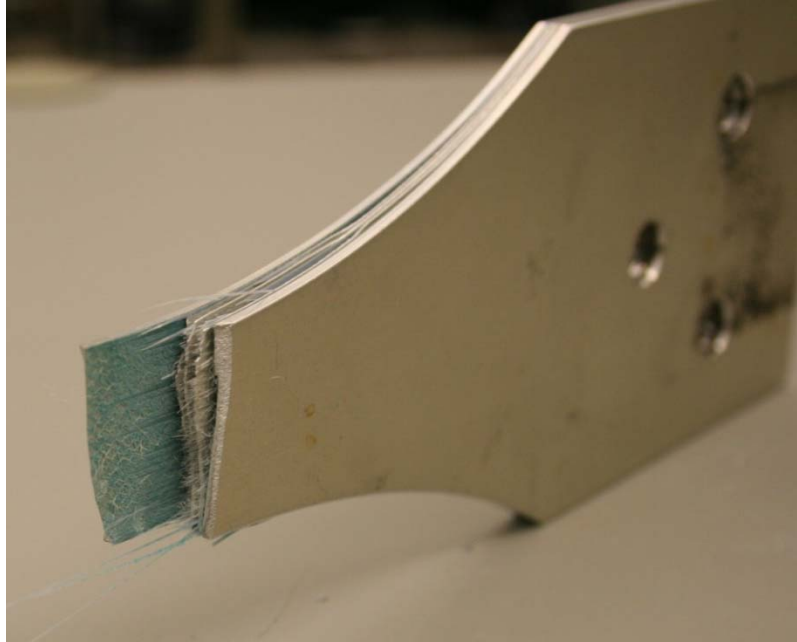Figure 164 : Failed Fatigue Specimen Number 31 - 448 MPa

Figure 165 : Failure Region for Failed Fatigue Specimen Number 31 - 448 MPa

Here again, the failure region is clearly seen as "clean" in that there are not a great number of fibers exposed in the failure area. Unlike the failure region of specimen 43, the bond between the aluminum and the fibrous layers has remained somewhat intact. At this stress level, the magnitude of disbonding did not occur. While not a significant amount of disbonding is not seen in the immediate failure region, notice the slight delamination present a distance away from the failure region. Here, the separation between the individual lamina is clearly seen.

Figure 166 : Another View of Failure Region for Failed Fatigue Specimen Number 31 - 448 MPa

As the maximum fatigue stress level decreases, the amount of fibrous material in the failure region increases. The first example of this behavior is shown below in fatigue failure at 350 MPa.
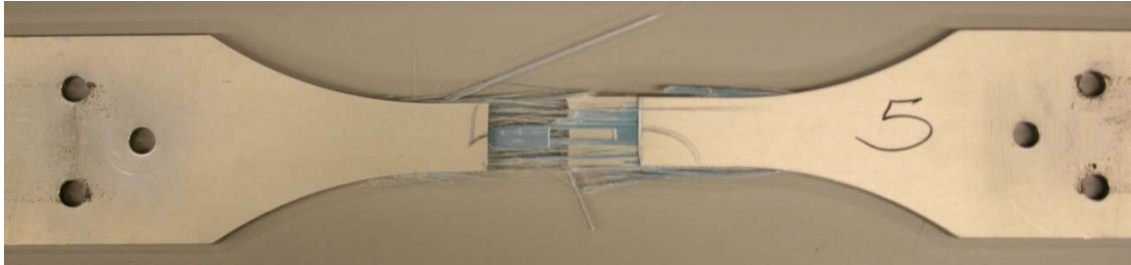

Figure 167 : Failed Fatigue Specimen Number 5 - 350 MPa

Notice at this maximum stress value, there is still delamination between the BondPreg® and the outer facing sheets. However, because of the testing duration, there was more time to permit the bond between FM94K adhesive matrix material and the S2-Glass fibers to fail. The "clumping" seen are areas of intact prepreg and BondPreg® wherein the fiber and matrix remains a single entity. Some of the bonds holding the fibrous layers together have broken, while at the same time, some are seen to be intact. For both of the specimens tested at this maximum fatigue stress of 350 MPa, this failure mechanism was common. An alternate view of this failure region is shown below.
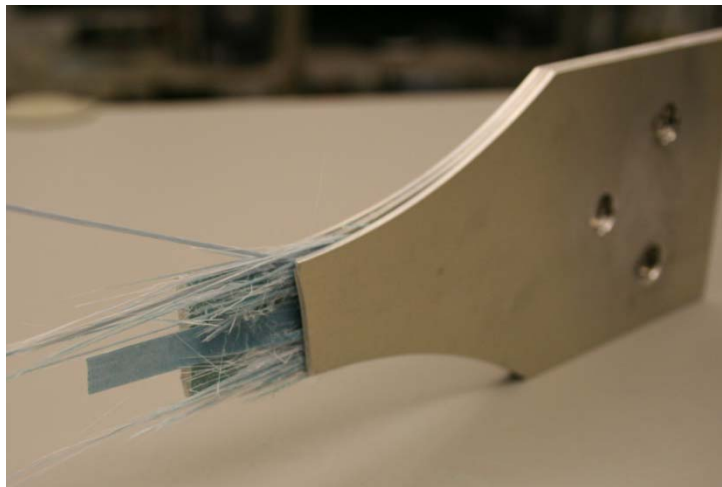

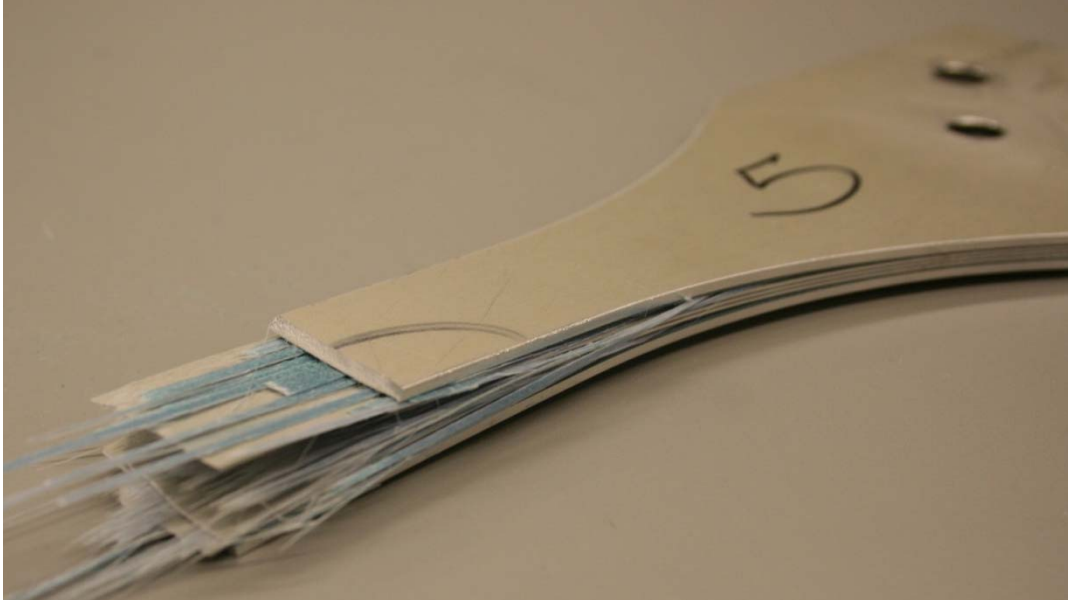Figure 168 : Failure Region for Failed Fatigue Specimen Number 5 - 350 MPa

Figure 169 : Another View of Failure Region for Failed Fatigue Specimen Number 5 - 350 MPa

At the lowest maximum fatigue stress level which actually caused material failure, 250 MPa, the failure region was extremely fibrous. Because of the testing duration, the bonds between the individual fibers and matrix material were broken. Additionally, the bonds between the aluminum and fibrous layers, has also be destroyed. Examination of the failed specimen is evident of this behavior.
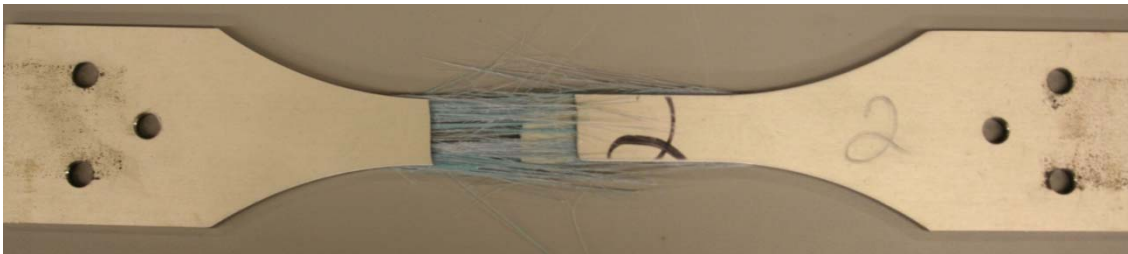

Figure 170 : Failed Fatigue Specimen Number 2 - 250 MPa

Notice at this stress level there is no clear evidence of large sections of intact prepreg or BondPreg®. The individual fibers and matrix material have been separated.
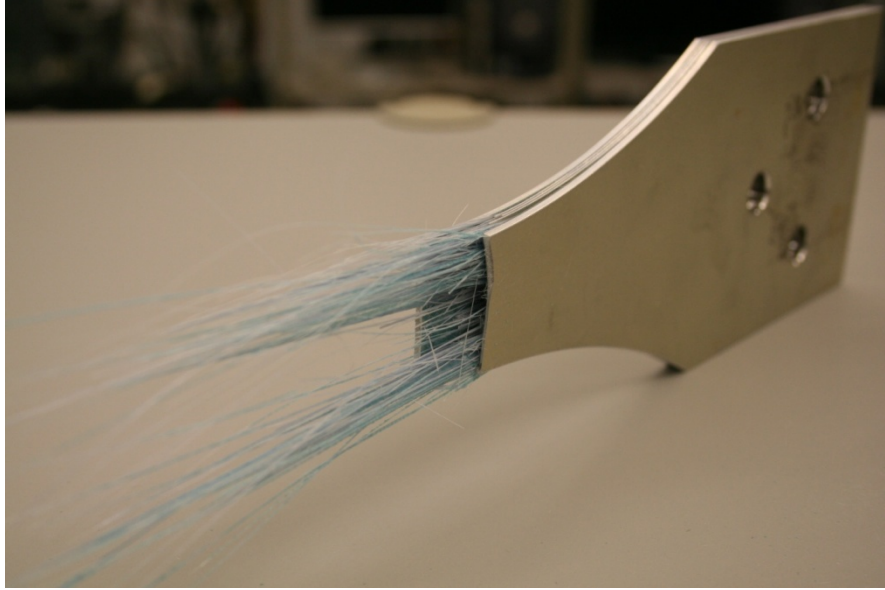
Figure 171 : Failure Region for Failed Fatigue Specimen Number 2 - 250 MPa

IX. Concluding Remarks

From the results of the initial modulus tests, it is seen how the metal volume fraction approach does indeed lend itself to predicting CentrAl's elastic modulus. The percent difference between the theoretical values obtained via the metal volume fraction approach and the room temperature experimentally obtained values for the four fiber orientations - 0°, 45°, 67.5^o, and 90° - was 4.07%, 4.59%, 2.59%, and 1.27% respectively. For the elevated temperature results, a direct comparison was made to those results of the room temperature experimental values, as the metal volume fraction methodology used in this thesis research did not accommodate changes in temperature; the theory was used for predicting room temperature values.

When comparing the elevated temperature results to those found during the room temperature experiments, the ratio of these two moduli (elevated temperature to room temperature) for each of the fiber orientation was 0.997, 0.998, 1.016, and 0.999 respectively. The percent change from the room temperature values to the elevated temperature values was 0.26%, 0.23%, 1.58% and 0.13% respectively. From these results it is shown that CentrAl's elastic modulus does not vary by an appreciable amount at the elevated temperature. In contrast to traditional GLARE, which has a decreased amount of aluminum by volume, this newest fiber metal laminate does not exhibit noticeable change in stiffness at this temperature.

With regard to the reduced temperature testing, the laminate is shown to exhibit a very slight increase in modulus. The ratio between the reduced temperature to the room temperature modulus, for each of the fiber orientations was 1.07, 1.07, 1.13, 1.07,

252

respectively, indicating a stiffness increase. The percent difference between the reduced and room temperature values were 6.67%, 7.18%, 13.25%, and 6.82%. This increased percent difference is due to the slight increase in elastic modulus realized by the laminate at the reduced temperature.

The monotonic tensile testing was conducted in an effort to investigate the laminate's stress-strain curves. The results from this series of experiments leave questions to their accuracy. For each of these tests, only a single specimen was used for each of the four fiber orientations. This questionable accuracy is especially true for the elevated temperatures tests. For these tests, the results showed an increased in overall laminate strength over that of both the room temperature and reduced temperature tensile tests. Due to the statistical inaccuracies associated with performing only a single test on a single specimen, only one single data point is seen. For additional confidence, further tensile testing should be performed on the laminate. A minimum of three tests should be performed for a given fiber orientation in order to garner more meaningful results.

The results of the blunt notch tests proved to be useful in that they were statistically accurate and provided insight into the laminate's strength characteristics in the presence of a hole. The average stiffness values for the room temperature and reduced temperature results are shown to closely correlate with one another. Each of these values is very close in magnitude with one another throughout the entire range of fiber angles. The elevated temperature stiffness values, especially for the off-axis results, are shown to be below both the room and reduced temperature tests on the order of 14-17%. With the 45° fiber orientation, the stiffness of the elevated temperature blunt notch specimens show a reduction of approximately 21%. With the ultimate tensile strength, the elevated

temperatures serve to consistently reduce the laminate's capability. The overall magnitude of the values approaches a minimum at the 90° fiber angle. The room temperature results are shown to be an approximate median value between the two temperature extremes. The reduced temperature ultimate tensile strength is shown to have the greatest increase over the room temperature results at the 45° fiber angle. This increase is on the order of 13.5%. The elevated temperature results show a relatively small decrease in ultimate tensile strength across the entire range of fiber angles. This decrease in strength is on the order of 5-8% for the intermediate fiber angles of 45° and 67.5° and approximately 1.5-2% for the 0° and 90° fiber angles respectively. The yield strength values follow a similar trend, in that the elevated temperature results are consistently lower than the reduced temperature results. There is one exception found during testing, however. For the 0° fiber orientation, the reduced temperature yield strength was shown to be approximately 5% lower than the results shown with the corresponding room temperature results. Other than this single anomaly, the trend shown with the ultimate tensile strength results is repeated. All values approach a minimum at the 90° fiber angle, and the elevated temperature results are consistently lower than both the room and elevated temperature values. In the intermediate fiber angles, 45° and 67.5° respectively, the reduction in yield strength as measured from the room temperature values was seen to be approximately 6% and 8% respectively. Additional research in this area would include a specimen re-design. This would ensure any edge effects induced by the hole's close proximity to the laminate free edge would be negated.

The room temperature tension-tension fatigue test results provided an S-N curve for the laminate. Of interest is the striking accuracy the CLPT technique provided with

254

the approximate number of cycles for crack initiation. Because CentrAl contains more aluminum by volume than traditional GLARE, this technique proved to reasonably accurate in predicting the number of cycles to failure for CentrAl. Additionally, the elastic modulus was measured throughout each fatigue test. It is remarkable to illustrate that the modulus for CentrAl remains nearly unaffected throughout cyclic loading - that is, until ultimate failure is imminent. This has both positive and negative implications. A positive consequence is that the laminate's overall stiffness remains fairly constant throughout fatigue loading. A drawback to this behavior is the sudden loss in stiffness at the moment failure occurs; there is little to no warning a catastrophic failure is forthcoming. During testing, the accumulation of strain was also measured. At the lower stress levels, thereby implying a longer duration test, the accumulation of strain was seen to remain somewhat constant. This mirrors the behavior seen in the elastic modulus results. The greatest increase in strain seen at the moment failure occurs. Additional research in the area of CentrAl fatigue should focus on the microscopic behavior of the laminate at both the high and low maximum fatigue stress levels. At the higher maximum fatigue stress levels, the failure mechanism is unknown. The higher stresses may induce early delamination within the laminate, and thus the fatigue process is simply a matter of the aluminum fatigue process. The lower maximum fatigue stress levels may permit sustained fibrous influence for the overall laminate fatigue process. These questions can be answered with additional research.

Appendix A: CentrAl NDE C-Scan Images

This appendix contains the C-Scan images produced during the material post-processing phase of the research. The specimen number can be seen in each image, indicating the specimens undergoing the inspection. The images are produced in color. The color indicates the amount of sound transmitted though the laminate. Yellow, reds, and white indicate better sound transmission, while blue, green, violet, and gray hues indicate poorer transmission. Areas of delamination appear as gray regions on the figures.
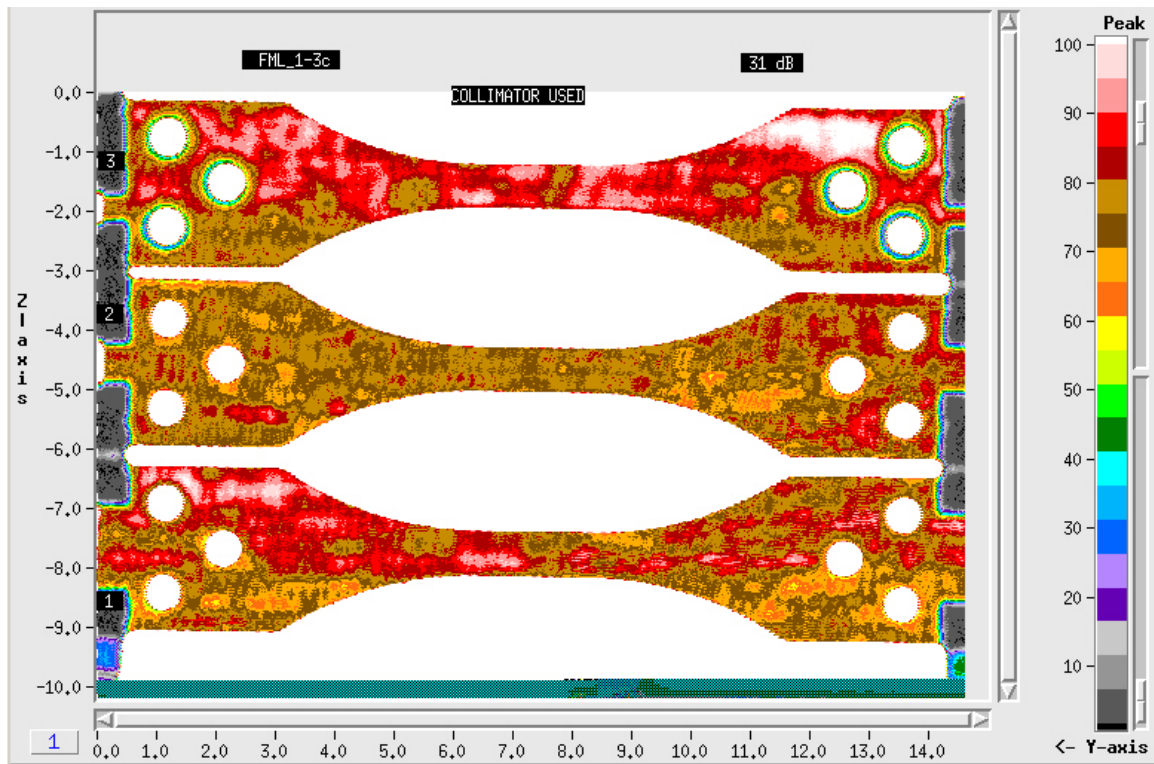
Figure 172 : CentrAl C-Scan - Specimens 1-3
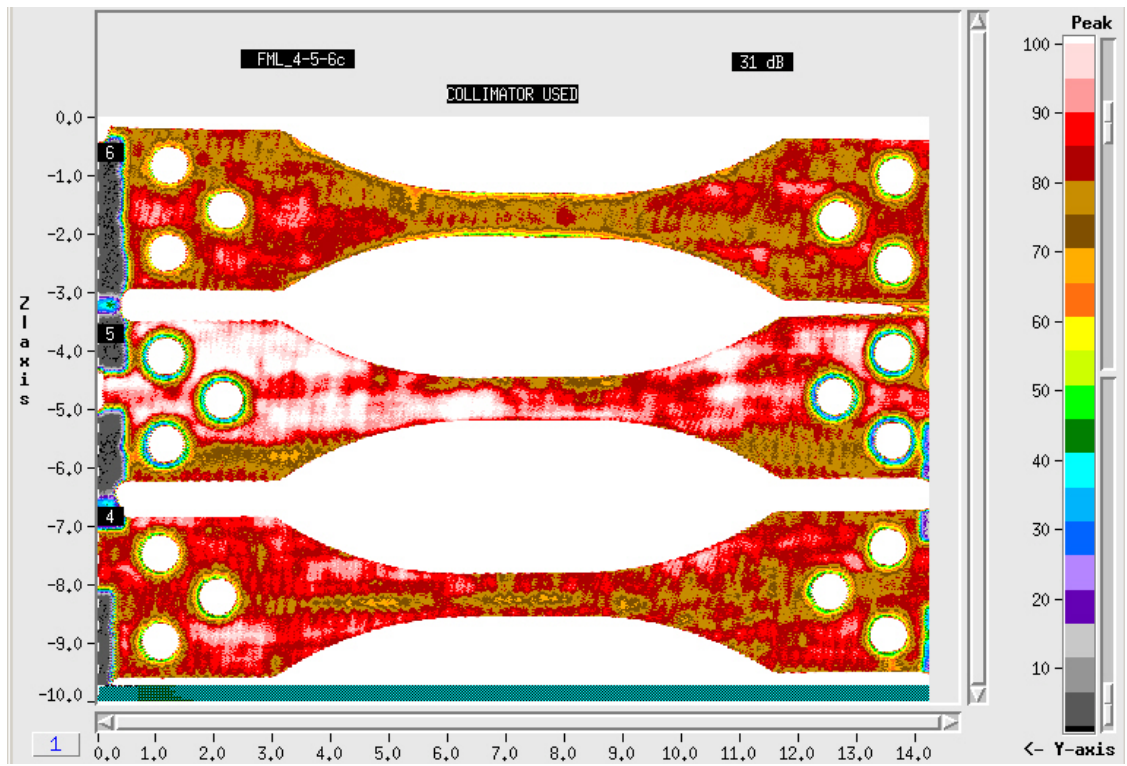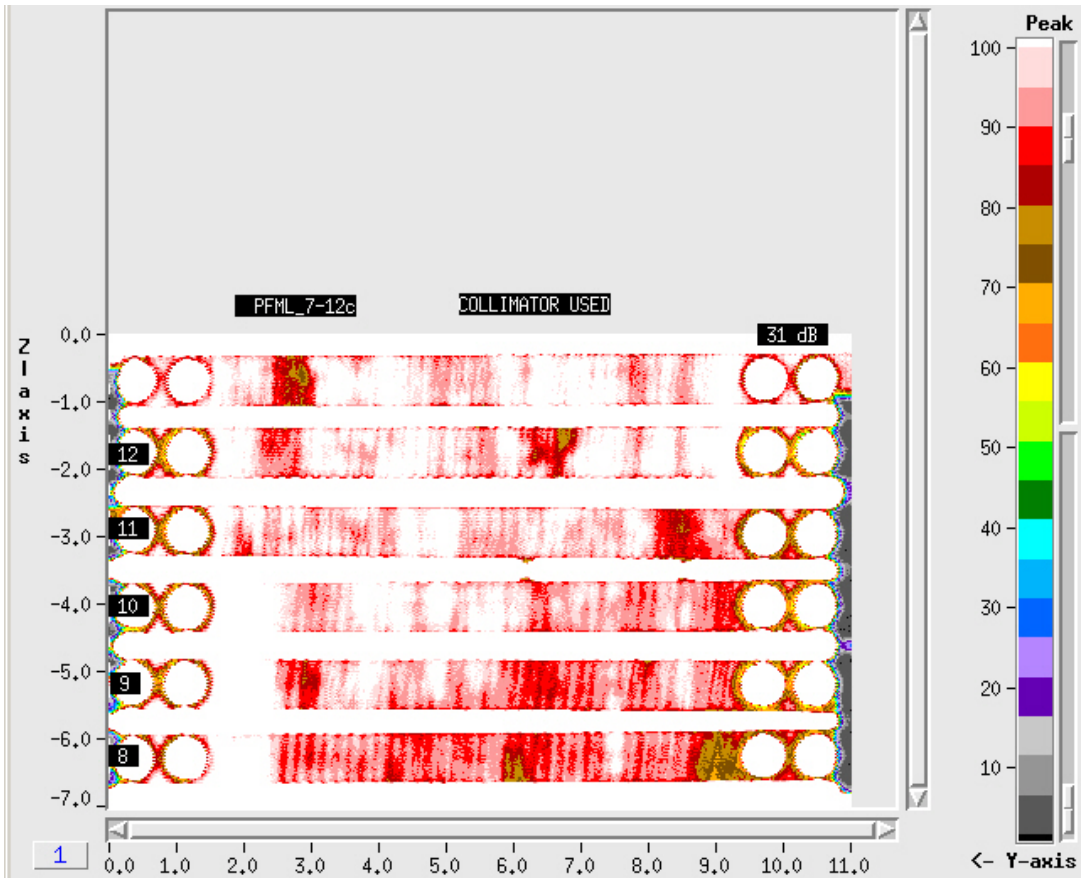
Figure 173 : CentrAl C-Scan - Specimens 4-6

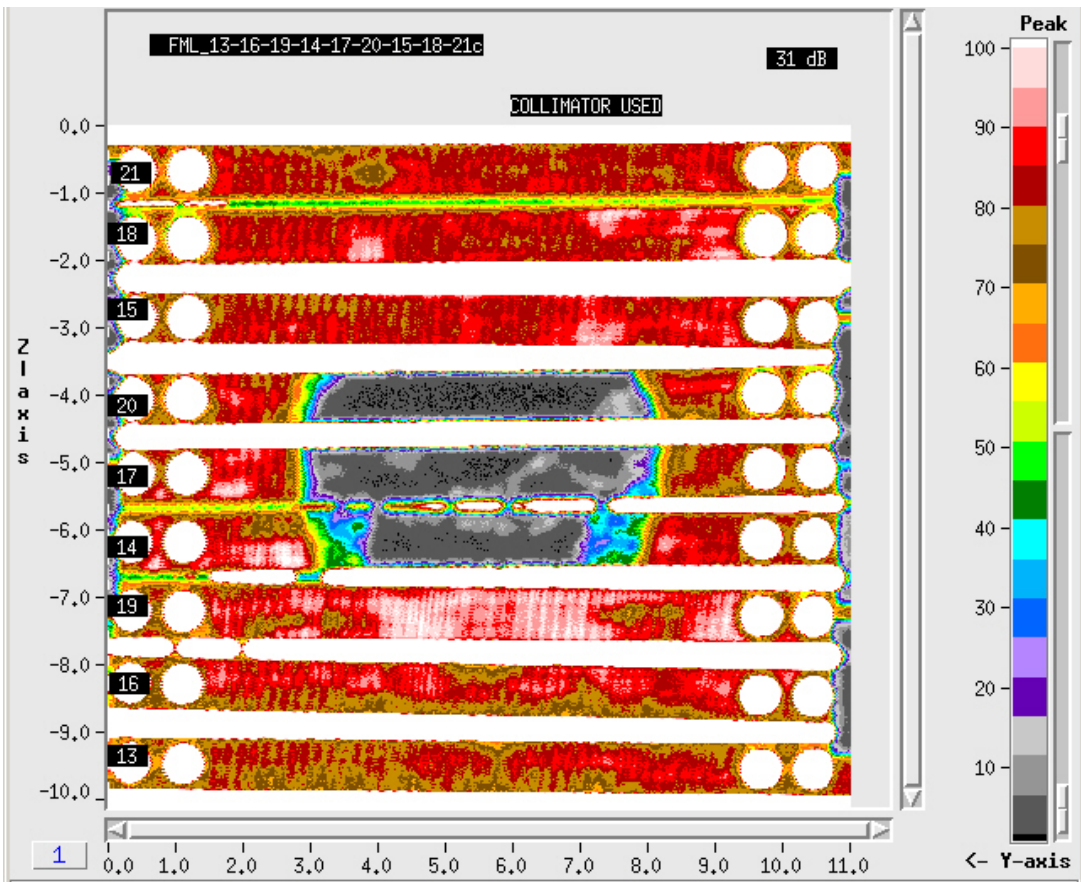Figure 174 : CentrAl C-Scan - Specimens 8-12
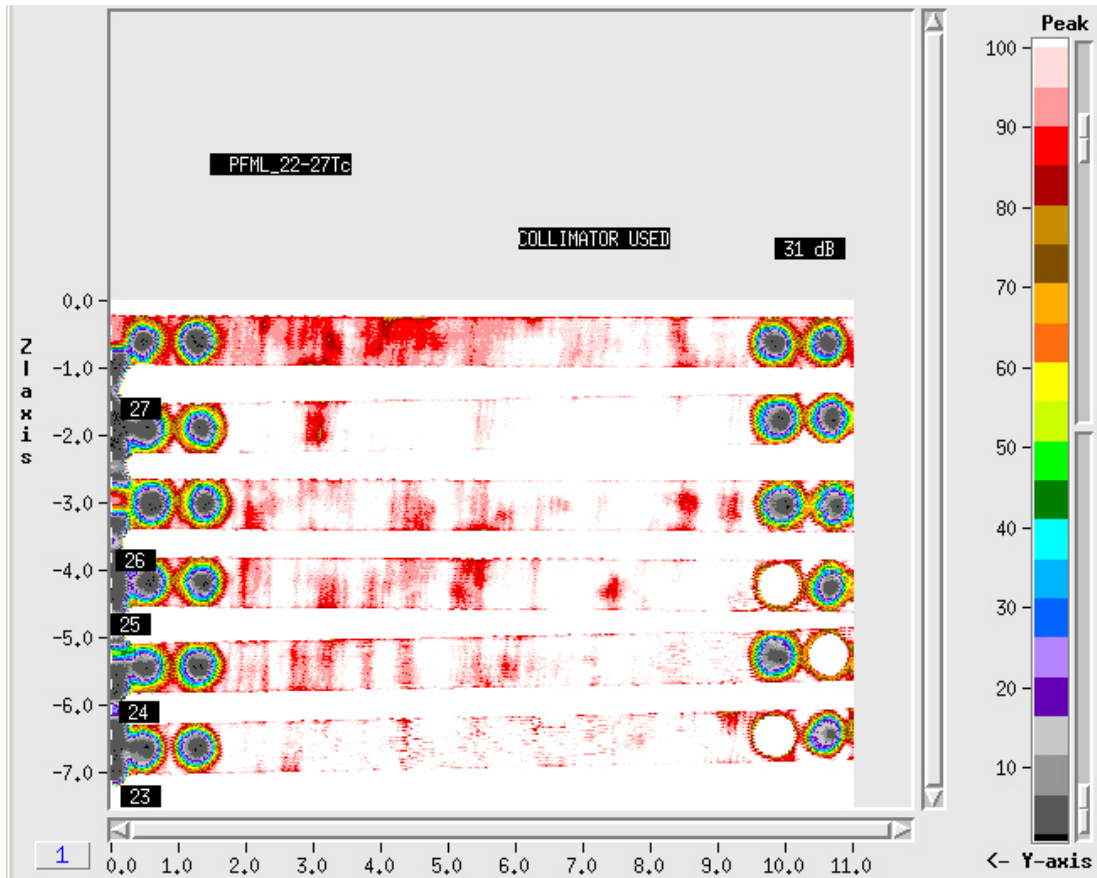
Figure 175 : CentrAl C-Scan - Specimens 13-21

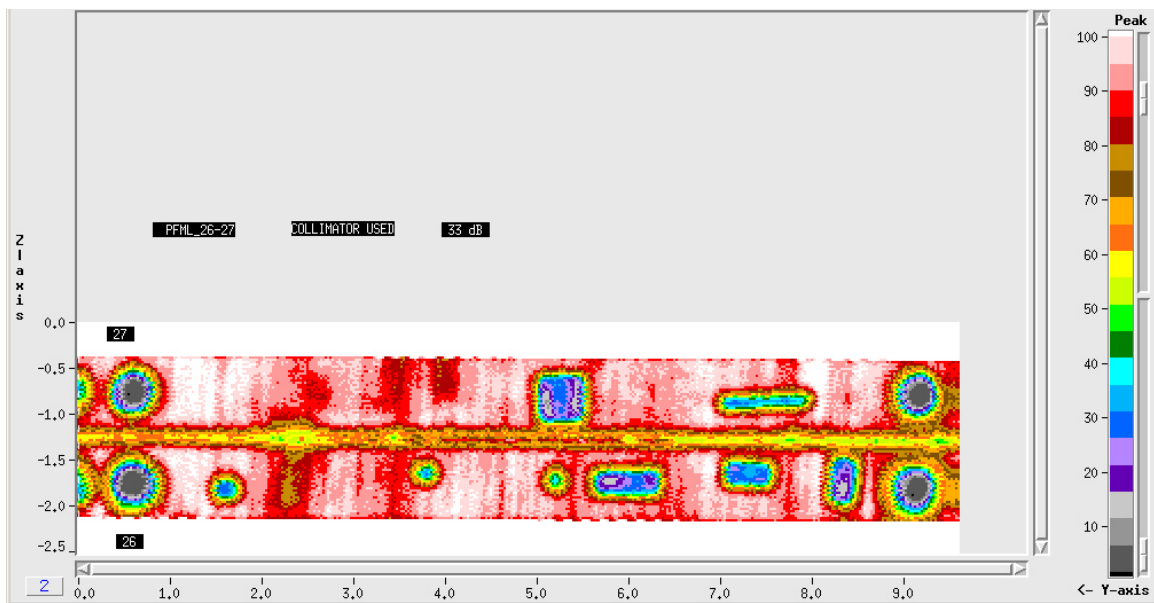Figure 176 : CentrAl C-Scan - Specimens 22-27

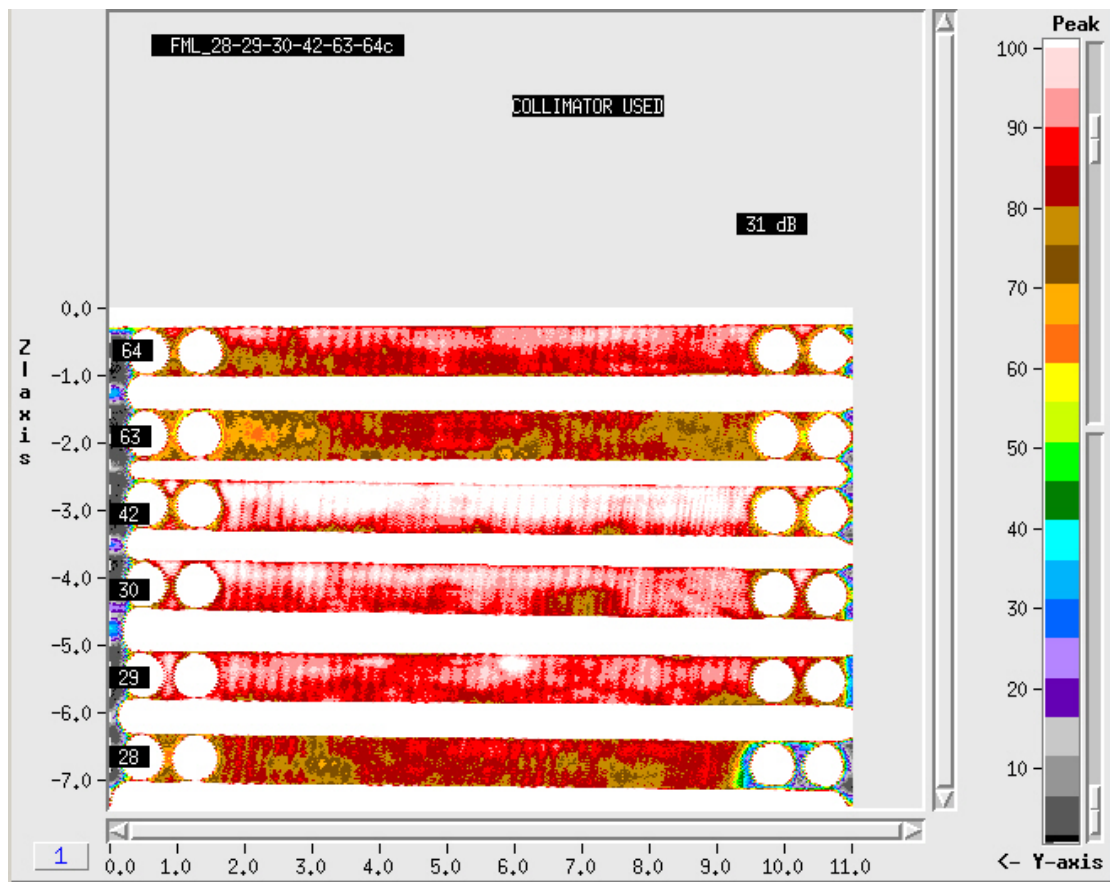Figure 177 : CentrAl C-Scan - Specimens 26-27

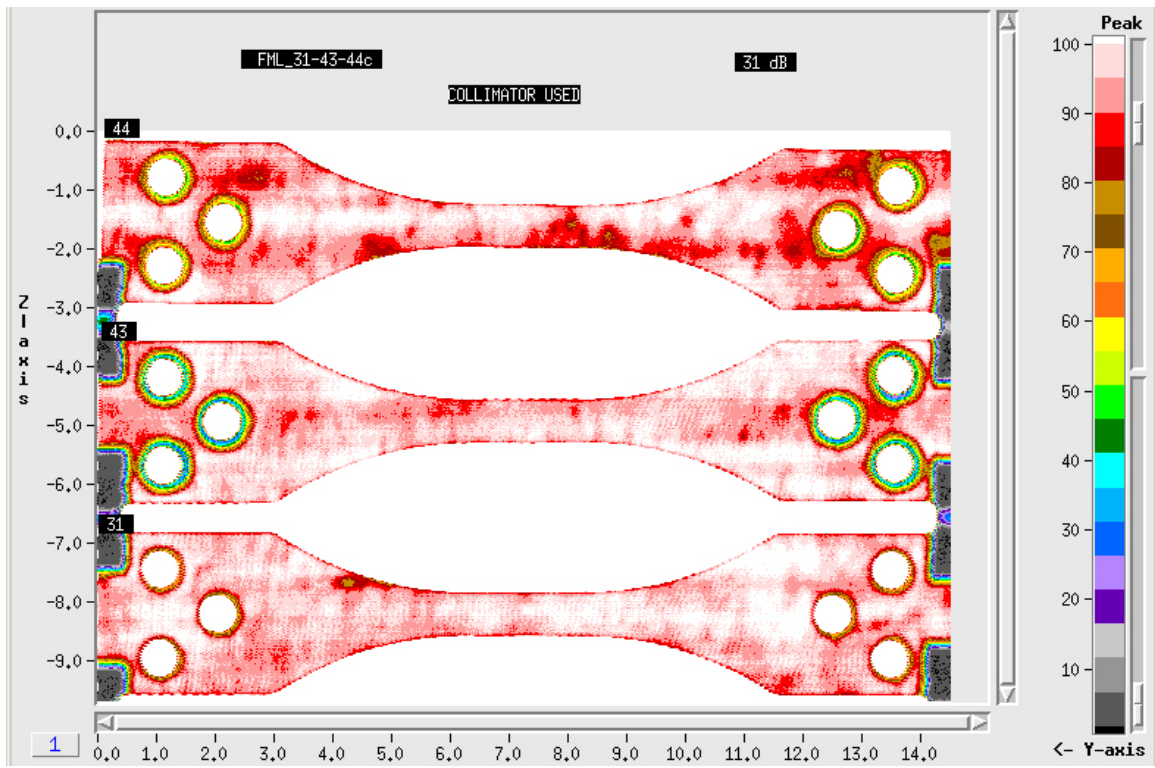Figure 178 : CentrAl C-Scan - Specimens 28-30, 42, 63, 64
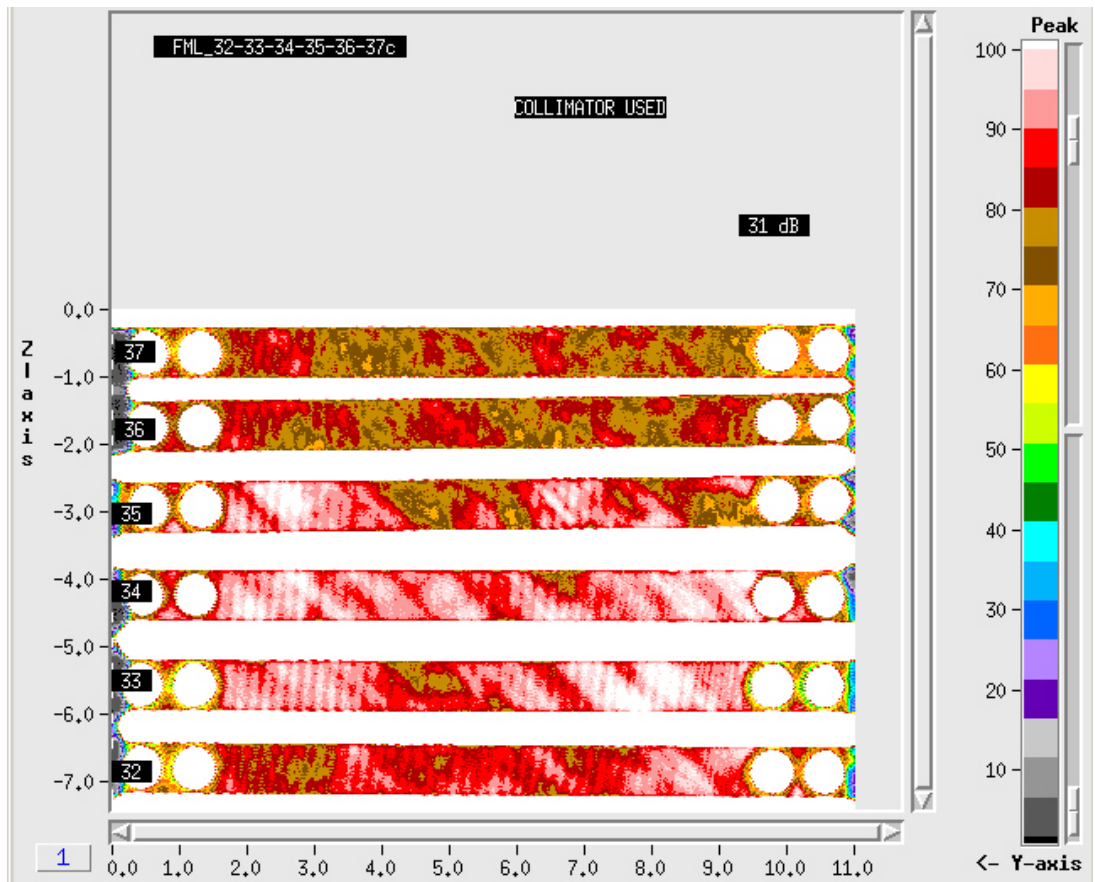
Figure 179 : CentrAl C-Scan - Specimens 31, 43, 44

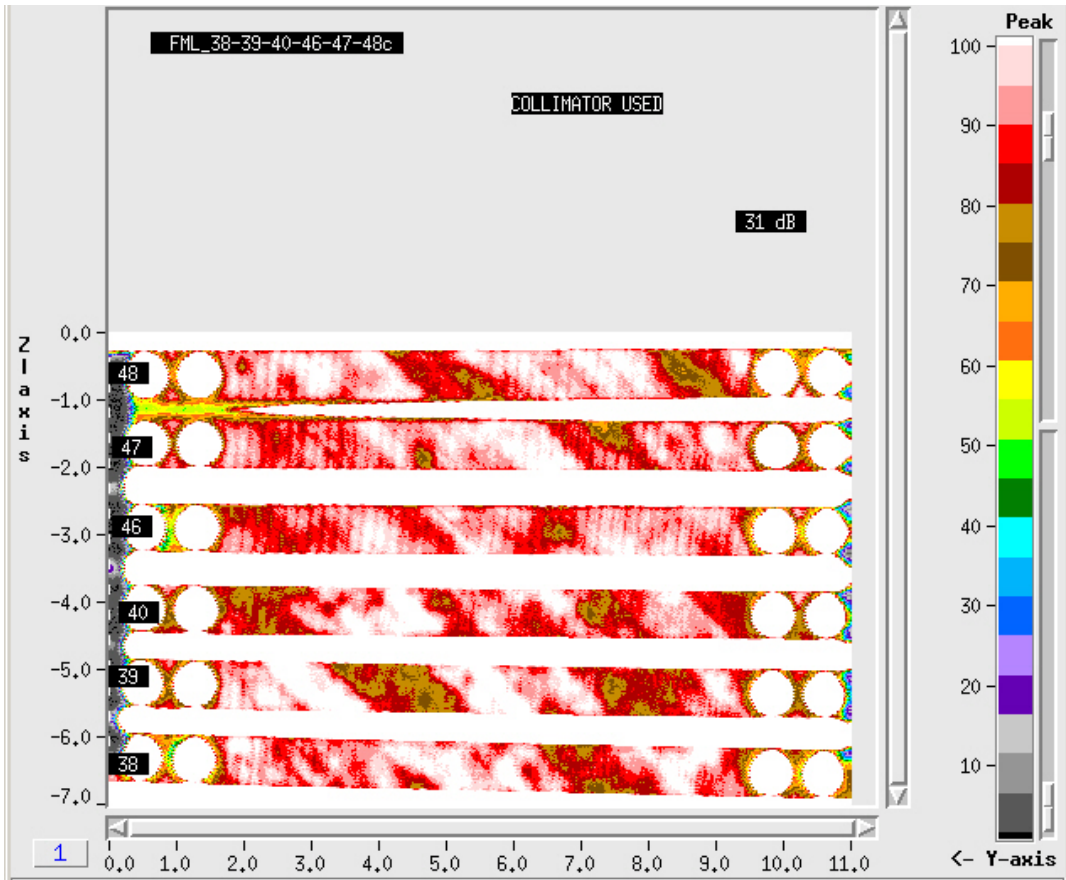Figure 180 : CentrAl C-Scan - Specimens 32-37

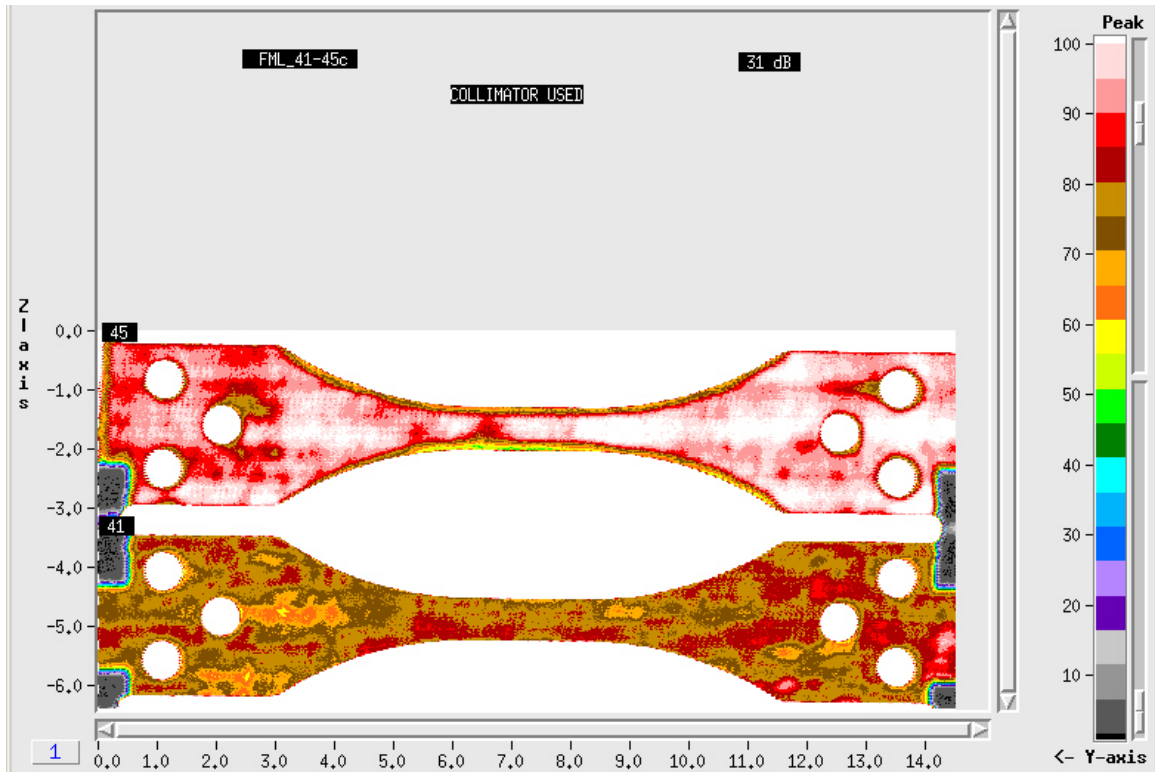Figure 181 : CentrAl C-Scan - Specimens 38-48

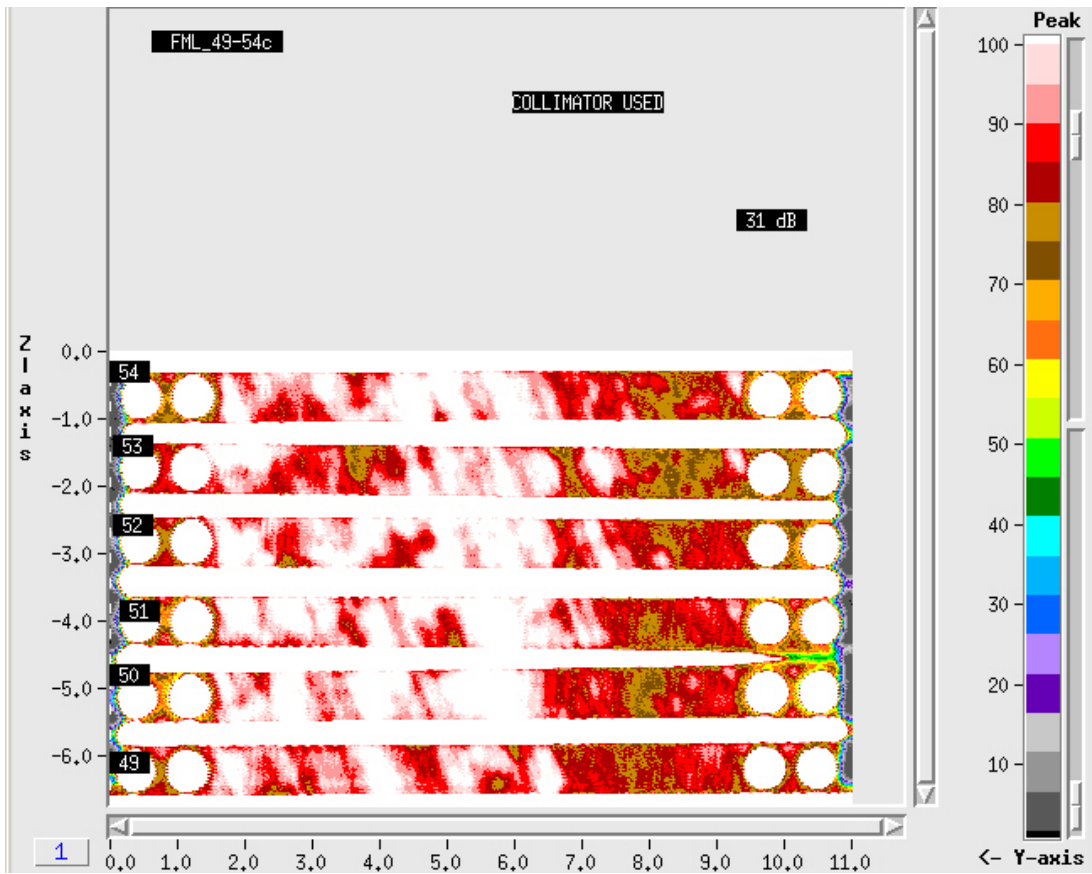Figure 182 : CentrAl C-Scan - Specimens 41, 45

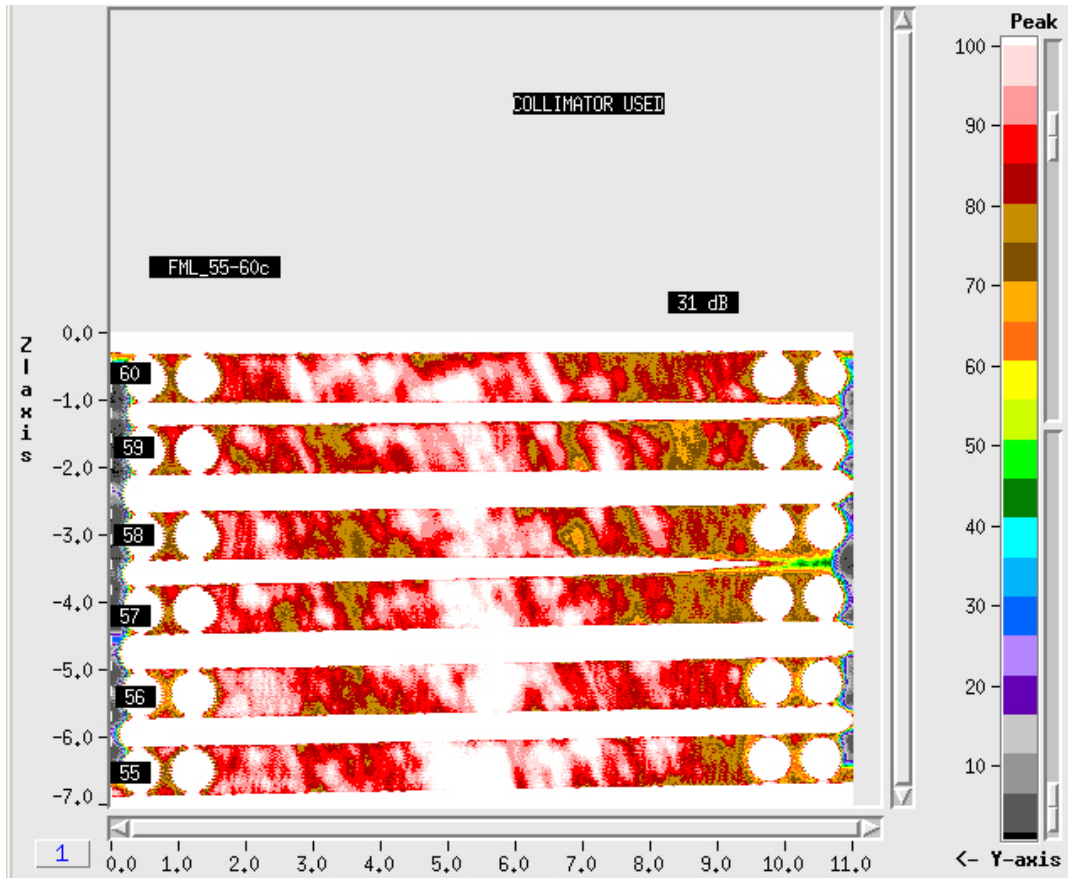Figure 183 : CentrAl C-Scan - Specimens 49-54

Figure 184 : CentrAl C-Scan - Specimens 55-60

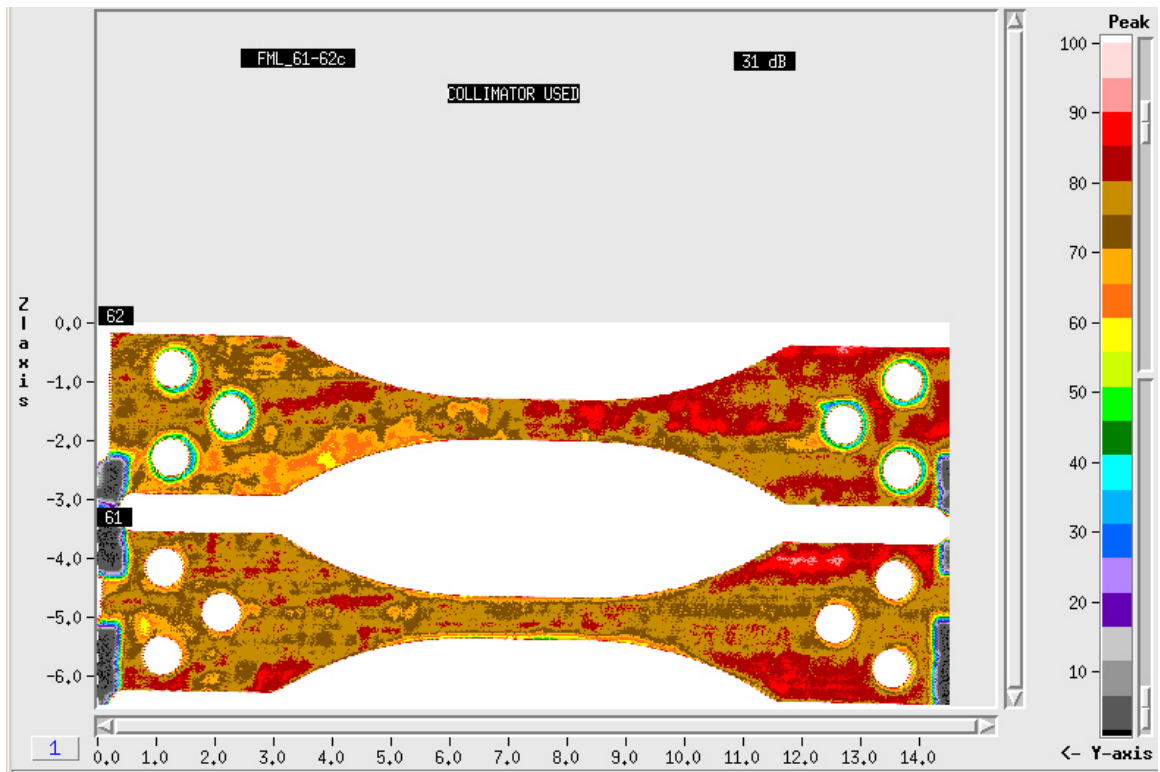Figure 185 : CentrAl C-Scan - Specimens 61, 62

Appendix B: CentrAl Specimen Test Matrix

Specimen Number	Fiber Orientation	RT Modulus	-55C Modulus	80C Modulus	RT Dogbone Failure	-55C Dogbone Failure	80C Dogbone Failure	RT Open Hole Failure	-55C Open Hole Failure	80C Open Hole Failure
13	0		X						X	
15	0			X						X
16	0				X					
18	0							X		
19	0						X			
21	0			X						X
28	0		X						X	
29	0							X		
30	0					X				
42	0							X		
63	0			X						X
64	0								X	
32	45		X						X	
33	45			X						X
34	45				X					
35	45							X		
36	45						X			
37	45			X						X
38	45		X						X	
39	45							X		
40	45					X		X		
46	45							X		
47	45									X
48	45		X						X	
49	67.5		X						X	
50	67.5			X						X
51	67.5				X					
52	67.5							X		
53	67.5						X			
54	67.5			X						X
55	67.5		X						X	
56	67.5							X		
57	67.5					X		X		
58	67.5							X		
59	67.5			X						X
60	67.5		X						X	
7	90		X						X	
8	90			X						X
9	90				X					
10	90							X		
11	90						X			
12	90			X						X
22	90		X						X	
23	90							X		
24	90					X		X		
25	90							X		
26	90			X						X
27	90		X						X	

Bibliography

1.   ASTM E8-04 : Standard Test Methods for Tension Testing of Metallic Materials. 2004.

2.   Cytec Engineered Materials., "FM 94 Modified Epoxy Film Technical Data Sheet." 1997.

3.   Daniel, Isaac M. and Ori, Ishai., *Engineering Mechanics of Composite Materials.* New York : Oxford University Press, 1994.

4.   Engineering Services Data Unit (ESDU)., "Standard Fatigue Loading Sequences - ESDU 97018." July 2003.

5.   Hagenbeek, Michiel., *Characteristics of Fibre Metal Laminates under Thermo-mechanical Loadings.* Delft University of Technology. Delft : 2005. PhD Thesis.

6.   Hartman, David, Greenwood, Mark E. and Miller, David M., *High Strength Glass Fibers.* AGY. Aiken : 1996. Technical Report.

7.   Herakovich, Carl T., *Mechanics of Fibrous Composites.* New York : John Wiley & Sons, Inc., 1998.

8.   Homan, J. J., "Fatigue Initiation in Fibre Metal Laminates." International Journal of Fatigue, July 2006, Issue 28, pp. 366-374.

9.   Jones, Robert M., *Mechanics of Compostite Materials.* : Hemisphere Publishing Corporation, 1975.

10.   Konish, Harold J. and Whitney, James M., "Approximate Stresses in an Orthotropic Plate Containing a Circular Hole." Journal of Composite Materials, April 1975, Issue 2, Vol. 9, pp. 157-166.

11.   MTS Systems Corporation., "Product Manual - Series 647 Hydraulic Wedge Grips." 1994.

12.   Peterson, R. E., *Stress Concentration Factors.* New York : 1974.

13.   Plokker, H. M., Alderliesten, R. C. and Benedictus, R., *Crack Closure in Fibre Metal Laminates.* Delft University of Technology. Delft : 2007. Technical Report.

14.   Rice, Richard C., et al., *Metallic Material Properties and Standardization.* Office of Aviation Research. Washington D.C. : 2003. Scientific Report. DOT/FAA/AR-MMPDS-01.

15.   Roebroeks, Geert H. J. J., et al., *The Development of CentrAl.* TU Delft. Delft : Technical Report.

16.   Schwartz, R. T. and Schwartz, H. S., "Fundamental Aspects of Fiber Reinforced Plastic Composites." Journal of Applied Polymer Science, New York : John Wiley & Sons, Inc., 1970, Issue 5, Vol. 14.

17.   Snider, H. Lawrence, Reeder, Franklin L. and Dirkin, William., *Residual Strength and Crack Propagation Tests on C-130 Airplane Center Wings With Service Imposed Fatigue Damage.* Lockheed-Georgia Company. Marietta : 1972. Technical Report.

18.   Vlot, Ad and Gunnink, Jan Willem., *Fiber Metal Laminates - An Introduction.*: Springer, 2001.

19.   Vlot, Ad., *Glare : History of the Development of a New Aircraft Material.* Dordrecht : Kluwer Academic Publishers, 2001.

20.   de Vries, Tjerk Johan., *Blunt and Sharp Notch Behaviour of Glare Laminates.* Delft : 2001. PhD Thesis.

21.   WesDyne Company : A Westinghouse NDE., "IntraSpect Ultrasonic and Eddy Current Inspection System Operations Manual (ver. 6.23)." 2008.

22.   Wu, H. F., et al., "Use of Rule of Mixtures and Metal Volume Fraction for Mechanical Property Predictions of Fibre-Reinforced Aluminium Laminates." Journal of Materials Science, 1994, Issue 17, Vol. 29, pp. 4583-4591.

23.   Young, Warren C. and Budynas, Richard G., *Roark's Formulas for Stress and Strain.* [ed.] Larry Hager. 7th Edition. New York : McGraw - Hill, 2002.

Vita

Capt Cox enlisted in the Air Force in May 1997. In May 2003, he graduated from the United States Air Force Academy with a degree in mechanical engineering and a commission as a 2nd Lieutenant. Upon graduation, he was assigned to the Warner Robins Air Logistics Center at Robins Air Force Base, GA. At Robins AFB, he worked as an engineer in the C-5 Galaxy Sustainment Office on various systems to include landing gear, primary flight controls, and cockpit instrumentation. He was also assigned to the Engineering Directorate at the Air Logistics Center where he served as direct supervisor for all new military engineers and as the primary instructor for the AFMC Aircraft Battle Damage Repair engineering program. In this capacity, Capt Cox ensured all deploying engineers were trained and well versed on the myriad of structural repair techniques for aircraft. He also authored the current Aircraft Battle Damage Repair Engineering Handbook. After graduating from the Air Force Institute of Technology, Capt Cox will be assigned to the Air Vehicles Directorate, Air Force Research Lab, Wright-Patterson AFB, OH.

REPORT DOCUMENTATION PAGE

Form Approved
OMB No. 0704–0188

1. REPORT DATE (DD–MM–YYYY)	2. REPORT TYPE	3. DATES COVERED (From — To)
26-03-2009	Master's Thesis	March 2008 - February 2009

4. TITLE AND SUBTITLE	5a. CONTRACT NUMBER
Thermomechanical Properties of Center-Reinforced Aluminum	5b. GRANT NUMBER
	5c. PROGRAM ELEMENT NUMBER

6. AUTHOR(S)	5d. PROJECT NUMBER
Cox, Geofrey S., Captain, USAF	5e. TASK NUMBER
	5f. WORK UNIT NUMBER

7. PERFORMING ORGANIZATION NAME(S) AND ADDRESS(ES)	8. PERFORMING ORGANIZATION REPORT NUMBER
Air Force Institute of Technology Graduate School of Engineering and Management (AFIT/ENY) 2950 Hobson Way WPAFB OH 45433-7765	AFIT/GAE/ENY/09-M04

9. SPONSORING / MONITORING AGENCY NAME(S) AND ADDRESS(ES)	10. SPONSOR/MONITOR'S ACRONYM(S)
Air Force Research Lab / Air Vehicles Directorate Edwin E. Forster, Ph. D. Aerospace Engineer 2130 8th St., Bldg 45, Rm. 121 WPAFB, OH 45433-5664 (937)255-5664	AFRL / RBSA
	11. SPONSOR/MONITOR'S REPORT NUMBER(S)

12. DISTRIBUTION / AVAILABILITY STATEMENT

APPROVED FOR PUBLICE RELEASE; DISTRIBUTION UNLIMITED

13. SUPPLEMENTARY NOTES
This material is declared a work of the U.S. Government and is not subject to copyright protection in the United States.

14. ABSTRACT

The rule of mixture approach was shown to produce an accurate theoretical prediction of the room temperature elastic modulus values when compared to the experimental results. The laminate's modulus value remained relatively constant over the -55C to 80C temperature range, indicating stable behavior despite temperature changes. Blunt notch tests also revealed that the laminate's strength was not significantly reduced due to the presence of small holes. Finally, fatigue testing demonstrated that the laminate retains its stiffness properties throughout its fatigue life, until failure.

15. SUBJECT TERMS
Glare, Fiber Metal Laminate, Hybrid Materials, Center Reinforced Aluminum

16. SECURITY CLASSIFICATION OF:			17. LIMITATION OF ABSTRACT	18. NUMBER OF PAGES	19a. NAME OF RESPONSIBLE PERSON Dr. Marina B. Ruggles-Wrenn , AFIT/ENY
a. REPORT	b. ABSTRACT	c. THIS PAGE	UU	300	19b. TELEPHONE NUMBER (Include Area Code)
U	U	U			(937) 255 -3636 x4641 marina.ruggles-wrenn@afit.edu

Standard Form 298 (Rev. 8–98)
Prescribed by ANSI Std. Z39.18